THÈSE

En vue de l'obtention du

DOCTORAT DE L'UNIVERSITÉ DE TOULOUSE

Délivré par :

Institut National Polytechnique de Toulouse (INP Toulouse)

Discipline ou spécialité :

Dynamique des fluides

Présentée et soutenue par :

M. THIBAULT BRIDEL BERTOMEU

le lundi 21 novembre 2016

Titre :

Investigation of unsteady phenomena in rotor/stator cavities using Large Eddy Simulation

---

Ecole doctorale :

Mécanique, Energétique, Génie civil, Procédés (MEGeP)

Unité de recherche :

Centre Européen de Recherche et Formation Avancées en Calcul Scientifique (CERFACS)

Directeur(s) de Thèse :

M. LAURENT GICQUEL

M. GABRIEL STAFFELBACH

Rapporteurs :

M. ERIC SERRE, CNRS MARSEILLE

M. MATTHEW JUNIPER, UNIVERSITE DE CAMBRIDGE

Membre(s) du jury :

M. GREGOIRE CASALIS, ISAE TOULOUSE, Président

M. KILIAN OBERLEITHNER, TECHNISCHE UNIVERSITAT BERLIN, Membre

M. LAURENT GICQUEL, CERFACS, Membre

M. PATRICE LE GAL, AIX-MARSEILLE UNIVERSITE, Membre

Résumé

Les phénomènes vibratoires ont souvent rendu difficile la conception des turbopompes spatiales. Aujourd'hui, malgré les nombreuses mesures de sécurité appliquées durant les étapes de design, les campagnes d'essai révèlent toujours de nouveaux phénomènes instationnaires au sein des cavités rotor/stator des turbines. Ces phénomènes, nommés 'bandes de pression', limitent fortement les performances de la machine. Comprendre et identifier la source de ces 'bandes de pression' sont les motivations premières de cette thèse. Dans cette optique, ce travail présente une étude numérique et théorique portant sur les écoulements tournants transitionnels et turbulents. L'accent de ce travail de recherche est porté sur la compréhension et l'identification des mécanismes présents dans une cavité rotor/stator à haut Reynolds. Ces écoulements sont en effet fortement influencés par des procédés rendus fortement tri-dimensionnels dûs à la présence des couches limites sur les disques et le long des parois cylindriques extérieure (carter) et/ou intérieure (moyeu). Les écoulements tournants à haut nombre de Reynolds sont ainsi le siège de phénomènes uniques qui induisent une réorganisation des fluctuations de pression et de vitesse sous forme de structures axisymmétriques et spirales, à la fois dans le coeur homogène de l'écoulement et dans les couches limites. Une question légitime est donc d'identifier le lien potentiel entre les 'bandes de pression' et ces diverses structures de ces écoulements.

Ce travail peut être divisé en deux sous-parties. Dans un premier temps, les cavités industrielles sont modélisées par de simples cavités lisses pour y étudier la dynamique de l'écoulement. Les campagnes de test révèlant de dangereux phénomènes instationnaires au sein des machines industrielles, l'accent est mis sur l'obtention et l'étude des fluctuations de pression dans les écoulements modèles. A l'aide de traitements de signaux ponctuels extrait de Simulations Grandes Échelles (SGE), il est démontré que les fluctuations de pression existent dans l'ensemble de la cavité et sont partout constituées des mêmes fréquences. Une Décomposition Modale Dynamique (DMD) est ensuite réalisée et révèle que chaque fréquence constituante est la fréquence d'un mode de cavité tri-dimensionnel sous-jacent. L'analyse est poursuivie pour montrer que la totalité de la dynamique de l'écoulement rotor/stator n'est en réalité pilotée que par un petit nombre de ces modes. Deux autres cavités de rapport d'aspect et rayon de courbure moyen différents sont ensuite introduites pour analyser l'impact des facteurs géométriques sur les fluctuations de pression et les modes sous-jacents. Pour compléter les conclusions tirées des SGE, des Analyses de Stabilité Linéaire (ASL) sont conduites sur la base de l'écoulement moyenné temporellement et azimutalement. Les modes DMD sont reconstruits grâce à une approche spatiale afin de montrer que ce comportement instationnaire peut être prédit. Dans un second temps, les SGE de trois configurations de turbine industrielle réelle sont réalisées pour étudier les fluctuations de pression *in situ*. Contrairement aux problèmes académiques, les différentes sous-cavités et anfractuosités présentes dans la géométrie industrielle influencent l'organisation spatiale et l'amplitude des fluctuations de pression, bien que leurs fréquences restent égales partout dans la géométrie. Les diagnostics et les techniques de post-traitement éprouvés sur les écoulements académiques sont ensuite appliqués aux problèmes industriels et révèlent que malgré la complexité de

la géométrie, les phénomènes instationnaires détectés expérimentalement au sein de la cavité rotor/stator de la turbine sont eux aussi liés à une superposition d'un nombre fini de modes identifiés par DMD.

Abstract

Vibrations are known to have caused problems during the development of space engine turbopumps. Even today, despite the numerous palliative measures taken during the design phases, test programmes often reveal unidentified unsteady pressure phenomena in rotor/stator cavities of turbines. Such features, named 'pressure bands', have proven highly detrimental to the proper operation of the turbopump. Understanding and eventually identifying the source of the 'pressure bands' are the primary motivations for this thesis. As such, this work provides a numerical and theoretical investigation of transitional and turbulent enclosed rotating flows, with a focus on the formation of macroscopic coherent flow structures. The underlying processes within such flows are strongly three-dimensional due to the presence of boundary layers on the discs and on the walls of the outer (resp. inner) cylindrical shroud (resp. shaft). Therefore, high-Reynolds transitional rotating flows are strongly influenced by unique phenomena manifesting through an organization of velocity and pressure fluctuations under the form of coherent axisymmetric and/or spiral structures in the disc boundary layers as well as the homogeneous core flow. A legitimate question hence relates to the potential link between the reported 'pressure bands' of the real applications and the large scale structures of these flows.

To address this question, the present work focuses of two major investigations. First, industrial cavities are modelled by smooth rotor/stator cavities and therein the dominant flow dynamics is investigated. The emphasis of the associated analysis is put on the monitoring of unsteady pressure fluctuations within the smooth cavities. Using pointwise spectral analysis obtained from the Large Eddy Simulation (LES) predictions, the pressure fluctuations are shown to exist everywhere in the cavity and with the same constituent frequencies. Dynamic Modal Decomposition (DMD) is then performed on the flow and reveals that each constituent frequency matches the frequency of an underlying three-dimensional cavity mode. Their combination is proven to be the main driver of the flow dynamics, and it therefore shows how the unsteady structures in the different layers of the flow communicate. Two cavities of different aspect ratios and mean curvatures are then similarly investigated to point out the strong changes induced by geometrical factors. To complete the LES findings, Linear Stability Analyses (LSA) are performed on the temporally- and azimuthally-averaged flows and observed DMD modes are reconstructed using a spatio-temporal approach to show that the unsteady behaviour of such a rotating flow can be predicted. Then, the LES of three configurations of real industrial turbines are conducted to study *in situ* the pressure fluctuations. Contrary to the model cases, the flows in the different sub-cavities present in the industrial geometries behave differently from one another. The spatial organization of the unsteady phenomena is observed to change accordingly, inducing fluctuations in the amplitude of the pressure perturbations, although the constituent frequencies are the same throughout the geometry. The diagnostics and high-fidelity post-processing techniques validated on academic problems are then applied to the industrial problems. They show that despite the geometrical complexity, the strong unsteady pressure phenomena detected experimentally in the turbine cavities are also related to a superposition of a few DMD modes.

Acknowledgements

To my parents,
To my grand-parents,

Contents

Chapter 1

Foreword

This Ph.D. work relates to the spatial context and its requirement that any development should yield e cient, robust products. Such objectives are however more and more di cult to meet especially in the current context where more and more actors are present and time of development for new products is highly reduced. This work is issued speci cally from the long-term collaboration between CNES//DLA (Centre National d Études Spatiales//Division des LAnceurs) and Snecma-DMS (Division des Moteurs Spatiaux). More speci cally, It inscribes itself in the context of space propulsion and design of cryogenic engines turbomachinery. To introduce the topic, this foreword starts with a concise history of rocketry with a focus on the concepts that led to the need for turbopumps in cryogenic engines. It is followed by a broad presentation of the literature dealing with rotating ows. Finally, a detailed overview of the present work is proposed where the content of each chapter is summarized.

1.1   Introduction

The Russian mathematics professor Tsiolkovsky (Fig. 1.1*a*) was the first to properly describe the fundamental principles and rocket flight equations necessary to build rocket vehicles. In opposition to what had been known since the 10th century thanks to the Chinese early solid propellant rocket missiles ("fire lances", Pan (1987)), Tsiolkovsky's work (1903) is the first to expose the possibility of reactive propulsion and even interplanetary travel using liquid hydrogen and oxygen combustion. The key contribution from this work is that to produce thrust, one must bring together an oxidizer and a fuel that can be burnt together, the reaction products being directed in a nozzle located at the rear of the rocket, hence giving thrust for the forward motion. In 1923, the initial ideas proposed by Tsiolkovsky (1903) are further developed by Oberth. His Ph.D. thesis indeed contains very advanced theoretical work and introduces the ideas of multistage vehicles and fuel-cooled thrust chambers. At the same period, the American Robert H. Goddard (Fig. 1.1*b*) publishes a monograph called "A Method for Reaching Extreme Altitudes" (Goddard, 1919) in which he presents groundbreaking theoretical work in space flight theory. His developments are of the same standing as Oberth's contribution but he focuses his work on three-axis control and steerable thrust so as to effectively improve rocket flight control. Goddard's work yields the first successful flight using a liquid propellant rocket engine in 1926[1].

The rocket launched by Goddard was 3 m long and reached an altitude of 56 m with a maximum speed of 27 m/s. With such characteristics, it is often referred to as a proof of concept in the literature rather than a pre-production prototype. The first practical rocket, i.e. capable of carrying a payload, was the German V2 (*Vergeltungswa e 2*, "Retribution Weapon 2") built by a team originally formed and lead by Wernher Von Braun (Fig. 1.1*c*), with a first successful launch in 1942. Aside from the numerous

---

[1]The interested reader is further referred to Goddard & Pendray (1970), Yur'yev (1951), Von Braun & Ordway (1974) or Sutton (2006) for an in-depth historical perspective on liquid propellant rocket engines.

(a) (b) (c)
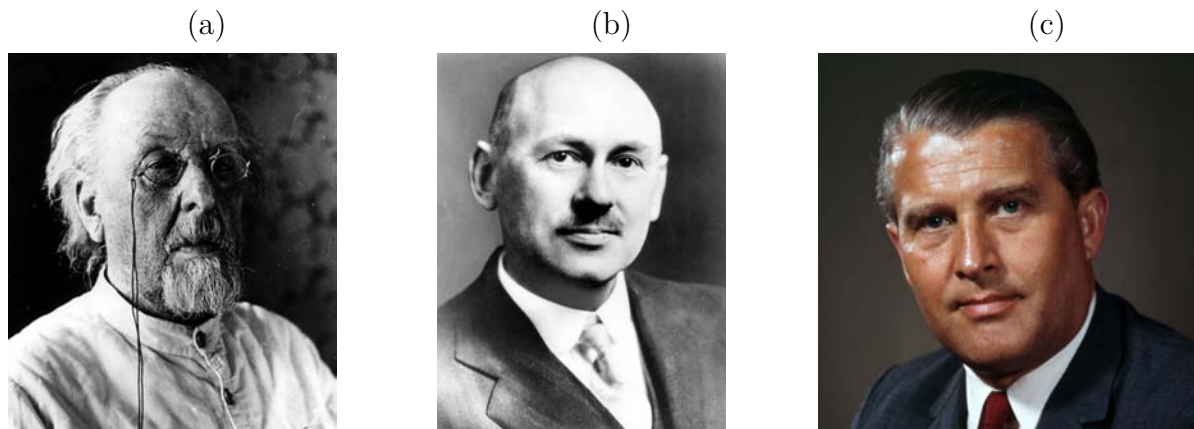
Figure 1.1 − (*a*) Konstantin Tsiolkovsky, 1857-1935 (*b*) Robert H. Goddard, 1882-1945 (*c*) Wernher Von Braun, 1912-1977

technological revolutions in structure and hydraulics that the German engineers had to come up with so that the 14 m long rocket could sustain a maximum velocity of 1600 m/s and a flight range of 320 km, the high-performance C_2H_6O/O_2 (ethanol/oxygen) engine required the addition of a rotating machinery called a turbopump (TP). This specific and fundamental device just invented in 1942 was designed to feed the liquid propellants in the combustion chamber at a sufficiently high pressure to ensure high thrust levels. Figure 1.2 presents the details of the two basic configurations used for liquid-propellant rocket engines: a typical pressure-fed system (Fig. 1.2*a*) similar to that used by Goddard and mostly used today for low thrust, low total energy propulsion systems, and a turbopump-fed system (Fig. 1.2*b*) typically used in applications with larger amounts of propellants and higher thrusts such as in space launch vehicles.

A TP is a high-pressure rotating piece of machinery usually consisting of a turbine driving one or two axial and/or centrifugal compressors. Its primary purpose is to raise the propellant pressure before delivering them into the piping system that will feed the thrust chamber(s). Naturally, there exists many possible TP configurations to match engine requirements - the most common solutions are summarized on Fig. 10-4 in Sutton & Biblarz (2001). Obviously the overall space occupied by the machinery or the maximum allowable turbine gas inlet temperature have to be taken into account during the design phase. Developed by Safran Snecma DMS, Vulcain 2 engine for example possesses two complete separate turbopumps, one for the liquid hydrogen LH_2 and the other for the liquid oxygen LOx as seen on Fig. 1.3*a*, both systems being equipped with two-stage turbines fed by warm gases coming from a single common gas generator chamber shown on Fig. 1.3*b*.

An additional constraint of such a device that is of prime interest to the present thesis can be described as follow (Sutton & Biblarz, 2001):

> *the TP should not stimulate or cause any significant vibration in the engine, or should not be adversely affected by externally caused vibrations and should function properly in all operating conditions encountered during the flight of*
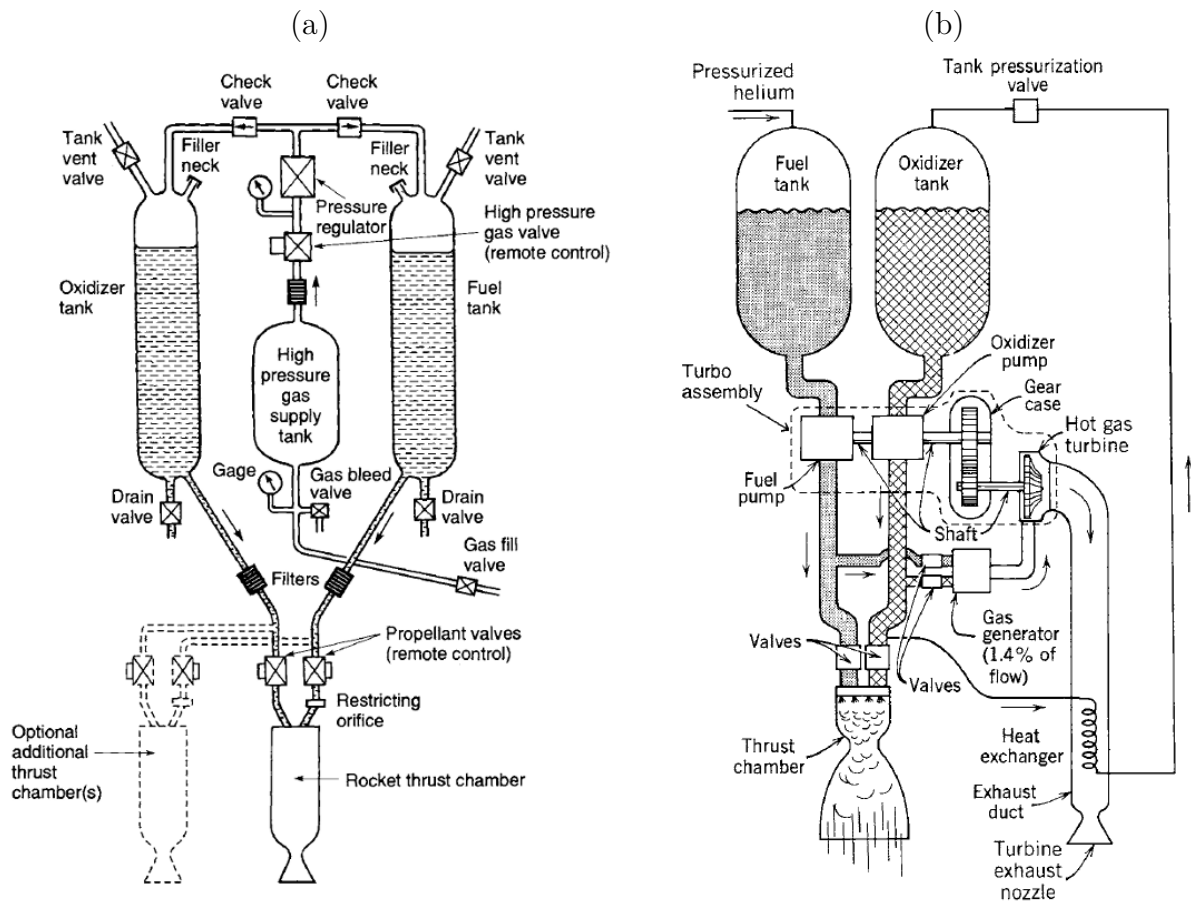
Figure 1.2 − (*a*) Schematic flow diagram of a liquid propellant rocket engine with a gas pressure feed system. (*b*) Simplified schematic diagram of one type of liquid propellant rocket engine with a turbopump feed system and a separate gas generator generating "warm" gas for driving the turbine. Source : Sutton & Biblarz (2001)
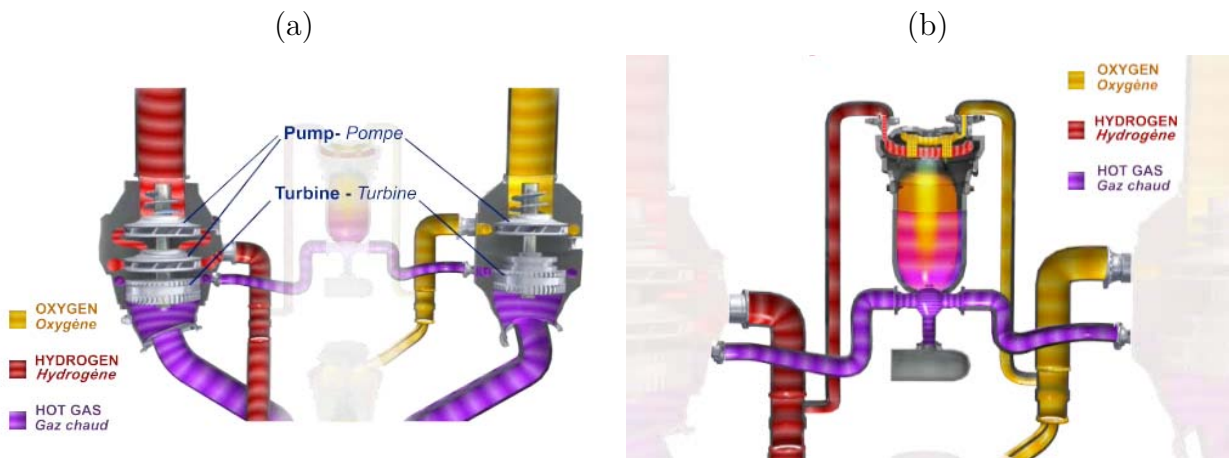
Figure 1.3 − (*a*) Representation of the two turbopumps used in the Vulcain 2 engine and their gas generator. (*b*) Detail of the gas generator feeding both turbopumps of the Vulcain 2 engine. Source : *How Do Our Engines Work ?*, Safran Snecma

the rocket.

Vibrations have indeed often caused problems during the development of turbopumps, and although numerous palliative measures have become common practice over the years, some fluctuating phenomena that remain unexplained are still spotted today, for example in turbine rotor/stator cavities. Indeed and despite the high Reynolds number of such industrial flow configurations, benchmarking campaigns often reveal the existence of unidentified unsteady pressure phenomena registered within the rotor/stator cavities of the first stage of the turbine. Dedicated spectral analyses show that signals are often marked by a handful of constituent frequencies indicative of strong oscillatory and coherent phenomena. Such features, named 'pressure bands' by experimentalists due to the patterns appearing on the spectrograms, have proven highly detrimental to the proper operation of the turbopump, eventually threatening the structural integrity of the rocket. Upon investigation, the experimentalists observed that even the slightest change in the geometry of the rotor/stator cavity could trigger a wide range of modifications in the response of the flow, and 'pressure bands' can be seen to cancel, be damped or amplified, their frequencies blue- or red-shifted. Another interesting fact about those 'pressure bands' is that, for a fixed geometry, their frequencies and amplitudes appear to be a function of the operating point of the machine and the thermal state of the flow in the cavity. Understanding and eventually finding the source of the 'pressure bands' phenomenon are the prime motivation of this Ph.D. work.

The first interrogations about rotating flows appear in the literature in 1905, brought up by Ekman in relation with oceanography and the study of wave motion and currents. Rapidly, several authors generalize the configuration of Ekman (1905) to model all sort of rotating flows and from that time on the interest for rotating flows did not cease to grow, revealing a flow configuration that is both easy to generate in an experiment and astonishingly rich in terms of applications. More than a century after Ekman, the study of his mathematical models, especially for the rotating flow between two finite discs, is still of great interest. Indeed on one hand, even if laminar rotating flows over or between rotating discs yield a simplified set of Navier-Stokes equations that can be easily solved, the existence and also the uniqueness of the solution often have yet to be proven mathematically. On the other hand, more complex cases such as high Reynolds number turbulent and/or enclosed rotating flows are still under study for all the unsteady phenomena arising therein are not fully understood.

Rotating disc(s) flows are also relevant to many industrial applications in a number of different domains such as astrophysics (Ferrari *et al.*, 1981, 1982), geophysics, chemistry, electronics (Hendriks, 2010; Shirai *et al.*, 2013), meteorology, oceanography (Ekman, 1905) and especially turbomachinery design (Owen & Rogers, 1989, 1995) - some of which we detail in the following. In astrophysics, one can quote for instance the galactic discs (Ferrari *et al.*, 1981), or any kind of accretion discs, that are objects with a diameter of the order of several hundreds of astronomic unities and inside which the rotation speed is found to strongly depend on the radius. Such a differential rotation induces an increased sensitivity to shear instabilities of the same nature as those found at the interface between the boundary layer and the core flow of a rotor/stator flow. In geophysics on the other

hand, inside rapidly rotating telluric planets with a liquid core and a solid mantle, the flow organizes according to convection cells and is subjected to Rossby waves, a behaviour similar to what has already been observed in high aspect ratio rotor/stator cavity flows. When it comes to aeronautical and spatial engines, cavity flows prove to be an essential components. For instance, in gas turbines, a network of cavities is calibrated and managed to divert part of the main cold stream which is then re-injected in the hot regions of the engine to shield walls from the hot combustion products. On the other hand, for pumps, cavities are naturally present at the junction of fixed and rotating parts. In both contexts, mastering the flow stability in rotor/stator cavities appears anyway essential to avoid imposing too large flow variations like those generated by the 'pressure bands' phenomenon which could lead to miss-tuned operating conditions in the engine and/or a drastic loss of performance or life-span.

As mentioned above, the present thesis has been motivated by the industrial need formulated by SNECMA DMS (Vernon) to understand the instability of the flow triggered in high-speed rotating machinery and to pinpoint the source of the unsteady pressure phenomenon known as 'pressure bands'. This work consequently focuses on the flows existing in the first stage of a turbopump turbine. To do so however, a thorough presentation of the basic theoretical concepts of rotating flows (Chap. 2) and a preliminary study of academic rotor/stator flows (Chap. 3) are necessary steps leading to the study of the dynamics of a real industrial configuration (Chap. 4). This work inscribes itself in the continuity of all the numerical investigations bearing on the dynamics of academic smooth rotor/stator cavity flows (see e.g. Serre *et al.*, 2001; Séverac *et al.*, 2007) and of all the coupled analytical-numerical studies using linear stability analysis (see e.g. Serre *et al.*, 2004) to examine the structures present in the discs boundary layers. Naturally, rather than merely reproducing the work of others, we use published data as a reference to validate our unstructured Large Eddy Simulation (LES) approach. This being done, we then use our results to assess the impact of geometrical characteristics and investigate the dynamics of a smooth rotor/stator flow. The latter investigation leads to creating diagnostics dedicated to the identification and analysis of unsteady pressure phenomena in rotating flows that will be used in the following study of real industrial flows. Furthermore, we use linear stability analyses to show that it is possible to find the three dimensional representation of the globally unstable modes in a cavity using only a mean flow instead of a full 360° LES.

1.2   Overview of this thesis

A detailed description of the underlying theoretical concepts and definitions is given in Chap. 2. Therein, a thorough literature review is conducted, followed by the comprehensive development of the systems of differential equations based on the cylindrical Navier-Stokes equations that describe the laminar motion of a fluid over a single disc or within a two-discs rotor/stator cavity. These equations, although well known, are included in the present work for clarity purpose and so the laminar profiles can be used in the study of the LES predictions presented in Chaps. 3 and 4. Then, the notion of

decomposition of the coherent velocity in normal modes is introduced and leads to an outline of the theoretical concepts pertaining to linear stability analysis. Again, the description of the techniques pertaining to linear stability analyses has been added to ease the later discussion about global modes in enclosed rotor/stator flows (Sec. 3.7). The chapter ends with the strategies used in the implementation of the numerical linear stability solver created during the present thesis, and the validation of the latter code based on well known test-cases from the literature.

The main part of this thesis is organized in two chapters, which correspond to two numerical investigations (Chaps. 3 & 4) of academic and industrial rotor/stator flows respectively. The former has for principal objective to validate the LES solver used throughout this work and closely study the dynamics of a simplified rotor/stator flow in order to gain some insight about the 'pressure bands' phenomenon. The latter on the other hand is dedicated to the study, *in situ*, of the unsteady pressure phenomenon and uses all the diagnostics and post-processing techniques validated in Chap. 3. Each chapter begins with a short abstract, followed by a brief introductory section dedicated mostly to a review of the most recent advances found in the literature. A comprehensive section presenting the results of the investigation follows and the chapter is concluded by a summary and discussion of the major results.

In the following, the major concepts tackled in each investigation are summarized.

- **Chapter 3**: This investigation focuses on the formation of large scale structures in enclosed smooth rotor/stator cavity flow and their relation to known boundary layer instabilities. The preliminary objective of this chapter is to assess the ability of Large Eddy Simulation (LES) to capture with accuracy the dynamics of such high Reynolds numbers rotating flows. Once validated, numerical predictions in a simplified cylindrical configuration are probed in order to study the relation between pressure fluctuations monitored in the cavity and the two- & three-dimensional structures present in the boundary layers or in the core flow. For the purpose of understanding, simulations and analyses are extended to a low aspect ratio cavity without and with a central shaft in order to assess the impact of geometry and provide results for a geometry more relevant to turbomachinery applications: i.e. with an interdisc gap only a fraction of the discs radii and a stationary cylindrical shroud. Expectedly, all stator boundary layers are found unstable at such high rotation Reynolds numbers and display known coherent patterns. It is shown by Dynamic Modal Decomposition (DMD) that the boundary layer structures relate to macro-structures confined to the homogeneous core of the cavity and previously unidentified in the literature. Those structures have a modal nature and result from the combination of a handful modes possessing given rotation frequencies that coincide with the constituent frequencies of the pointwise signals. The comparison of the three configurations provide clear evidence that the entire dynamics of any rotor/stator cavity flow is similarly driven by few fundamental modes superimposed onto the mean flow. The chapter ends with a discussion about linear stability analyses of the mean cavity flow. We show that in some cases, the three-dimensional boundary layer structures are related to globally unstable linear modes. By nature, such modes influence the whole flow, thus explaining why the 'pressure bands'

frequencies are seen everywhere in the cavity.

- **Chapter 4**: This chapter deals with the flow in the turbine stage of a space engine turbopump, for which the geometry is complex and the rotation Reynolds number is much higher than in the academic cavities investigated in Chap. 3. The first goal of this investigation is to pursue the validation work started in the previous chapter and demonstrate the ability of LES to accurately reproduce the flow in a complex industrial rotor/stator 360°-cavity as well as the sensitivity to large scale motions and spectral content observed in experiments. Attention is then focused on a specific unsteady pressure phenomenon named 'pressure bands' observed during benchmarking campaigns. Even though boundary layer structures cannot be identified as clearly as in academic cavities, the same strategy as in Chap. 3 is applied and the same modal decomposition algorithm (DMD) is used on the flow. The conclusions drawn in Chap. 3 are found to hold for the industrial grade flow: its dynamics is driven by a handful modes with frequencies matching the constituent frequencies of the "pressure bands" phenomena and even if the boundary layers are fully turbulent, the core stays organized. Since experimentalists noticed that the slightest changes in the geometry or operating point could trigger a wide range of modifications in the characteristics of the 'pressure bands', several configurations are investigated in this chapter.

  - In the first configuration, the computational domain is restricted to the rotor/stator cavity itself and the turbine stream channel.

  - This investigation is therefore completed by the study of a second geometry closer to the real machinery due to the inclusion of a previously omitted high-radius cavity. In that case, the entire spectral content of the flow, including the rotation frequencies of the constituent modes is shifted towards lower frequencies after the addition of this high-radius cavity.

  - Finally, the third configuration reproduces an operating point where the average temperature in the cavities in higher in order to assess the sensitivity of the 'pressure bands' phenomenon to the thermal environment. The impact on the flow is found to be much greater since the local Reynolds number on the discs is modified everywhere and the flow organization completely overhauled.

All in all, the results from Chap. 3 and Chap. 4 can be condensed to the following statements. At high enough Reynolds number, instability of the stator layer is triggered in smooth cavities as well as industrial complex geometry cavities and an unstructured wall-resolved LES approach is able to capture such a complex dynamics. After a few convection times, large scale structures attached to the stator layer patterns appear in the homogeneous core of the cavity which may trigger the transition of the rotor boundary layer if the Reynolds number is high enough. These structures are modal in nature and result from the combination of a handful of modes identifiable using Dynamic Modal Decomposition (DMD, Schmid (2010)). The three-dimensional modes, present everywhere in the cavity, control the spectral content and the constituent frequencies of all pointwise

unsteady phenomena are, in fact, the rotation frequencies of those constituent modes. In some cases, the DMD modes are related to globally unstable modes of the mean cavity flow, which explains why they influence the whole flow and why their frequencies can be monitored everywhere in the cavity.

Chapter 2

Theory of rotating flows

Contents

In this first chapter we discuss in detail the theoretical concepts and definitions pertaining to rotating flows and their linear stability. After a historical perspective summarizing the literature on the subject, the analytical models existing for one- and two-disc flows are thoroughly presented. That presentation ends with an opening on enclosed rotor/stator cavities and the description of the different flow regimes susceptible to arise. Although the systems of equations as well as the flow regimes have already been described in numerous documents by previous workers, we mention them again in the present thesis to simplify the later discussions about the LES results (Chaps. 3-4). Indeed, the velocity profiles generated by these simplified sets of equations will serve as reference to qualify the level of turbulence of the enclosed rotor/stator cavity flows so as to classify them in the right flow regime. Moreover, as the use of these profiles eventually leads to the validation of the LES solver, the present theoretical description also participates in understanding the source(s) of the pressure bands phenomenon in industrial turbine stages. The second part of the chapter is dedicated to an outline of the main concepts of linear stability analysis and their numerical implementation. Once again, these notions are well known, but their thorough presentation is necessary as it allows to clarify the global mode reconstruction presented in Chap. 3. That outline represents the necessary foundation that leads to showing that in some cases the unsteady phenomena occurring in a rotor/stator cavity are related to the stability of the mean flow.

2.1 Characterization of disc flows

2.1.1 Introduction

The interest in rotating flows can be traced back to the Norwegian North Polar Expedition (1893-1896), when Pr. Nansen (1902) found that the ice-drift produced by a given wind did not follow exactly the direction of the wind but rather deviated 20-40° to the right of it. He correctly assumed that the supplementary drift was caused by the Earth's rotation. He indeed explained that when the wind is weak enough, the Coriolis forces introduced by the planet's rotation are not negligible anymore. Following this remark, Ekman (1905) studied analytically the problem of a wind-driven rotating flow subject to a pressure gradient, Coriolis and frictional forces. Ekman confirmed the explorer's hypothesis by proving that the flow has indeed a boundary-layer-like structure with a mean velocity vector whose length changes exponentially with depth and whose angle grows linearly with depth: it forms the well-known Ekman spiral, depicted on Fig. 2.1.

Later, Von Kármán (1921) studied analytically the structure of a laminar flow above an infinite rotating disc without assuming, contrary to Ekman (1905), a bulk motion of the system; he rather hypothesized that the fluid far from the disc is at rest. Within such a framework he produced a self-similar profile, exact solution of the axisymmetric stationary Navier-Stokes equations in cylindrical coordinates. Cochran (1934) then using a technique known today as the method of matched asymptotic expansions, obtained a
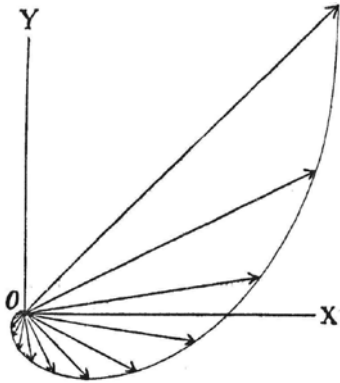
Figure 2.1 – Illustration of the "Ekman spiral". The direction and velocity of the flow current at different depths within the boundary layer are represented by the arrows, the longest arrow referring to the surface where the drift-current is directed 45° to the right (resp. left) of the velocity of the wind in the northern (resp. southern) hemisphere. The direction of the y-axis is the direction of the wind-velocity relative to the water. Source: Ekman (1905).

more accurate solution to the problem. It revealed that the mean axial velocity far from the disc converged to a constant negative value, a property that later came to be known in textbooks as the "von Kármán viscous pump" phenomenon (see e.g. Panton, 1996; White, 2006). In other words, in this configuration, a thin layer of fluid above the disc is put in rotation under viscous effects; as particles from this layer are radially ejected due to the centrifugal and Coriolis forces, an axial flux bringing particles into the boundary layer appears to balance the radial flux. This flow is represented on Fig. 2.2.
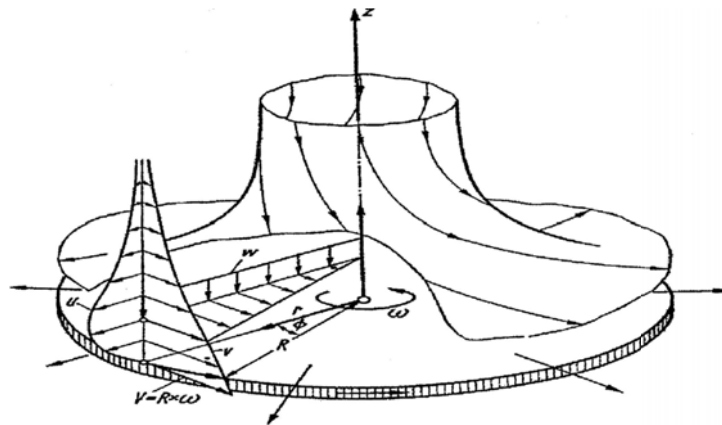
Figure 2.2 – Flow of a fluid initially at rest put into motion by a rotating disc. Source: Schlichting (1960).

Bödewadt (1940) applied the same strategy as Cochran (1934) to produce a self-similar solution to the flow produced by a rotating fluid impinging on a stationary infinite disc and corresponding to Fig. 2.3. In this configuration, the fluid particles far from the disc are in equilibrium due to the centrifugal force exactly balancing the radial pressure gradient. However, when a particle gets closer to the disc its circumferential velocity has to decrease, and as a consequence the centrifugal force diminishes. As a result the fluid close to the disc settles into a centripetal motion balanced by an axial flux of particles moving away from the disc.

The first researcher to work with the mathematical resemblance of the three aforementioned flows was Batchelor (1951). In his now famous note, he shows how the ratio of the fluid and the disc rotation velocities is sufficient to characterize the flow over a single
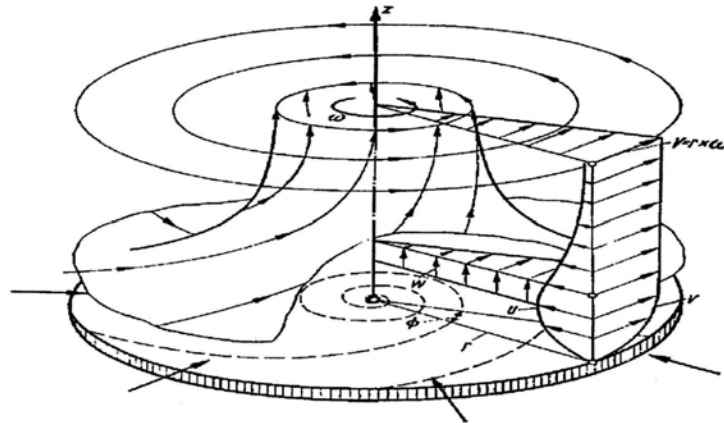
Figure 2.3 – Flow of a fluid in solid rotation impinging on a stationary disc. Source: Schlichting (1960).

disc, and presented for each relevant case the streamlines of the flow (see Batchelor, 1951, Fig. 1-4). Rogers & Lance (1959) published an analytical version of the phenomenological description provided by Batchelor (1951). In that work, they solve numerically the three sets of equations using the same technique as Cochran (1934), thereby confirming the results obtained by Cochran (1934) and the streamlines presented by Batchelor (1951). Surprisingly however, Rogers & Lance (1959) computations did not yield the same asymptotic axial velocity in the case of the Bödewadt (1940) layer. This discrepancy was later attributed to numerical inaccuracies by Nydahl (1971) who solved the same equations with 16 significant figures and found the same values as Bödewadt (1940). The similarities between the laminar Ekman (1905) layer, the Von Kármán (1921) boundary layer and the Bödewadt (1940) boundary layer solutions are today well established. The reader can refer to, for example, the early unifying work by Tatro (1966) and Tatro & Mollo-Christensen (1967), Faller (1991) or more recently, Lingwood (1995*a*, 1997). The model used in this thesis for the description of the laminar steady flow over a single disc is actually due to an original effort by Faller (1991) to unite all three fundamental flows under one parametrized set of equations.

In the same fundamental work, Batchelor (1951) showed how Von Kármán (1921) solution could be extended to the steady flow of a viscous incompressible fluid between two infinite rotating discs. The former author, in addition to obtaining the differential equations governing the motion (see Sec. 2.1.2.b), gave a qualitative discussion of the nature of the flow field one might expect for various values of the ratio of the angular velocities of the two discs. The chief characteristic of the predicted flows is that at high Reynolds numbers, in almost all cases, the main body of the fluid is also rotating and transitions from the bulk rate of rotation to the discs take place in a narrow layer. Some of Batchelor (1951) conclusions, especially those concerning the cases where the two discs rotate in opposite directions or one disc is stationary, were later criticized by Stewartson (1953). In his case, the tangential velocity outside the boundary layer goes to zero and the radial velocity in the homogeneous core of the flow is negative. This is indeed contrary to Batchelor (1951) predictions although the mathematical solutions and experimental data obtained by Stewartson (1953) are in agreement. A few years later,

the first in-depth study of the special case where one disc is at rest was lead by Grohne (1956) who used numerical methods to integrate the differential equations ; in doing so, he found solutions for small rotation velocities that actually behave like Batchelor (1951) solutions. The controversy ends with Kreiss & Parter (1983). The authors thoroughly analysed mathematically the existence and uniqueness of the solution for the flow between two infinite discs with given rotation speeds and proved the existence of a whole class of solutions depending on the initial state of the flow. Holodniok *et al.* (1977) and Holodniok (1981) had already noted that the key parameter was the interdisc Reynolds number $Re_h = h^2\Omega/\nu$ (with h the interdisc distance, Ω the system rotation rate and ν the kinematic viscosity of the fluid) and observed a unique branch solution of the problem for small Re_h whereas for $Re_h > 220$ the number of solutions became multiple. The numerical simulations performed by Cousin-Rittemard (1996) during her PhD thesis confirm the existence of the two branches obtained by direct mathematical resolution of the system of the previous authors: a first branch starting from $Re_h = 0$ where the flow matches the predictions by Batchelor and a second unstable branch starting from $Re_h = 217$ that yields solutions of the Stewartson kind.

The following sections rely on this rich history to present analytical solutions to the basic problems tackled in the present chapter: one-disc flows and rotor/stator flows. These solutions will be used regularly throughout the following sections and chapters with multiple purposes. The analytical velocity profiles will be first considered as reference data to assess the accuracy of Large Eddy Simulation (LES) predictions of flows in academic (Chap. 3) or industrial (Chap. 4) enclosed rotor/stator cavities. On the other hand, it is shown in Sec. 2.2 that the linear stability analysis of these profiles has already been documented in the literature. Therefore, the auto-similar solutions obtained from the simplified Navier-Stokes equations (Sec. 2.1.2) will also serve as test-cases to validate the behaviour of the Linearized Navier-Stokes Equations (LNSE) solver (Sec. 2.2.4.e) developed during this thesis. Once validated, the solver is used in relation with academic rotor/stator cavity flows to show that the unstable modes predicted by the LES are related to globally unstable linear modes in some cases. This further leads to showing that in these cases, some of the three-dimensional structures present in the LES solutions can be obtained by integration of successive local stability analyses.

2.1.2 Modeling the laminar disc flows

As mentioned earlier, the first part of this chapter concerns the analytical solutions to the infinite one- and two-disc flow problems. These solutions stem from simplified sets of Navier-Stokes equations obtained by assuming that the velocity and pressure profiles are auto-similar over (between) the infinite disc(s). We mention these developments in the present thesis to support and simplify the analysis of the LES results obtained in the following chapters (Chaps. 3 & 4).

The coordinate system used throughout Sec. 2.1, if nothing else specified, is shown in Fig. 2.4. Note also that when a distinction is necessary, dimensional variables will be superscripted with an asterisk, i.e. (r^*, θ, z^*).
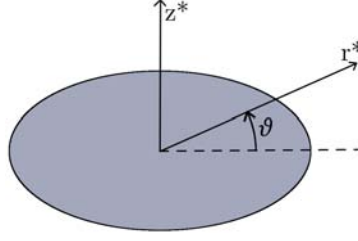
Figure 2.4 − Cylindrical coordinate system (r^*, θ, z^*) used throughout Sec. 2.1.

2.1.2.a The Bödewadt-Ekman-Karman (BEK) model for the laminar flow over a free disc

The model presented here describes a family of boundary-layer flows caused by a differential rotation rate between a solid boundary (a disc) and an incompressible fluid in rigid-body rotation above it. Particular cases of this family are the Ekman (1905), Von Kármán (1921) and Bödewadt (1940) boundary layer flows, hence the family being referred to as the BEK system. Note that the first and last are of special interest as they arise in the study of the rotor-stator cavity flows (see Sec. 2.1.2.b). The radius of the disc and the extent of the fluid above the disc are considered to be infinite. The disc and fluid rotate about the same vertical axis - the axis z shown in Fig. 2.4 - with angular velocities Ω_d^* and Ω_f^*, respectively. The Bödewadt (1940) layer arises when the disc is stationary and the fluid rotates, i.e $\Omega_d^* = 0$ and $\Omega_f^* \neq 0$ while for the Ekman (1905) layer $\Omega_d^* \simeq \Omega_f^*$ and for the Von Kármán (1921) layer $\Omega_d^* \neq 0$ and $\Omega_f^* = 0$. Between these particular examples are flows in which both the disc and the fluid rotate but with differing angular velocities.

The continuity and momentum equations for the axisymmetric mean steady flow are formulated in cylindrical-polar coordinates (r^*, θ, z^*) in a reference frame rotating at Ω_d^* and can be written as,

$$\frac{1}{r^*}\frac{\partial(r^*U^*)}{\partial r^*} + \frac{\partial W^*}{\partial z^*} = 0, \tag{2.1.1}$$

$$U^*\frac{\partial U^*}{\partial r^*} + W^*\frac{\partial U^*}{\partial z^*} - \frac{V^{*^2}}{r^*} - 2\Omega_d^* V^* $$
$$= -\frac{1}{\rho^*}\frac{\partial P^*}{\partial r^*} + \nu^*\left(\frac{1}{r^*}\frac{\partial}{\partial r^*}\left(r^*\frac{\partial U^*}{\partial r^*}\right) + \frac{\partial^2 U^*}{\partial z^{*^2}} - \frac{U^*}{r^{*^2}}\right), \tag{2.1.2}$$

$$U^*\frac{\partial V^*}{\partial r^*} + W^*\frac{\partial V^*}{\partial z^*} + \frac{U^*V^*}{r^*} + 2\Omega_d^* U^* = \nu^*\left(\frac{1}{r^*}\frac{\partial}{\partial r^*}\left(r^*\frac{\partial V^*}{\partial r^*}\right) + \frac{\partial^2 V^*}{\partial z^{*^2}} - \frac{V^*}{r^{*^2}}\right), \tag{2.1.3}$$

$$U^*\frac{\partial W^*}{\partial r^*} + W^*\frac{\partial W^*}{\partial z^*} = -\frac{1}{\rho^*}\frac{\partial P^*}{\partial z^*} + \nu^*\left(\frac{1}{r^*}\frac{\partial}{\partial r^*}\left(r^*\frac{\partial W^*}{\partial r^*}\right) + \frac{\partial^2 W^*}{\partial z^{*^2}}\right), \tag{2.1.4}$$

where $\mathbf{U}^* = [U^*, V^*, W^*]$ denotes the mean radial, azimuthal and axial velocities, respectively, and P^* is the mean pressure. By extension of the exact similarity solution for the Von Kármán (1921) flow, it is assumed that the dimensionless mean flow variables take

the following form :

$$U(z) = \frac{U^*}{r^* \Delta\Omega^*} = \frac{U^*}{r^* \Omega^* Ro}, \tag{2.1.5}$$

$$V(z) = \frac{V^*}{r^* \Delta\Omega^*} = \frac{V^*}{r^* \Omega^* Ro}, \tag{2.1.6}$$

$$W(z) = \frac{W^*}{L^* \Delta\Omega^*} = \frac{W^*}{L^* \Omega^* Ro}, \tag{2.1.7}$$

$$P(r,z) = \frac{P^*}{\rho^* L^{*2} \Delta\Omega^{*2}} = \frac{P^*}{\rho^* L^{*2} \Omega^{*2} Ro^2}. \tag{2.1.8}$$

Here, $\Delta\Omega^* = \Omega_f^* - \Omega_d^*$, r and z are the dimensionless forms of r^* and z^*, where $L^* = (\nu^*/\Omega^*)^{1/2}$ is the non-dimensionalizing length scale, Ω^* is a system rotation rate and Ro is the Rossby number (flow dependent). Both parameters are respectively defined by,

$$Ro = \frac{\Delta\Omega^*}{\Omega^*}, \tag{2.1.9}$$

$$\Omega^* = \frac{\Omega_f^*}{2 - Ro} + \frac{\Omega_d^*}{2 + Ro} = \frac{\Omega_f^* + \Omega_d^*}{4} + \left[\left(\frac{\Omega_f^* + \Omega_d^*}{4} \right)^2 + \frac{\Delta\Omega^{*2}}{4} \right]^{1/2}. \tag{2.1.10}$$

Based on such definitions, for the Bödewadt (1940) layer $Ro = 1$ and $\Omega^* = \Omega_f^*$; for the Ekman (1905) layer $Ro = 0$ and $\Omega^* = \Omega_f^* = \Omega_d^*$ whereas for the Von Kármán (1921) layer, $Ro = -1$ and $\Omega^* = \Omega_d^*$. Substituting Eqs. (2.1.5)-(2.1.8) in Eqs. (2.1.1)-(2.1.4) gives the following dimensionless equations for the mean flow :

$$2U + W' = 0, \tag{2.1.11}$$

$$Ro \left(U^2 + WU' - (V^2 - 1) \right) - Co \, (V - 1) - U'' = 0, \tag{2.1.12}$$

$$Ro \, (2UV + WV') + Co \, U - V'' = 0, \tag{2.1.13}$$

$$Ro \, (WW' + P') - W'' = 0, \tag{2.1.14}$$

where the prime denotes differentiation with respect to z, $Co = 2\Omega_d^*/\Omega^* = 2 - Ro - Ro^2$ is a Coriolis parameter: Co is equal to 2 for the Von Kármán (1921) and the Ekman (1905) layers, whereas $Co = 0$ for the Bödewadt (1940) layer. Please refer to App. A for more details.

Equations (2.1.11)-(2.1.14) can then be solved numerically with the following boundary conditions:

$$U(0) = V(0) = W(0) = 0, \tag{2.1.15}$$

$$U(z \to \infty) = 0, \quad V(z \to \infty) = 1. \tag{2.1.16}$$

Figure 2.5 shows (a) U, (b) V and (c) W evolutions against z for the three remarkable Rossby numbers $Ro \in \{-1, 0, 1\}$. The profiles were computed using the numerical strategy described in App. C. For the Von Kármán (1921) flow, i.e. $Ro = -1$, only the mean radial velocity profile is inflectional. The azimuthal and axial profiles become inflectional

only with an increasing Rossby number while for $Ro = 1$, U, V and W are all inflectional. This being established, the signs of the dimensional velocities U^*, V^* and W^* depend on the sign of the Rossby number Ro. Note for instance that, according to Eq. (2.1.7) and Eq. (2.1.8), for $Ro = 0$ the axial velocity and static pressure $W^* = P^* = 0$ whereas the radial and azimuthal velocity components, U^* and V^* are respectively non-zero because of the dependency on r^* (these $Ro = 0$ solutions of the BEK model are thus expectedly equivalent to the laminar solution to the Ekman (1905) layer).
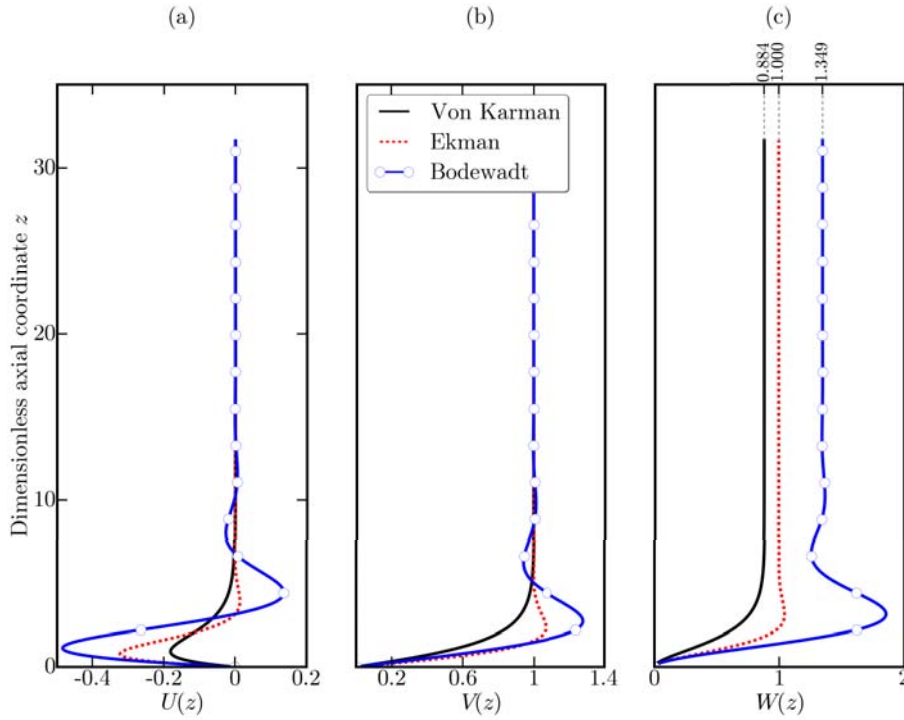
Figure 2.5 – Auto-similar velocity profiles of the laminar BEK flows. (*a*) Radial velocity U, (*b*) azimuthal velocity V and (*c*) axial velocity W.

2.1.2.b Flow between two radially infinite discs

Consider now the physical situation of two infinite discs mounted about the same axis. Cylindrical polar coordinates (r^*, θ, z^*) are used (Fig. 2.4) and the lower disc, in the plane $z^* = 0$, has an angular velocity Ω_d^* while the upper disc, at $z^* = h$, is stationary. Once again, for the steady incompressible and viscous fluid between the two discs, the governing equations are the Navier-Stokes equations described earlier - Eqs. (2.1.1)-(2.1.4). Following Batchelor (1951) (and similarly to the previous description of the BEK model - Sec. 2.1.2.a), we seek axially symmetric solutions of the Navier-Stokes equations in the form,

$$U(z) = \frac{U^*}{r^* \Omega_d^*}, \tag{2.1.17}$$

$$V(z) = \frac{V^*}{r^* \Omega_d^*}, \tag{2.1.18}$$

$$W(z) = \frac{W^*}{\sqrt{\nu \Omega_d^*}} = \frac{W^*}{L^* \Omega_d^*}, \tag{2.1.19}$$

$$P(r,z) = \frac{P^*}{\rho^* L^{*2} \Omega_d^{*2}} = P_0(z) + \frac{1}{2} r^2, \tag{2.1.20}$$

where h (the interdisc distance) is the relevant length scale such that $z = z^*/h$ and contrary to the definition given for the BEK model, $L^* = (\nu^*/\Omega_d^*)^{1/2}$ since now the relevant pulsation of the system becomes that of the rotating disc Ω_d^*. Substituting Eqs. (2.1.17)-(2.1.20) in Eqs. (2.1.1)-(2.1.4) gives the following dimensionless equations for the mean flow:

$$2\sqrt{Re_h} U + W' = 0, \tag{2.1.21}$$

$$+ \sqrt{Re_h} W U' + Re_h \left[U^2 - (V+1)^2 + 1 \right] - U'' = 0, \tag{2.1.22}$$

$$\sqrt{Re_h} W V' + 2 Re_h (1+V) U - V'' = 0, \tag{2.1.23}$$

$$\sqrt{Re_h} (W W' + P_0') - W'' = 0, \tag{2.1.24}$$

where the prime denotes differentiation with respect to z and is an absolute constant corresponding to the pressure rise due to centrifugal acceleration. Please refer to App. B for more details.

Equations (2.1.21)-(2.1.24) can then be solved numerically with the following boundary conditions:

$$U(0) = V(0) = W(0) = 0, \tag{2.1.25}$$

$$U(1) = W(1) = 0, \quad V(1) = -1. \tag{2.1.26}$$

Figure 2.6 shows (*a*) U, (*b*) V and (*c*) W evolutions against z for three interdisc Reynolds numbers $Re_h \in \{10^2, 10^3, 10^4\}$. To ensure consistency between the two kinds of disc flows, the three profiles of U, V and W have also been computed using the parameters and solver described in App. C. Note here that the initialization of the solver has been chosen identically in all cases and such that the profiles are all of the Batchelor kind - see Holodniok *et al.* (1977); Holodniok (1981) for an extensive study of the multiple solution branches of Eqs. (2.1.21)-(2.1.24).

Although for all three Reynolds numbers the same category of solution branch has been selected, there are marked differences in the flow organization as the interdisc Reynolds number increases. For low Reynolds numbers (e.g. $Re_h = 100$ in Fig. 2.6 (full line)), a continuous variation in velocity exists across the axial gap h which can be seen as the two discs boundary layers merge. As Re_h increases, (see Fig. 2.6 (dashed line) & (marked line)), three regions appear clearly: each disc has a boundary layer and the combined thickness of the two is less than the axial gap h. In between the boundary layers a core region exists in which no change in velocity is expected to occur and that rotates in bulk at $V_{\text{core}} = K$, sometimes referred to as the 'entrainment coefficient'. From the single-disc flows point of view, the high Reynolds Batchelor flows can therefore be seen as the connection of an Ekman (1905) profile and a Bödewadt (1940) profile through

a region of zero radial and constant azimuthal velocities. As can be seen on Fig. 2.6*b*, for high enough values of Re_h, K reaches a constant value. Note that Rasmussen (1971) showed using an asymptotic analysis that all laminar flows converge to $K = 0.313$, a value confirmed later by Marchand (1986) who further demonstrated that this value was actually correct as soon as $Re_h \geq 400$.
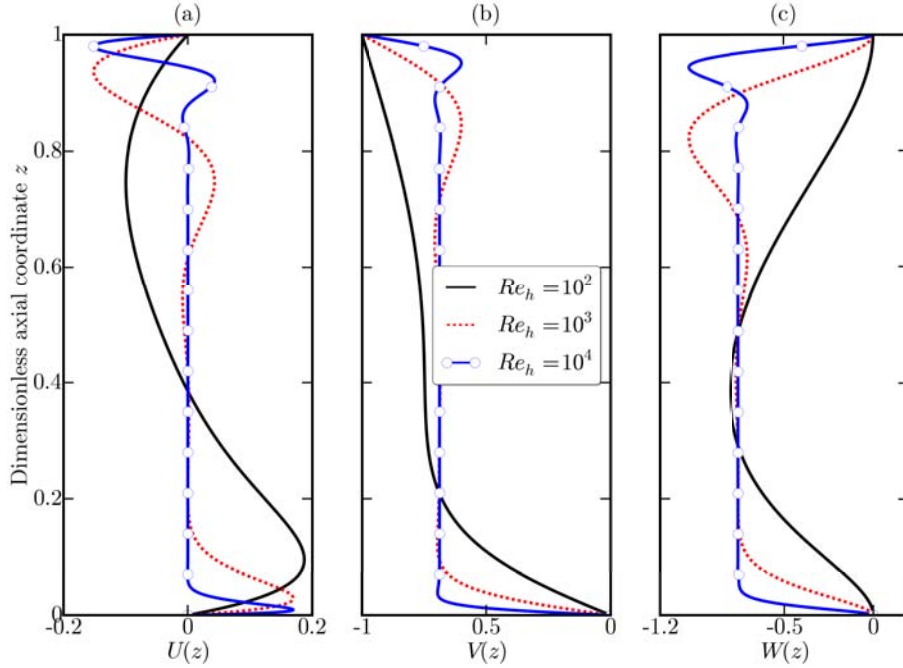
Figure 2.6 – Auto-similar velocity profiles of the laminar flow between a rotor and a stator for different interdisc Reynolds numbers Re_h: (*a*) Radial velocity, U, (*b*) azimuthal velocity, V and (*c*) axial velocity, W, components.

2.1.3   Enclosed cavity flow regimes

Aside from the developments of the set of reduced equations describing the laminar disc flows (Sec. 2.1.2), it appears necessary to describe the possible flow regimes existing in enclosed cavities. In this case, due to the presence of the outer cylindrical boundary (and/or the inner shaft), the Navier-Stokes equations cannot be reduced to a simplified set and consequently all the following remarks are qualitative. Later, Chap. 3 presents all the quantitative results obtained about enclosed rotor/stator cavity flows by LES.

As discussed earlier, Rogers & Lance (1962) showed numerically, and it was later confirmed experimentally by several authors like Sirivat (1991), that the laminar flows in an enclosed or partially enclosed rotor/stator cavity can be classified into two distinct categories depending on the size of the axial gap h. If h is large enough, the Böde-wadt (stator) and Ekman (rotor) layers are separated. For small values of h however, the boundary layers merge and the flow behaves like a 'torsional Couette flow'. Daily & Nece (1960) extended the categorization to turbulent rotor/stator flows by an impressive experimental work and concluded the existence of only four categories characterized by

two dimensionless parameters: the disc Reynolds number $Re = R_1^2 \Omega_d^* / \nu^*$ and the aspect ratio of the cavity $G = h/R_1$, where R_1 is the outer radius of the discs and ν^* the kinematic viscosity of the fluid. Following this work, Owen & Rogers (1989) used boundary layer equations to pinpoint the transitions between the four regimes and established the following expressions for the boundaries between the regimes in the (Re, G) plane:

- The two laminar regimes (category I for merged boundary layers, II for separated) are separated by a line $Re \, G^{11/5} \simeq 2.9$.

- The transition to turbulence for flows with separated boundary layers (regime II to IV) occurs at $Re \simeq 1.58 \times 10^5$.

- The common boundary to the two turbulent regimes (category III for merged boundary layers, IV for separated) is defined by $Re \, G^{16/3} \simeq 7.8 \times 10^{-3}$.

- The line between regimes I and III is such that $Re \, G^{10/9} \simeq 366$.

- The common boundary to regimes II and III satisfies the equation $Re \, G^{16/15} \simeq 4.6 \times 10^6$.

Figure 2.7 reproduces a diagram first showed by Owen & Rogers (1989), that summarizes these results and gives a visual representation of the domains of definition of all four regimes in the (Re, G) plane.

2.2 Hydrodynamic stability of a rotating flow

This second section outlines the main concepts pertaining to linear stability analysis. Similarly to Sec. 2.1, the notions presented here are described in the literature by previous workers. However, these concepts in the specific situation of one- or two-disc flows is necessary to prepare for the search for globally unstable modes in enclosed rotor/stator cavities exposed in Sec. 3.7. It is indeed shown in that section that, in some cases, the unsteady phenomena observed in the LES solutions can be related to the stability of the mean flow. In these cases, we furthermore show that the frequencies of the 'pressure bands' are detected everywhere in the configurations because the corresponding modes are globally unstable linear modes of the mean flow, which propagate by nature everywhere in the cavity.

2.2.1 Historical perspective

The study of hydrodynamic stability goes back to the theoretical work of Helmholtz (1868), Kelvin (1871) and Rayleigh (1879) on inviscid flows and, maybe the most remarkable, the experimental investigations presented by Reynolds (1883), which initiated the study of the stability of viscous flows. Reynolds experimental studies were soon supplemented with the theoretical work of Orr (1907) and Sommerfeld (1908), who independently considered infinitesimal travelling disturbances within an otherwise steady and parallel flow and derived what is today known as the Orr-Sommerfeld equations.
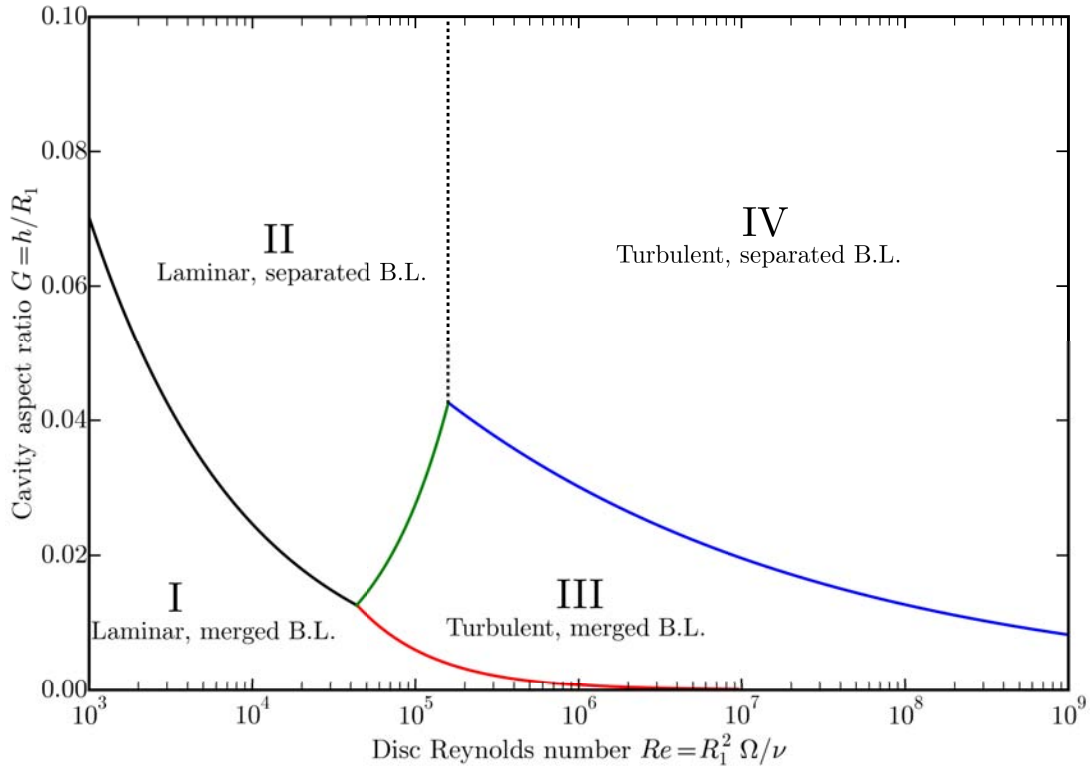
Figure 2.7 – The four categories of flow encountered in an enclosed rotor/stator cavity, based on an original figure by Owen & Rogers (1989). Regime I is a laminar regime with merged boundary layers whereas regime III is the turbulent pendant. Regimes II and IV describe respectively the laminar and turbulent flows with separated boundary layers.

Following their work, stability criteria for laminar viscous flows have been considered a primary goal of studies in theoretical fluid dynamics for many years. However due to the inherent intricacies involved in the solution of the hydrodynamic perturbation equations, exact solutions were found only for some families of flows. Originally, it was confined to physical situations that could be described by two-dimensional flows, among which for example, the well-known inviscid Kelvin-Helmholtz instability - the reader is referred to Lin (1955) for an extensive survey. For three-dimensional flows, the early stability studies were primarily experimental and a number of papers deserve specific mention in any bibliographical description of previous work.

- In relation to jet flows, Mollo-Christensen (1967) was among the first to describe in details the near-field pressure fluctuations, noting with reason that they come in 'packets' similar in shape and random only with respect to the place and time of their origin. A few years later, Michalke (1971) produced the first analytical study of the linear stability of a round free jet and inspired numerous authors to pursue similar work on different configurations, amongst which but not limited to Crighton & Gaster (1976), Liu (1989), Chomaz *et al.* (1991*a*) and more recently Gallaire & Chomaz (2003*a*) or Oberleithner (2012).

- Regarding rotating flows, it is of note that the flow induced by a rotating circular

disc in a still fluid has received considerable attention over the years starting around
1947, although the work by Savas (1983) is probably the earliest to discuss the sta-
bility of the Bödewadt layer. The susceptibility of the BEK flows (see Sec. 2.1.2.a)
to inviscid crossflow instability (often referred to as type-1 instability) is to be
expected from the inflectional nature of the velocity profiles (see the detailed math-
ematical analysis by Fjortoft (1949) of the stability criteria for laminar flows). Such
stability issues were first noticed by Smith (1947) during his experiments on the
oscillations of the laminar boundary layer over a rotating disc. Further evidence
of the crossflow instability of the Von Kármán and Ekman layers is provided by
Gregory *et al.* (1955) and Faller (1963), who determined experimentally a critical
Reynolds number for the onset of instability. The latter authors also pointed out
that the Ekman flow often displays a second convectively unstable mode (named
type-2 instability) that dominates at low Reynolds numbers and becomes stable in
the inviscid limit. A conclusion they confirmed in a later paper (Faller & Kaylor,
1966*a*) and extended to the Von Kármán flow the same year (Faller & Kaylor,
1966*b*). The stability of the Bödewadt flow was only investigated later by Savas
(1983, 1987) who conducted spin-down experiments in a cylindrical cavity and ob-
served type-1 and type-2 instabilities as well. In 1991, Faller not only produced
the first unifying theory for the BEK flows, but was also among the first to present
a detailed analytical development of the stability of all three flows. The extensive
work accomplished by Lingwood (1995*a*, 1997) during her PhD is however the most
recent contribution where all three BEK flows were considered and compared. She
discovered an absolute instability in the Von Kármán boundary layer (Lingwood,
1995*a*), produced by the coalescence of the inviscid unstable mode (type-1) and a
third mode that is spatially damped. She also suggested that this instability might
be responsible for the onset of turbulence in such a configuration. Later, Lingwood
(1997) extended these conclusions to the Ekman and Bödewadt layers and found
analytical values for the Reynolds numbers beyond which the flows become abso-
lutely unstable that matched the laminar-to-turbulent transition Reynolds numbers
obtained in previous experiments, like for instance that of Faller & Kaylor (1966*a*)
for the Ekman layer.

The present section first presents an outline of the theory of linear stability analysis
for one- or two-discs isothermal flows based mainly on the previous works by Malik
et al. (1981), Malik (1986), Faller (1991), Lingwood (1995*b*) and Tuliszka-Sznitko &
Soong (2000). In a second time, we present in details the Linearized Navier-Stokes
Equations (LNSE) solver (called AVLP hereafter) implemented during the course of this
Ph.D. Numerical strategies necessary to solve the set of linearised equations are discussed
and the validation of the LNSE solver is proposed to conclude the present chapter. A
presentation of original results pertaining to enclosed rotor/stator cavity flow stability is
indeed given in the next chapter (Chap. 3).

2.2.2 Linear stability analysis

The mathematical strategy inspired by the conclusions of Reynolds (1883) and initially used by Orr (1907) and Sommerfeld (1908) is the one considered in the present work. It assumes that all components of the velocity field and the static pressure can be written as the sum of a steady part (called 'base flow' or 'carrier flow') and an unsteady part representing the infinitesimal fluctuations under study. In other words, we write

$$
\begin{aligned}
\mathbf{u}^*(r^*, \theta, z^*, t^*) &= \mathbf{U}^*(r^*, \theta, z^*) + \tilde{\mathbf{u}}^*(r^*, \theta, z^*, t^*), \\
p^*(r^*, \theta, z^*, t^*) &= P^*(r^*, \theta, z^*) + \tilde{p}^*(r^*, \theta, z^*, t^*).
\end{aligned}
\tag{2.2.1}
$$

where $\mathbf{U}$ represent the base flow velocity, $\tilde{\mathbf{u}}$ the fluctuations of velocity, P the steady pressure field and $\tilde{p}$ the fluctuations of pressure.

The analysis presented later in this work characterizes the response of a disc flow (be it a boundary layer flow or a core flow) to an external periodic excitation, on the basis of the parallel-flow approximation. The analysis is therefore restricted to the local stability characteristics of the flow, i.e. the stability characteristics are determined at a given radius as though the flow was invariant in the radial direction. Hence, to follow the streamwise evolution of a perturbation, a succession of linear stability analyses are conducted, one for each streamwise location and the overall shape of a mode is then reconstructed from the local solutions (Huerre & Monkewitz, 1990).

2.2.2.a The perturbation equations for the BEK flows

In the case of single-disc flow, let us assume a linear stability analysis is applied at a radius r_a^*. Following the developments made for the description of the laminar BEK flows (Sec. 2.1.2.a), we use L^* as the reference length, $r_a^*\Omega^* Ro$ as the velocity scale, $\rho^* r_a^{*2}\Omega^{*2} Ro$ as the reference pressure and $L^*/(r_a^*\Omega^* Ro)$ the time scale. This being said, the local Reynolds number of interest becomes

$$
Re_\delta = \frac{r_a^*\Omega^* L^* Ro}{\nu^*} = \frac{r_a^* Ro}{L^*} = r_a Ro,
\tag{2.2.2}
$$

where $r_a = r_a^*/L^*$ and the instantaneous dimensionless velocities and pressure are given by,

$$
u(r, \theta, z, t) = \frac{rRo}{Re_\delta}U(z) + \tilde{u}(r, \theta, z, t),
\tag{2.2.3}
$$

$$
v(r, \theta, z, t) = \frac{rRo}{Re_\delta}V(z) + \tilde{v}(r, \theta, z, t),
\tag{2.2.4}
$$

$$
w(r, \theta, z, t) = \frac{Ro}{Re_\delta}W(z) + \tilde{w}(r, \theta, z, t),
\tag{2.2.5}
$$

$$
p(r, \theta, z, t) = \frac{Ro^2}{Re_\delta^2}P(r, z) + \tilde{p}(r, \theta, z, t),
\tag{2.2.6}
$$

where $\tilde{u}$, $\tilde{v}$, $\tilde{w}$ and $\tilde{p}$ are small perturbation quantities in accordance with Eq. (2.2.1). The dimensional continuity equation and Navier-Stokes equations written in the frame

rotating at Ω_d^* (Eqs. (2.1.1)-(2.1.4)) are made dimensionless and linearised with respect to the perturbation quantities, yielding:

$$\frac{\partial \tilde{u}}{\partial r} + \frac{\tilde{u}}{r} + \frac{1}{r}\frac{\partial \tilde{v}}{\partial \theta} + \frac{\partial \tilde{w}}{\partial z} = 0, \tag{2.2.7}$$

$$\frac{\partial \tilde{u}}{\partial t} + \frac{rU}{Re_\delta}\frac{\partial \tilde{u}}{\partial r} + \frac{V}{Re_\delta}\frac{\partial \tilde{u}}{\partial \theta} + \frac{RoW}{Re_\delta}\frac{\partial \tilde{u}}{\partial z} + \frac{RoU\tilde{u}}{Re_\delta} - \frac{2RoV + Co}{Re_\delta}\tilde{v} + \frac{rU}{Re_\delta}\tilde{w} =$$
$$- \frac{\partial \tilde{p}}{\partial r} + \frac{1}{Re_\delta}\left(\frac{\partial^2 \tilde{u}}{\partial r^2} + \frac{1}{r^2}\frac{\partial^2 \tilde{u}}{\partial \theta^2} + \frac{\partial^2 \tilde{u}}{\partial z^2} + \frac{1}{r}\frac{\partial \tilde{u}}{\partial r} - \frac{2}{r^2}\frac{\partial \tilde{v}}{\partial \theta} - \frac{\tilde{u}}{r^2}\right), \tag{2.2.8}$$

$$\frac{\partial \tilde{v}}{\partial t} + \frac{rU}{Re_\delta}\frac{\partial \tilde{v}}{\partial r} + \frac{V}{Re_\delta}\frac{\partial \tilde{v}}{\partial \theta} + \frac{RoW}{Re_\delta}\frac{\partial \tilde{v}}{\partial z} + \frac{RoU\tilde{v}}{Re_\delta} + \frac{2RoV + Co}{Re_\delta}\tilde{u} + \frac{rV}{Re_\delta}\tilde{w} =$$
$$- \frac{\partial \tilde{p}}{r\partial \theta} + \frac{1}{Re_\delta}\left(\frac{\partial^2 \tilde{v}}{\partial r^2} + \frac{1}{r^2}\frac{\partial^2 \tilde{v}}{\partial \theta^2} + \frac{\partial^2 \tilde{v}}{\partial z^2} + \frac{1}{r}\frac{\partial \tilde{v}}{\partial r} + \frac{2}{r^2}\frac{\partial \tilde{u}}{\partial \theta} - \frac{\tilde{v}}{r^2}\right), \tag{2.2.9}$$

$$\frac{\partial \tilde{w}}{\partial t} + \frac{rU}{Re_\delta}\frac{\partial \tilde{w}}{\partial r} + \frac{V}{Re_\delta}\frac{\partial \tilde{w}}{\partial \theta} + \frac{RoW}{Re_\delta}\frac{\partial \tilde{w}}{\partial z} + \frac{RoW}{Re_\delta}\tilde{w} =$$
$$- \frac{\partial \tilde{p}}{\partial z} + \frac{1}{Re_\delta}\left(\frac{\partial^2 \tilde{w}}{\partial r^2} + \frac{1}{r^2}\frac{\partial^2 \tilde{w}}{\partial \theta^2} + \frac{\partial^2 \tilde{w}}{\partial z^2} + \frac{1}{r}\frac{\partial \tilde{w}}{\partial r}\right), \tag{2.2.10}$$

where the prime denotes differentiation of the dimensionless velocity components $\mathbf{U} = [U(z), V(z), W(z)]$ with respect to z.

For values of the local Reynolds $Re_\delta \gg 1$, Eqs. (2.2.7)-(2.2.10) may be re-written by replacing factors of r by Re_δ and neglecting terms of order Re_δ^{-2} or smaller (Malik *et al.*, 1981). The latter assumption was shown to have little to no effect on the results of the linear stability analysis (refer to Malik *et al.*, 1981; Faller, 1991; Lingwood, 1995*b*) However the replacement of r by Re_δ implies that non-parallel flow effects are neglected, which might induce a loss of accuracy in the cases where the analysed boundary layer is growing. The main advantage of such an approximation is that Eqs. (2.2.7)-(2.2.10) yield a set of equations that are separable in r, θ and t so that the perturbation quantities may be assumed to have a normal mode representation:

$$[\tilde{u}, \tilde{v}, \tilde{w}, \tilde{p}] = [iu, v, w, p](z) \exp\left[i\left(\alpha r + m\theta - \omega t\right)\right], \tag{2.2.11}$$

where u, v, w and p are the spectral representations (in Fourier space) of the fluctuation velocities and pressure (resp.), ω is the complex frequency of the disturbance in the frame rotating at Ω_d^*, α the complex radial wavenumber and m the real azimuthal wavenumber. Due to the periodic nature of the BEK flows in the azimuthal direction, the values of m are actually restricted to the set of integers.

Upon substituting the modal decomposition (see Eq. (2.2.11)) into the linearised Navier-Stokes equations, Eqs. (2.2.7)-(2.2.10), the system becomes (not yet dropping terms of order Re_δ^{-2}):

$$0 = \left(i\alpha + \frac{Ro}{Re_\delta} \right) u + \beta v - iw \,, \tag{2.2.12}$$

$$u = \left(\alpha^2 + \beta^2 + iRe_\delta \left(\alpha U + \beta V \right) - iRe_\delta \omega + RoU + T_3 \right) u + RoWu$$
$$+ i(2RoV + Co + T_2)v - i\frac{dU}{dz}Re_\delta w + \alpha Re_\delta p, \tag{2.2.13}$$

$$v = \left(\alpha^2 + \beta^2 + iRe_\delta \left(\alpha U + \beta V \right) - iRe_\delta \omega + RoU + T_3 \right) v + RoWv$$
$$+ i(2RoV + Co + T_2)u + \frac{dV}{dz}Re_\delta w + i\beta Re_\delta p, \tag{2.2.14}$$

$$w = \left(\alpha^2 + \beta^2 + iRe_\delta \left(\alpha U + \beta V \right) - iRe_\delta \omega + RoW - T_1 \right) w + RoWw$$
$$+ Re_\delta p \,, \tag{2.2.15}$$

where $\beta = m/Re_\delta$ and T_1, T_2 and T_3 are the terms that may be neglected under the parallel flow approximation, such that

$$T_1 = \frac{i\alpha}{Re_\delta}, \ T_2 = -\frac{2im}{Re_\delta^2} \ \text{ and } \ T_3 = \frac{1}{Re_\delta^2} - T_1. \tag{2.2.16}$$

The boundary conditions imposed at $z = 0$ by the presence of the disc is a Dirichlet condition for the three velocity components,

$$u(0) = v(0) = w(0) = 0, \tag{2.2.17}$$

complemented by the fact that as $z \to \infty$, it is required that all perturbations decay.

2.2.2.b   The perturbation equations for the flow between two discs

Contrary to the flows over a single-disc which have attracted attention for decades, an interest for the hydrodynamic stability of the mean flow between two discs has only recently arisen. Itoh (1991) was the first to thoroughly analyse the hydrodynamic nature of the flow using as basic state auto-similar profiles of the Batchelor kind (refer to e.g. Holodniok, 1981, for more details). The following choices of non-dimensionalizing scales and the development of the linearised equations are inspired from Itoh (1991) original work and the more recent study on incompressible non-isothermal rotor/stator cavity flow stability by Tuliszka-Sznitko & Soong (2000).

Let r_a^* be the radius at which is applied the stability analysis. As mentioned in Sec. 2.1.2.b, the relevant length scale of the system is now the interdisc distance, h. In addition, we use $r_a^*\Omega_d^*$ as the velocity scale, $\rho^* r_a^{*2} \Omega_d^{*2}$ as the reference pressure and $h/(r_a^*\Omega_d^*)$ the time scale. In this case, the relevant radial 'Reynolds number' becomes simply the dimensionless radial coordinate $r_a = r_a^*/h$, and a second control parameter, Re_h, becomes necessary to completely characterize the problem. Since the scales chosen

for the fluctuations of the flow are identical to those previously chosen to seek axially symmetric solutions of the Navier-Stokes equations (Sec. 2.1.2.b), the instantaneous velocity components and pressure field are given by

$$u(r, \theta, z, t) = U(z) + \tilde{u}(r, \theta, z, t), \tag{2.2.18}$$
$$v(r, \theta, z, t) = V(z) + \tilde{v}(r, \theta, z, t), \tag{2.2.19}$$
$$w(r, \theta, z, t) = W(z) + \tilde{w}(r, \theta, z, t), \tag{2.2.20}$$
$$p(r, \theta, z, t) = P(r, z) + \tilde{p}(r, \theta, z, t). \tag{2.2.21}$$

Furthermore, introducing the same normal mode decomposition as before (Eq. (2.2.11)), the LNSE for the flow between two infinite discs become:

$$0 = i\alpha + \frac{1}{r}\ u + \beta v - iw\,, \tag{2.2.22}$$

$$u = \left(\alpha^2 + \beta^2 + ir Re_h \left(\alpha U + \beta V\right) - ir Re_h \omega + T_3\right) u + \sqrt{Re_h} W u$$
$$+ i(2Re_h + 2Re_h V + T_2)v - ir Re_h \frac{dU}{dz}w + \alpha r Re_h p, \tag{2.2.23}$$

$$v = \left(\alpha^2 + \beta^2 + ir Re_h \left(\alpha U + \beta V\right) - ir Re_h \omega + Re_h U + T_3\right) v + \sqrt{Re_h} W v$$
$$+ i(Re_h V - 2Re_h + T_2)u + r Re_h \frac{dV}{dz}w + i\beta r Re_h p, \tag{2.2.24}$$

$$w = \ \alpha^2 + \beta^2 + ir Re_h \left(\alpha U + \beta V\right) - ir Re_h \omega + \sqrt{Re_h} W\ - T_1\ \ w + \sqrt{Re_h} W w$$
$$+ r Re_h p\,, \tag{2.2.25}$$

where $\beta = m/r$ and T_1, T_2 and T_3 are the terms that may be neglected under the parallel flow approximation, such that

$$T_1 = \frac{i\alpha}{r},\ T_2 = -\frac{2im}{r^2}\ \text{ and }\ T_3 = \frac{1}{r^2} - T_1. \tag{2.2.26}$$

The presence of two discs respectively at $z = 0$ and $z = 1$ forces all perturbations to zero and therefore the boundary conditions necessary to close the system read:

$$u(0) = v(0) = w(0) = 0,$$
$$u(1) = v(1) = w(1) = 0. \tag{2.2.27}$$

For a given mean velocity profile, the system of equations Eqs. (2.2.12)-(2.2.17) (resp. Eqs. (2.2.22)-(2.2.27)) describes an eigenvalue problem. This eigenvalue problem relates the wavelength of the perturbation injected in the base flow to its frequency. As such, one can see it as a dispersion problem that can therefore be written under the form of a dispersion relation $\mathcal{D}(\alpha, \omega, \chi) = 0$, where χ represents the set of all parameters other than the two aforementioned complex numbers, including the parameters describing the mean flow profiles. Consequently, at a given pair (m, Re_δ) (resp. triplet (m, r, Re_h)), a non-zero solution of (u, v, w, p) exists if and only if the dispersion relation $\mathcal{D}(\alpha, \omega, \chi) = 0$ is verified by at least one pair of complex numbers (α, ω).

2.2.2.c   Physical interpretation of the normal mode ansatz

To avoid confusion during the presentation of the linear stability results in the rest of this work, it is important to clarify the physical meaning of the wavenumbers α and m and the frequency ω of a perturbation. First of all, recall that the perturbation quantities have been decomposed in normal modes in the following form:

$$\tilde{\mathbf{u}} = \mathbf{u}(z) \exp\left[i\left(\alpha r + m\theta - \omega t\right)\right], \tag{2.2.28}$$

where α is the radial wavenumber, m the azimuthal wavenumber and ω the complex frequency. Naturally, the real parts of Eq. (2.2.11) are taken to obtain physical quantities,

$$\tilde{\mathbf{u}}^* = \mathbf{u}(z)e^{[i(\ r+m\theta-\ t)]} + \overline{\mathbf{u}}(z)e^{[-i(\overline{\ }r+m\theta-\overline{\ }t)]} \tag{2.2.29}$$

where the overline denotes the conjugate of the complex. Hence instability modes can be evenly represented by the triplets

$$(\alpha, m, \omega) \quad \text{or} \quad (-\overline{\alpha}, -m, -\overline{\omega}) \tag{2.2.30}$$

In the following, except during validation test-cases (Sec. 2.2.4.e), note that we restrict the stability analyses to positive values of α_r out of simplicity.

To clarify the meanings of α, m and ω, remark first that Eq. (2.2.29) can be rewritten as:

$$\tilde{\mathbf{u}}^* = |\mathbf{u}|(z)\cos\left(\alpha_r r + m\theta + \arg(\mathbf{u})(z) - \omega_r t\right)e^{-\ _i r + \ _i t} \tag{2.2.31}$$

where $|\cdot|$ and $\arg(\cdot)$ are the modulus and phase of a complex number. At a given axial location z, if the temporal and spatial amplifications, respectively ω_i and $-\alpha_i$, are taken to be zero, Eq. (2.2.31) exactly corresponds to the polar parametric equation for spiral and axisymmetric patterns. The azimuthal wavenumber m drives the number of 'arms' of the patterns: if $m = 0$, the pattern will be axisymmetric, whereas for $|m| > 0$ the pattern will be a spiral with $|m|$ arms. The sign of m drives the winding direction of the spiral arms and assuming in the rest of this work that the mean direction of the geostrophic flow in all rotor/stator configurations is counter-clockwise, the spirals are said to be

- co-winding if $m < 0$,

- counter-winding if $m > 0$.

On the other hand, the radial wavenumber α_r gives a representation of the number of arms in a given radial extent: if α_r is small, then the angle the arms make with the direction of the geostrophic flow is high, whereas if α_r is high, then the density of arms increases and their angle with the direction of the geostrophic flow decreases. Generic combinations of α_r and m are displayed in Fig. 2.8 to illustrate the previous statements.
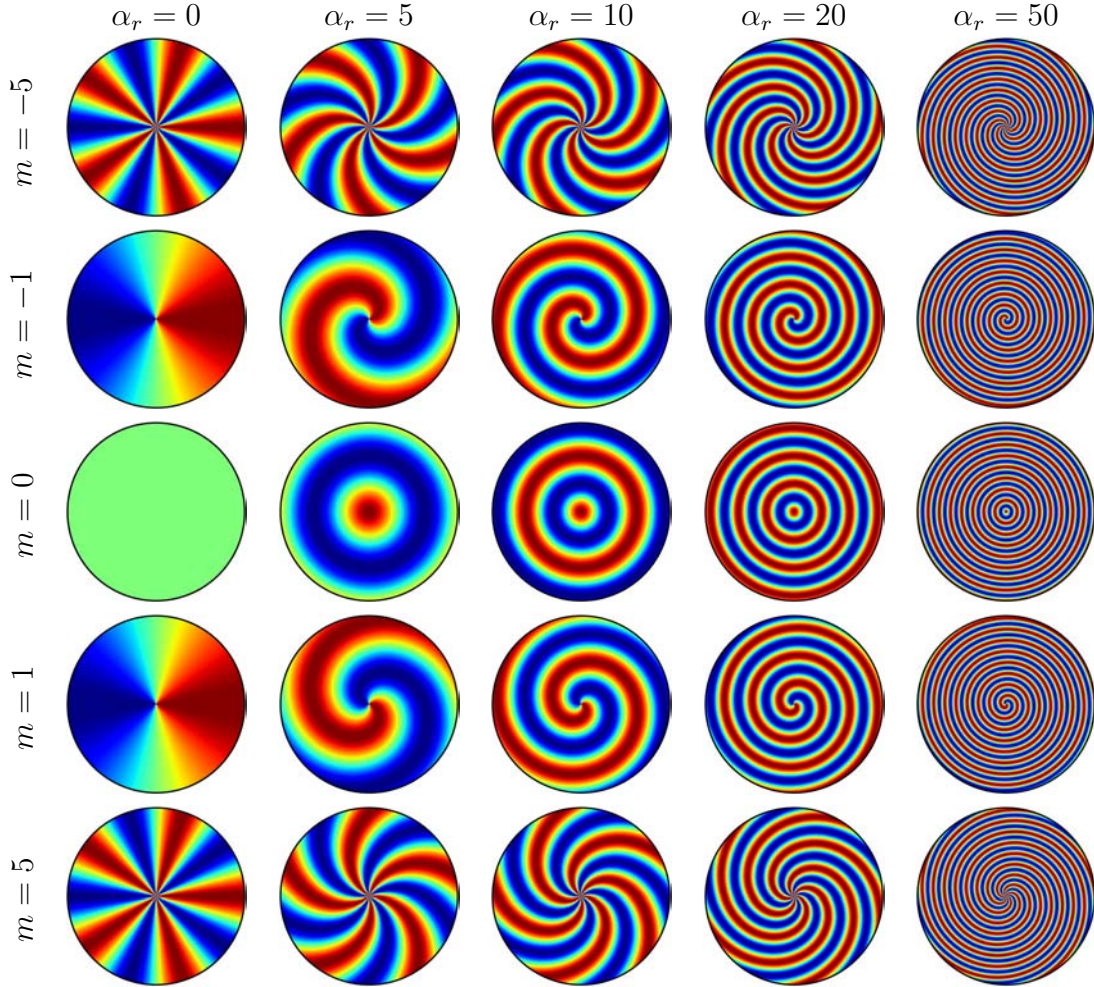
Figure 2.8 – Two-dimensional representations of $\cos(\alpha_r r + m\theta)$ (Eq. (2.2.31)) for combinations of $\alpha_r \in \{0, 5, 10, 20, 50\}$ and $m \in \{-5, -1, 0, 1, 5\}$. Parameters and function are dimensionless, $0 \leq r \leq 1$ and $0 \leq \theta \leq 2\pi$.

Adding the term for the phase of the eigenfunctions $\arg(\mathbf{u})$ merely introduces a phase shift that is perceived as an extra rotation of the pattern in the (r, θ)-plane. The same remark goes for the the last term in the cosine, $-\omega_r t$ that induces a temporally evolving phase shift of the pattern. This is illustrated on Fig. 2.9a where the spiral with $(\alpha_r, m) = (20, 5)$ is shown at three different values of $(\arg(\mathbf{u}) - \omega_r t)$, respectively -1.3π, 0 and $+1.5\pi$.

Finally, the effects of a non-zero spatial amplification rate α_i on the patterns is shown on Fig. 2.9b where the spiral with $(\alpha_r, m) = (20, 5)$ was drawn for $\arg(\mathbf{u}) - \omega_r t = 0$
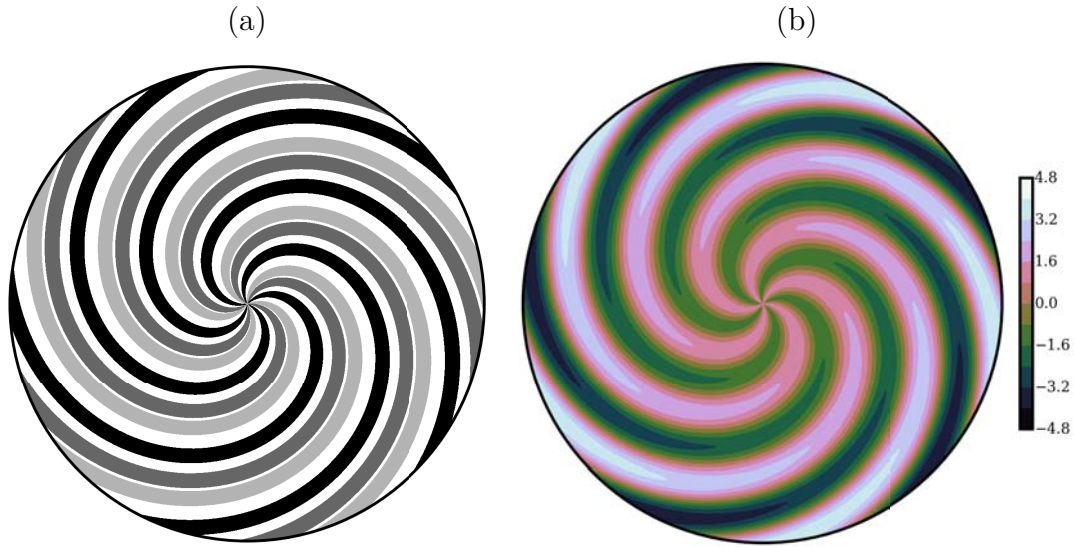
Figure 2.9 – Two dimensional representation of a spiral with $\alpha_r = 20.$ and $m = 5$ (refer to Eq. (2.2.31)) with (*a*) different values of the eigenfunction phase (black: $\arg(\mathbf{u}) - \omega_r t = -1.3\pi$, dark gray: $\arg(\mathbf{u}) - \omega_r t = 0$, light gray: $\arg(\mathbf{u}) - \omega_r t = +1.5\pi$) and (*b*) $\alpha_i = 1.4$.

and $\alpha_i = 1.4$. Note that the effects of ω_i are similar to those of α_i, only they induce a growth or decay of the whole pattern magnitude in time and with no radial segregation.

Figures 2.8 and 2.9 may serve as a visual aid that comes in handy during the discussion of the stability analyses presented in Sec. 2.2.4.e and Sec. 3.7.

2.2.3   Spatial, temporal and spatio-temporal strategies

The dispersion relation $\mathcal{D}(\alpha, \omega, \chi) = 0$ can be solved in one of three ways: for a complex ω and a fixed real α, for a complex α and a fixed real ω, or with no restrictions on the domains of definition of α and ω, i.e. for a complex α and a complex ω. In the context of disc flows, the first approach is known to provide interesting information (Serre *et al.*, 2004; Tuliszka-Sznitko & Soong, 2000) about the instabilities developing in the boundary layers but some shortcomings (see Sec. 3.7) make it inadequate to predict exactly the characteristics and three-dimensional organization of the dominant instabilities. The second approach is especially pertinent for spatially developing flows like jets or wakes and consequently it is only described here since its underlying concepts are also relevant to the third approach. We describe this last approach in great details for it is at the origin of the global mode reconstruction conducted in Sec. 3.7 that evidences that some of the unsteady phenomena observed in the LES solutions are related to globally unstable linear modes of the mean flow.

(*a*) The first method yields *temporal modes* $\omega(\alpha, \chi)$ that can be either growing ($\mathfrak{Im}(\omega) > 0$) or decaying ($\mathfrak{Im}(\omega) < 0$) with time. Note that for a single complex number ϕ, we shall thereafter use the notations ϕ_i and ϕ_r for $\mathfrak{Im}(\phi)$ and $\mathfrak{Re}(\phi)$ respectively. Such

an analysis is most useful in cases where the flow is bounded with no freestream velocity and a perturbation made at a given streamwise location cannot grow spatially, i.e. all perturbations are forced to have $\alpha_i = 0$. Common examples are the Taylor-Couette flow (see Grossmann *et al.*, 2016, for a recent review) or a Rayleigh-Bénard convection cell (of finite size). Used within the framework of local linear stability analysis, this method provides ample information about the local dynamics of the flow. However for lack of data on the spatial organization of the fluctuations up- and downstream of the specified location, one can hardly draw conclusions regarding the overall shape of the mode.

(*b*) Conversely, the second technique produces *spatial modes* $\alpha(\omega, \chi)$ that can either be spatially growing ($\alpha_i < 0$) or decaying ($\alpha_i > 0$). This approach is especially applicable to open flows where fluid particles have the possibility to be advected out of the physical domain of definition of the base flow. Amongst those spatially developing flows one finds the open shear flows that were the targets of the earliest theoretical linear stability analyses (see Ho & Huerre, 1984, for a review of such analysis applied to mixing layers). As stated by Huerre & Monkewitz (1990), for flows that are strictly parallel or weakly non-parallel, i.e. for which the length scale of evolution of the base flow is large compared to the wavelength of the instability, at leading order one can approximate the shape of the global disturbance velocity field using a succession of local stability analyses:

$$
\begin{matrix} \tilde{u} \\ \tilde{v} \\ \tilde{w} \end{matrix} (r, \theta, z, t) = \mathfrak{Re} \left\{ A_0(r) \begin{matrix} iu \\ v \\ w \end{matrix} (r, z) \exp\left[i \left(\int_0^r \alpha(\xi) d\xi + m\theta - \omega_f t \right) \right] \right\}
$$

$$(2.2.32)$$

where $\omega_f \in \mathbb{R}$ is the fixed temporal frequency at which the flow is excited, $m \in \mathbb{Z}$ the fixed azimuthal wavenumber of the perturbation under study and $\alpha = \alpha_r + i\alpha_i$ (resp. $[iu, v, w]^\dagger$) is the eigenvalue (resp. eigenvector) verifying the dispersion relation $\mathcal{D}(\alpha, \omega_f, \chi) = 0$. A_0 is a corrective amplitude function necessary to account for the streamwise variations of a weakly non-parallel base flow. If the latter assumption is indeed valid, then the correction is found to evolve slowly with the streamwise location r while α evolves fast with ξ (Crighton & Gaster, 1976; Huerre & Monkewitz, 1990). In the present work however, it is assumed that A_0 is uniform over the physical domain (we then consider $A_0 = 1$) and the focus is put on an accurate determination of the fast streamwise variations of α. The argumentation for this choice is mostly based on the conclusions by Crighton & Gaster (1976) or Huerre & Monkewitz (1990) and the more recent investigation by Juniper (2011), all stating that the influence of assuming a constant A_0 on the ability to retrieve the right global shape of the mode is much smaller than the influence of imprecisions in α.

More importantly, in practice the assembling of the moduli of the eigenvectors yield by each local stability analysis on the one hand, and of their phase on the other hand needs to be done carefully.
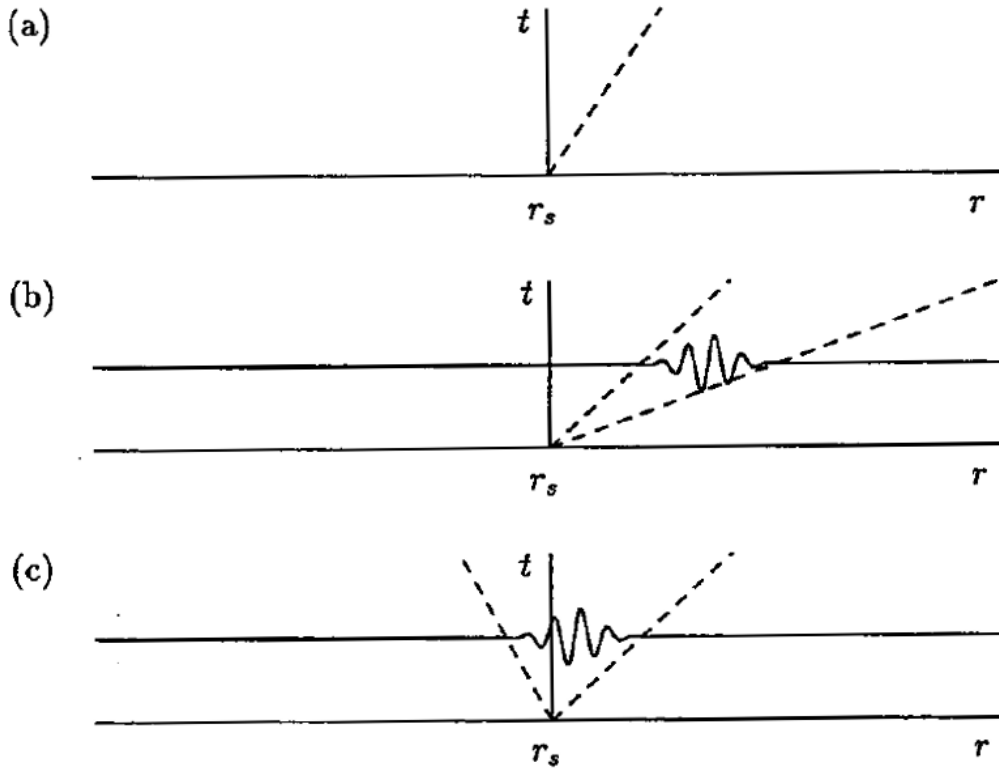
Figure 2.10 – Typical responses of a base flow to a perturbation generated at $r = r_s$: (*a*) stable, (*b*) convectively unstable and (*c*) absolutely unstable. Source: Lingwood (1995*b*, Chap. 1, p. 7)

      – The eigenvector moduli have to be made compatible by the use of the same normalization at each streamwise location. Based on remarks from Juniper (2011) and Oberleithner (2012), the velocity components are normalized in this work by the L²-norm of the velocity at each slice $K = \int_0^1 \left(|u|^2 + |v|^2 + |w|^2 \right)^{1/2} dz$.

      – The eigenvector phases are arbitrary as they all stem from independent local linear stability analyses and therefore a sensible clocking needs to be applied. In this sense, a height of clocking z_c is chosen arbitrarily, and at $z = z_c$ it is imposed that for all streamwise locations r, $\arg\left([iu, v, w]^\dagger(r, z_c) \right) = \arg\left([iu, v, w]^\dagger(r_0, z_c) \right)$ where r_0 indicates the first streamwise location considered in the analysis.

(*c*) In the previous analysis, the response of the flow to a perturbation of known *real* frequency ω_f is examined. This being said, certain spatially evolving flows are also known to develop and sustain self-excited global modes in the absence of any external forcing (Monkewitz, 1988; Huerre & Monkewitz, 1990; Gallaire *et al.*, 2006) at a *complex* frequency ω_G. In these cases, the eigenvalue problem $\mathcal{D}(\alpha, \omega, \chi) = 0$ needs to be solved for $(\alpha, \omega) \in \mathbb{C} \times \mathbb{C}$. This approach is called a *spatio-temporal analysis* and the issue becomes to determine the frequency-selection criterion for ω_G. The procedure is well detailed in Huerre & Monkewitz (1990) but for the sake

of completeness we recall here the main steps leading to the evaluation of ω_G.

With the review proposed by Davis (1976), the work by Koch (1985) and the study proposed by Pierrehumbert (1984), it was concluded (Huerre & Monkewitz, 1990) that the self-sustained oscillations of a global instability are connected to the presence of a wide-enough region of local absolute instability. That is a wave can be emitted from this specific location that propagates up- and downstream. This notion of absolute instability comes as a pendant to the notion of convective instability: in such regions, waves are emitted that are convected and growing exclusively downstream. Figure 2.10 provides a visual representation of the typical responses of a base flow to a perturbation generated at a given radius r_s. Figure 2.10a shows a stable case, Fig. 2.10b shows a convectively unstable case and Fig. 2.10c an absolutely unstable case.

Before considering the absolute stability of the flow, a preliminary temporal stability analysis (Sec. 2.2.3a) has to be performed at an arbitrarily chosen radial location (say r_a) in the flow where the maximum temporal growth rate is identified - say $\omega_{i,\max}$ found at $\alpha_{r,\max}$. Under the parallel flow assumption, $\omega_{i,\max}$ indeed represents the upper bound for the absolute growth rate at this location (Chomaz *et al.*, 1991a), which naturally has to be positive for the existence of an absolute instability to be possible. To distinguish between convective and absolute instabilities, it is then necessary to characterize the long-time behaviour of the perturbation of wavenumber $\alpha \in \mathbb{C}$ at r_a. In other words, one has to identify its *absolute frequency* - say, $\omega_0 \in \mathbb{C}$ - that is solution of the constrained eigenvalue problem,

$$
\begin{aligned}
&\mathcal{D}(\alpha, \omega_0, \chi) = 0, \\
&\frac{\partial \omega}{\partial \alpha} = 0.
\end{aligned}
\tag{2.2.33}
$$

In practice, ω_0 is found by seeking the saddle points made by ω in the complex α-plane in the neighbourhood of $\alpha_{r,\max}$. Thereupon, the flow is said to be absolutely unstable if $\omega_{0,i} > 0$ and convectively unstable if $\omega_{0,i} < 0$. Naturally, the absolute frequency can be found at each streamwise location and a streamwise distribution $\omega_0(r)$ can be obtained. To conclude this analysis, the line $\omega_0(r)$ ($r \in \mathbb{R}$) must then be assumed to be analytically continuable in the near complex r-plane, that is, single-valued and holomorphic in the neighbourhood of the real r-axis (Chomaz *et al.*, 1991b). If so, letting $\tilde{\omega}_0$ represent the analytical continuation of ω_0 for $r \in \mathbb{C}$, the complex frequency of the globally linear mode, ω_G, is given by the saddle point of $\tilde{\omega}_0(r \in \mathbb{C})$ closest to the real axis:

$$
\omega_G = \omega_0(\mathfrak{Re}(r_s)) \quad \text{where} \quad \frac{\partial \tilde{\omega}_0}{\partial r}(r_s) = 0 \quad \text{and} \quad r_s \in \mathbb{C}.
\tag{2.2.34}
$$

Once again, the whole flow is then said to be globally unstable if $\omega_{G,i} > 0$ and globally stable if $\omega_{G,i} < 0$. In order to reconstruct an approximation of the shape of this global mode (be it stable or not), it is necessary to solve the eigenvalue problem

$\mathcal{D}(\alpha, \omega_G, \chi) = 0$ for $\alpha \in \mathbb{C}$ (and the corresponding eigenvectors) at each streamwise location. The global mode velocity field is then given by an expression similar to Eq. (2.2.32):

$$\begin{array}{c} \tilde{u} \\ \tilde{v} \\ \tilde{w} \end{array} (r, \theta, z, t) = \mathfrak{Re} \begin{array}{c} iu \\ v \\ w \end{array} (r, z) \exp \left[i \int_0^r \alpha(\xi) d\xi + m\theta - \omega_G t \right] \quad . \quad (2.2.35)$$

In practice, note that the position of the saddle point r_s is estimated by fitting (in the least-square sense) a well-behaved function to $\omega_0(r \in \mathbb{R})$ and continuing it in the complex r-plane. Following the remarks by Juniper (2011), we use in this work Padé polynomials of equal numerator- and denominator-order to fit $\omega_0(r)$. Indeed they are known (Cooper & Crighton, 2000) to provide highly accurate low-order fits and better behave upon continuation in the complex plane than usual polynomial fitting functions.

2.2.4 Numerical resolution

The resolution of the previously discussed eigenvalue problem has been systematised and automatized for *all kind of axially symmetric base flow*[1] by the implementation of a massively parallel LNSE solver that will be hereafter referred to as AVLP. Note that the implementation was done entirely from scratch by the author of this document. A brief description is proposed under the form of a flowchart shown in Fig. 2.11.

This section is organized as follows. First the key points of the implementation of AVLP are discussed with details of the numerical strategies related to, mainly, the discretization and construction of the matrix system. Although AVLP can be used to analyse the stability of any axisymmetric base flow, the implementation choices shall be justified using arguments based on disc flow properties only to conserve the coherence of the present document. Finally, test-cases are presented to thoroughly validate the results yield by AVLP against known literature before using on actual enclosed rotor/stator flows (Sec. 3.7).

2.2.4.a Discretization

The two systems of equations, Eqs. (2.2.12)-(2.2.15) and Eqs. (2.2.22)-(2.2.25), are solved numerically using a spectral collocation method. This choice was made in light of the combined conclusions of the works by Malik *et al.* (1981, 1985) and Khorrami *et al.* (1989). They show that spectral collocation techniques are especially adequate to the study the stability of swirling flows, thanks to their convergence properties, for one. Furthermore, the collocation relies here on the base of Chebyshev polynomials (Orszag, 1971): the first-order differentiation matrix can indeed be computed analytically (see Canuto *et al.*, 1988, Eq. (2.4.31)) thus leading to minimal errors in the evaluation of the

---

[1]This includes naturally one- and two-disc flows but also open or confined jet flows for example.
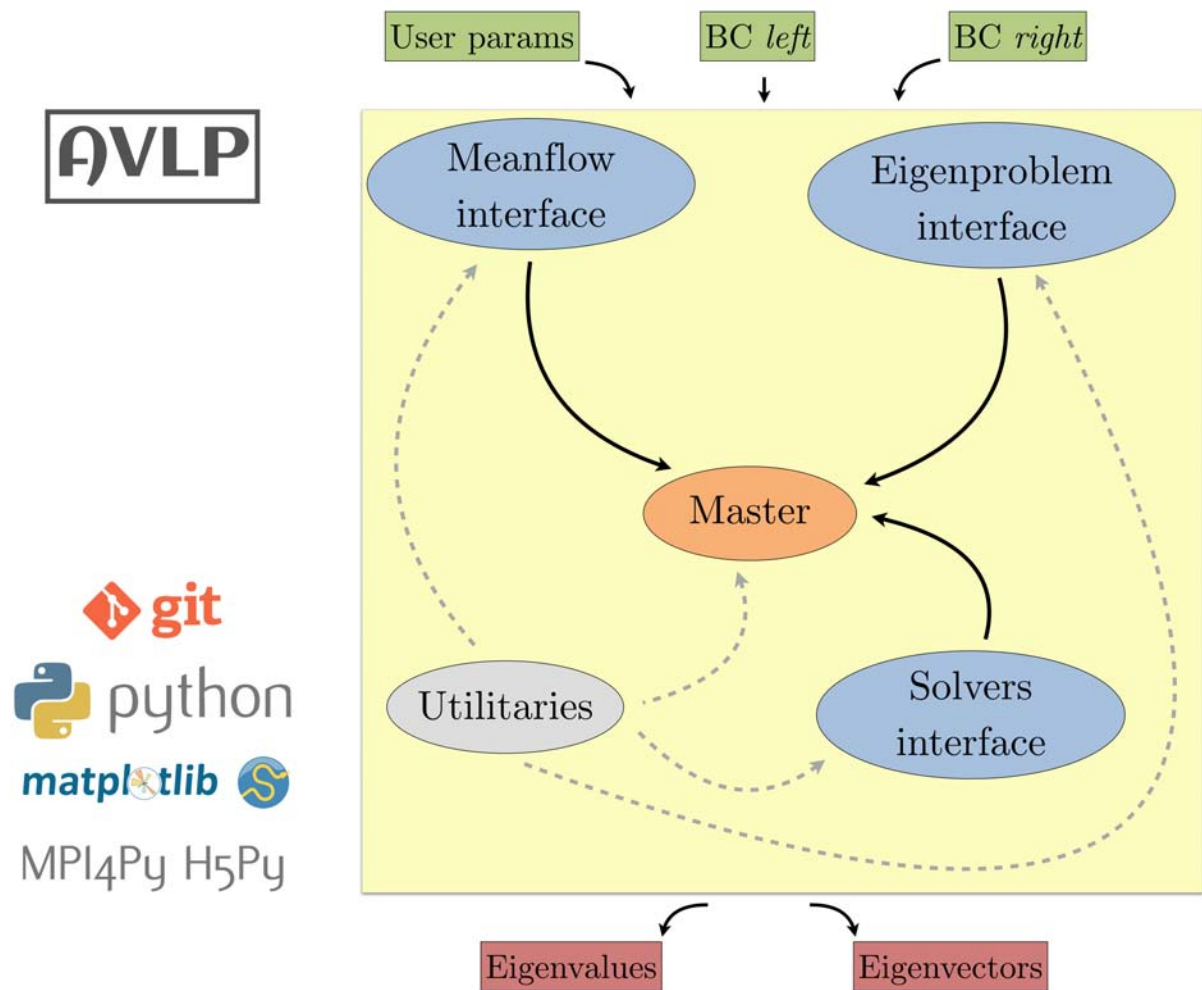
Figure 2.11 − Flowchart of the LNSE solver AVLP

first and second derivatives. Note that the implementation in AVLP uses the optimized functions proposed by Weideman & Reddy (2000).

The velocity components and the pressure are discretized at N_{GL} Chebyshev-Gauss-Lobatto (GL) collocation points where we solve the continuity and the three momentum equations too (refer to Canuto *et al.*, 1988, for more details on collocation techniques). The continuous dispersion relation $\mathcal{D}(\alpha, \omega, \chi) = 0$ is hence transformed into a matrix generalized eigenvalue problem that can be written:

$$\mathbf{A}(\alpha, \chi) \cdot \mathbf{X} = \omega \mathbf{B} \cdot \mathbf{X}, \tag{2.2.36}$$

where $\mathbf{A}$ and $\mathbf{B}$ are both square matrices of size $(4N_{GL}, 4N_{GL})$, and $\mathbf{X}$ is the vector of unknowns. Note that $\mathbf{B}$ is singular because of the absence of a pressure term in the incompressible Navier-Stokes continuity equation. To give rise to matrices that exhibit a

band structure, the vector of unknowns is organized in the following way:

$$\mathbf{X} \equiv [u, v, w, p]^{\dagger} = [u_0, v_0, w_0, p_0, u_1, v_1, w_1, p_1, \ldots, u_N, v_N, w_N, p_N], \qquad (2.2.37)$$

where $N = N_{\mathrm{GL}} - 1$ and the governing equations are also solved in the same alternating way. This strategy yields a matrix with seven diagonals and some extra-diagonal terms that is very sparse and therefore allows for the use of highly efficient algorithms to solve the generalized eigenvalue problem. Note that the implementation of new linearised problem should be done in the same fashion to conserve efficiency.

The boundary conditions necessary to close the system of equations (either Eq. (2.2.27) or Eq. (2.2.17)) are then added to the matrices, in which the index 0 represents the left bound of the interval, i.e. $z = 0$, and the index N represents the right bound of the interval, i.e. $z \to \infty$ or $z = 1$. With future developments in mind and for modularity purposes, AVLP accepts any Robin boundary condition on each variable and at each bound of the interval. In other words, one can input up to four boundary conditions at the 'left' bound and up to four at the 'right' bound, written as

$$[a_1, a_2, a_3, a_4] \cdot [u, v, w, p]_{\mathrm{bound}} + [b_1, b_2, b_3, b_4] \cdot \left. \frac{\partial [u, v, w, p]}{\partial z} \right|_{\mathrm{bound}} = c \qquad (2.2.38)$$

where the operator $\cdot$ represents here a scalar product, and the a_i, b_i and c are user-given constants. Finally, it is noteworthy that the boundary conditions on the 'left' bound of the interval are implemented in the first four rows of $\mathbf{A}$ and $\mathbf{B}$, whereas the 'right' boundary conditions use the last four rows of the matrices.

2.2.4.b   Mapping applications

By definition, Chebyshev polynomials are defined on the interval $[-1, 1]$ with the GL points taking values $\xi_j = \cos{(j\pi/(N_{\mathrm{GL}} - 1))}$ for $0 \leq j < N_{\mathrm{GL}}$. A coordinate transformation is thus necessary to map the Chebyshev collocation points $-1 \leq \xi \leq 1$ onto the physical domain, that is $0 \leq z \leq z_{\mathrm{max}}$ for a BEK flow or $0 \leq z \leq 1$ in the case of the flow between two discs. By nature, the distribution of GL points is denser near the boundaries of the interval. It appears hence already particularly adapted to the treatment of the stability of the flow between two discs where most of the features are expected to concentrate close to the discs. However, the flows from the BEK family possess only one physical boundary where significant features are most likely to gather. In this situation, a redistribution of the points near the disc can lead to much more efficient approximations. AVLP therefore offers two possibilities:

- a trivial linear mapping function, such that

$$f_{\mathrm{lin}} : \left| \begin{array}{ccc} \xi & \mapsto & z \\ [-1, 1] & \mapsto & [z_{\mathrm{min}}, z_{\mathrm{max}}] \end{array} \right. \qquad f_{\mathrm{lin}}(\xi) = \frac{z_{\mathrm{max}} + z_{\mathrm{min}}}{2} + \frac{z_{\mathrm{max}} - z_{\mathrm{min}}}{2}\xi, \qquad (2.2.39)$$

- a two-parameter rational mapping function defined by

$$f_{\text{rat}} : \left| \begin{array}{ccc} \xi & \mapsto & z \\ [-1, 1] & \mapsto & [0, z_{\max}] \end{array} \right. \qquad f_{\text{rat}}(\xi) = z_c \frac{1 + \xi}{1 - \xi + 2z_c/z_{\max}}, \qquad (2.2.40)$$

that allows half the collocation points to be redistributed in the interval $0 \leq z \leq z_c$.

Note that f_{rat} is originally dedicated to the projection of semi-infinite intervals $[0, \infty[$ onto $[0, 1]$, in which case ∞ is approximated by a large enough value of $z_{\max}$. The differences between the distribution of the GL points yield by the two mappings are illustrated in Fig. 2.12 with a simple sine function: in both cases, $N_{\text{GL}} = 40$, but the concentration coordinate for f_{rat} has been set at $X_c = 0.15$, which leads to the use of 20 points to describe the sine for $0 \leq X \leq 0.15$, and 20 for the rest of the domain.
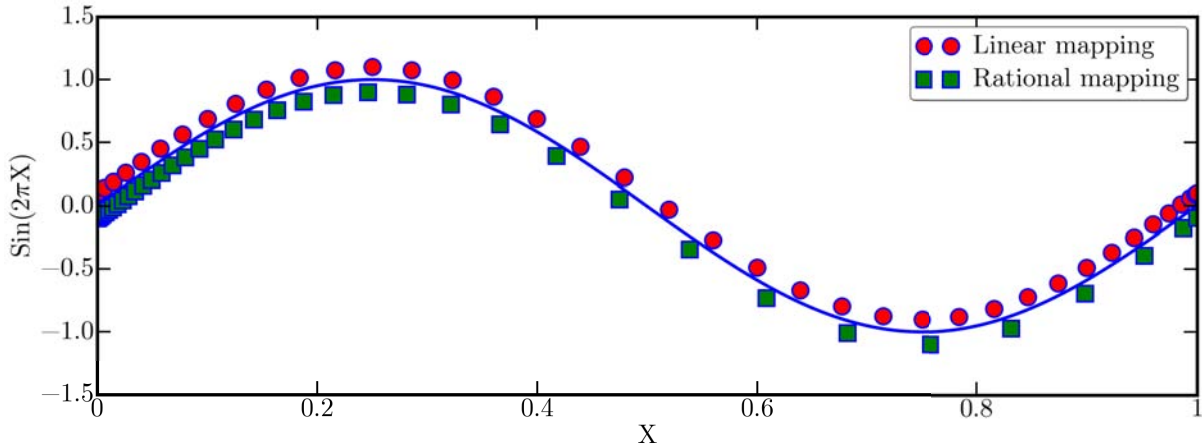
Figure 2.12 − Influence of the mapping function on the distribution of the mesh points: (red dots) linear mapping Eq. (2.2.39), (green squares) rational mapping with $X_c = 0.15$ Eq. (2.2.40).

2.2.4.c Multi-domain decomposition

To further facilitate the capture of the important mean flow features, the code offers the possibility to split the definition interval into sub-domains and mesh the sub-domains with independent numbers of GL points (G. Casalis, 2016, private communication). As an illustration, this section presents the steps realized by AVLP for the decomposition of a problem into two sub-problems.

Let $\mathbb{I} = [z_0, z_1]$ be the 1D interval for which a mean flow is input into AVLP for stability analysis. Let z_c be the coordinate at which $\mathbb{I}$ is split into two, and $N_{\text{GL},0}$ and $N_{\text{GL},1}$ be the number of GL points required for the description of $\mathbb{I}_0 = [z_0, z_c[$ and $\mathbb{I}_1 = [z_c, z_1]$ respectively. For this case the respective numbers of points are noted $N_i = N_{\text{GL},i} - 1$, $i \in \{0, 1\}$. Then two generalized eigenvalue problems can be written on the first sub-domain

$\mathbb{I}_0$

$$
\begin{bmatrix} \ddots & & \cdot{}^{\cdot{}^{\cdot}} \\ & \mathbf{A}_0 & \\ \cdot{}_{\cdot{}_{\cdot}} & & \ddots \\ \hline & 4N_{\mathrm{GL}\,0} & \end{bmatrix} \cdot \mathbf{X}_0 = \omega \begin{bmatrix} \ddots & & \cdot{}^{\cdot{}^{\cdot}} \\ & \mathbf{B}_0 & \\ \cdot{}_{\cdot{}_{\cdot}} & & \ddots \\ \hline & 4N_{\mathrm{GL}\,0} & \end{bmatrix} \cdot \mathbf{X}_0, \tag{2.2.41}
$$

and on the second sub-domain $\mathbb{I}_1$

$$
\begin{bmatrix} \ddots & & \cdot{}^{\cdot{}^{\cdot}} \\ & \mathbf{A}_1 & \\ \cdot{}_{\cdot{}_{\cdot}} & & \ddots \\ \hline & 4N_{\mathrm{GL}\,1} & \end{bmatrix} \cdot \mathbf{X}_1 = \omega \begin{bmatrix} \ddots & & \cdot{}^{\cdot{}^{\cdot}} \\ & \mathbf{B}_1 & \\ \cdot{}_{\cdot{}_{\cdot}} & & \ddots \\ \hline & 4N_{\mathrm{GL}\,1} & \end{bmatrix} \cdot \mathbf{X}_1, \tag{2.2.42}
$$

where $\mathbf{X}_i$ represents the restriction of $\mathbf{X}$ to $\mathbb{I}_i$ and the $\mathbf{A}_i$ and $\mathbf{B}_i$ are square matrices. 'Left' boundary conditions, to be applied at $z = z_0$, are implemented on the first four rows of $\mathbf{A}_0$ and $\mathbf{B}_0$, whereas the 'right' boundary conditions, to be applied at $z = z_1$, are implemented on the last four rows of $\mathbf{A}_1$ and $\mathbf{B}_1$. Naturally, if the domain is divided in more than two sub-domains, the 'left' boundary conditions are imposed in the sub-problem posed on the sub-interval containing z_0, and the 'right' boundary conditions on the sub-interval containing z_1.

To close the problem, interface conditions have to be implemented at z_c. More precisely, $\mathcal{C}^0$ and $\mathcal{C}^1$ conditions are imposed at the interface, such that

$$
\begin{aligned}
[u, v, w, p](z_c)_0 &= [u, v, w, p](z_c)_1 \\
\left. \frac{\partial [u, v, w, p]}{\partial z}(z_c) \right|_0 &= \left. \frac{\partial [u, v, w, p]}{\partial z}(z_c) \right|_1
\end{aligned}, \tag{2.2.43}
$$

the former being implemented on the last four rows of $\mathbf{A}_0$ and $\mathbf{B}_0$, and the latter on the first four rows of $\mathbf{A}_1$ and $\mathbf{B}_1$. The complete generalized eigenvalue problem is finally

obtained by combining all the sub-problems into a block diagonal matrix:

$$
\left.\begin{array}{c}
\left[\begin{array}{ccc}
\text{Left B.C.} & & 0 \\
\ddots \quad \mathbf{A}_0[4:4N_{\mathrm{GL},0}-4,:] \quad \cdot^{\cdot} & & 0 \\
\cdot^{\cdot} \qquad\qquad \ddots & & \\
& \begin{array}{c}\mathcal{C}^0 \text{ conditions} \rightarrow \\ \mathcal{C}^1 \text{ conditions} \rightarrow\end{array} & \\
0 & \ddots \quad \mathbf{A}_1[4:4N_{\mathrm{GL},1}-4,:] \quad \cdot^{\cdot} & \\
0 & \cdot^{\cdot} \qquad \text{Right B.C.} \qquad \ddots & \\
\end{array}\right] \\
\hline
\mathbf{A}
\end{array}\right\} \cdot \mathbf{X} =
$$

$$
\omega \left.\begin{array}{c}
\left[\begin{array}{ccc}
\text{Left B.C.} & & 0 \\
\ddots \quad \mathbf{B}_0[4:4N_{\mathrm{GL},0}-4,:] \quad \cdot^{\cdot} & & 0 \\
\cdot^{\cdot} \qquad\qquad \ddots & & \\
& \begin{array}{c}\mathcal{C}^0 \text{ conditions} \rightarrow \\ \mathcal{C}^1 \text{ conditions} \rightarrow\end{array} & \\
0 & \ddots \quad \mathbf{B}_1[4:4N_{\mathrm{GL},1}-4,:] \quad \cdot^{\cdot} & \\
0 & \cdot^{\cdot} \qquad \text{Right B.C.} \qquad \ddots & \\
\end{array}\right] \\
\hline
\mathbf{B}
\end{array}\right\} \cdot \mathbf{X}
$$

$$(2.2.44)$$

where 'B.C.' stands for 'boundary condition', the notation $\mathbf{M}_i[a{:}b,:]$ stands for the sub-matrix of $\mathbf{M}_i$ containing the rows between row a (included) and b (excluded) and all its columns, and $\mathbf{X}$ is the full vector of unknowns on $\mathbb{I}$.

The differences between the distribution of the GL points induced by the number of sub-domains are illustrated in Fig. 2.13 with a simple sine function. Although the total number of GL points remains the same in both cases ($N_{\mathrm{GL}} = 40$ and $N_{\mathrm{GL},0} = N_{\mathrm{GL},1} = 20$), the combined use of a linear mapping and subdivision in two domains leads to a much higher concentration of points in the vicinity of $z_c = 0.25$. Using multiple domains can thus facilitate the capture of the meanflow features if one places, for instance, a cut point at each important inflexion point of a mean profile Doing so furthermore makes the use of f_{rat} unnecessary, thus preserving the spectral accuracy and convergence properties of the Chebyshev collocation technique (the interested reader is referred to Canuto *et al.*, 1988, for more details on loss of spectral accuracy due to the use of rational mappings).

2.2.4.d   Resolution methods

The last features of importance to be discussed for the LNSE solver that is AVLP are the three different options offered to solve the generalized eigenvalue problem, Eq. (2.2.36).
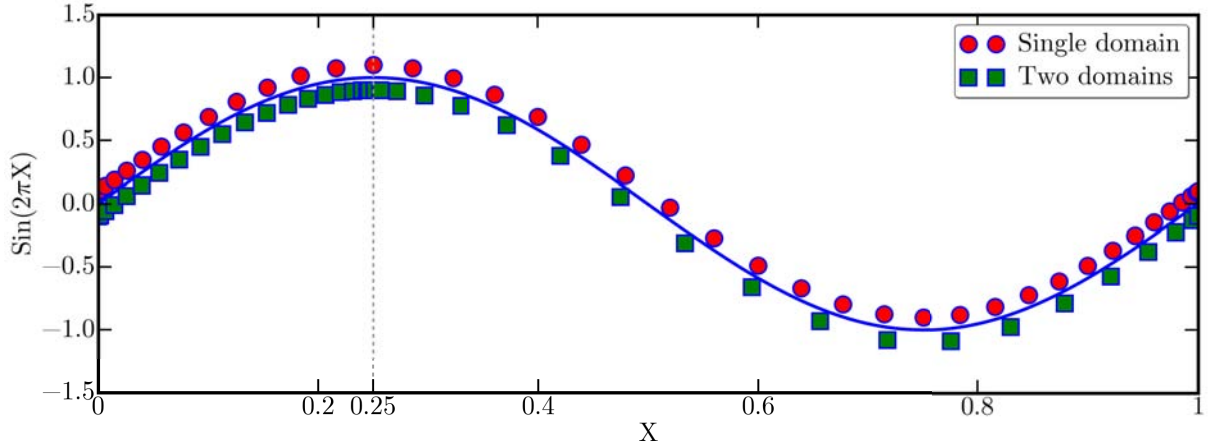
Figure 2.13 – Influence of the number of sub-domains on the distribution of the mesh points: (red dots) single domain with $N_{\mathrm{GL}} = 40$, (green squares) two domains with $z_c = 0.25$ and $N_{\mathrm{GL},0} = N_{\mathrm{GL},1} = 20$. In both case, a linear mapping f_{lin} has been used.

- The first mode of the solver, referred to as *spectrum* in the user parameters file, is reserved for a direct resolution of the eigenvalue problem. It relies on the SciPy (Jones *et al.*, 2001) wrap, called EIG, of the LAPack routine ZGEEV (Anderson *et al.*, 1999) that computes all the eigenvalues and eigenvectors of a complex generalized eigenvalue problem. In other words, knowing the values of the radial wavenumber $\alpha = \alpha_r + i\alpha_i$ and azimuthal wavenumber m along with all the local characteristics of the mean flow (base flow $\mathbf{U}$, local Reynolds number Re_δ), the *spectrum* mode yields all the eigenvalues, $\omega = \omega_r + i\omega_i$, and eigenvectors, $\mathbf{X}$, that satisfy the dispersion relation $\mathcal{D}(\alpha, \omega, \chi) = 0$. Once all the eigenvalues are known, they are sorted by decreasing temporal amplification rate ω_i and, by default, only the most amplified mode is output by AVLP with its corresponding eigenvector. Upon request, the user can output all the eigenvalues produced by EIG and therefore by sweeping an interval of α it becomes possible to visualize all the temporal branches at the given location of the local analysis.

- The second mode of the solver, historically referred to as *shooting* in the user parameters file, is used to converge to a specific solution ω of the eigenvalue problem Eq. (2.2.36) given an initial estimate ω_0, and knowing all other parameters α and χ (recall χ represents the set of all parameters others than the two complex numbers α & ω). In this mode, two techniques are proposed to the user to achieve the aforementioned convergence.

    – The first possibility is to use a complex version of Newton's method to find the ω-roots of the linear problem $\mathbf{L} \cdot \mathbf{X} = 0$, where $\mathbf{L} = \mathbf{A} - \omega\mathbf{B}$, for a given initial value ω_0 (G. Casalis, 2016, private communication). The main idea is to make the system inhomogeneous by replacing one of the Dirichlet boundary conditions Eq. (2.2.17) (or Eq. (2.2.27)) by a non-zero Neumann boundary condition and iterate on ω until the original Dirichlet boundary condition is

actually verified.

As an example, let us consider the case of the stability of a one-disc flow described in Sec. 2.2.2.a. The no-slip Dirichlet boundary condition at the disc, $w(0) = 0$, is arbitrarily replaced by the Neumann condition $u(0) = 1$. The singular system $\mathbf{L} \cdot \mathbf{X} = 0$ therefore becomes $\mathcal{L} \cdot \mathbf{Y} = \mathbf{b}$ where $\mathbf{b}$ is a vector with the same dimension as $\mathbf{Y}$ filled with zeros but on the third row (where the third boundary condition at $z = 0$ is written, see Sec. 2.2.4.a) filled with a one, i.e. $\mathbf{b}_3 = 1$. Also, by definition, $\mathcal{L}$ is no longer singular and one can therefore define the application

$$ F \ : \ \left| \begin{array}{l} \mathbb{C} \to \mathbb{C} \\ \omega \mapsto \mathbf{Y}_3 \end{array} \right. \tag{2.2.45} $$

that we assume to be holomorphic, and the value $\mathbf{Y}_3$ is obtained by the inversion of the problem, i.e. $\mathbf{Y} = \mathcal{L}^{-1} \cdot \mathbf{b}$. A classical Newton's method can then be used to solve $F(\omega) = 0$, noting that the holomorphicity of F allows to iterate only on the real part of ω and therefore the problem can be seen as seeking the root of a real-valued function defined over the real numbers.

– The second techniques uses the SciPy (Jones *et al.*, 2001) wrap, called EIGS, of the ARPack routine ZNEUPD (Lehoucq *et al.*, 1998), which is designed to solve a complex generalized eigenvalue problem and then return only one eigenvalue that is closest to a given estimate.

Note that the use of EIGS is recommended as the values of ω yield by the program are ensured to be eigenvalues of the problem, whereas the Newton's method does not provide any such insurance.

The present mode of resolution is especially useful when one wants to track a specific temporal branch throughout the parameter space $(\alpha_i, Re_\delta, m, \alpha_r)$. Indeed, starting from a known solution ω_1 at a known quadruplet $(\alpha_i, Re_\delta, m, \alpha_r)_1$, it is possible to use this solution as the starting guess to seek the solution ω_2 at a second quadruplet $(\alpha_i, Re_\delta, m, \alpha_r)_2 = (\alpha_i, Re_\delta, m, \alpha_r)_1 + (0, 0, 0, \delta\alpha_r)$ infinitesimally close to the first quadruplet. Linear extrapolation can then be used to estimate the starting guess at a third quadruplet. If more quadruplets are to be treated (at $3\delta\alpha_r$, $4\delta\alpha_r$, etc...) then the initial guesses are derived from cubic extrapolation of the already obtained solutions. This line of reasoning is naturally valid for small increments in any directions of the parameter space.

• The third mode of use of AVLP, referred to as *tracking* in the user parameters file, is designed to invert the problem and give the possibility to the user to solve for one or more parameters, all other quantities being known and given the value of ω_r, ω_i or $\omega_r + i\omega_i$. To proceed, the SciPy (Jones *et al.*, 2001) routine EIGS is embedded within the SciPy (Jones *et al.*, 2001) optimization function FMIN that uses the Nelder & Mead (1965) simplex algorithm to minimize the distance between the current value of ω and the given target by optimizing the vector of unknown

parameters. This mode is particularly useful to track the evolution of modes with a given frequency throughout the parameter space for instance or to get an outline of the neutral stability curve of a given base flow by computing all points that verify $\alpha_i = \omega_r = \omega_i = 0$ in the parameter space. Note that if only ω_r or ω_i is specified, the other component will evolve freely without constraints.

2.2.4.e Validation of the LNSE solver AVLP

Before using AVLP on enclosed rotor/stator cavity flows (see Chap. 3) to establish a predictive strategy and detect the modes most susceptible to be triggered in a real flow (see Sec. 3.7), a validation step is necessary to ensure the correctness and accuracy of the LNSE solver.

The code being written for any axially symmetric mean flow, the known literature is very rich of test-cases, both for disc flows (Malik *et al.*, 1981; Malik, 1986; Balachandar *et al.*, 1992; Lingwood, 1995*b*, 1997) and jet flows (Khorrami *et al.*, 1989; Griffond *et al.*, 2000; Gallaire & Chomaz, 2003*b*; Abu-Irshaid *et al.*, 2007; Parras & Fernandez-Feria, 2007) - refer to App. D for the complete set of stability equations implemented for jets in AVLP. Such problems are therefore selected to represent a variety of flow domains and boundary conditions which could be studied with the spectral collocation code. The primary goal of this presentation is therefore to use these sample calculations to demonstrate the accuracy and efficiency of AVLP, rather than to attempt to duplicate the earlier work of others naturally.

Stability of Poiseuille flow in a pipe
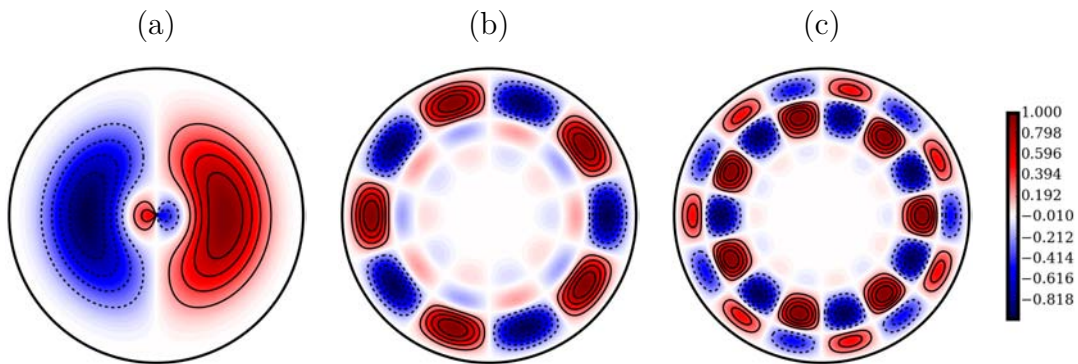
Figure 2.14 – Fluctuations of radial velocity for the most temporally amplified mode at (*a*) $Re = 200$, $m = 1$, $\alpha_r = 1$, (*b*) $Re = 1000$, $m = 5$, $\alpha_r = 1$ and (*c*) $Re = 1000$, $m = 7$, $\alpha_r = 1$.

The transition from laminar to turbulent flow of a viscous fluid in a pipe was first observed experimentally by Reynolds (1883). Subsequently, in an effort to explain the phenomenon of transition, numerous studies on the temporal stability ($\alpha_i \equiv 0$, $\omega \in \mathbb{C}$ unknown) of pipe flow have been carried out (e.g. Lessen *et al.*, 1968). They all

demonstrated the stability to infinitesimal axisymmetric ($m = 0$) and non-axisymmetric ($|m| > 0$) disturbances that are applied at an initial instant everywhere in the fluid and let grow or decay with time. Visualization of the radial velocity fluctuations imposed by such instabilities are shown on Fig. 2.14.

For the physically more realistic problem of spatial stability ($\omega_i \equiv 0$, $\alpha \in \mathbb{C}$ unknown) where a disturbance, imposed at a specific location in the fluid, grows or decays with the axial distance, both experimental and theoretical studies (e.g. Garg & Rouleau, 1972) also demonstrated the stability of the flow to all infinitesimal disturbances. The objective of the present paragraph is therefore to show the results obtained with AVLP also evidence that the circular Poiseuille flow is found temporally and spatially stable to all infinitesimal perturbations.

The mean velocity profile for this problem is the well-known profile given by

$$U(r) = V(r) = 0 \ \text{ and } \ W(r) = 1 - r^2, \ r \in [0, 1] \tag{2.2.46}$$

for which the boundary conditions (Khorrami *et al.*, 1989) are

$$\text{at } r = 1, \ \forall m, \ u(1) = v(1) = w(1) = 0 \ \text{ and } \ p\,(1) = 0$$

$$\text{at } r = 0, \quad \begin{aligned} &\text{if } m = 0, \quad u(0) = v(0) = 0 \ \text{ and } \ w\,(0) = p\,(0) = 0 \\ &\text{if } m = \pm 1, \quad w(0) = p(0) = 0, \ u(0) + mv(0) = 0, \\ &\qquad\qquad\quad 2u\,(0) + mv\,(0) = 0 \\ &\text{if } |m| > 1, \quad u(0) = v(0) = w(0) = p(0) = 0 \end{aligned} \tag{2.2.47}$$

Using a shooting method, Lessen *et al.* (1968) found no temporal instability for $m = 1$ perturbations. Their results, later verified by Khorrami *et al.* (1989) are tabulated in Tab. 2.1 along with the present calculations. Excellent agreement is clearly obtained. Note that accuracy to the fifth digit (as in Khorrami *et al.* (1989)) is reached with AVLP for $N_{\text{GL}} \geq 15$ at $Re = 200$ and $N_{\text{GL}} \geq 21$ at $Re = 2200$, when Khorrami *et al.* (1989) mention that their results are obtained for $N_{\text{GL}} \geq 30$. To complete this test, we extend the temporal problem to higher values of m, keeping the axial wavenumber and Reynolds number fixed at $\alpha = 1.0$ and $Re = 1000$ respectively. The solutions are shown in Tab. 2.2 and are again in agreement with the reference data.

Although AVLP has been designed as a direct temporal linear stability solver, several options to inverse the problem and solve for the spatial stability of a flow have been discussed in Sec. 2.2.4.d. Since Garg & Rouleau (1972) published results pertaining to the spatial stability of the pipe Poiseuille flow (that were later verified by Khorrami *et al.* (1989)), we conclude the present test case with the comparison of the values of $\alpha \in \mathbb{C}$ for two modes $m = 0$ and $m = 1$, at $Re = 10^4$ and a fixed temporal frequency $\omega = 0.5 \in \mathbb{R}$. The results are given in Tab. 2.3. They can be seen to be as accurate as the eigenvalues obtained for the temporal stability problems. However the value of the real frequency is

	Lessen *et al.* (1968)		Khorrami *et al.* (1989)		Present method	
Re	ω_r	ω_i	ω_r	ω_i	ω_r	ω_i
200	0.645	-0.129	0.64526	-0.129205	0.6452613	-0.1292054
2200	—	-0.067	0.39797	-0.067709	0.397967	-0.0677087
2200	—	—	0.89663	-0.048114	0.896633	-0.0481145

Table 2.1 – Comparison of the results of Lessen *et al.* (1968) and Khorrami *et al.* (1989) with those of AVLP for the temporal stability of the cylindrical Poiseuille flow. All computations were done at $m = 1$ and $\alpha = 1.0 \in \mathbb{R}$.

	Metcalfe & Orszag (1973)	Khorrami *et al.* (1989)	Present method
m	ω_i	ω_i	ω_i
5	-0.180604	-0.180604	-0.18060442
7	-0.207943	-0.207943	-0.20794339
9	-0.245645	-0.245645	-0.24564488
21	-0.710998	-0.710998	-0.71099796
51	-3.37925	-3.37925	-3.3792484
101	-12.0699	-12.0699	-12.069928

Table 2.2 – Comparison of the variation of the imaginary part of the least stable temporal mode as a function of the azimuthal wavenumber m, with $\alpha = 1.0 \in \mathbb{R}$ and $Re = 1000$.

only accurate to the seventh digit, i.e. $\omega \simeq 0.5 \pm O(10^{-7})$. For this specific test case, convergence was therefore pushed further until the frequency target is reached *exactly*, i.e. $\omega \simeq 0.5 \pm O(10^{-17})$. With this new constraint, obtained results are presented in the second column of Tab. 2.3 and can be seen to differ from the results published in the literature, after the sixth digit only.

	Garg & Rouleau (1972)	Khorrami *et al.* (1989)
m	α	α
0	$0.51998925173 + 0.02083549388i$	$0.51998925171 + 0.02083549388i$
1	$0.5352510831 + 0.0172276439i$	$0.53525108 + 0.01722763i$

	Present method	
m	α	α
0	$0.51998925173 + 0.02083549388i$ for $\omega = 0.49999989 - 1.43 \times 10^{-9}i$	$0.5199893712997 + 0.02083549834788i$ for $\omega = 0.5 + 4.09 \times 10^{-19}i$
1	$0.5352510831 + 0.0172276439i$ for $\omega = 0.49999989 - 2.09 \times 10^{-9}i$	$0.5352512001991 + 0.01722764782608i$ for $\omega = 0.5 - 3.5 \times 10^{-17}i$

Table 2.3 – Comparison of the variation of the spatial wavenumber of the least stable spatial mode as a function of the azimuthal wavenumber m, with $\omega = 0.5 \in \mathbb{R}$ and $Re = 10^4$.

Stability of the flow over a single rotating disc

We consider now the stability of the flow over an infinite rotating disc, also known as the Von Kármán (1921) pump (see Fig. 2.2). Early experimental work focused on the boundary layer developing above a rotating disc (Smith, 1947; Gregory *et al.*, 1955) showed that it was sensitive to an inviscid instability because of the inflectional nature of the velocity profiles close to the disc. Later investigations (Kobayashi *et al.*, 1980; Littell & Eaton, 1994) revealed that at high enough local Reynolds numbers the Von Kármán layer is also subject to viscous crossflow-like instabilities. Altogether, these instabilities organize the fluctuations of velocity and pressure in the boundary layer under the form of axisymmetric ($m = 0$) and/or three-dimensional spiral patterns ($|m| > 0$) - refer to Fig. 2.8 or Sec. 3.6 for examples of such patterns. In this paragraph, we first fix the local Reynolds number $Re_\delta = 450$ and study the temporal response of the flow to the injection of infinitesimal perturbations with $0 \leq \alpha_r \leq 1$ and $m \in [\![0, 100]\!]$. At such a Reynolds number, both the inviscid and the viscous branches are expected to appear as shown in Balachandar *et al.* (1992). The neutral curves for stationary disturbances, i.e. for $\omega_r = \omega_i = \alpha_i = 0$, is then computed to assess the ability of AVLP to qualify correctly the response of the rotating flow at all Reynolds numbers. In this exercise, the values of the transitional Reynolds numbers for the viscous and the inviscid branches are compared to known literature. Finally, at a given location in the parameter space $(\alpha, Re_\delta, m, \omega) = (0.3618, 430, 32.35, 0.0041i)$ we validate the eigenvectors obtained with AVLP to reference data from Appelquist & Imayama (2014).

As already mentioned in Sec. 2.1.2 and Sec. 2.1.2.a, the base flow for this problem belongs to the BEK family and is characterized by a Rossby number $Ro = -1$ (see Eq. (2.1.9)). Upon substitution in Eqs. (2.1.11)-(2.1.14) and after numerical resolution using the 4th-order Runge-Kutta solver implemented in App. C, one obtains the mean velocity components represented in Fig. 2.15.

In the present test-case, the domain was divided into two sub-domains, D_1 and D_2 spanning respectively the intervals $[0, 10[$ and $[10, 100]$, with $N_{\text{GL},1} = N_{\text{GL},2} = 20$. The boundary conditions necessary to close the set of four ordinary differential equations Eqs. (2.2.12)-(2.2.15) are the same used, for example, by Balachandar *et al.* (1992):

$$\text{at } z = 0, \ u(0) = v(0) = w(0) = 0,$$
$$\text{at } z \to \infty, \ u(\infty), v(\infty), w(\infty) \to 0. \tag{2.2.48}$$

Figures 2.16 and 2.17 show contour plots of amplification rate and frequency of the instability of the Von Kármán (1921) flow in the (α_r, m)-plane for $Re_\delta = 450$. In these figures, the radial and azimuthal wavenumbers are normalized by $\alpha_{1s} = 0.328$ and $Re_\delta \beta_{1s} = 31.455$ as in Balachandar *et al.* (1992) to allow for an easy comparison with their data. The results are overall in very good agreement and show that AVLP captures with accuracy the same mode as Balachandar *et al.* (1992) both in terms of amplification rate (Fig. 2.16) and frequency (Fig. 2.17). What is more, it appears that AVLP is capable of better capturing the secondary region of positive amplification rate
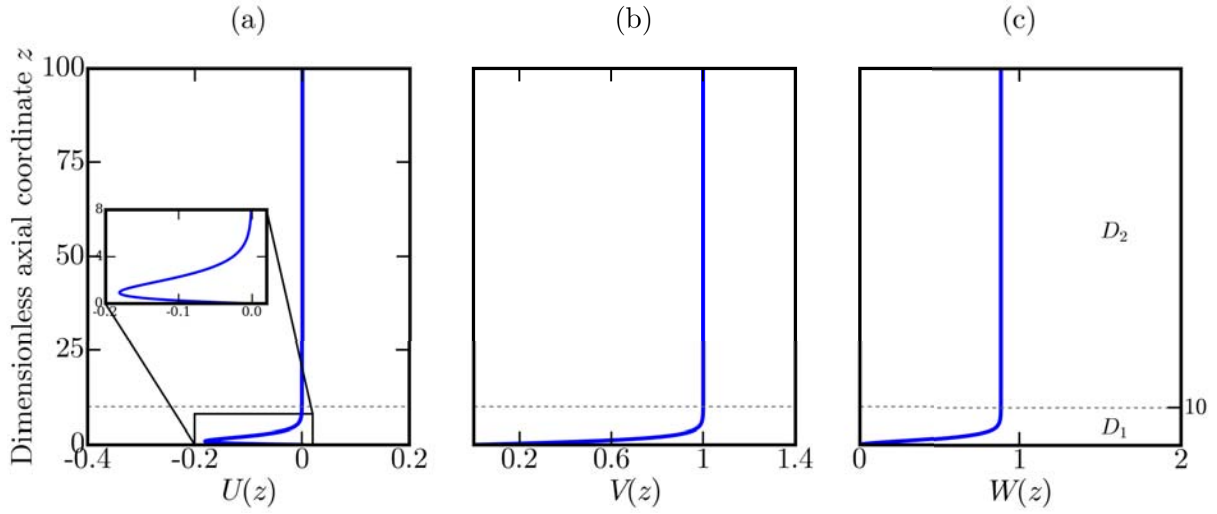
Figure 2.15 – Auto-similar velocity profiles of the laminar Von Kármán (1921) flow with relevant notations. (*a*) Radial velocity U, (*b*) azimuthal velocity V and (*c*) axial velocity W.

(bottom left corner of Fig. 2.16*b*). Note also that given the continuous character of the frequency map, it is reasonable to conclude that the two regions of positive amplification are generated by the same (temporal) branch.
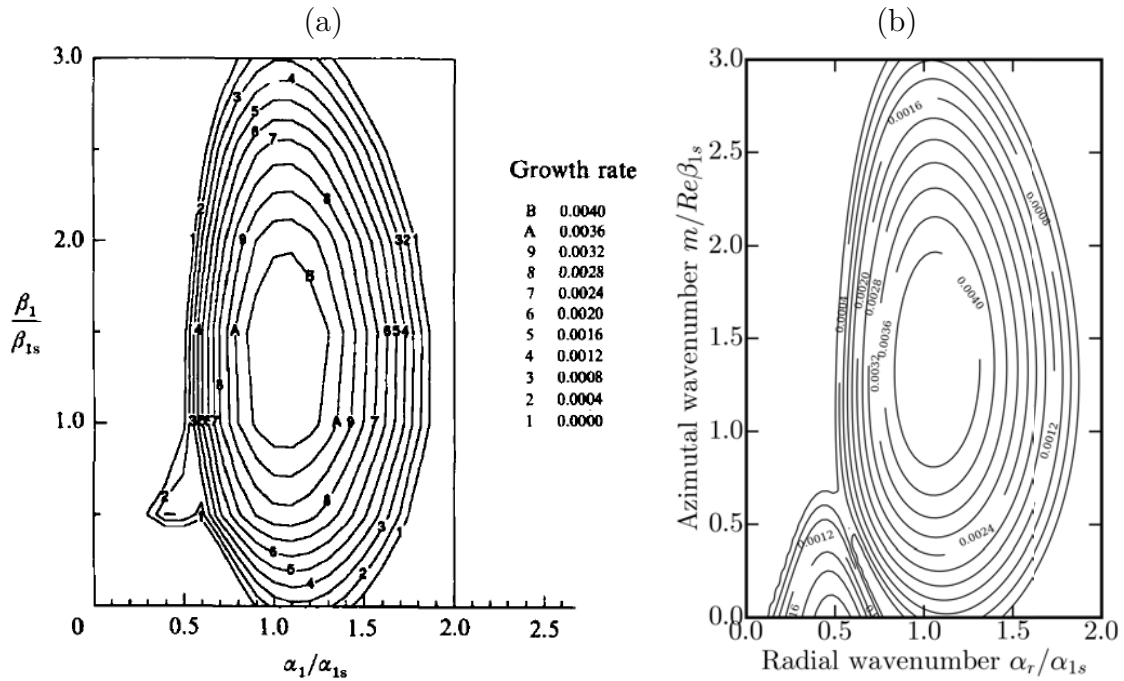
Figure 2.16 – Contour plot of amplification rate in the wavenumber (α_r,m)-plane for $Re_\delta = 450$ - comparison between (*a*) Balachandar *et al.* (1992) results and (*b*) AVLP results. Here the radial and azimuthal wavenumbers are normalized by $\alpha_{1s} = 0.328$ and $Re_\delta\beta_{1s} = 31.455$.

Finally, according to these authors, the most amplified stationary mode is found at
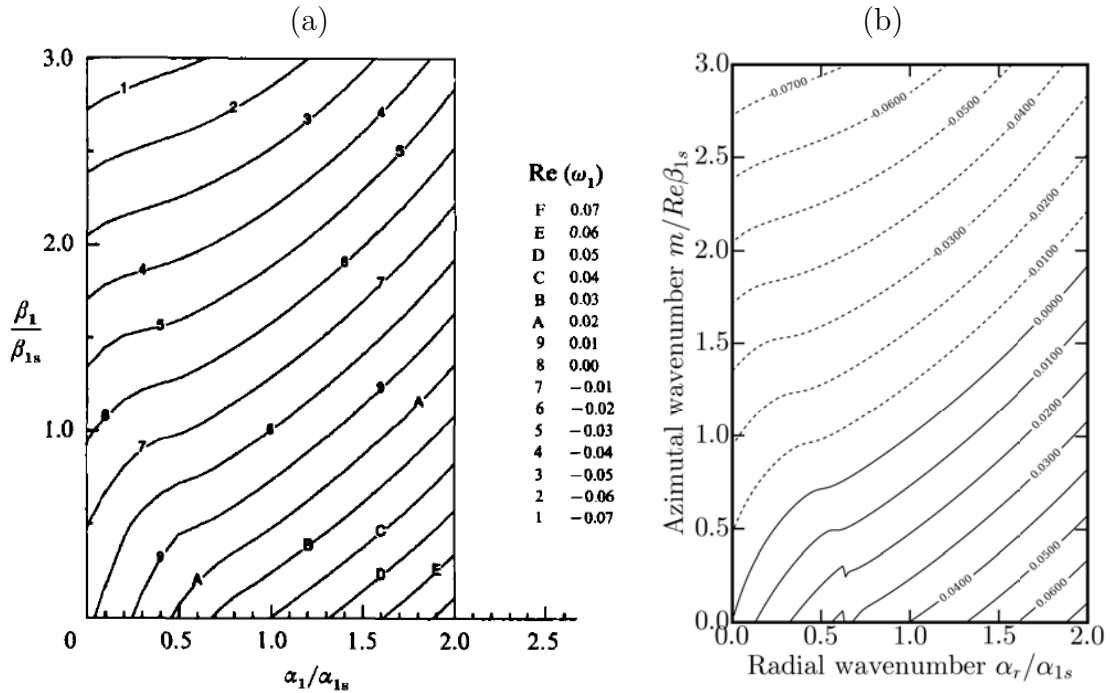
Figure 2.17 – Contour plot of frequency in the wavenumber (α_r,m)-plane for $Re_\delta = 450$ - comparison between (*a*) Balachandar *et al.* (1992) results and (*b*) AVLP results. Here the radial and azimuthal wavenumbers are normalized by $\alpha_{1s} = 0.328$ and $Re_\delta\beta_{1s} = 31.455$.

($\alpha_{1s}, Re_\delta\beta_{1s}$) and the most amplified travelling mode at approximately ($\alpha_{1s}, 1.5Re_\delta\beta_{1s}$). We present in Tab. 2.4 the comparison between these coordinates and the coordinates of the corresponding modes as yield by AVLP. This comparison shows that although the results yield by AVLP match qualitatively well those presented by Balachandar *et al.* (1992), there is nonetheless some non-negligible quantitative differences in the locations of the most amplified modes. Such differences naturally raise doubts concerning the precision of AVLP, but the following three points support the correctness of the present work:

- It has been demonstrated in previous paragraphs how AVLP reaches the same precision as existing results in the literature for different cases, and can even better converge in some cases.

- The present work relies on the trivial linear mapping f_{lin} whereas Balachandar *et al.* (1992) use a complex mapping function involving the composition of a third-order polynomial function with a rational fraction akin to f_{rat}. This is known (see e.g. Canuto *et al.*, 1988) to hinder the accuracy and convergence properties of the Chebyshev collocation technique.

- Finally, Balachandar *et al.* (1992) use $N_{\text{GL}} = 128$ collocation points which is suspiciously high to solve the stability of the Von Kármán (1921) flow when more modern works (Tuliszka-Sznitko & Soong, 2000, 2001; Appelquist, 2014) assert that $32 \lesssim N_{\text{GL}} \lesssim 64$ is sufficient to reach convergence for similar configurations.

	Balachandar *et al.* (1992)	Present method
M.a. stationary mode	$(0.328, 31.455)$	$(0.36, 33.706)$
	$\mathfrak{Im}(\omega) \gtrsim 4.0 \times 10^{-3}$	$\omega = 4.437678 \times 10^{-3} i$
M.a. travelling mode	$(0.328, 47.1825)$	$(0.347, 42.91)$
	$\mathfrak{Re}(\omega) \simeq -0.017$ $\mathfrak{Im}(\omega) \gtrsim 4.0 \times 10^{-3}$	$\omega = -0.0109956 + 0.00460204 i$

Table 2.4 – Comparison of the results of Balachandar *et al.* (1992) with those of AVLP for the coordinates in the (α_r, m)-plane of the most amplified stationary and most amplified travelling modes of the Von Kármán (1921) flow at $Re_\delta = 450$. The abbreviation 'M.a.' stands for 'most amplified'.

Another diagnostic commonly used in the literature to qualify the stability of the Von Kármán (1921) flow is to plot the neutral curves for stationary disturbance, i.e. the lines such that $\omega_r = 0$, $\omega_i = 0$ and $\alpha_i = 0$. These are presented in both the (Re_δ, α_r) and the (Re_δ, m)-planes on Fig. 2.18 where results yield by AVLP are compared with the work of Lingwood (1997) and the more recent data produced by Appelquist & Imayama (2014). All three datasets are very close to each other, but it can however be noted that the branch due to viscous mechanism (upper branch, minimum at $Re_\delta \simeq 285.5$) matches exactly the data by Appelquist & Imayama (2014) whereas the branch due to the inviscid mechanism (lower branch, minimum at $Re_\delta \simeq 450.5$) is closest to the results of Lingwood (1997). A quick summary of the values of the local minimum Reynolds numbers found in the literature is given in Tab. 2.5. It can be reasonably concluded that the values yield by AVLP are satisfactorily within the range of reference values given by the literature.

	Viscous branch	Inviscid branch
Malik (1986)	285.36	440.88
Lingwood (1997)	290	458
Appelquist & Imayama (2014)	285	460
Present work	285.5	450.5

Table 2.5 – Comparison of the values of the critical Reynolds numbers Re_δ

It is interesting to conclude this section by a comparison of the eigenvectors produced by AVLP with some reference data from the literature. In particular, Appelquist & Imayama (2014) present the eigenfunction related to the stationary mode with highest amplification rate, that they place at $Re_\delta = 430$, $m = 32.35$, $\alpha_r = 0.3618$ and $\omega = 0.0041 i$. This mode is also captured by AVLP which yields $\omega = 4.08013 \times 10^{-3} i$ and eigenvectors that match perfectly the ones obtained by Appelquist & Imayama (2014) as can be seen on Fig. 2.19.
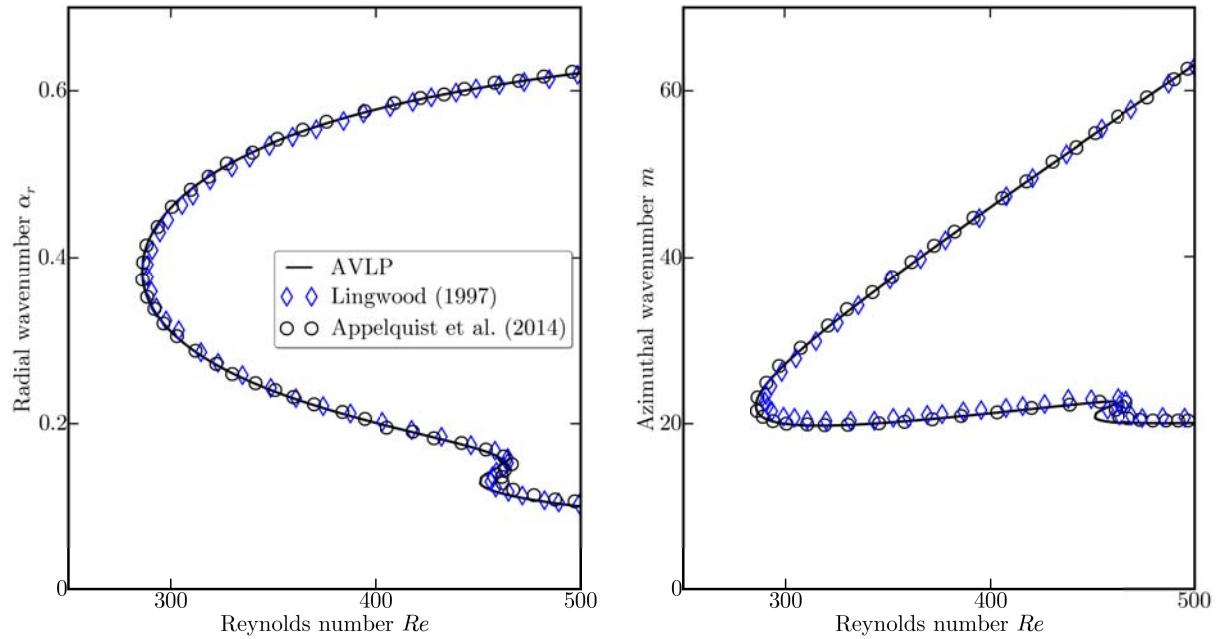
Figure 2.18 – Neutral curves for stationary disturbance ($\omega_r = 0$, $\omega_i = 0$, $\alpha_i = 0$). Comparison with the works by ($\diamond$, diamonds) Lingwood (1997) and ($\circ$, circles) Appelquist & Imayama (2014). *Re* stands for the local Reynolds number called Re_δ in Eqs. (2.2.12)-(2.2.15).
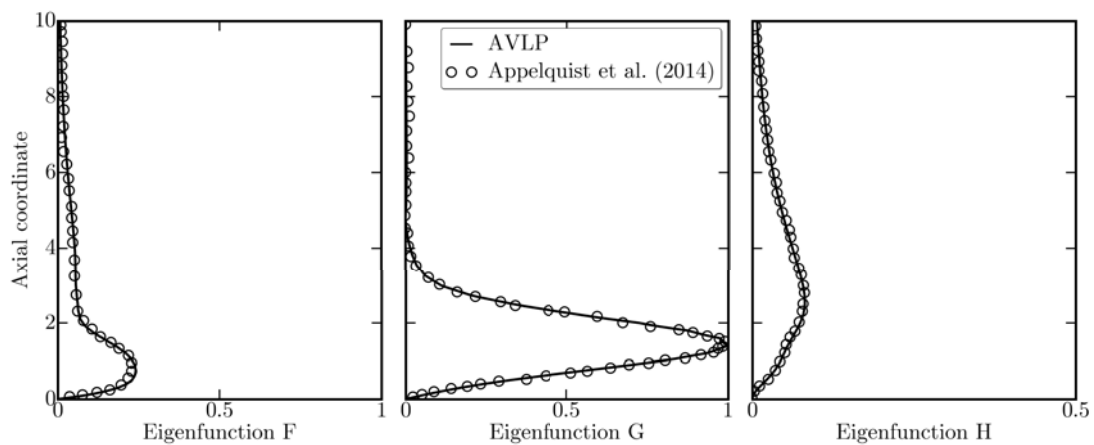
Figure 2.19 – Eigenfunctions for $Re_\delta = 430$, $m = 32.35$, $\alpha_r = 0.3618$, $\omega = 0.0041i$. Solid lines indicate the present results of AVLP. Local linear stability results from Appelquist & Imayama (2014) ($\circ$) are given as reference.

Stability of a swirling jet

Vortices with axial flow are encountered in many technical applications such as leading-edge vortices on delta wings or flame holders in combustion devices. Because of that, considerable effort (see Ash & Khorrami, 1995, for a complete review) has been turned towards understanding the stability characteristics of these flows since, depending on the amount of swirl and the base flow, they have been proven to be highly sensitive to perturbations and exhibit vortex breakdown (Billant *et al.*, 1998; Gallaire & Chomaz, 2003*a*). The interested reader is referred to Oberleithner (2012) for visual representations of such a phenomenon, or Fig. 2.25 where a two-dimensional representation of the fluctuations of velocity induced by a $m = 1$ mode are showed. We consider in the present paragraph both the temporal and spatial stability of a swirling jet flow, expecting the results to show that the jet is indeed unstable to infinitesimal perturbations over a wide range of α, m and ω. First, the accuracy of AVLP is checked by comparing the computed eigenvalues with those calculated by direct numerical simulation by Gallaire & Chomaz (2003*a*) in the case of a pure jet flow. The correctness of the computed eigenvalues allows us then to apply the analyses to a more complex base flow originally exploited by Oberleithner (2011). In this last case, one also tries to reconstruct the global $m = 1$ mode dominating the flow.
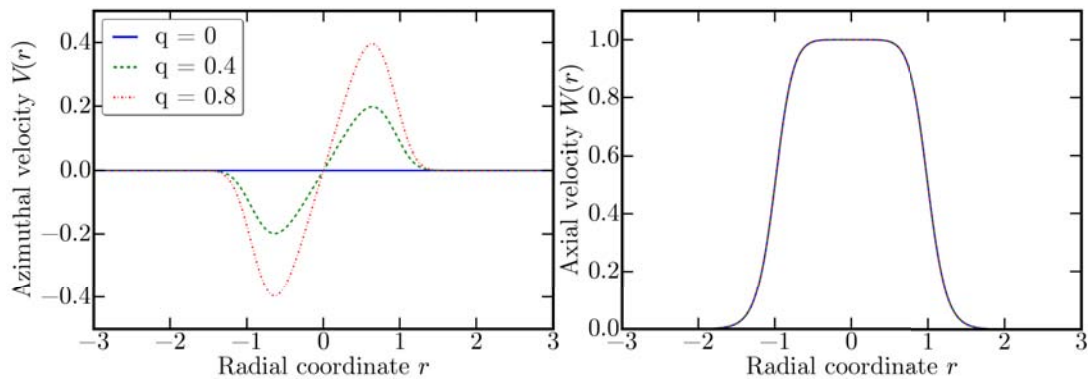
Figure 2.20 – Basic flow field from Eq. (2.2.49): (*left*) azimuthal velocity profile and (*right*) axial velocity profile. Parameters fixed at $N = 3$, $r_v = 0.9$ and $a = 4$.

The analytical representation of a swirling flow used by Gallaire & Chomaz (2003*a*) to study its temporal stability was originally introduced by Monkewitz (1988). The expressions for the three velocity components in non-dimensional variables read

$$
\begin{aligned}
U(r) &= 0, \\
V(r) &= qr \exp\left(-(r/r_v)^a\right), \\
W(r) &= \left[1 + \left(\exp\left(r^2 \log(2)\right) - 1\right)^N\right]^{-1},
\end{aligned}
\tag{2.2.49}
$$

where the non-dimensional parameters N, r_v and a have been set to the values $N = 3$, $r_v = 0.9$ and $a = 4$ (originally proposed to fit the experimental profiles investigated in the work by Gallaire & Chomaz (2003*a*)). Note that the last parameter noted q is the swirl number and determines the steepness of the azimuthal velocity component in the

core of the jet. Such typical azimuthal and axial velocity distributions are displayed in Fig. 2.20, for a case with a Reynolds number fixed at $Re = 667$ and used throughout the following temporal analysis.

Figure 2.21 compares the results obtained with AVLP to those published by Gallaire & Chomaz (2003a) for no swirl ($q = 0$) and obtained by direct numerical simulations of the linear impulse response of this jet. The left hand side represents a plot of the temporal amplification rate ω_i against the axial wavenumber α_r whereas the right hand side represents the evolution of ω_r, i.e. the opposite of the temporal frequency, with α_r. In this case, Fig. 2.21 clearly shows that both numerical methods - DNS and AVLP - retrieve the same solutions for $|m| \leq 2$, although for $m = \pm 3$, it appears that AVLP slightly under-predicts the amplification rate for $\alpha_r \lesssim 1.5$.
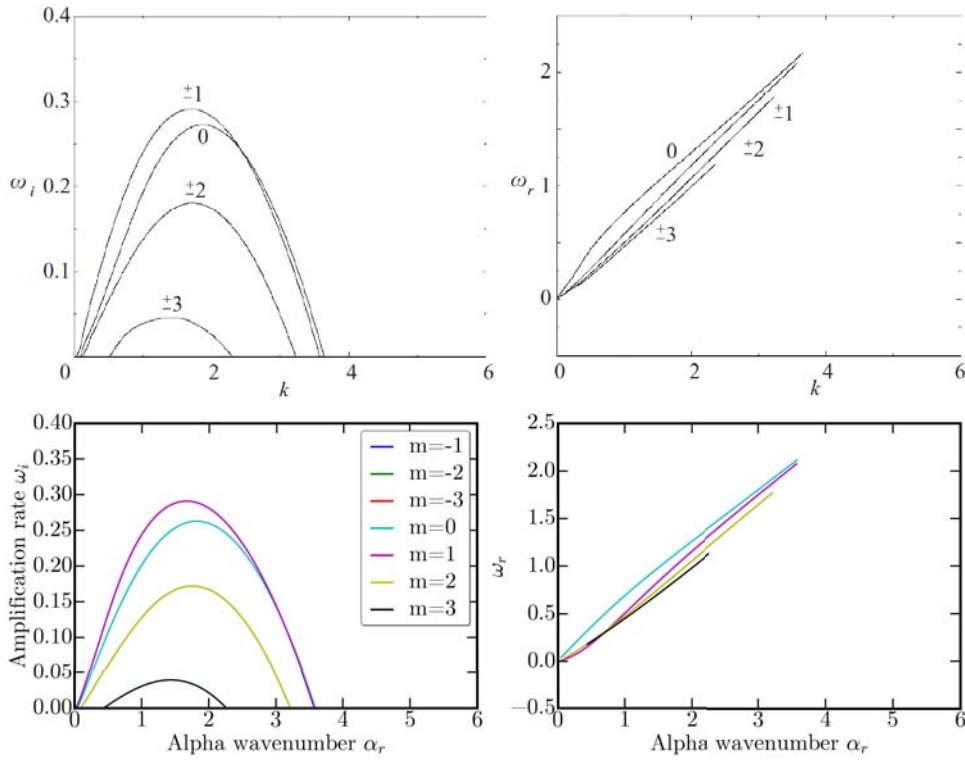
Figure 2.21 – Temporal instability of a pure jet, i.e. at $q = 0$. (*left*) amplification rate ω_i ; (*right*) ω_r. Comparison between (*top*) results by Gallaire & Chomaz (2003a) and (*bottom*) AVLP. Only the unstable part of ω_r is displayed.

The second base flow investigated here was used by Oberleithner (2011, 2012) and is more complex in nature as it consists of two axial and two azimuthal shear layers. Again, in dimensionless variables, the profiles are computed with the following expressions

$$\begin{aligned}
U(r) &= 0, \\
V(r) &= 4F_3(1 - F_4)S_{\text{loc}}, \\
W(r) &= 4BF_1(1 - BF_2),
\end{aligned} \qquad (2.2.50)$$

where the F_j are given by Monkewitz (1988),

$$F_j = \left[1 + \left(\exp\left(r^2 b_j \right) - 1 \right)^{N_j} \right]^{-1}, \qquad (2.2.51)$$

and B, S_{loc}, the N_j and the b_j are flow parameters given at a fixed axial position z and obtained by fitting the corresponding experimental profiles - see Oberleithner (2011), Tabs. 2 & 3 for more details. Corresponding azimuthal and axial velocity distributions obtained with Eq. (2.2.50) are displayed in Fig. 2.20 for four distinct axial positions $z = 0.47$, $z = 0.98$, $z = 1.48$ and $z = 1.99$.
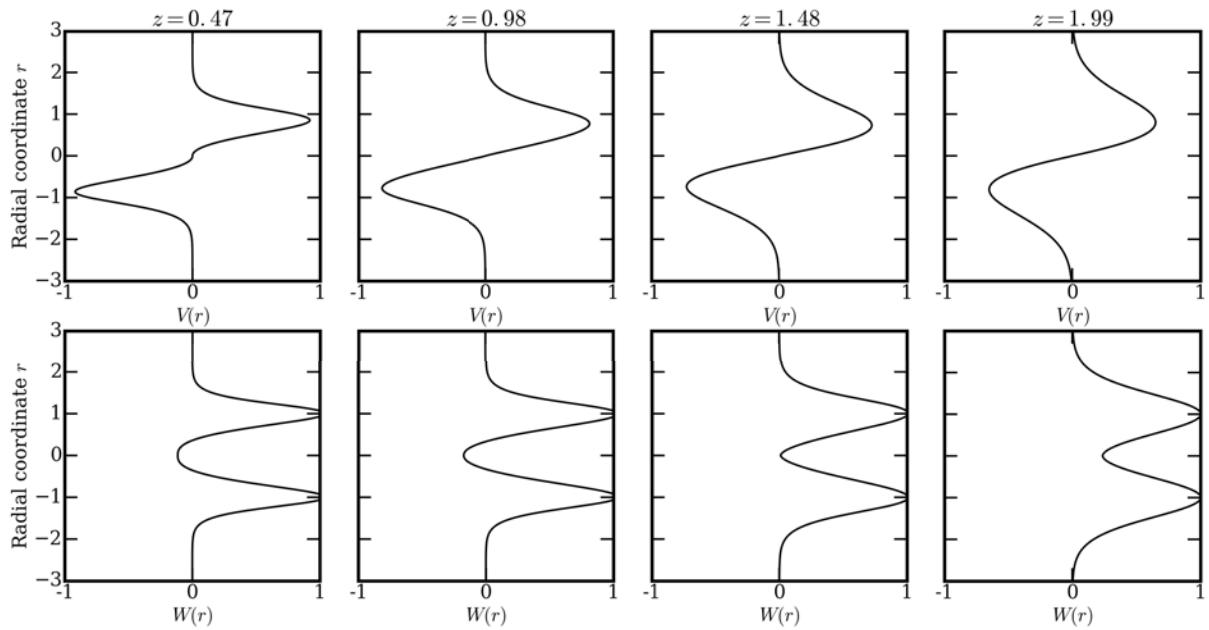
Figure 2.22 – Azimuthal velocity (*top*) and axial velocity (*bottom*) profiles taken at four distinct dimensionless axial locations $z = 0.47$, $z = 0.98$, $z = 1.48$ and $z = 1.99$ as a function of the dimensional radial coordinate r. Profiles generated with the set of equations Eq. (2.2.51) and parameters from Oberleithner (2011).

Contrary to the case of Gallaire & Chomaz (2003a) where the choices of non-dimensionalizing scales yield a constant Reynolds number throughout the flow, the local Reynolds number used by Oberleithner (2011) is computed based on the characteristic length and velocity scales and is therefore also varying with z - refer to Fig. 2.23.

Before trying to reconstruct the two dimensional shape of the most amplified mode, we fix the analysis location at the downstream station $z = 0.5$ in order to check whether AVLP is first able to reproduce correctly the results of a local spatial stability analysis. To proceed, the number of collocation points is fixed at $N_{\text{GL}} = 200$ and a rational mapping function f_{rat} (see Eq. (2.2.40)) with $r_c = 3.0$ and $r_{\text{max}} = 100$ is used to project the meanflows from $r \in [0, 100]$ to $\xi \in [-1, 1]$ - as used by Oberleithner (2011, 2012).

Figure 2.24 shows the spatial amplification rate of the most amplified mode with $m = 1$ against the dimensionless frequency ω_r at $z = 0.5$. The results obtained with AVLP (full line) are compared to the data presented by Oberleithner (2011, 2012) and the
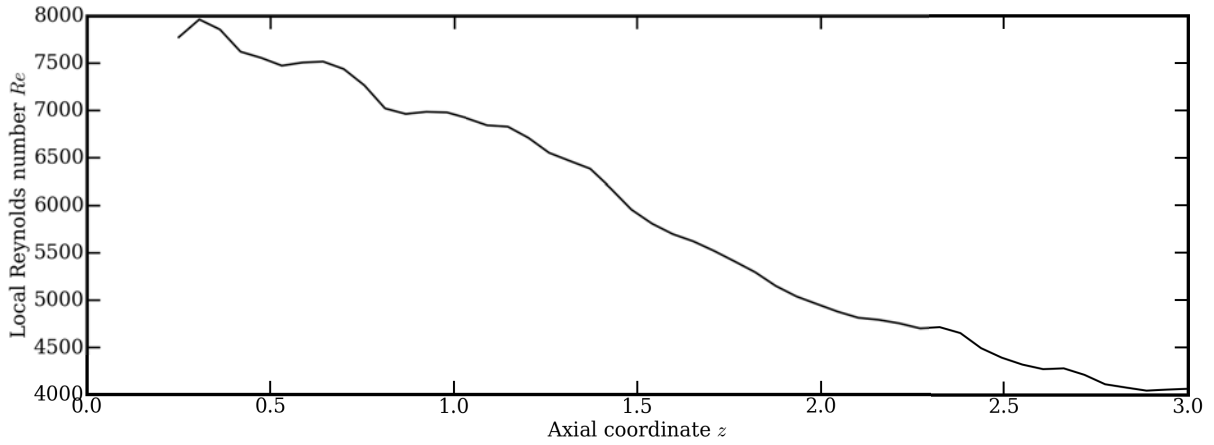
Figure 2.23 – Axial evolution of the local Reynolds number based on local characteristic length and velocity scale extracted from Oberleithner (2011).
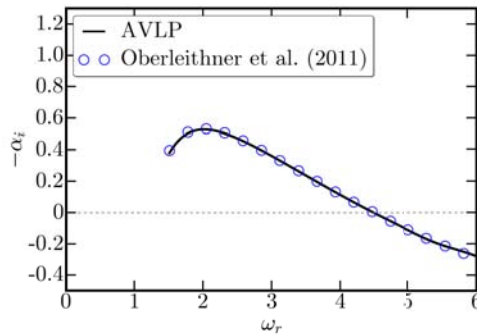
Figure 2.24 – Spatial amplification rate of the mode $m = 1$ versus dimensionless ω_r at $z = 0.5$. Comparison between ($\circ$) the data obtained by Oberleithner (2011) and (-) the present results with AVLP.

agreement is excellent on the whole range of $\omega_r \in [1.4, 6.]$. The maximum amplification rate is here equal to $\alpha_{i,\max} \simeq -0.527$ and is reached for $\omega_r \simeq 0.201$. Note that the use of the third method of resolution offered by the solver, referred to as *tracking*, was used exclusively to obtain this data and consequently the exact match with the data obtained by Oberleithner (2011, 2012) using a direct spatial resolution also serves as validation for this method of resolution of AVLP.

Next, the process is repeated for all axial locations $0.2 \leq z \leq 3$ and at each position the eigenvector corresponding to the frequency of the most amplified mode of the experiments (see Oberleithner (2011)), i.e 48 Hz, is extracted to reconstruct the three-dimensional coherent velocity field using the technique described in Sec. 2.2.3. Figure 2.25 shows the reconstructed fluctuation of radial velocity in a two dimensional (r, z)-plane, comparing the data presented in Oberleithner (2011, 2012) (Fig. 2.25a) and the results obtained with AVLP (Fig. 2.25b). Note that in both cases, to consistently assemble the local eigenmodes to form a global solution, the eigenvectors are normalized using their 1-norm $\|F\|_1 = \max|F|$, and the phase angle is equalized at a characteristic length scale. Except for the region close to the second outer shear layer ($r \simeq 1$) and the farthest region
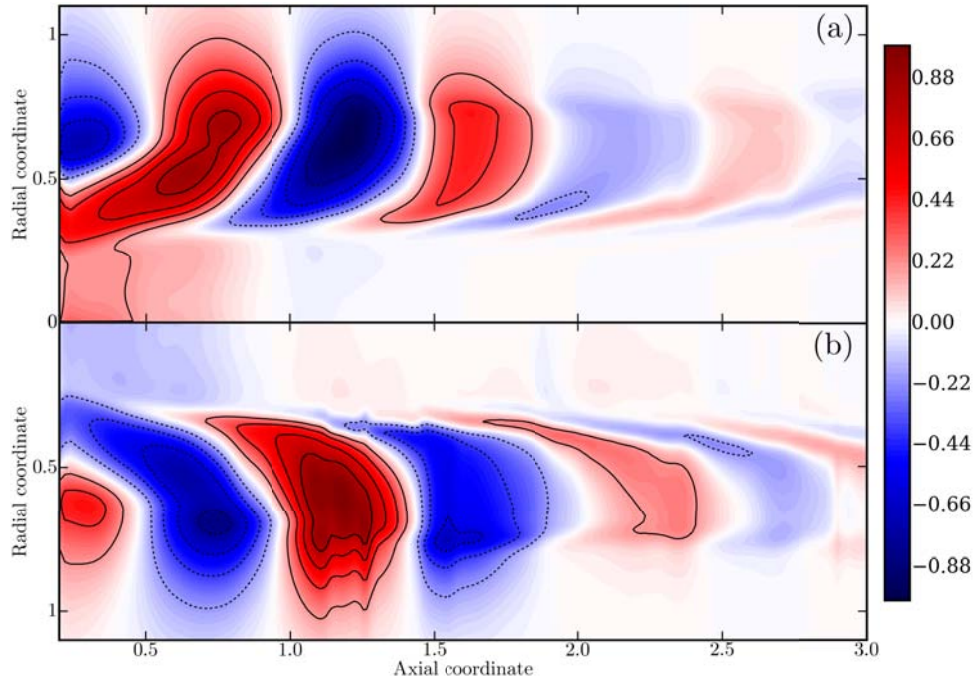
Figure 2.25 – Fluctuating radial velocity of the mode $m = 1$ pulsing at 48 Hz. Comparison between (*a*) the data obtained by Oberleithner (2011) and (*b*) the present results obtained with AVLP. Eigenfunctions are clocked at an arbitrary phase angle. The contour lines represent $u/\max(u) = [-1.0, -0.8, -0.6, -0.4, -0.2, 0.2, 0.4, 0.6, 0.8, 1.0]$.

downstream, the AVLP computation agrees well with the literature. The axial wavelength and the radial amplitude distribution are well estimated, as well as the downstream spatial growth and decay rates, with a maximum coherent amplitude at $z \simeq 1.3$ matching that found by Oberleithner (2011) (resp. $z \simeq 1.25$), and a decaying region further downstream.

Underlying theoretical concepts and definitions pertaining to rotating flows and their linear stability have been presented. Although well-known and often described in the literature, their mention in the present thesis is necessary to ease the discussions about the numerical simulation results proposed in the following chapters.

- The profiles of velocity and pressure for the laminar disc flows will be used as a reference to qualify the level of turbulence in the LES predictions and therefore participate in the validation of out unstructured approach.

- In turn, the simulations will be detailed focusing on the potential occurrence of the unsteady pressure phenomena in the academic smooth rotor/stator cavities that could lead to preliminary conclusions regarding the source of the 'pressure bands' phenomenon at the heart of the present work.

- On the other hand, the linear stability analysis developments are later used to investigate the possible links between the 'pressure bands' phenomenon and the stability of the mean flow in the academic smooth rotor/stator cavities.

Chapter 3

Dynamics and large scale motions of high Reynolds number rotor/stator cavities

Contents

In the present chapter, the large scale dynamics of high Reynolds number, smooth rotor/stator cavity flows is investigated to gain insight about the unsteady pressure phenomena appearing in an enclosed rotating flow. Understanding the dynamics in simplified cavities is indeed a necessary first step before working in the next chapter on the source of the pressure band phenomenon in real industrial cavities. As such, this study aims at improving our understanding of the influence of curvature and aspect ratio on the large scale organisation and stability of a rotating flow at a known Reynolds number. Through an a posteriori validation, the Large Eddy Simulation (LES) predictions are found to capture with precision the disc boundary layer patterns while providing at the same time information on the spectral content of the flow everywhere in the cavity. It is then showed that in addition to the observations made in previous studies on disc boundary layers, the rotating flows exhibit characteristic patterns at mid-height in the homogeneous core. Furthermore, Dynamic Modal Decomposition (DMD) applied to the predictions reveals that the entire dynamics of the flow is driven by only a handful of atomic modes whose combination is linked to the oscillatory patterns observed in the boundary layers and in the core of the cavity. These fluctuations are observed to form macro-structures, born in the unstable stator boundary layer and extending through the homogeneous inviscid core to the rotating disc boundary layer, causing its instability under some conditions. This also leads us to show that the constituent frequencies of pointwise temporal spectra exactly match the frequencies of the identified modes, along with harmonics and frequencies resulting from the combination of these fundamental modes. More importantly, the macro-structures significantly differ depending on the configuration simulated, pointing the need for deeper investigation of their triggering and selection mechanisms in relation to geometrical parameters and operating conditions. The final part of the chapter is dedicated to the establishment of a link between the unsteady phenomena observed in the cavities and the linear stability of the mean flow. In this matter, we use spatio-temporal stability analyses and show that in certain cases the DMD modes are each related to a linear instability of the mean flow. It suggests that the pressure bands phenomenon is the result of the expression of globally unstable linear modes born in the discs boundary layers and propagating to the whole flow. In the other cases, the analyses reveal the presence of multiple globally unstable modes at the same locations in the cavity suggesting nonlinear interactions between the mode take place that lead to the solution given by LES.

3.1 Introduction

The motivation for the study presented in this chapter naturally comes from its application in turbomachinery rather than an academic interest in crossflow boundary layer instabilities (although links may appear). Indeed, issues of structural integrity of engines and departure from nominal operating points due for instance to the 'pressure band' phenomenon at the source of this thesis become paramount today. They consequently

bring us back to the need for fundamental understanding of cavity flows, their instabilities
and large scale organization at high Reynolds numbers. The aim of this investigation is
hence to characterize the spectral content produced by the flow in a rotor/stator cavity
and associate, if possible, observed constituent frequencies to reported boundary layer
instabilities such as the one described earlier or to other phenomena that are yet to be
identified. To deal with high Reynolds number unsteady flows, the use of wall resolved
LES (Pope, 2001; Sagaut, 2006) is preferred in this specific chapter and analysis. Once
validated, numerical predictions in a simplified cylindrical configuration are probed to
study the relation between pressure fluctuations monitored in the cavity and the two- &
three-dimensional structures present in the core flow or in the boundary layers. For the
purpose of understanding, simulations and analyses are extended to a low aspect ratio
cavity without and with a central shaft to 1/ assess the impact of the aspect ratio G and
of the curvature parameter R_m as well as 2/ provide results for a geometry more relevant
to turbomachinery applications: i.e. with an interdisc gap only a fraction of the discs
radii and a stationary cylindrical shroud.

The flows between a stationary and a rotating disc, or more generally between two
rotating discs are known to be of fundamental importance as they are among the simplest
prototype flows with three dimensional boundary layers (e.g. Kang *et al.*, 1998; Littell
& Eaton, 1994; Lygren & Andersson, 2001). Also, due to their occurrence in numerous
industrial applications ranging from computer hard-drives to aeronautical turbine stages
(refer to Owen & Rogers, 1989, 1995, for complete reviews), these flows actually prove
to be of high practical relevance. Despite this pertinence to numerous applications, the
effective response of such a fundamental flow problem at very high Reynolds numbers still
remains misunderstood and recurrent oscillatory motions are reported that cause many
practical device to fail. Numerous works, both experimental and numerical, have been
recently devoted to the investigation of the instabilities related to and characteristics of
single-disc flows (see e.g. Kobayashi *et al.*, 1980; Littell & Eaton, 1994; Lingwood, 1995*a*,
1997; Pier, 2003; Lopez *et al.*, 2009) but also to those associated with two-discs flows
(see e.g. Lopez, 1996; Serre *et al.*, 2001, 2004; Séverac *et al.*, 2007; Tuliszka-Sznitko &
Zielinski, 2007; Tuliszka-Sznitko *et al.*, 2009; Lopez, 2012). The aforementioned studies
revealed that the structure of a rotor/stator flow depends almost exclusively on three
dimensionless numbers related to the dimensions of the cavity and the rotation speed
of the rotor Ω: the Reynolds number based on the outermost radius (denoted by R_1
hereafter) of the cavity $Re_{R_1} = R_1^2 \Omega / \nu$, the aspect ratio of the cavity $G = h/(R_1 - R_0)$
where R_0 stands for the innermost radius and in the case of an annular cavity the average
curvature parameter $R_m = (R_1 + R_0)/(R_1 - R_0)$, where h is the interdisc distance. In a
central article, Daily & Nece (1960) detailed the results of an extensive theoretical and
experimental campaign designed to characterize as exhaustively as possible the flows that
appear in a rotor/stator cavity. They found out four different flow regimes, two of which
are laminar (resp. noted I and II), the other two being turbulent (resp. noted III and IV),
each sub-type being qualified as merged (I and III) or separated (II and IV) boundary
layer flows. Note that hereafter, we refer to the boundary layer of the rotating disc as
an Ekman (1905) layer and to the boundary layer developing on the stationary disc as a

Bödewadt (1940) layer. Daily & Nece (1960) observed also that the separated boundary layers for flows of the second or fourth kind (II or IV) are susceptible to transition to turbulence for local Reynolds numbers $Re_r = r^2\Omega/\nu$ 10^5 when $G \geq 0.04$ and $R_m \approx 1.0$, with r being the local radial coordinate.

Early experimental work focused on the boundary layer developing above a rotating disc (see e.g. Smith, 1947; Gregory *et al.*, 1955; Kobayashi *et al.*, 1980; Littell & Eaton, 1994). These showed that the Ekman layer is subject to crossflow-like instabilities (more in the review by Reed & Saric, 1989), creating visible axisymmetric annular or three-dimensional spiral patterns in the boundary layer. Wu & Squires (2000), aside from being the first to use Large Eddy Simulation (LES) (Ferziger, 1997; Sagaut, 2006) to investigate the behaviour of the turbulent flow over a rotating disc, confirmed the conclusions reached for instance by Littell & Eaton (1994). The main outcome is that crossflow interactions promote the appearance of sweeping structures and/or centrifugal ejections depending on the sign difference between the mean flow vorticity and the streamwise vortices. Other numerical works contributed in showing how coherent fluctuations of the axial velocity component in the boundary layer are both time- and Reynolds-number-dependent, taking the form of axisymmetric patterns at low local Reynolds numbers or generating three-dimensional spiral sweeping vortices at intermediate to high Reynolds numbers (see e.g. Serre *et al.*, 2001, 2004; Tuliszka-Sznitko & Zielinski, 2006; Poncet *et al.*, 2009; Launder *et al.*, 2010).

Although an auto-similar solution of the velocity profile in a Bödewadt layer has been known since 1940, experimental difficulties to create a fluid in rotation over a stationary disc have made such a configuration the target of far less studies than the aforementioned Ekman layer. Savas (1983, 1987) experimentally and then Lopez & Weidman (1996) and Lopez (1996) both numerically (with a two-dimensional axisymmetric code) and experimentally, studied the characteristics of such a flow and its stability when initiated by an impulsive spin-down-to-rest set-up. Analogously to the results obtained for the Ekman layer, the authors observed axisymmetric waves and then spiral waves to appear over the stationary disc. In their experiments on the flow between a rotating and a stationary disc, Gauthier *et al.* (1999) also observed circular waves sometimes co-existing with spiral vortices for flows becoming increasingly disordered at large local Reynolds numbers. A more recent experimental work on a closed rotor/stator cavity by Schouveiler (2001) showed that the boundary layer forming over the stationary disc indeed becomes unstable to spiral vortices, either stationary or sweeping centrifugally.

Since then several numerical studies of the Bödewadt layer appeared to complement these observations. For instance Serre *et al.* (2001) performed three-dimensional DNS at low to intermediate Reynolds numbers (Re_{R_1}) in both annular and cylindrical cavities, and obtained results showing the instability of the stationary layer to axisymmetric and spiral vortices. Lopez *et al.* (2009) showed that the Bödewadt layer was for rotor/stator configurations most sensitive to the axisymmetric waves but that these waves are noise sustained and always found to decay in time in the absence of external forcing. Contrarily, spiral waves are shown to be rather independent of any external forcing but tend to appear spontaneously as the result of a Hopf bifurcation of the basic state (Lopez *et al.*, 2009). These last authors further show that in the case of co-existence, there is little to no

interaction between the two categories of waves for the considered value of G.

The objective of this chapter, aside from the work on academic rotor/stator cavity instability in itself, is to establish a preliminary strategy to identify the source of the 'pressure band' phenomenon in the industrial cavities. To do so, the chapter is organized as follows. First the three geometries are detailed, with a focus on the three characteristic dimensionless numbers: Re_{R_1}, G and R_m. Following is a general presentation of the CFD approach, the modelling and the numerical set-up used for LES. The third section then addresses the validation of the base flows produced by the wall-resolved LES against available literature. The fourth section is dedicated to the presentation of signals monitored at different points in space within the two cavities, including the constituent frequencies present in the numerical predictions, their radial and axial evolutions. We then move on to a detailed description of the advanced post-processing diagnostics used to connect the spectral activity to the dynamic behaviour of the flow in these high Reynolds number rotor/stator cavities. These diagnostics and post-processing techniques will be validated on the three academic configurations discussed in this chapter so they can be used on the real industrial flows to analyse their unsteady pressure content. The last discussion of this chapter bears on the linear stability of the enclosed rotor/stator flows and the identification of the global modes to be compared to the DMD modes using only successive local linear stability analyses.

3.2   Geometrical models and physical parameters

Before heading to the validation of the LES predictions and the further analysis of the high Reynolds dynamics of enclosed rotor/stator flows, this section offers a thorough description of the three cases under study and refers the reader to the corresponding reference literature.

The geometrical models correspond to two smooth discs enclosures of either cylindrical or annular shape with a relative radial extent $\Delta R = R_1 - R_0$, where R_0 and R_1 are respectively the internal (shaft) and external (shroud) radii of the cavity. If $R_0 = 0$, we call the cavity *cylindrical* whereas for $R_0 > 0$ the cavity is referred to as *annular*. The geometrical domains of interest hence correspond to the views of Fig. 3.1: cylindrical or annular volumes of height h. By construction one disc of the cavity is stationary (the stator), filled in grey in Fig. 3.1, while the other (the rotor) rotates with an uniform angular velocity $\Omega = \Omega e_z$. Note that throughout the discussion e_z is the unit vector along the z-axis and Ω (in rad/s), with a coordinate system origin that is centred on the symmetry axis of the rotor wall. These smooth cavities have been designed so as to be representative of basic elements found in a turbine engine, Fig. 3.1c being the closest to the end application of Chap. 4.

For all three cases and based on literature, the flow solution is expected to be driven by three main parameters: the Reynolds number Re and two geometrical parameters which are the cavity aspect ratio $G = h/\Delta R$ and the curvature parameter $R_m = R/\Delta R$, where $R = R_1 + R_0$. However for the configurations such as the ones presented in Fig. 3.1,
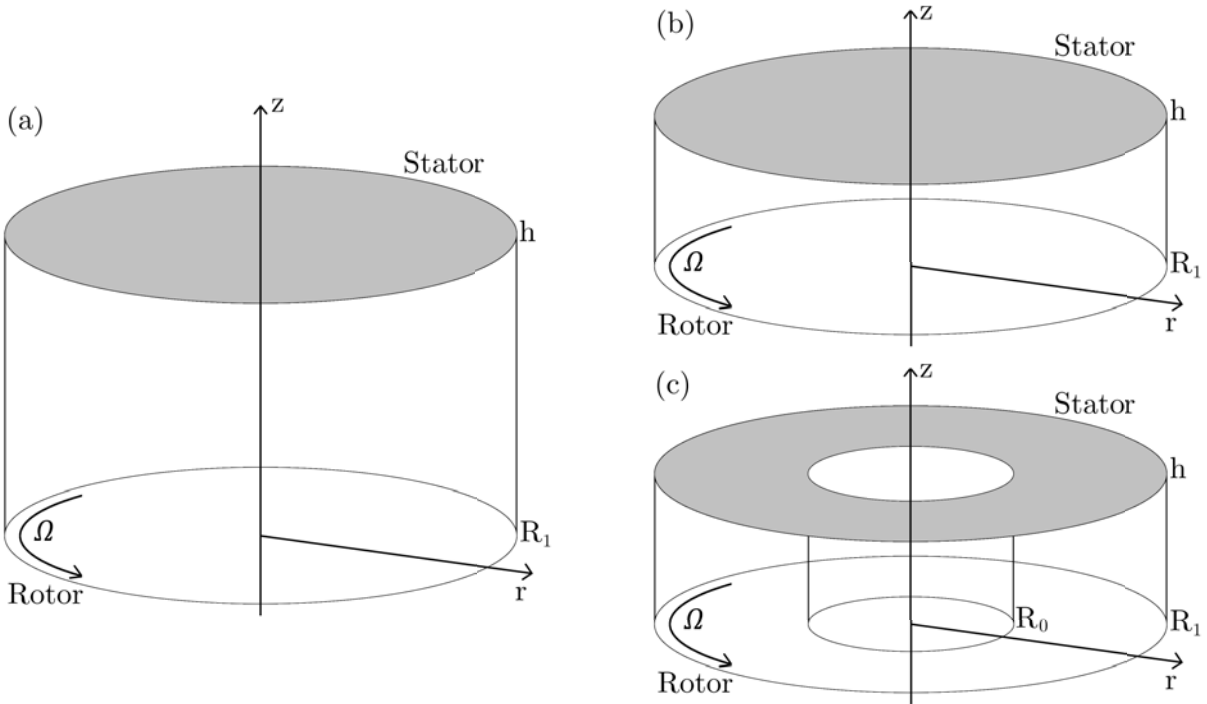
Figure 3.1 – Schematic diagram of the rotating cavities. (a) Cylindrical cavity $G = 1.18$. (b) Cylindrical cavity $G = 0.2$. (c) Annular cavity $G = 0.2$, $R_m = 1.8$.

three different length scales h, R_0, R_1 can be identified and used in the definition of the flow Reynolds number. It is common in the literature to characterize a rotor/stator cavity with the Reynolds number based either on the outermost radius of the cavity, $Re_{R_1} = R_1^2/\delta^2$ (see e.g. Schultz-Grunow, 1935; Daily & Nece, 1960; Owen & Rogers, 1989; Lopez & Weidman, 1996; Lopez, 1996; Serre *et al.*, 2004; Séverac *et al.*, 2007) or its height $Re_h = h^2/\delta^2$ (see e.g. Dijkstra & Heijst, 1983; Gauthier *et al.*, 1999; Serre *et al.*, 2001), in which case $\delta = \sqrt{\nu/\Omega}$ originates from the radius-independent Ekman layer and is representative of this standalone model flow. Note that δ is also often used as a thickness factor for the Bödewadt (1940) layer. By definition, Re_h gives an estimate of the proportion of the cavity where the flow is purely driven by viscosity and large values of Re_h typically correspond to flows of the second or fourth kind (Daily & Nece, 1960). Small values on the other hand tend to indicate a flow of the first or third kind. Consequently for large enough values of Re_h, it is possible to treat the two boundary layers independently as two flows over single discs. Earlier studies of such flows (Faller, 1991; Littell & Eaton, 1994; Lingwood, 1995*a*, 1997) demonstrated that the relevant Reynolds number was rather a *local* Reynolds number $Re_\delta = r/\delta$. With this definition, the cavity Reynolds number Re_{R_1} can thus be defined as an upper bound to Re_δ^2.

In this document, we will consider Re_{R_1} to be the relevant flow parameter but we will also often use the parameter δ, and by extension the local Reynolds number Re_δ in parts of the discussion dedicated to the boundary layers. Note that to improve readability, the radial Reynolds number Re_{R_1} shall be simply named Re thereafter.

	Case 1	Case 2	Case 3	
R_0	—	—	71	mm
R_1	34	178	250	mm
h	40	35	35	mm
Ω	525	615	315	rad/s
Re	10^5	10^5	10^5	—
G	1.18	0.2	0.2	—
R_m	1.0	1.0	1.8	—
δ_1	2	—	0.85	mm
δ_2	—	—	0.1	mm

Table 3.1 – Characteristic parameters of the three rotor/stator cavities. Parameters δ_1 and δ_2 represent respectively, when relevant, the rotor/shroud clearance and the stator/shaft clearance present in the experimental counterparts.

Table 3.1 summarizes the characteristics of the three cases investigated in this chapter. These are:

- **Case 1**: a high aspect ratio *cylindrical* cavity first presented by Lachize *et al.* (2015) in an experimental study of the large scale non-axisymmetric structures existed in a high-Reynolds rotor/stator cavity flow. The values of the geometrical parameters have been chosen to be relevant of industrial devices and to ease technical constraints such as pressurization and thermalization of the cavity. Note that in the experimental cavity, there exists a small clearance between the rotor and the shroud because of obvious mechanical constraints, $\delta_1 \simeq 2$ mm, that will not be resolved in the numerical simulations described hereafter.

- **Case 2**: also a *cylindrical* cavity and was chosen to be the low aspect ratio equivalent of the cavity used in **Case 1**. Comparing the results of these two cases shall allow to assess the effect of the parameter G on the flow in the cavity. For this case, $G = 0.2$ is selected as it is often considered in the literature (e.g. Serre *et al.*, 2001, 2004; Andersson & Lygren, 2006; Tuliszka-Sznitko & Zielinski, 2007; Lopez *et al.*, 2009) as relevant to model industrial cavities. Experimental results for such a configuration can be found in Daily & Nece (1960) or Czarny *et al.* (2002).

- Finally, **Case 3** is a low aspect ratio *annular* cavity with $G = 0.2$ and $R_m = 1.8$. It only differs from **Case 2** by the presence of the shaft ($R_0 > 0$). It allows to discuss the effect of a non-unit curvature parameter on the rotor/stator cavity flow and its natural response to local perturbations. This specific value of $R_m = 1.8$ was chosen because the corresponding flow was extensively studied by Séverac *et al.* (2007) experimentally as well as numerically and later by Tuliszka-Sznitko *et al.* (2009), both using very accurate LES methods. Similarly to **Case 1**, in the experimental cavity used by Séverac *et al.* (2007) to conduct PIV measurements, there exists a

rotor/shroud clearance, $\delta_1 = 0.85$ mm, as well as a stator/shaft clearance, $\delta_2 = 0.1$ mm, that will not be resolved in the numerical simulation of **Case 3**.

3.3 Numerical model

The understanding of large scale flow structures implies to numerically simulate accurately high Reynolds number flows while preserving the inherent unsteady features of the problem. To do so, current modelling capabilities naturally point to Large Eddy Simulations (LES) (Sagaut, 2006; Ferziger & Peric, 2002; Gicquel *et al.*, 2012) which is intrinsically unsteady in nature and addresses turbulence through the modelling of the smaller dissipative flow scale while preserving the large scale features. In the specific context of wall-bounded flows these specificities need to be carefully addressed so as to ensure reliable modelling of the near wall turbulent characteristics as detailed in numerous works (Jimenez & Moin, 1991; Piomelli, 2008) and detailed in the following. As mentioned in introduction of this chapter (Sec. 3.1) and in the previous section (Sec. 3.2), the three configurations studied here have already been investigated numerically in the literature. Naturally, this is not merely an attempt to duplicate the earlier work of others, but rather to validate the results produced by our general unstructured LES solver against DNS or LES solvers tuned specifically for rotating flows. What is more, the validation represents only a first necessary step after which we use the predictions of the LES to study the dynamics of these model rotor/stator cavity flows to gain insight about the 'pressure band' phenomenon. In order to prepare the study of the industrial turbine cavities proposed in Chap. 4, the investigations of the academic LES are also used to establish and validate specific post-processing strategies dedicated to the monitoring and analysis of pressure fluctuations.

This section is organized as follow. A short description of the unstructured LES solver used throughout this thesis is followed by the description of the boundary conditions and criteria of initialization and convergence common to all cases. Finally, we conduct an *a posteriori* study of the meshes resolutions to ensure the near-wall resolution is high enough to capture the boundary layer dynamics.

3.3.1 Numerical method

The code chosen to perform the simulations, AVBP (Gourdain *et al.*, 2009), is widely used both for basic research and applied research of industrial interest. This parallel code solves the full compressible Navier-Stokes equations using a finite-element scheme TTGC (Colin & Rudgyard, 2000) based on a two step Taylor-Galerkin formulation. It relies on a cell-vertex formalism and schemes (Lamarque, 2007; Colin & Rudgyard, 2000) specifically designed for LES on multi-element meshes. The low diffusion and low dispersion properties of this explicit solver makes it indeed highly suitable for LES by providing 3rd order space and time accuracy. The subgrid scale modelling is here closed using the WALE model (Nicoud & Ducros, 1999). It allows for a better behaviour of the turbulent

subgrid eddy viscosity for wall bounded flows. It is also known to produce zero eddy viscosity in case of pure shear, thus leading to a better prediction of the laminar to turbulent transition process through the growth of linear unstable modes.

3.3.2 Computational details

First of all, note that the computational domains match exactly the geometries shown on Fig. 3.1, i.e. 360° cylindrical or annular enclosures. Regarding the numerical boundary treatments, radial and axial no-slip boundary conditions are applied on the rotating discs (and shaft for **Case 3**). On those surfaces, $u_r = u_z = 0$ and $u_\theta = r\Omega$, where $\mathbf{u} = (u_r, u_\theta, u_z)$ are the three components of velocity in the cylindrical coordinates system (r, θ, z). A no-slip boundary condition is enforced on the stationary discs so $u_r = u_\theta = u_z = 0$. Note that the fluid is allowed to slip along the impermeable outer cylindrical shrouds to alleviate the CPU cost associated with the fine near wall resolution of the LES simulations as well as the numerical treatment of the corner singularity. Finally, all boundaries are set to behave like fully adiabatic walls, with the direct consequence that viscous friction slowly heats the fluid and increases the static pressure in the cavity (the fluid follows the perfect gas law).
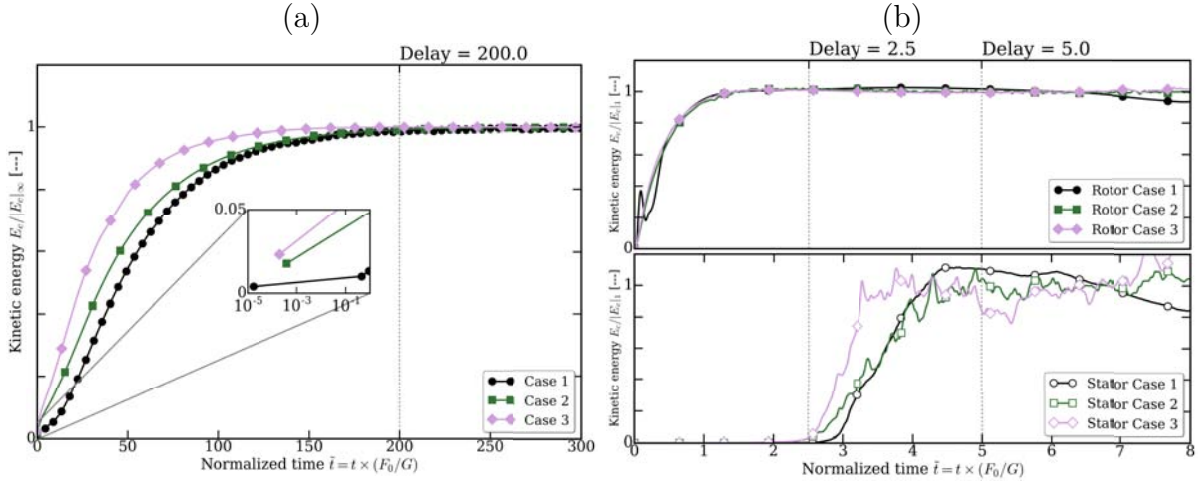
Figure 3.2 – (*a*) Evolution of the dimensionless volume-averaged kinetic energy for the entire flow. (*b*) Evolution of the dimensionless kinetic energy of the rotor boundary layer (filled symbols) and stator boundary layer (open symbols) during the first instants of the LES. Comparison between **Case 1** (circles), **Case 2** (squares) and **Case 3** (diamonds) - see Tab. 3.1 for details. Time has been normalized by F_0/G. Notation $|E_c|_\infty$ refers to the infinity norm and $|E_c|_1$ to the 1-norm of the kinetic energy.

Although experimental studies concerned with the steady-state of such flows often have the fluid initially in a state of pre-rotation for $t_{\exp} < 0$, all simulations presented in this document have the fluid initially at rest and the two discs, the shaft and the shroud are stationary. At $t = 0$, the rotor is instantaneously brought to its rotation speed Ω rad/s (see Tab. 3.1) and the fluid in the cavity is subsequently put in motion due to viscous entrainment. The base flows of the rotor/stator cavities used during this investigation are then considered to have reached a numerically converged state when

1/ the volume-averaged cavity kinetic energy reaches a plateau and 2/ the slope of the volume-averaged cavity static temperature becomes almost constant, i.e. controlled by the constant heating of the flow due to viscous forces. Note however that this is only a convention used in this investigation as it is known that rotor/stator cavity flows display unsteady sweeping structures in the discs boundary layers even when the mean flow has reached its steady state (see e.g. Serre *et al.*, 2001 or the review by Crespo del Arco *et al.*, 2005). To illustrate this, we present in Fig. 3.2*a* the temporal evolution of the volume-averaged kinetic energy of the flow in the whole cavity for **Case 1**, **Case 2** and **Case 3**. Time has been scaled by F_0/G where F_0 is the *frequency of the rotor* (in Hz with $\Omega = 2\pi F_0$ rad/s) and the kinetic energy has been normalized by its ∞-norm. Note that the horizontal axis starts at the time of the first iteration rather than exactly at $t = 0$. The choice of these non-dimensionalizing factors provoke the effective collapse of all three lines that reach their plateau after a common delay $\tilde{t} = tF_0/G = 200$ hinting that F_0/G is an adequate time scale to describe the overall fluid motion in the cavity.

On the other hand, it is also interesting to qualify the response of the two boundary layers separately to better understand how the mean flow organizes after the machine start-up. To this end, we consider two surfaces in the boundary layers, at $z \simeq \delta$ and $z \simeq h - \delta$ (recall that $\delta = \sqrt{\nu/\Omega}$ is representative of the thickness of single-disc rotating flows boundary layers) respectively in the rotating disc layer and stator layer. We then consider that the kinetic energy of each boundary layer can be approximated by the average kinetic energy on the corresponding surface. Figure 3.2*a* represents the evolution of the kinetic energy in both the rotor (top) and the stator (bottom) boundary layers for all three simulations during the first instants of the computations. From such plots, the fluid layers located immediately above the rotating discs can be seen to respond rapidly to the acceleration whereas the layers close to the stationary discs have a delayed response and stay in their initial resting state for a longer time. The time scale F_0/G appears once again very adequate as the rotoric kinetic energies also collapse and the response time after which the plateau is reached is constant and independent of the configuration, evaluated at $\tilde{t} = 2.5$. Figure 3.2*b* also shows that $\tilde{t} = 2.5$ is the time needed for the statoric layers to start evolving and also the time span after which they reach a first plateau (i.e. at $\tilde{t} = 2.5 + 2.5$).

3.3.3 Spatial resolution

Now that clear criteria for the initialization and the convergence of the computations have been discussed, the last primordial issue to address is that of the near-wall resolution that has to be high enough to capture on its own the boundary layer dynamics.

The present investigation has been carried out using three different geometries (see Tab. 3.1) with their respective meshes. Starting from a two-dimensional triangular mesh of the rotating disc, the meshes are extruded along the z-axis to produce a 3D grid made exclusively of prismatic elements to facilitate the resolution of the discs boundary layers. Figures 3.3*a-c* present the schematic structures of the three meshes used for **Case 1**, **Case 2** and **Case 3**. In all cases, the layers of prisms have a constant thickness z_1 of
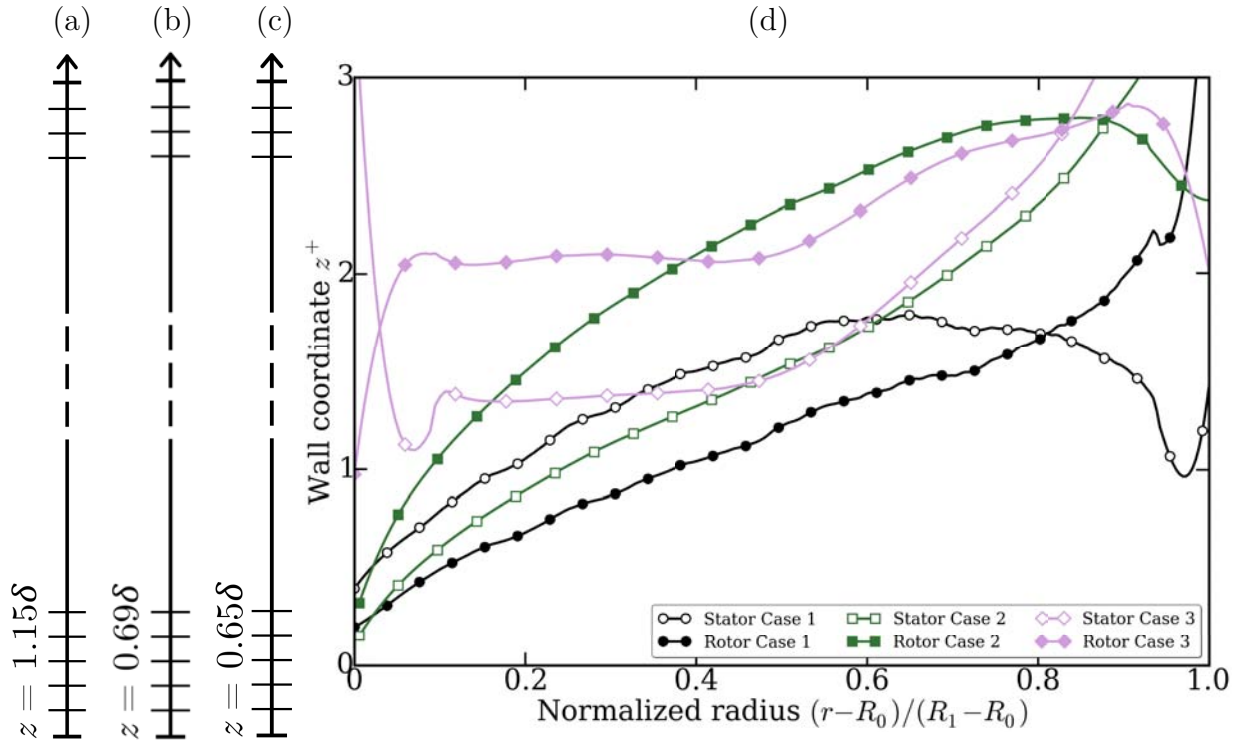
Figure 3.3 – (*a*)-(*b*)-(*c*) Schematic structures of the wall-resolved LES meshes for **Case 1**, **Case 2** and **Case 3** respectively. (*d*) Radial evolution of the wall coordinate z^+ near the rotors (filled symbols) and the stators (open symbols) for **Case 1** (circles), **Case 2** (squares) and **Case 3** (diamonds). Note that symbols do not indicate mesh nodes.

the order of the parameter δ to allow for the proper discretization of the disc boundary layers and the unsteady phenomena occurring therein. Table 3.2 summarizes the values of the key parameters pertaining to each mesh: the constant height of the prism layers z_1, the number of layers N_{layers}, the number of nodes N_{nodes} and cells N_{cells} in the mesh, as well as the average LES timestep Δt.

For such simulations a wall-resolved type LES is guaranteed *a posteriori* by calculating the first grid node wall normal coordinate $z^+ = z_1 u_\tau / \nu$, where u_τ is the total wall-friction velocity defined as $u_\tau = \sqrt{\tau_w / \rho}$, with τ_w standing for the flow shear stress at the wall. Figure 3.3*d* presents the radial distribution of the time- and azimuth-averaged axial wall coordinate z^+. As u_τ increases towards the outer shroud, z^+ is an increasing function of the radius, but in all layers the first mesh point is always located within the viscous sublayer (usually bounded by $z^+ \simeq 5.0$ - see e.g. Schlichting, 1960 or Sagaut, 2006, chap.10). Furthermore, far from the cylindrical walls, Fig. 3.3*d* shows that the viscous sublayers of all three cases are described by 2 to 3 mesh points, which is well within the recommendations for a wall-resolved LES (Sagaut, 2006). Table 3.2 also recapitulates the maximum and minimum values of z^+ for layers of **Case 1**, **Case 2** and **Case 3**, supplemented with an estimate of the average wall coordinates in the radial and azimuthal directions denoted respectively r_{ave}^+ and θ_{ave}^+ to provide a comprehensive qualification of the meshes and associated flow predictions.

	Case 1	**Case 2**	**Case 3**	
δ	1.08×10^{-4}	5.65×10^{-4}	7.91×10^{-4}	m
z_1	1.24×10^{-4}	3.90×10^{-4}	5.14×10^{-4}	m
z_1/h	0.3	1.1	1.4	%
N_{layers}	322	91	70	—
N_{nodes}	3.5×10^6	4.7×10^6	5.5×10^6	—
N_{cells}	7.0×10^6	9.2×10^6	10.8×10^6	—
Δt	2.4×10^{-7}	7.1×10^{-7}	7.6×10^{-7}	s
z_{min}^+	$[0.197, 0.394]$	$[0.321, 0.153]$	$[0.975, 1.10]$	—
z_{max}^+	$[4.03, 1.79]$	$[2.79, 5.79]$	$[2.87, 5.45]$	—
r_{ave}^+	$[10.3, 5.3]$	$[4.85, 9.27]$	$[6.97, 11.88]$	—
θ_{ave}^+	$[5.93, 3.07]$	$[2.74, 5.24]$	$[2.3, 7.5]$	—

Table 3.2 – Characteristic parameters of the three meshes related to **Case 1**, **Case 2** and **Case 3**. z_1 is the thickness of the layers of prisms. Bracketed values indicate the rotor and the stator values, in this order.

To conclude this presentation, indications on the solver performance for the aforementioned settings and configurations, i.e. the related computational costs and efficiency, are reported. The computation of **Case 1** was performed on Sandy Bridge nodes (8 cores, 2.6 GHz) mounted in a Bullx B510 cluster (peak performance of 53 Tflops/s) whereas the computations of **Cases 2** & **3** were performed on Intel Haswell nodes (E5-2680v3, 12 cores, 2.5 GHz) mounted in a LENOVO cluster (peak performeance of 242 Tflops/s). Both clusters are located within the facilities of CERFACS. **Case 1** was computed using 32 nodes and for approximately 530 periods (to converge low frequencies relevant for the dynamics of the flow, see Sec. 3.6.2) which yield a runtime of approximately 81 days. On the other hand, **Case 2** was computed using 30 nodes and for approximately 400 periods which yield a runtime of approximately 17 days. Finally, **Case 3** was also computed using 30 nodes and for approximately 300 periods, which yield a runtime of approximately 17 days too.Tab. 3.3 summarizes all performance data.

3.4 Basic state and mean flow description

The base flows developing in rotor/stator cavities identical or similar to Fig. 3.1 have been extensively investigated and discussed in previous contributions (see e.g. Serre *et al.*, 2001; Séverac *et al.*, 2007; Lopez *et al.*, 2009). We hence only propose here a brief overview, with two objectives: assess the accuracy of the simulations upon which the present study is based and characterize the changes introduced by different values of G and/or the presence of a shaft (i.e. $R_m > 1.0$). These two objectives are discussed, in this order, in the two following separate sections and serve as foundation for the study of the pressure fluctuations in the smooth cavities (Sec. 3.5 *et sqq.*) as well as the investigation *in situ*

	Case 1	Case 2	Case 3	
$\overline{\Delta t}$	0.236×10^{-6}	0.709×10^{-6}	0.763×10^{-6}	s
N_{it}	26 906 377	5 700 000	7 054 628	—
$t_{phys,max}$	530	400	300	periods
t_{CPU}	~500	152 722	144 060	h
N_{CPU}	256	360	360	—
$t_{runtime}$	81	17	17	days

Table 3.3 – Summary of the solver performances for all three academic cases and related computational costs. **Case 1** computation has been performed on 32 Sandy Bridge nodes (8 cores, 2.6 GHz) whereas **Cases 2** & **3** computations have been performed on 30 Intel Haswell nodes (E5-2680v3, 12 cores, 2.5 GHz).

of the 'pressure band' phenomenon in the real industrial turbine cavities (Chap. 4). The datasets presented in this section are extracted from the plateau of Fig. 3.2*b* and averaged both in time as well as in the azimuthal direction unless explicitly stated otherwise.

3.4.1   Accuracy of the simulations

As mentioned in section 3.2, **Case 3** was selected for the present investigation because of the next-to-exhaustive study of this flow proposed by Séverac *et al.* (2007). It therefore serves to validate the base flows produced by the present LES predictions and associated modelling.

The axial profiles of the dimensionless mean radial $u_r^* = u_r/(r\Omega)$ and azimuthal $u_\theta^* = u_\theta/(r\Omega)$ velocity components at mid-radius $r^* = (r - R_0)/(R_1 - R_0) = 0.5$ are shown in Fig. 3.4. The dimensionless mean axial velocity component is very small compared to the other two and therefore shall not be discussed here but the following conclusions hold. In accordance with the predictions presented by Daily & Nece (1960) for the Reynolds number and the aspect ratio of **Case 3** ($Re = 10^5$, $G = 0.2$), the mean flow displays separated boundary layers, showing it belongs to regime IV. Within the boundary layers, the fluid is accelerated centrifugally on the bottom disc while it follows a centripetal motion on the top disc. A nearly homogeneous core region separates the two boundary layers where the radial velocity is close to zero and the tangential velocity is constant $u_\theta^* = K$. For future reference, K is usually termed as the entrainment coefficient and $K = \{0.379, 0.351, 0.383\}$ in **Case 1**, **2** & **3** respectively. The agreement with the experimental results of Séverac *et al.* (2007) (see Fig. 3.4($\square$)) is here excellent. Finally, the comparison at this station with the auto-similar laminar profile developed by Rogers & Lance (1962) (see Fig. 3.4(– –)) provides an illustration of the effect of cavity enclosure on the mean flow: i.e. mainly inferred by a confinement which will be discussed in more details in the next section.

Additional information about the mean flow is also provided by a polar plot of the azimuthal and radial velocity in the whole axial extent of the cavity at $r^* = 0.5$ shown on
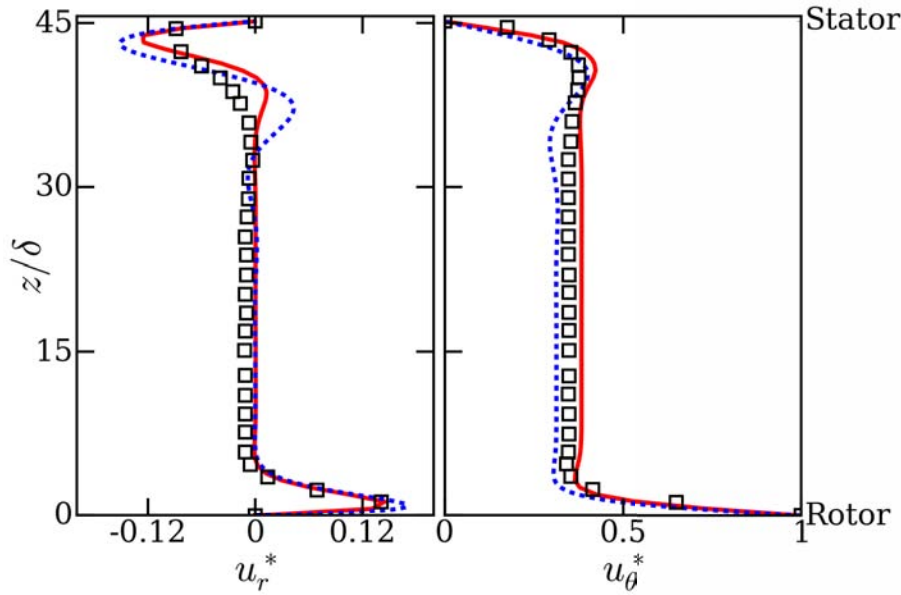
Figure 3.4 − Axial profiles of the dimensionless mean radial u_r^* and azimuthal u_θ^* velocity components at $r^* = 0.5$. Comparison between (−) the LES results, ($\square$) the LDV data by Séverac *et al.* (2007) and (− −) the auto-similar solution by Rogers & Lance (1962).

Fig. 3.5*a*. The LES polar profile is correctly located between the laminar solution (Rogers & Lance, 1962) and the fully turbulent DNS (Lygren & Andersson, 2001) realized at a slightly greater Reynolds number $Re = 4 \times 10^5$. On the stator side ($u_r^* < 0$), the LES profile markedly differs from the laminar solution, which confirms the turbulent nature of this boundary layer, as expected at the present Reynolds number $Re = 1 \times 10^5$ (see e.g. Poncet, 2005). The same applies for the rotor side ($u_r^* > 0$), although the LES profile appears to be somewhat closer to the auto-similar laminar solution: the flow might hence be in a transitional rather than a fully turbulent regime. Another argument in favour of the latter observation would be that contrary to the DNS results (see Fig. 3.5*a*(− ∘ −)), neither the line on the rotor side nor on the stator exhibits the characteristic triangular form commonly found for three-dimensional fully turbulent boundary layers (more in Lygren & Andersson, 2001). Finally, the present LES predictions match closely the experimental profiles (Séverac *et al.*, 2007) which further supports the quality of the results investigated in this chapter. Note also that although DNS is often thought to be more accurate than LES, the LES results are here the closest to the experimental data because the Reynolds number used by Lygren & Andersson (2001) is not exactly that of the experiment, i.e. 4×10^5 for the former against 1×10^5 for the latter. Furthermore the geometry chosen for the DNS has a much smaller aspect ratio, i.e. $G_{\mathrm{DNS}} = 0.02$ whereas $G_{\mathrm{exp}} = 0.2$. Focusing on Fig. 3.5*b* allows to draw similar conclusions for **Case 1** and **Case 2**. In all three cases, the polar plots of the dimensionless mean velocity distribution are located further from the laminar solution (− −) (Rogers & Lance, 1962) than from the DNS results produced by Lygren & Andersson (2001). **Case 2** and **Case 3**, which have similar aspect ratio and only differ by the presence of the shaft (**Case 3**), display almost identical boundary layer behaviours. Nonetheless, according to the interpretation of the

distance between the profiles as proposed by Lygren & Andersson (2001), one can note that the addition of an inner cylindrical shaft (**Case 3**) seems to induce a higher level of turbulence in the boundary layers as the corresponding profile (Fig. 3.5$b(-\blacklozenge-)$) is closer to the DNS predictions. Finally, one can notice that the profile obtained for **Case 1** crosses the line corresponding to the DNS results (Lygren & Andersson, 2001). Extreme care must be taken when interpreting this fact, since the cavity used in **Case 1** strongly differs geometrically from that used by Lygren & Andersson (2001). This being said, the profile for **Case 1** should only be compared with those from **Case 2** & **3** and not those from the literature.
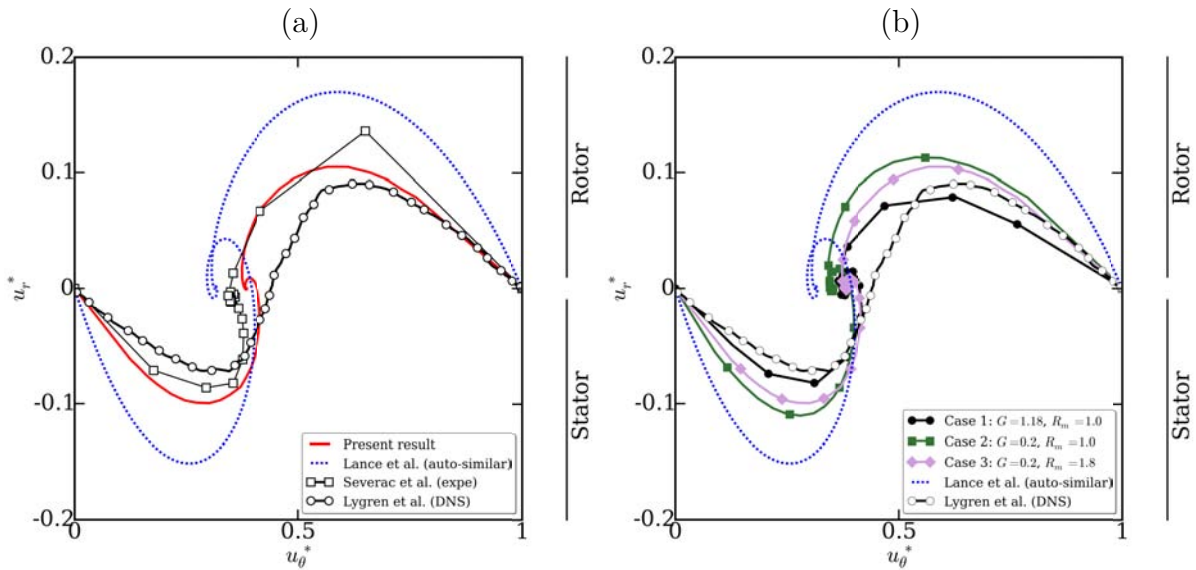
Figure 3.5 − Polar plot of the dimensionless mean velocity distribution at $r^* = 0.5$. (*a*) Comparison between (–) the LES results, (−□−) the LDV data by Séverac *et al.* (2007), (− −) the auto-similar solution by Rogers & Lance (1962) and (− ∘ −) the DNS results by Lygren & Andersson (2001). (*b*) Comparison between the results from (− • −) **Case 1**, (−■−) **Case 2** and (−♦−) **Case 3**, along with the (− −) auto-similar solution by Rogers & Lance (1962) and (− ∘ −) the DNS results by Lygren & Andersson (2001).

3.4.2   Mean flow organization

In the previous section, the accuracy of the mean flow predicted by the LES has been validated against known literature. Therefore, we can now use the results of the three configurations to draw general remarks about the mean organization of a smooth rotor/stator cavity flow and assess the impact of the aspect ratio and the curvature parameter by comparing the three cases.

The base flow solutions are steady, axisymmetric, composed of boundary layers on each disc and contain a central core flow in near solid body rotation. This conclusion drawn for **Case 3** (see section 3.4.1) is also valid for **Case 1** & **Case 2**. These solutions are displayed hereafter for the three configurations in a dimensionless set of coordinates,

Rotation axis located on the left of the contour maps.
Coordinates normalized to span from 0 to 1 to keep the same visual aspect ratio.

Case 1	Case 2	Case 3
(a)	(b)	(c)

Streamlines

(d)	(e)	(f)

Vortex lines

(g)	(h)	(i)

Azimuthal vorticity
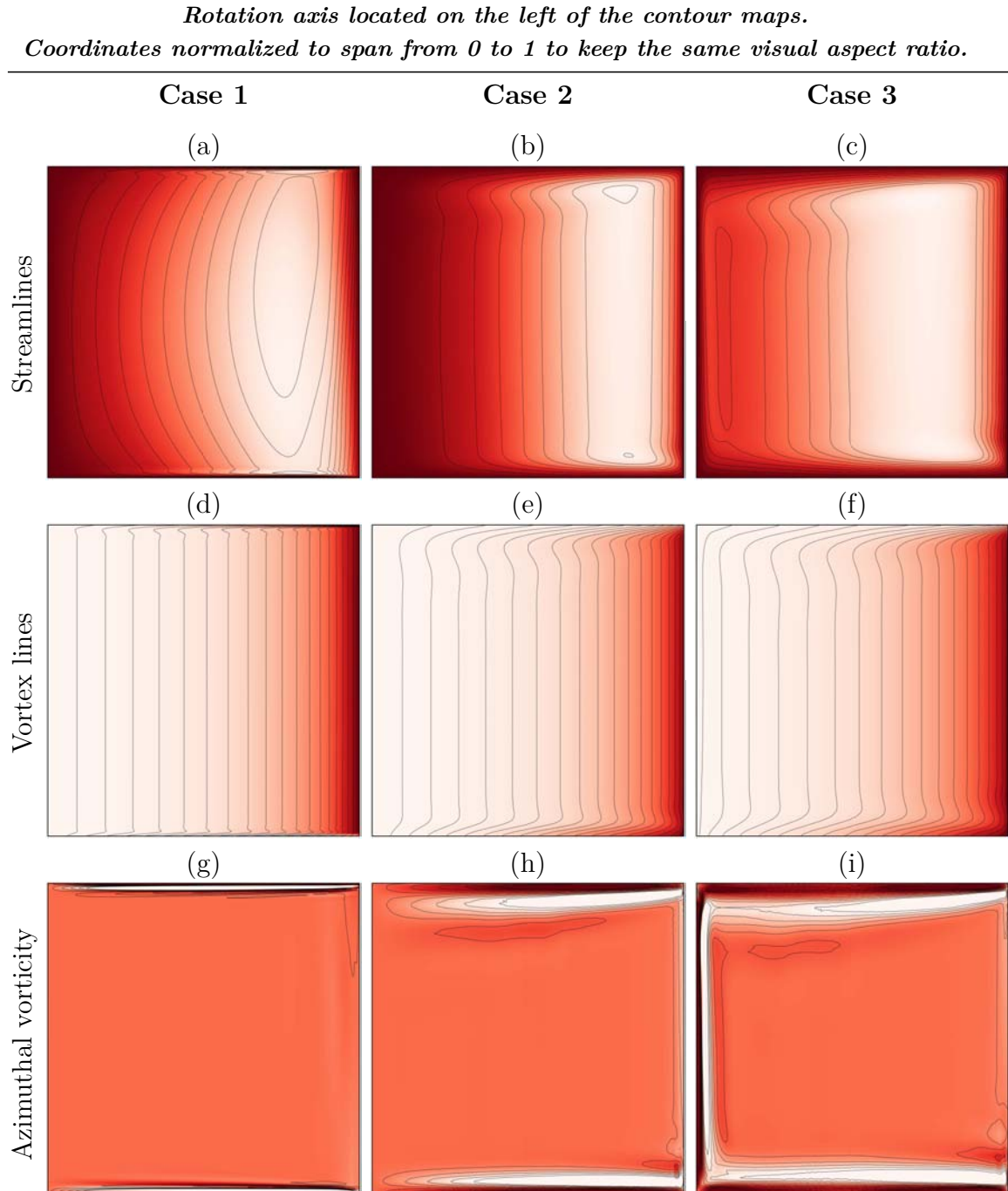
Figure 3.6 − Contours of (top) streamlines, (middle) vortex lines and (bottom) azimuthal vorticity for (left) **Case 1**, (centre) **Case 2** and (right) **Case 3**. Streamlines are in the range $\psi \in \left[-1.0 \times 10^{-5}, 0\right]$ for **Case 1** and $\psi \in \left[-2.0 \times 10^{-3}, 0\right]$ for **Case 2** & 3. For all cases, vortex lines span (quadratically) $r^{*2}u_\theta^* \in [0, 1]$ and vorticity $\eta_\theta \in [-1, 1]$.

i.e. $r^* = (r - R_0)/(R_1 - R_0) \in [0, 1]$ and $z^* = z/h \in [0, 1]$. The figure layout is as follows: the cylindrical cavity at $R_m = 1$, $G = 1.18$ corresponds to Figs. 3.6a, 3.6d, 3.6g, the cylindrical cavity at $R_m = 1$, $G = 0.2$ to Figs. 3.6b, 3.6e, 3.6h and the annular cavity at $R_m = 1.8$, $G = 0.2$ to Figs. 3.6c, 3.6f, 3.6i. For each case, the streamlines (top row), the vortex lines ru_θ (middle row) and the azimuthal vorticity $_\theta$ (bottom row) for the steady axisymmetric state are shown. Note that in the specific case of a fully axisymmetric flow, these quantities are linked to the cylindrical velocity components by $r\mathbf{u} = r(u_r, u_\theta, u_z) = (-\partial \ /\partial z, ru_\theta, \partial \ /\partial r)$ and $r \ \times \mathbf{u} = (-\partial ru_\theta/\partial z, r \ _\theta, \partial ru_\theta/\partial r)$ (detailed e.g. in White, 2006).

As can be seen from the streamline plots (Fig. 3.6, top row), all the computed flows show a clear distinction between the layers close to the discs and the core of the cavity, further supporting that they all are of the separated boundary layers types (see Daily & Nece, 1960). Besides, as discussed further later, the boundary layers on the stationary discs have the characteristic spatial oscillations associated with Bödewadt (1940) single-disc flow solution. Likewise, the boundary layers on the rotating discs display the same behaviour as the boundary layers developing over a disc rotating in a slower rotating fluid and as described by Schultz-Grunow (1935). Also in all cases, it is clear that it is the outer cylinder that closes the circulation of the flow. The flow is indeed ejected radially outward on the rotor, moves upwards along the shroud to travel radially inward along the stationary disc before returning to the rotating disc boundary layer at the position $r^* = 0$. Note that Fig. 3.6a evidences a *secondary* recirculation loop confined at high radial locations $r^* \geq 0.7$ (similar to Lopez, 1996, figure 2) that does not appear in Fig. 3.6b or Fig. 3.6c - independently of the number of -isocontours. This observation is consistent with the streamlines of the flows presented by Gelfgat (2015), obtained for multiple cylindrical cavities of different aspect ratios going from $G = 0.1$ to $G = 1.0$. Since the present **Cases 2** & **3** do not display any secondary vortex, it is reasonable to think that its appearance only occurs at high aspect ratios, with little to no dependency on the curvature of the cavity.

Note that vortex lines are here plotted using a ***quadratic*** distribution of the isocontours between $(r^{*2}u_\theta^*)_{\min} = 0.0$ and $(r^{*2}u_\theta^*)_{\max} = 1.0$, following the work by Lopez *et al.* (2009). In such a view, the intent is to illustrate the departure of the core rotor/stator flow from a flow in solid-body rotation (see e.g. the auto-similar solution by Rogers & Lance, 1962) caused by the confinement between the axis $r^* = 0$ (or the shaft, in **Case 3**) and the shroud. Indeed, were the flows in exact solid-body rotation in the core of the cavity, the vortex lines would behave like $r^{*2}u_\theta^* \quad r^{*2}$, and consequently the isocontours on Fig. 3.6 (middle row) would appear radially equidistant. This is the case for $r^* < 0.5$, but for $r^* > 0.5$ the presence of the outer shroud obviously forces the flow to adapt to the boundary condition (see part 3.3.2) and the isocontours get closer to each other. When $R_m > 1.0$ (Fig. 3.6f), the same deviation appears when approaching the shaft, although the adaptation of the flow to this boundary condition is faster since it is eased by the azimuthal velocity component of the inner wall.

Vortex lines also clearly show the typical features of a rotating disc boundary layer on the bottom and of the stationary disc boundary layer on the top. Assuming that, at

leading order, the boundary layer thickness can be evaluated as the minimum distance from the wall at which $u_\theta^* = K$, it is noticeable (see Fig. 3.6, middle row) that the thicknesses along the bottom rotating discs are quite uniform. The boundary layers along the top stationary discs however vary significantly with r^*, thinning out as r^* increases to 1. This fact maybe more evidently illustrated by the isocontours of azimuthal vorticity $_\theta$ shown on Fig. 3.6 (bottom row). Indeed, since the flow is virtually independent of z^* and only slowly varies with r^* outside of the boundary layers (as seen in Fig. 3.4 and 3.6, top & bottom rows), one expects to find $_\theta \neq 0$ within the boundary layers only, which makes the azimuthal vorticity an ideal marker.

All present points finally contribute in the assessment of the simulations' accuracy. Many workers indeed report similar behaviours for the Bödewadt and Ekman layers in a rotor/stator cavity: Lopez (1996) & Lopez *et al.* (2009) numerically and Gauthier *et al.* (1999) experimentally in cylindrical cavities with different aspect ratios (resp. $G = 1.0$, $G = 0.2$ and $G = 0.048$). Likewise Randriamampianina *et al.* (1997) report similar features on the basis of numerical simulations in an annular cavity at $R_m = 1.20$ and $G = 0.1$. In the latter contribution, the authors also varied the Reynolds number Re from 10^2 to 1.75×10^5 and showed (see Randriamampianina *et al.*, 1997, figure 3) that the radial decay of the Bödewadt layer occurred only for $Re \geq 10^4$, which is in agreement with the present situation. Figure 3.6*i* adds to these observations that a non-unit curvature parameter R_m induces the creation of a boundary layer along the shaft, similar to the centrifugally unstable sidewall boundary layer found in rotating cylinder configurations (see e.g. Lopez, 1998), linking together the top and bottom discs layers.

3.5 Flow instantaneous structures and organizations

We will now present the different flow patterns observed in the three cavities studied in this document. First the instability patterns known to appear in the disc boundary layers (refer e.g. to Serre *et al.*, 2001) are discussed to show that our unstructured wall-resolved LES approach is capable of reproducing such a dynamics. It is however only a necessary step before focusing the attention on the whole-cavity flow dynamics to try and identify macro-structures that could potentially be responsible for the 'pressure bands'.

The velocity fluctuations, denoted by a tilde superscript in what follows (i.e. $\tilde{u}_r$, $\tilde{u}_\theta$ and $\tilde{u}_z$ for the radial, azimuthal and axial fluctuations respectively), are used to display the local spatial flow structures present in the LES predictions. These time-dependent fluctuations are computed at specific instants with respect to the azimuthally-averaged flow solution at this instant. Note that this procedure is chosen because when instability arises (Smith, 1947; Gregory *et al.*, 1955; Faller, 1963), the base flow is known to depart from a purely parallel flow and the perturbations can be measured by the magnitude of the axial velocity fluctuation which then varies around a zero mean (see e.g. Serre *et al.*, 2001; Lopez *et al.*, 2009). The following analysis will hence focus exclusively on $\tilde{u}_z$ as a marker of the rotating flow patterns.

For all considered cases, the stationary discs boundary layers evidence instability patterns, whether axisymmetric or three-dimensional. The rotating disc boundary layers however remain globally undisturbed except in the presence of an inner rotating shaft (**Case 3**). Aside from the viscosity-driven boundary layers, the homogeneous core flow also exhibits characteristic patterns and a coherent azimuthal organization that shall be discussed last.

3.5.1 Vortex structures related to stationary disc boundary layer instability

To start we examine the flow patterns also referred to as spatial instabilities hereafter in the stationary discs boundary layers. The focus is first put on the azimuthal layout and will then shift to the temporal evolution of the patterns in the respective simulations.

3.5.1.a Spatial organization

As in Schouveiler *et al.* (1999) or Serre *et al.* (2001, 2004) the present LES results show the existence of two types of patterns in the Bödewadt boundary layer: axisymmetric annuli and three-dimensional spirals. These are commonly referred to as type-2 (Gregory *et al.*, 1955; Faller, 1963; Lilly, 1966) and type-1 (Smith, 1947; Reed & Saric, 1989) instabilities. Figure 3.8 presents the isocontours of axial velocity fluctuations in a horizontal section positioned in the Bödewadt layer at $z^* \simeq 1 - \delta/h$ for all three cases. Contours show that while the boundary layers in the two cylindrical cavities only display three-dimensional spiral patterns, the annular cavity of **Case 3** also presents quasi-axisymmetric structures close to the shaft. With further extension in mind, we define the radial wavenumber of an instability as $k_r = n_r/\Delta r^*$, where Δr^* is the radial length occupied by n_r rolls, and measure it with respect to δ as is usually done in the literature (Lingwood, 1995*a*, 1997; Gauthier *et al.*, 1999; Serre *et al.*, 2001). We also define the angle ε made by a spiral arm with the normal to the geostrophic flow as explained by the sketches in Fig. 3.7.

In the high aspect ratio configuration (Fig. 3.8*a*), the solution ultimately stabilizes after $t^* = tF_0^{-1} = 150$ with a spatially oscillatory state characterized by a 3-, 4- or 5-armed spiral. Note that such uncertainty on the exact azimuthal organisation tends to imply that the visible pattern may result from the superposition of several underlying structures. As indicated on the label, the critical local Reynolds number above which the base flow of **Case 1** spatially destabilizes is around $Re_{\delta,I} \simeq 90$, producing spiral arms that extend to the outer rim of the cavity where they merge with the cylindrical boundary layer. The inclination of the arms with respect to the normal to the geostrophic flow evolves radially from $\varepsilon \simeq 60.9°$ close to the z-axis to $\varepsilon \simeq 21.8°$ at the shroud. The wavefront has a radial wavenumber $k_r\delta \simeq 0.018 \pm 0.003$, the uncertainty being evaluated by computing the wavenumber along the radial direction at each azimuthal station and extracting average and standard deviation. To the authors knowledge, the existing literature on high aspect ratio rotating cavity flows does not provide any direct means to validate the nature of the presently observed pattern. However and indirectly, the isocontours of $\tilde{u}_z$ presented by Gelfgat (2015) show a radially oscillating structure in the stationary disc boundary
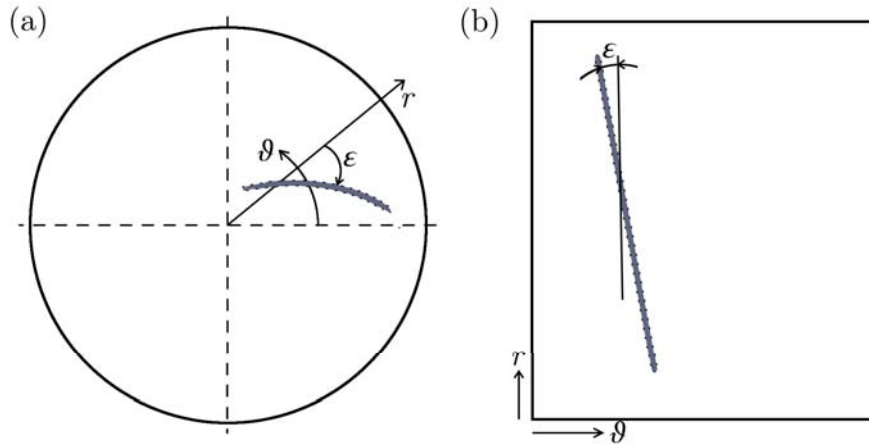
Figure 3.7 – Definition of the angle ε between a spiral arm (bold grey dash-outlined streak) and the normal to the geostrophic flow in (*a*) polar view and (*b*) equivalent Cartesian coordinates.

layer with 2 to 5 vortices, which would tend to support the present observation.

Similarly to **Case 1**, **Case 2** also exhibits (see Fig. 3.8*b*) a purely three-dimensional spiral in its stator boundary layer. However the smaller aspect ratio ($G = 0.2$) induces a markedly different pattern. Contrary to the previous case (Fig. 3.8*a*) where the spiral arms extend throughout the boundary layer to finally merge with the cylindrical outer layer, the vortices in **Case 2** are restrained to a fixed radial range corresponding to $Re_{\delta,I} \in [Re_{\delta,c}; Re_{\delta,f}] \equiv [45, 250]$. Outside the flow is either stable (close to the z-axis) or interactions with the outer cylindrical boundary layer induce loss of coherence. It is noteworthy that the number of arms fluctuates within this radial range. Close to $Re_{\delta,c}$ one can count 7 spiral arms inclined at $59.03° \leq \varepsilon \leq 64.8°$ (decreasing with the increasing radial position). At larger distances from the z-axis, the structure possesses 16 arms (starting from $Re_\delta \simeq 150$ and outwards) with a much smaller inclination with respect to the normal to the geostrophic flow $39.29° \leq \varepsilon \leq 46.55°$ (*idem*). Note also that further dislocation yield 18 spiral vortices close to $Re_{\delta,f}$. Within the identified unstable interval, the wavefront has a wavenumber $k_r\delta \simeq 0.33 \pm 0.025$, with the minimum being reached for the 7-armed spiral and the maximum corresponding to the 18-armed spiral on the outer edge of the interval. These observations are supported for instance by the linear stability results obtained by Itoh (1991) or Tuliszka *et al.* (2002) who found a critical local Reynolds number $Re_{\delta,c,\text{LSA}} = 48.1$ (resp. 47.5) for a wavefront propagating with a wavenumber $0.260 \leq k_r\delta \leq 0.265$ (resp. $0.258 \leq k_r\delta \leq 0.296$). They can also be compared to the DNS at $Re = 4 \times 10^4$ of Serre *et al.* (2001) which revealed 16 spiral arms close to the shroud in the stationary disc boundary layer, yielding $Re_{\delta,c,\text{DNS}} \simeq 86.5$ and a wavenumber $0.37 \leq k_r\delta \leq 0.71$.

Introducing **Case 3** indicates that the presence of a rotating shaft, i.e. $R_m = 1.8$ (**Case 3**, Fig. 3.8*c*), has a deep impact on the characteristics of the structure within the stationary disc boundary layer. In the range $Re_{\delta,I} \in [150, 260]$, the base flow loses its stability and a 29-armed spiral inclined at a constant angle $\varepsilon \simeq 18.4°$ appears over this range. For $Re_\delta < 150$, the inner cylindrical boundary layer induces the dislocation

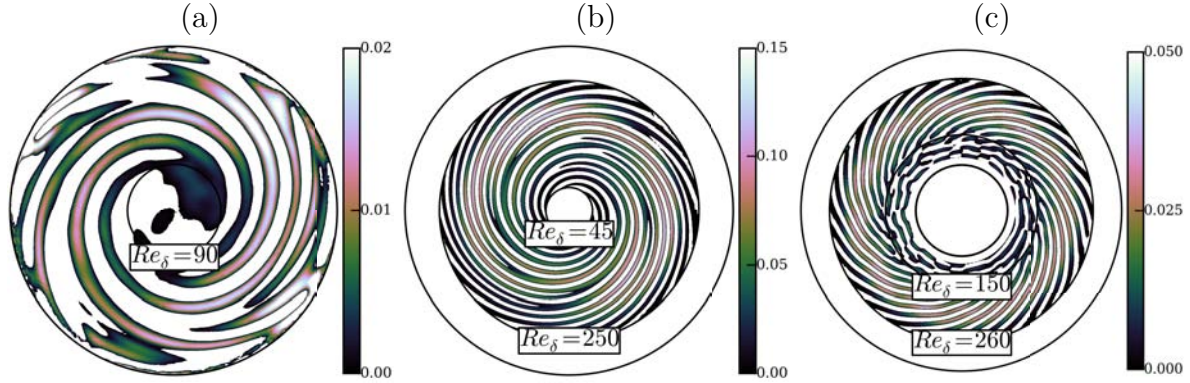***Relatively to the cuts below, the rotor rotation is counter-clockwise***

Figure 3.8 – Snapshots of the dimensional axial velocity fluctuations $\tilde{u}_z$ in the stationary disc boundary layer at $z^* \simeq 1 - \delta/h$ for (a) **Case 1**, (b) **Case 2** and (c) **Case 3**. Labels indicate radial positions of interest and/or the radial extent of the patterns. Bold circles without labels mark the limits of the computational domain.

of the spiral into a quasi-concentric structure but just like the spiral of **Case 1**, it is highly probable that it results from the superposition of several structures. Both waves propagate with similar wavenumbers: the annular wavefront has $k_r\delta \simeq 0.32 \pm 0.03$ and the spiral structure $k_r\delta \simeq 0.3 \pm 0.02$. Interestingly, these values are very similar to the one found theoretically by Lingwood (1997) ($k_r\delta \approx 0.33$) at the convective/absolute transition in the case of propagating circular waves in the Bödewadt flow above a single infinite disc. Note also that the co-existence of the two types of instabilities in the Bödewadt boundary layer has already been reported numerically and theoretically by several authors like Serre *et al.* (2001, 2004) for a $G = 0.2$, $Re = 3 \times 10^4$ (resp. 13200) cavity or Lopez *et al.* (2009) for a $G = 0.2$, $Re = 6 \times 10^4$ cavity. Although the number of spiral arms quoted in the aforementioned sources (resp. 16, 10 and 32) is somewhat compatible with the present observation, the authors consistently report the transient nature of the circular waves that can only be maintained through a forced periodic modulation of the rotor rotation speed. Consensus is however not reached since Gauthier *et al.* (1999) showed experimentally using a very low aspect ratio cylindrical cavity ($G = 0.047$) that annular structures (type II) can be observed in the Bödewadt boundary layer ($174 < Re_\delta < 247$) together with spirals (type I, $247 < Re_\delta < 295$). They also observe that the association is steady although the circular wave characteristics strongly depend on the noise level. It is noteworthy that in spite of the difference with **Case 3** ($G = 0.2$), our observations match quite accurately with Gauthier *et al.* (1999) findings and who report that the spiral pattern has 31 arms and that the annular wavefront evolves with a wavenumber $0.2 \lesssim k_r\delta \lesssim 0.5$.

3.5.1.b Temporal evolution

Features exposed in the previous paragraph can be supplemented with the study of the temporal evolution of the flow to focus on the establishment of axisymmetric and spiral
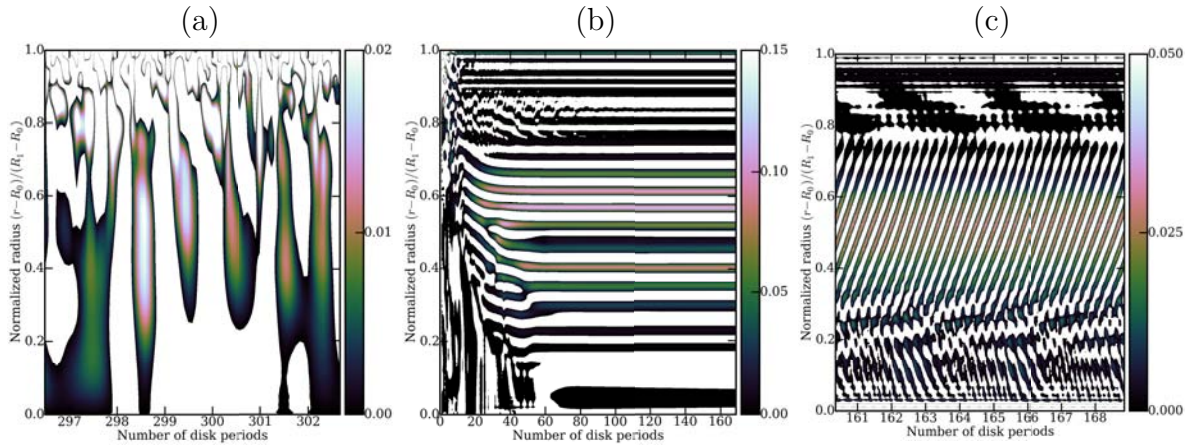
Figure 3.9 – Space-time plots of $\tilde{u}_z$ at $z^* \simeq 1 - \delta/h$, $\theta = 0$ with $r^* \in [0, 1]$ for (a) **Case 1**, (b) **Case 2** and (c) **Case 3**. Time range has been zoomed as needed to capture the right precession frequency. Values outside of the colour range have been blanked out.

patterns present in the Bödewadt layer of all three cases. Figure 3.9 shows the space-time plots of $\tilde{u}_z$ at $z^* \simeq 1 - \delta/h$ and $\theta = 0$ for the whole radius ($r^* \in [0, 1]$) for **Cases 1**, **2** and **3** (from left to right, resp.). These will allow assessing whether the structures precess with respect to the base flow and at which frequency.

In **Case 1**, Fig. 3.8*a* shows that the flow azimuthal arrangement is dominated by a spiral pattern, although it is unsure whether it has 3, 4 or 5 arms. This fact is supported by the space-time plot presented in Fig. 3.9*a* where no clear regular striping can be identified. This plot also reveals that the structure is not stationary but that it is made of rotating waves. In this case, the average precession is prograde with the bottom rotating disc, with a precession frequency $F_p \simeq F_0$ (recall F_0 is the *frequency of the rotor* in Hz). What is more, the spiral vortices propagate inward from the outer rim of the disc to the low local Reynolds number area with a velocity computable from Fig. 3.8*a* and estimated at $V_{\rm ph}/\Omega R_1 \simeq 9.5 \times 10^{-2}$.

The behaviour of the three-dimensional structure occurring in **Case 2** is opposite to **Case 1**. Figure 3.9*b* shows the space-time plot of $\tilde{u}_z$ in the stationary disc boundary layer of **Case 2** over the whole simulation time. For $t^* > 10$, structures closest to the edge of the disc are already established and appear not to be rotating with respect to the base flow. This latter conclusion can actually be extended to the whole spiral pattern observable in the boundary layer. The stripes representing the spiral arms crossing the $\theta = 0$ line are indeed all horizontal, thus showing that this spatial instability is stationary. This being said, it is of note that the establishment of the spiral arms is progressive. First the 18-armed spiral appears ($t^* \gtrsim 20$) in the high local Reynolds number area, and as the wavefront propagates towards the z-axis at $V_{\rm ph}/\Omega R_1 \simeq 6.7 \times 10^{-4}$ the 14- ($t^* \gtrsim 40$) followed by the 7-armed ($t^* \gtrsim 45$) spiral structures are created and established.

The temporal evolution of the patterns present in **Case 3** stator boundary layer (see Fig. 3.8*c*) is displayed in Fig. 3.9*c* over 10 periods of the rotor and chosen when all transients have been evacuated so the flow can be considered steady, albeit oscillatory ($\tilde{t} \gg 1$). The space-time plot reveals that the 29-armed spiral contained between $Re_\delta =$

150 and $Re_\delta = 260$ (see Fig. 3.8c) is precessing at a frequency $F_p \simeq 3.58 F_0$. Study of successive instantaneous shots further shows that the wave is a three-dimensional time-periodic state whose spatial structure is time invariant and precesses uniformly without any superposed radial convective motion. Close to the shaft ($Re_\delta < 150$) on the other hand one can observe the mark of the quasi-annular structure seen in Fig. 3.8c. The space-time diagram (Fig. 3.9c) actually confirms that the visible pattern is the result of the superposition of two or more underlying structures, one of which might be an inward propagating annular wavefront, coupled with one or more spiral wavefronts. A detailed decomposition of this visible pattern is done in the next section, as Fig. 3.8c alone does not allow to conclude on the characteristics of the constituent wavefronts. All the results from section 3.5.1 are summarized in Tab. 3.4.

3.5.2   Instability of the annular Ekman boundary layer

As stated earlier, the rotating discs boundary layers remain visibly undisturbed in all three cases under study, to the exception of **Case 3** where the presence of the inner rotating shaft makes the layer unstable enough for coherent structures characteristic of a transitional state to appear. Figure 3.10a displays an instantaneous contour plot of the axial velocity fluctuations $\tilde{u}_z$ in the $(r^*, \theta, z^* = \delta/h)$ section. The layer is apparently occupied by a superposition of structures that give rise to a visible co-winding spiral pattern exhibiting 6 or 7 arms over most of the radial extent of the disc, and up to 11 or 12 arms close to the outer cylindrical shroud. Close to the shaft on the other hand, it is of note that another three-dimensional instability occurs with the apparition of a 5-armed counter-winding spiral connected to the second spiral. The situation resembles the feature of the stationary disc of **Case 1**, where the number of spiral arms is unclear and points to a potential combination of several types of spirals. Also and because of the superposition of states, the evaluation of the wavenumbers of the two spirals suffers from great inaccuracy. Close to the shaft, the wavefront has $k_r \delta = 0.24 \pm 0.05$ while the outermost spiral wavefront evolves at $k_r \delta = 0.11 \pm 0.02$.

Figure 3.10b shows the temporal evolution of the aforementioned pattern, at $\theta = 0$ and for the whole radial extent, for 10 periods of the rotor during the steady phase. It tends to confirm that the visible pattern is actually a combination of multiple underlying structures. For instance, one can note two independent sets of oriented stripes close to the shaft. Similarly to the spiral found in the stationary disc boundary layer, the main instability is convected outwards from the shaft to the large local Reynolds number region with an approximate velocity $V_{\mathrm{ph}}/\Omega R_1 \simeq 6.5 \times 10^{-2}$. The innermost structure appears to have a very similar behaviour, that is, also convected outwards with the same approximate velocity. In terms of azimuthal motion, the space-time plot presented on Fig. 3.10b shows that the visible structure has a prograde precession with an approximate frequency $F_p \simeq 3.17 F_0 \pm 0.01 F_0$ (depending on whether 6 or 7 arms are considered). At the shroud, where the visible structure displays up to 11 arms, the space-time diagram shows a different behaviour from what was previously identified in this Ekman boundary layer. The vortices indeed appear to propagate inwards rather than outwards although they keep the same precession frequency as the rest of the structure.

References	Annular patterns			3D Spiral patterns			
	$Re_{\delta,II}$	$k_r\delta$	F_p	$Re_{\delta,I}$	$k_r\delta$	$F_pF_0^{-1}$	m
Present results							
Case 1 ( )	—	—	—	$[90, 315]$	$[0.015, 0.021]$	1.0	$[3, 5]$
Case 2 (✠)	—	—	—	$[45, 250]$	$[0.305, 0.355]$	0	$[7, 18]$
Case 3 (★)	$[30, 150]$	$[0.29, 0.35]$	—	$[150, 260]$	$[0.28, 0.32]$	3.58	29
Theory							
Itoh (1991)✠	—	—	—	$[48.1,]$	$[0.260, 0.265]$	—	—
Lingwood (1997)★	$[21.6,]$	0.34	—	—	—	—	—
Tuliszka et al. (2002)✠	—	—	—	$[47.5,]$	$[0.258, 0.296]$	—	—
3D simulations							
Serre et al. (2001)✠	—	—	—	$[86.5,]$	$[0.37, 0.71]$	—	16
Serre et al. (2004)★	—	—	—	$[52.5,]$	$[0.43, 1.43]$	—	10
Lopez et al. (2009)✠	—	—	—	$[122.5, 195.9]$	0.428	6.41	32
Experiments							
Gauthier et al. (1999)★	$[174, 247]$	$[0.2, 0.5]$	—	—	—	—	—

Table 3.4 – Summary of the results on Bödewadt layer instabilities, m represents the number of arms of a spiral pattern. Upper and lower values for a given parameters are indicated in brackets. Symbols , ✠ and ★ used to match present studies to relevant references. Dashed cells indicate au unknown value.

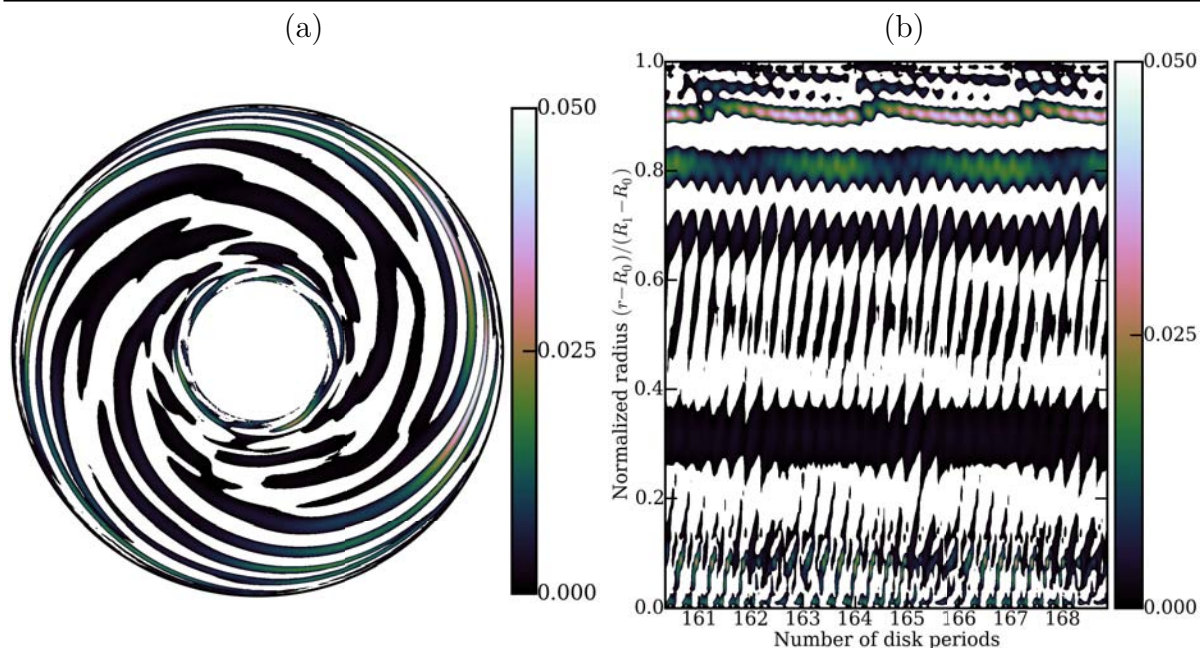*Relatively to the cuts below, the rotor rotation is counter-clockwise*

(a)   (b)

Figure 3.10 – (a) Snapshot and (b) space-time plot of the axial velocity fluctuations $\tilde{u}_z$ in the rotating disc boundary layer at $z^* \simeq \delta/h$ for **Case 3**. Values outside the colour ranges have been blanked out.

Even though theoretical studies such as the one by Lingwood (1995*a*) place the critical Reynolds for the triggering of Ekman layer instabilities at $Re_{\delta,I} \simeq 507.3$ (the maximum local Reynolds number reached at the rim of the rotor is only $Re_{\delta,\max} = 316.2$), the unsteadiness of the annular rotating disc boundary layer was expected. Several authors (e.g. Serre *et al.*, 2001, 2004) performing three-dimensional numerical simulations indeed already observed and reported that the primary effect of an increase in R_m (all other parameters being fixed) is to destabilize the boundary layers, both on the stationary and on the rotating discs. It is also reported to strongly decrease the value of the critical local Reynolds number. Serre *et al.* (2001) show for instance in a cavity with $G = 0.2$ that the Ekman layer is stable for $R_m = 1.0$ but becomes unstable to a 18-armed spiral when the curvature parameter increases to $R_m = 4.0$, a similar behaviour to the one observed in the present study with **Case 2** and **Case 3**.

3.5.3   Behaviour of the homogeneous core of the cavity

Historically, studies bearing on rotor/stator cavity instabilities focus on the behaviour of the discs boundary layers to present and identify structures born from the transitional state of the layers and characterize the geometry under investigation. In more recent years, a new interest has grown for the behaviour of the homogeneous core flow in the cavities. Initially studied in relation with vortex breakdown inside tall rotating-lid cylinder enclosures (see e.g. Gelfgat *et al.*, 1996; Lopez, 1996), the three-dimensional structures present in the homogeneous core of the flow and connecting the discs boundary layers

were only described later in a low aspect ratio cavity by Buisine *et al.* (2000) and Serre *et al.* (2001). Both reported the existence of a complex helicoidal structure, without further discussion. A very comprehensive study on the subject was done recently by Gelfgat (2015) who considers all kind of rotor/stator cavities with aspect ratios ranging from $G = 0.1$ to $G = 1$ concluding that this kind of flows are most unstable to patterns with up to 15 arms for Reynolds numbers as small as $Re \simeq 10^4$. In a previous study (Gelfgat *et al.*, 2001) the authors also show that high aspect ratio cavities ($1 \leq G \leq 3.5$) are most likely to be primarily unstable to circular waves or patterns with 1 or 2 arms.

This section will be dedicated to the description of the behaviour of the homogeneous core flow in solid rotation ($u_\theta^* = K$, $u_r^* = 0$) in all three cases used in the present study. Similarly to the stationary discs boundary layers, all three cases display specific patterns with an axial extent much greater than the previously documented patterns confined respectively to the Bödewadt and Ekman layers. Now that the boundary layer structures have been identified and thoroughly described, the objective of this study of the interdisc flow dynamics is to gain more understanding of the potential flow macro-structures. It is also an attempt to link such features to 'pressure bands' that can be monitored everywhere in the cavity and not only in the boundary layers.

3.5.3.a   Azimuthal organization

Figure 3.11 shows the isocontours of $\tilde{u}_z$ at mid-height ($z^* = 0.5$) for the three cases under study as well as the corresponding space-time plots. The three cavities exhibit specific azimuthal organizations characterized by spiral structures winding in the same direction as the rotor direction of rotation. The high aspect ratio cavity (**Case 1**, Fig. 3.11*a*) however displays a pattern that slightly differs from the two others. Indeed in most of the cavity the fluid appears to simply have a very low amplitude up-down oscillation (in the snapshot, the upper half-disc is filled with fluid going upward and the lower with fluid going downward). The flow is furthermore seen to organize itself only at large local Reynolds numbers $Re_\delta \geq 290$, where the fluctuations are shaped as a 5- or 6-armed co-winding spiral pattern. Unfortunately, the short radial extent of the structure induces high uncertainty on the radial wavenumber that shall consequently not be given here. The core structure on the other hand closely resembles a bipolar structure characterized by a zero radial wavenumber ($k_r \simeq 0$). Lachize *et al.* (2015) hypothesized that the flow in the cylindrical cavity of **Case 1** may indeed organize based on a combination of a bipolar, quadrupolar and sextupolar structures Unfortunately that assumption was not supported by further visual diagnostics that could validate the present LES prediction. The corresponding space-time plot (Fig. 3.11*d*) tends to show that the spiral arms may actually extend all the way to the centre of the cavity, although their amplitude (in absolute value) might be stronger close to the outer cylindrical shroud. In addition, this plot shows that this structure has also a non-zero precession frequency of the order of $F_p \simeq 1.09 F_0$, i.e. it rotates almost at the same velocity as the pattern observed in the stationary disc boundary layer (see Fig. 3.8*a* & 3.9*a*). Visualization of successive similar snapshots shows that the precession is prograde.

Figure 3.11*b* reveals that in the case of the low aspect ratio cylindrical cavity (**Case**

Relatively to the cuts below, the rotor rotation is counter-clockwise
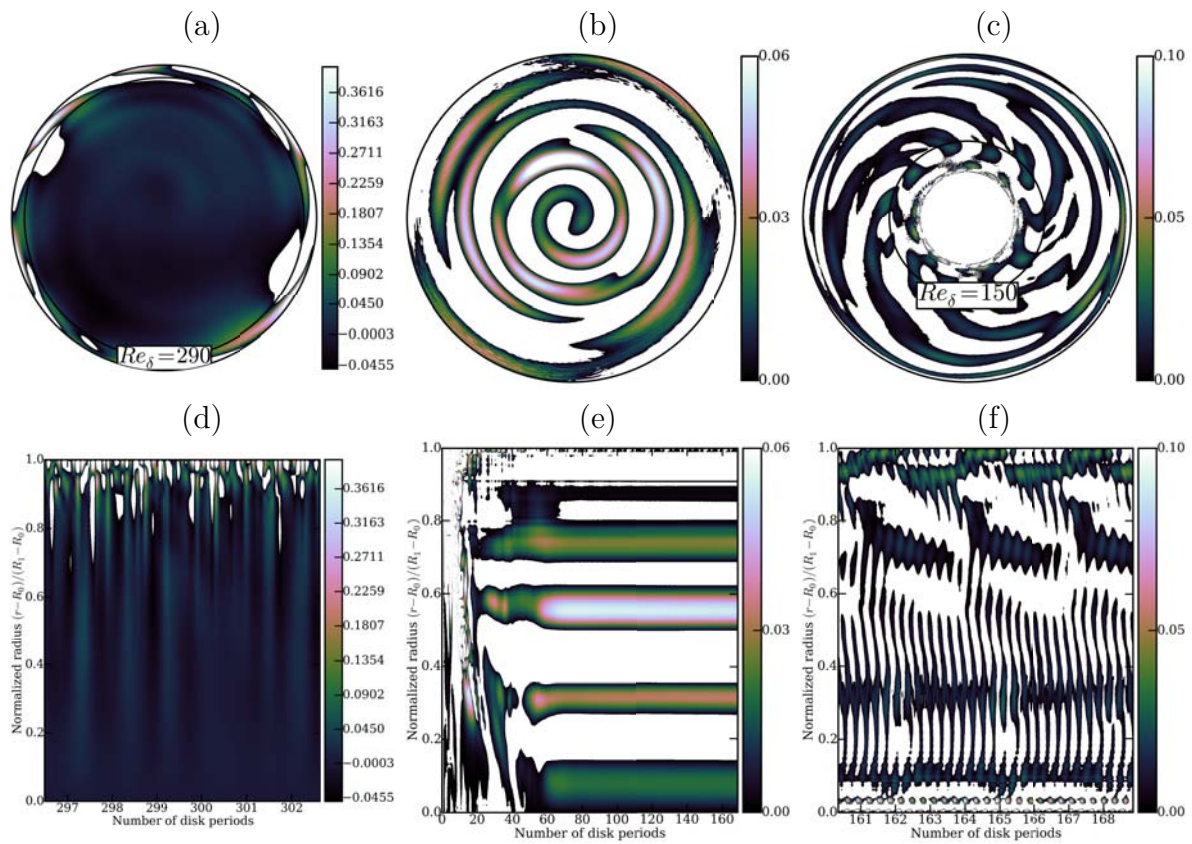

Figure 3.11 − Snapshots (top) and space-time plots (bottom) of the axial velocity fluctuations $\tilde{u}_z$ at $z^* = 0.5$ for (a-d) **Case 1**, (b-e) **Case 2** and (c-f) **Case 3** respectively. Labels indicate radial positions of interest and/or the radial extent of the patterns. Bold circles without labels mark the limits of the computational domain.

2), the fluctuations in the homogeneous core of the cavity organize themselves in a much clearer system. It consists in a single spiral arm occupying approximately 70% of the cavity and winding in the direction of the rotor's rotation. Using the same technique as before, the radial wavenumber of this pattern can be estimated at $k_r\delta \simeq 0.069 \pm 0.007$. Close to the external shroud, the structure dislocates into several elongated vortices no longer attached to each other. Not unlike the pattern present in the stationary disc boundary layer (see Fig. 3.8*b* & 3.9*b*), the structure formed by the fluctuations of velocity in the homogeneous core of the cavity seems to be stationary according to the corresponding space-time plot shown on Fig. 3.11*e*. This plot also shows that the single-armed spiral establishes itself after about 20 disc periods thus emerging slightly after the Bödewadt layer is organized (see Fig. 3.9*b*). It can furthermore be seen that soon after the establishment of the high-radius structure, the outermost vortex detaches and is convected inward to the centre of the cavity with a phase velocity $V_{\mathrm{ph}} \simeq 3.3 \times 10^{-3}\,\Omega R_1$ where it becomes stationary.

The situation for **Case 3** (Fig. 3.11*c* & 3.11*f*) is very similar to what can be observed in the rotating disc boundary layer (see Fig. 3.10). In the homogeneous core, the flow indeed organizes itself in a succession of co-winding spirals. Ten vortices can be observed attached to the shaft boundary layer and for local Reynolds numbers $Re_\delta \geq 150$, the fluctuations form a 6- or 7-armed spiral structure whose arms extend to the outermost wall where they merge with the cylindrical boundary layer. The two aforedescribed patterns have different radial wavenumbers, namely $k_r\delta \simeq 0.078 \pm 0.009$ for the innermost and $k_r\delta \simeq 0.06 \pm 0.008$ for the outermost spiral. The corresponding space-time plot (Fig. 3.11*f*) indicates that the allegedly different structures have the same precession frequency $F_p \simeq 3.6F_0$. It is however unclear whether the structures propagate radially inward or outward as the convection direction appears to be a function of the radial location.

3.5.3.b   Three-dimensionality

As already mentioned, the specificity of the structures found in the homogeneous core of the cavity is that they occupy a much greater axial extent than the structures confined to the two disc boundary layers. In fact, these core structures are found to be attached to patterns found in the fluid layers close to the discs and some features of the latter patterns, so far unexplained, are thought to be due to the core structures.

Figure 3.12 presents, within a Cartesian box, the isosurface $\tilde{u}_z = 0.02$ of the axial velocity fluctuations within the whole cavity $(r^*, \theta, z^*) \in [0, 1] \times [0, 2\pi] \times [0, 1]$ for **Case 1**. On the bottom plane ($z^* = 1$, the stator), the stripes due to the spiral pattern already discussed in section 3.5.1 can be seen, while the rotor layer (top, $z^* = 0$) is visibly undisturbed. The most important feature of the three-dimensional pattern present between the two discs boundary layers consists of vertical protrusions that extend over about 85% of the height of the cavity. These 'macro-structures' seem to emerge from the unstable Bödewadt layer (see circled area on Fig. 3.12) and propagate to the vicinity of the rotating disc boundary layer, which actually suggests that there exists a local low-magnitude pumping effect from the rotor.

The same visualization technique has been applied to **Case 2** and results are shown

Figure 3.12 − Isosurface of axial velocity fluctuation $\tilde{u}_z = 0.02$ in the core of the cavity for **Case 1**. A Cartesian projection has been chosen that spans over the whole radial extent ($0 \leq r^* \leq 1$), the whole axial extent ($0 \leq z^* \leq 1$) and the whole azimuthal extent ($0 \leq \theta \leq 2\pi$) of the cavity.
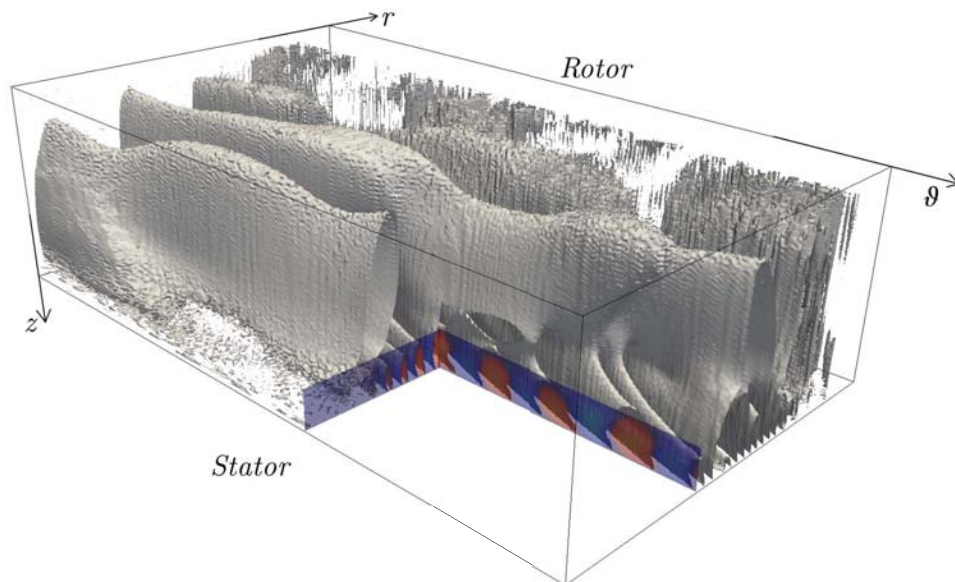
Figure 3.13 − Isosurface of axial velocity fluctuation $\tilde{u}_z = 8 \times 10^{-3}$ in the core of the cavity for **Case 2**. A Cartesian projection has been chosen that spans over the whole radial extent ($0 \leq r^* \leq 1$), the whole axial extent ($0 \leq z^* \leq 1$) and the whole azimuthal extent ($0 \leq \theta \leq 2\pi$) of the cavity.
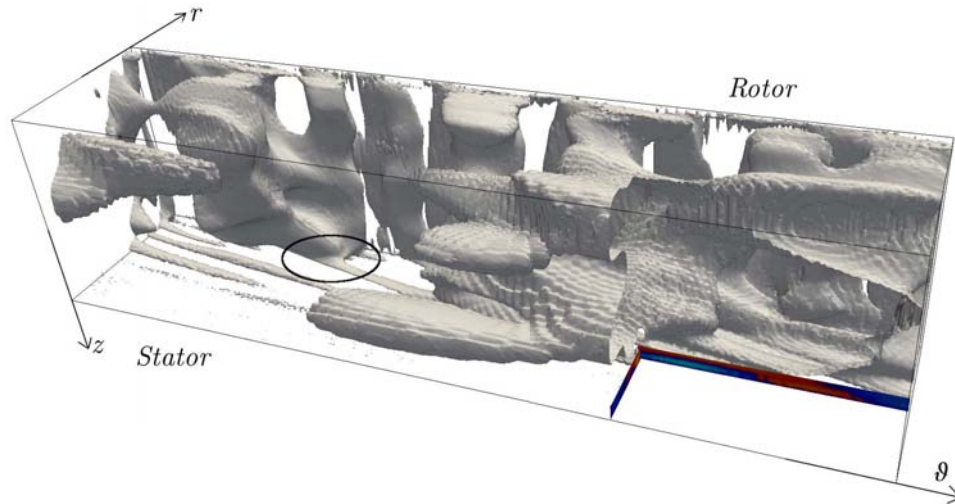
Figure 3.14 – Isosurface of axial velocity fluctuation $\tilde{u}_z = 0.01$ in the core of the cavity for **Case 3**. A Cartesian projection has been chosen that spans over the whole radial extent ($0 \leq r^* \leq 1$), the whole axial extent ($0 \leq z^* \leq 1$) and the whole azimuthal extent ($0 \leq \theta \leq 2\pi$) of the cavity.
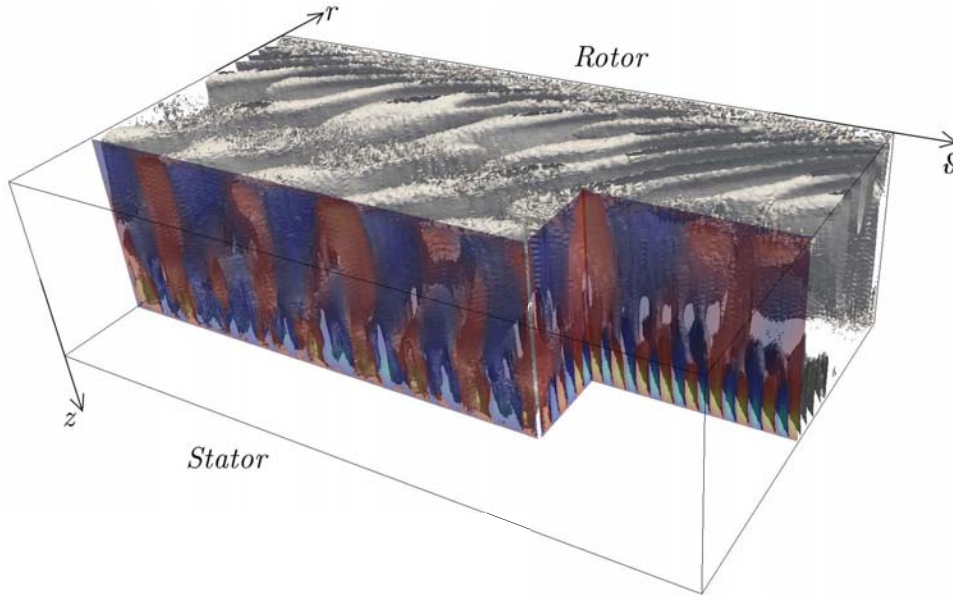
on Fig. 3.13. The isosurface $\tilde{u}_z = 8 \times 10^{-3}$ is drawn in the whole cavity to the exception of a cut-out portion (bottom right of Fig. 3.13) removed to facilitate the observation of the central features. Isocontours of $\tilde{u}_z$ in the stationary disc boundary layer have also been added to locate the vortices in the cut-out portion. As for **Case 1**, the spiral structure previously observed in the Bödewadt layer (see Fig. 3.8*b*) is present near the bottom plane of Fig. 3.13 under the form of elongated structures making a radius-dependent angle with the geostrophic flow, while the rotor boundary layer appears effectively undisturbed. The three-dimensional structures occupying most of the axial extent of the cavity exhibit two major features in this case. First of all, and similarly to **Case 1**, the fluctuating structures present in the homogeneous core of the cavity emerge from the unstable Bödewadt layer and subsist in the cavity until they reach the rotating disc laminar boundary layer. It is noteworthy that the emergence of a core vortex appears exactly at the local Reynolds numbers where the stator spiral dislocates switching from a 7- to a 14-armed structure ($Re_\delta = 150$) and later from a 14- to a 18-armed one. Surprisingly, as soon as the vortices grow out of the stationary disc boundary layer their direction with respect to the geostrophic flow changes markedly to the point where the spiral in the stator boundary layer is counter-winding when the core structure is co-winding (all with respect to the rotor rotation direction) immediately outside the Bödewadt layer.

For **Case 3**, the isosurface of axial velocity fluctuation $\tilde{u}_z = 0.01$ is presented in Fig. 3.14 for the whole cavity. For the same reasons as for **Case 2**, portions of the cavity have been removed to ease the visualization of the boundary layers, the core structures and replaced with planes showing the isocontours of $\tilde{u}_z$. Again, one can observe the presence of elongated vortices in the stationary disc boundary layer (bottom plane) corresponding to the 29-armed spiral described earlier (Fig. 3.8*c*). Likewise larger vortices in the rotating

		Shape	*Winding*	*Precession*
Case 1	Rotor	—	—	—
	Stator	Spiral	Co	Prograde
Case 2	Rotor	—	—	—
	Stator	Spiral	Counter	Stationary
Case 3	Rotor	Spiral	Co	Prograde
	Stator	[Annular, Spiral]	[—, Counter]	[Stationary, Prograde]

Table 3.5 – Summary of the major characteristics of the patterns observed in the boundary layers and in the core of **Case 1**, **Case 2** and **Case 3**.

disc boundary layer (top plane) correspond to the structure analysed in section 3.5.2 (Fig. 3.10). The core pattern in this case has a slightly different behaviour than for **Case 1** & **2** associated to the unsteadiness of the rotating disc boundary layer. The core structures are attached to both the Ekman layer structures and the Bödewadt layer structures. Isosurfaces from successive snapshots show that they actually emerge with the stationary disc spiral and propagate towards the rotor (same low-amplitude pumping effect hypothesized for **Case 1** & **2**). Immediately outside the stator boundary layer, the direction of the vortices with respect to the geostrophic flow changes. The whole core structures actually exhibit a torsional motion to adapt from the angle of the stator spiral pattern to the angle of the rotor spiral to which they eventually attach. Although we could not observe such a behaviour for **Case 1** & **2** (due to the laminar nature of the rotor boundary layer not imposing any direction to the core structures), such an helicoidal trajectory was actually already shown in the literature but for studies bearing on tall cylinder flows exclusively (see Lopez, 2012). The nature, the direction and the temporal behaviour of all patterns described in section 3.5 are summarized in Tab. 3.5.

3.6   Modal analysis of the rotating flows

Now that a thorough presentation of the structures present in the boundary layers and in the cores of the three cavities under study has been made, this section is dedicated to understanding the composition of the observed patterns. Indeed as it was pointed out on several occasions that the visible organization may be the result of the combination of several specific underlying structures. In what follows, the underlying structures are referred to as *atomic modes* or simply *modes* and shall be investigated using the Dynamic Modal Decomposition (DMD) technique established by Schmid (2010). Contrary to the Proper Orthogonal Decomposition (POD) technique (Lumley, 1970; Sirovich, 1987), DMD is built to be the equivalent of a global stability analysis in the case of a linearised flow. Indeed DMD acts as a three-dimensional linear stability analysis of the flow, i.e. it yields the modes most relevant to the structure of the unsteady and potentially non-linear base flow thanks to a coupled spatio-temporal analysis thus capturing even the least energetic

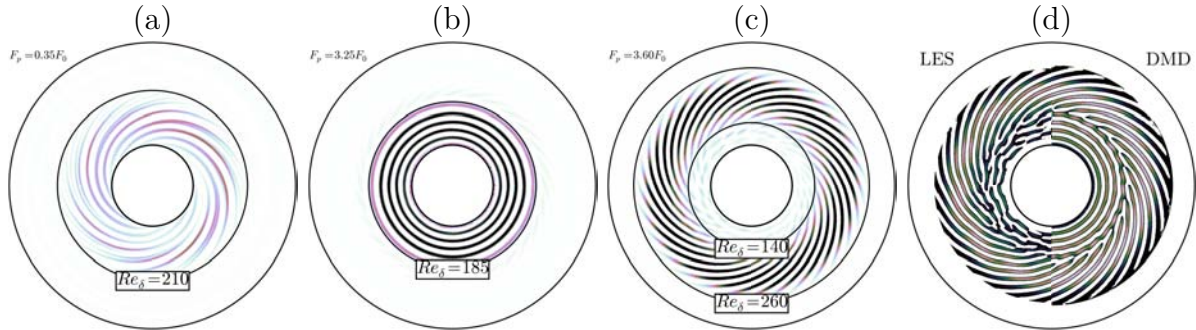*Relatively to the cuts below, the rotor rotation is counter-clockwise*

Figure 3.15 − Isocontours of $\tilde{u}_z \in [0, 0.05]$ at $z^* = 1 - \delta/h$ (stator) for (*a,b,c*) the three major DMD modes constituting **Case 3** sorted out by their respective frequencies and (*d*) a composite made of the LES prediction compared to the combination of the three DMD modes. Values outside the colour range have been blanked out. To improve visibility, the colour scale has been inverted for (*d*).

but most important constituent modes (Schmid, 2010).

In what follows, the modes that are presented have been selected out of all the modes yield by the DMD algorithm and identified as being the most energetic. They are also chosen so that their linear combination is closest to the structures observed in the LES visualizations. To compare with the visualizations shown in Fig. 3.8*c*, 3.10*a* and 3.11*c*, similar (r^*, θ) cuts are made in the DMD solutions: $z^* = 1 - \delta/h$, $z^* = \delta/h$ and $z^* = 0.5$ respectively. First we study the patterns appearing in the annular cavity (**Case 3**, $G = 0.2$, $R_m = 1.8$) as they happen to be a simple linear combination of a few constituent modes. The analysis is then extended to the equivalent cylindrical cavity (**Case 2**, $G = 0.2$) and finally the more complex case of the high aspect ratio cavity (**Case 1**, $G = 1.18$) is tackled.

Again and thanks to this decomposition, one tries to identify the potential appearance of macro flow structures in an attempt to link these oscillations to the 'pressure bands'. If they exist, links with the boundary layer structures should also appear at this occasion.

3.6.1   Spectral content of the annular cavity

In **Case 3**, the DMD algorithm is applied on a set of three-dimensional instantaneous snapshots all taken during the steady phase of the flow over $t^*_{\text{DMD}} = 15$ periods of the rotor and every $\Delta t^*_{\text{DMD}} = 0.05$ period. In this case, the algorithm yields *three* major modes that will be discussed below.

3.6.1.a   Composition of the Bödewadt boundary layer

Figure 3.15 presents the isocontours of $\tilde{u}_z \in [0, 0.05]$ in the statoric boundary layer ($z^* = 1 - \delta/h$) for the three major modes given by DMD. The first mode (Fig. 3.15*a*) is a counter-winding 12-armed spiral confined between the shaft and a local Reynolds number $Re_\delta \simeq 210$. Its radial wavenumber is $k_r\delta \simeq 0.26$ and its temporal frequency $F_p = 0.35F_0$. To obtain the dislocated pattern observed in the near-shaft area in Fig. 3.8*c*, the previous

spiral has to be combined with the axisymmetric pattern represented on Fig. 3.15b. This structure has a very similar radial wavenumber $k_r\delta \simeq 0.27$ but rather than precessing, DMD shows it propagates radially inward at a frequency $F_p = 3.25F_0$ within the top stationary disc boundary layer. Note also that it disappears as it merges with the shaft vertical cylindrical boundary layer. The third mode identified with DMD appears in the statoric boundary layer as a counter-winding 29-armed spiral (Fig. 3.15c) with a radial wavenumber $k_r\delta \simeq 0.31$ and a precession frequency $F_p = 3.60F_0$. These spiral waves and the previous annular wave seem to coexist with very small mutual interference, and the visible pattern shown on Fig. 3.8c is virtually identical to the linear superposition of these two modes. This observation is further supported by the almost exact match between the DMD frequency of the outermost 29-armed spiral ($F_p = 3.60F_0$) and the precession frequency identified previously using the axial velocity fluctuations of the LES prediction (Fig. 3.9c).

In addition, Fig. 3.15d presents a comparison between the visible pattern formed by the fluctuations of $\tilde{u}_z$ in the LES prediction and the pattern made from the combination of the three constituent modes identified above by DMD. Clearly the comparison supports the observations made previously and these three modes make most of the visible phenomena in the Bödewadt boundary layer. Nonetheless, a note has to be made about the fact that the near-shaft dislocation is not as accurately reproduced as the outermost spiral wavefront. The latter really appears to be the only mode responsible for the azimuthal organization of the flow in the LES prediction for local Reynolds numbers $Re_\delta \in [140, 260]$.

3.6.1.b Extension to the cavity

Following the conclusions of section 3.5.3.b that the macro-structures present within the homogeneous core of the cavity originate from the top disc Bödewadt boundary layer and interfere with the bottom disc Ekman boundary layer, we will now study the three-dimensional structure displayed by the DMD modes throughout the cavity.

Figures 3.16a, 3.16b & 3.16c respectively show the azimuthal organization of the three aforementioned constituent DMD modes at mid-height in the cavity, i.e. in the homogeneous inviscid-like core of the cavity. First of all, it is remarkable that the areas of influence of all three modes shift to a different radial location than what can be observed in the statoric boundary layer. The first mode, confined below $Re_\delta = 210$ in the statoric boundary layer (Fig. 3.15a), appears to mark the homogeneous core mostly as a 2-armed spiral. Its strongest magnitude is reached near the outer cylindrical shroud and has a much smaller radial wavenumber $k_r\delta \simeq 0.09$. The annular waves confined below $Re_\delta = 185$ in the Bödewadt boundary layer are seen to span the entire radial extent of the cavity albeit with a lesser amplitude. It can also be remarked that while five annuli are visible in the stator boundary layer (Fig. 3.15b), only three can be counted over the whole radial extent at mid-height in the cavity (Fig. 3.16b). This is again due to a strong decrease in radial wavenumber that is here estimated at $k_r\delta \simeq 0.0231$. The third spiral mode is also subject to strong transformations within the inviscid-like core of the cavity: previously marking the boundary layer as a 29-armed spiral mostly confined between
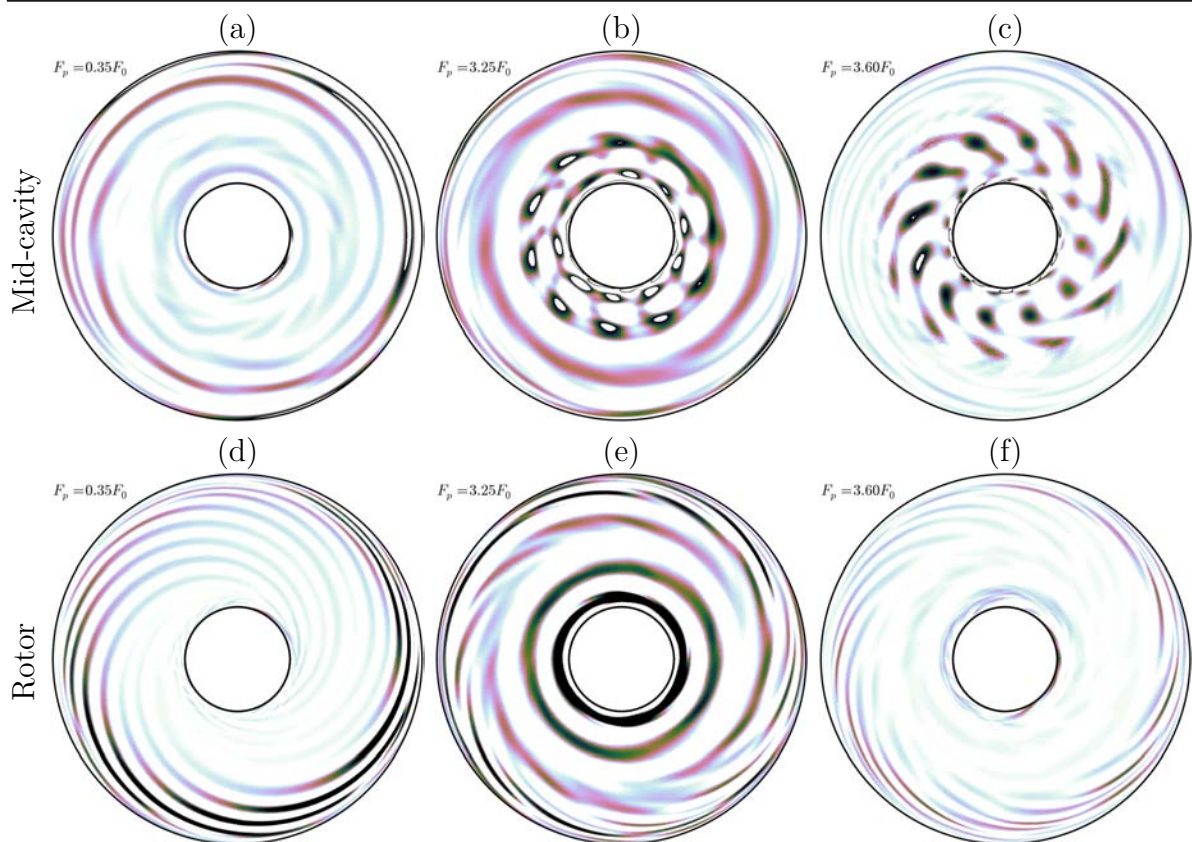
Figure 3.16 − Isocontours of $\tilde{u}_z \in [0, 0.05]$ at (a,b,c) $z^* = 0.5$ (mid-cavity) and (d,e,f) $z^* = \delta/h$ (rotor) for the three major DMD modes constituting **Case 3** sorted out by their respective frequencies. Values outside the colour range have been blanked out.

$Re_\delta = 140$ and $Re_\delta = 260$. It takes the form of a 12-armed spiral attached to the shaft and spans the flow field no further than $Re_\delta \simeq 170$. Similarly to the two other constituent DMD modes, the radial wavenumber of this third mode is also markedly decreased in the homogeneous core of the cavity where it is evaluated at $k_r\delta \simeq 0.069$.

In turn, Figs. 3.16*d*, 3.16*e* & 3.16*f* present the axial velocity fluctuations induced by each constituent DMD mode in the bottom rotating disc boundary layer. At this location, the modal patterns are seemingly present within the same radial interval as in the homogeneous core of the cavity, to the exception of the third mode ($F_p = 3.6F_0$). This specific mode appears to induce stronger fluctuations near the outer cylindrical shroud rather than at low and medium local Reynolds numbers as was the case in the stationary disc boundary layer (Fig. 3.15*c*) and in the core (Fig. 3.16*c*). Nonetheless, the transition from the homogeneous inviscid-like core flow to the Ekman boundary layer also alters the visible patterns. The first mode ($F_p = 0.35F_0$, Fig. 3.16*d*) again organizes the flow as a 12-armed spiral that however differs from the mark in the stationary disc boundary layer. It spans indeed the entire Ekman boundary layer rather than being confined below $Re_\delta \simeq 210$ with a slightly greater radial wavenumber $k_r\delta \simeq 0.3008$. The pattern created by the second mode ($F_p = 3.25F_0$, Fig. 3.16*e*) is identical to that already observed at mid-height in the cavity, namely an annular wavefront with $k_r\delta \simeq 0.25$, but at high local Reynolds numbers $Re_\delta \gtrsim 265$. It exhibits more of a spiral organization that can reasonably be related to the influence of the 12-armed spiral pertaining to the first mode. Finally, the last mode ($F_p = 3.6F_0$, Fig. 3.16*f*), whose radial extent has shifted from the low to the high local Reynolds numbers area, marks the bottom rotating disc as a 17-armed spiral with a radial wavenumber $k_r\delta \simeq 0.28$. It is thus closer in terms of behaviour to the pattern created in the stationary disc boundary layer (Fig. 3.15*c*).

A second phenomenon of importance that can be identified on Fig. 3.16 is the change in winding direction of the pattern depending on the axial location in the cavity. Indeed, the first and last modes ($F_p = 0.35F_0$ and $F_p = 3.6F_0$ respectively), organizing as counter-winding spiral wavefronts on the top disc Bödewadt boundary layer form co-winding spiral patterns at mid-height in the cavity and in the rotating disc boundary layer. Their arms actually bend in the same direction as the geostrophic flow (counter-clockwise on Fig. 3.15 & 3.16). Although the reconstruction of mid-cavity and Ekman layer patterns has not yet been discussed (see paragraph below and Fig. 3.17), this explains the behaviour of the structures observed in the LES predictions (section 3.5.3.b).

The last observation of note one may draw from the coupled study of Fig. 3.15 and Fig. 3.16 is the z-dependent energy redistribution that occurs between the three modes. It can indeed be seen that the annular and 29-armed spiral modes are strongest in the statoric boundary layer (Fig. 3.15, darker shades) but as z^* goes to 0 (rotor), there is marked energy transfer between the two spiral modes so that the 12-armed mode ($F_p = 0.35F_0$) actually becomes dominant in the Ekman boundary layer at the expense of the high-frequency mode. The annular mode on the other hand, albeit presenting smaller radial wavenumbers at mid-height and in the rotor boundary layer, induces axial velocity fluctuations of approximately constant magnitudes throughout the cavity.

To conclude the present discussion, Fig. 3.17 presents two comparisons between the visible patterns formed by the fluctuations of $\tilde{u}_z$ in the LES prediction and the patterns

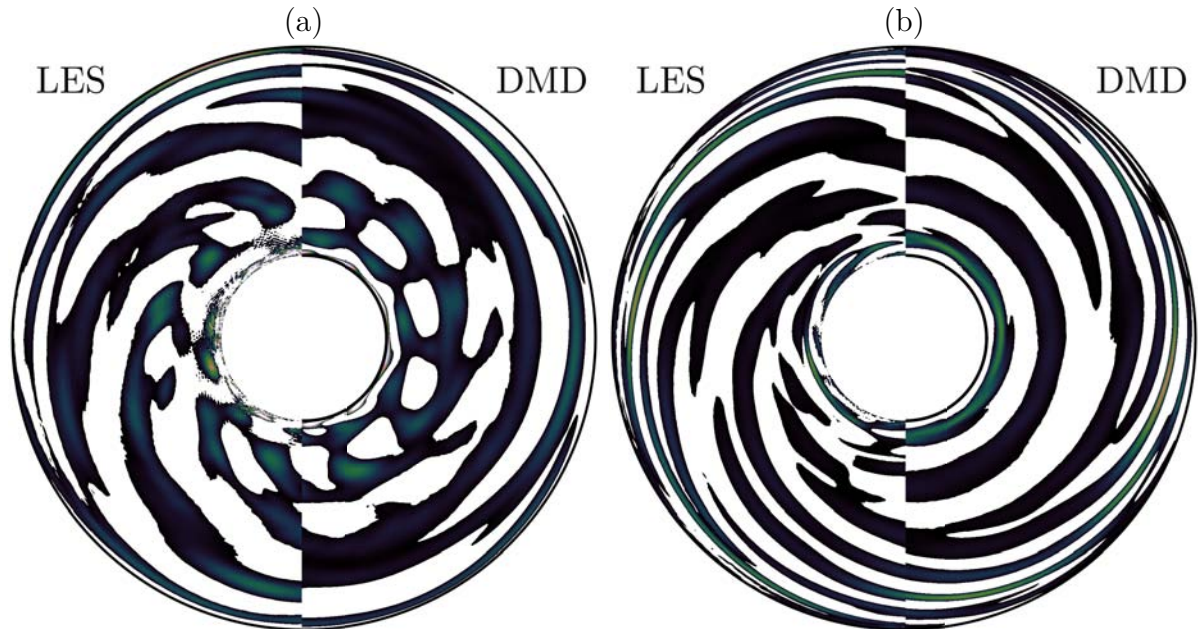*Relatively to the cuts below, the rotor rotation is counter-clockwise*

Figure 3.17 – Isocontours of $\tilde{u}_z \in [0, 0.05]$ for a composite made of the LES prediction for **Case 3** compared to the combination of the three DMD modes at (*a*) $z^* = 0.5$ (mid-cavity) and (*b*) $z^* = \delta/h$ (rotor). Values outside the colour range have been blanked out.

made from the combination of the three constituent modes yield by DMD. Visualization are provided at mid-height in the cavity (Fig. 3.17*a*) and in the bottom rotating disc boundary layer (Fig. 3.17*b*). The very close similarity between the reconstructions and the LES predictions proves that not only do the three constituent DMD modes entirely drive the dynamics of the stationary disc boundary layer but actually the dynamics of the whole flow. This appears to be independent of the axial location, as it was indeed shown that the patterns observed at different heights in the LES prediction are the prints of the same three combined atomic modes.

3.6.1.c   Identification of the one point temporal activity within the cavities

As stated earlier, the motivation for the present study is to characterize the spectral content of the flow in a high Reynolds number rotor/stator cavity and pinpoint the phenomena responsible for the different constituent frequencies. We saw in the latest paragraphs that oscillations of the flow were driven by only three principal atomic modes. Note that hereafter the three DMD modes will be exclusively referred to as 'first', 'second' and 'third', and their frequencies of precession or radial propagation will be noted F_1, F_2 and F_3 for $F_p = 0.35F_0$, $F_p = 3.25F_0$ and $F_p = 3.6F_0$ respectively. To monitor the pointwise-temporal dynamics of the flow, a set of numerical probes has been added to the geometry according to the distribution presented on Fig. 3.18. A total of fifteen circles of sixty probes is spread on three levels in the axial direction to gather data from the two discs boundary layers ($z^* = \delta/h$ for rotor and $z^* = 1 - \delta/h$ for stator) and from the

homogeneous core flow ($z^* = 0.5$). The probes will be referred to as C_xP_y where $x \in [\![1,5]\!]$ for the rotor layer, $x \in [\![6,10]\!]$ for the stator layer and $x \in [\![11,15]\!]$ at mid-height, as well as $y \in [\![0,59]\!]$ so that C_xP_y is located at the azimuth $\theta_y = 2\pi y/60$. A demonstration of the numbering system is done on Fig. 3.18 in the case of the rotor layer.
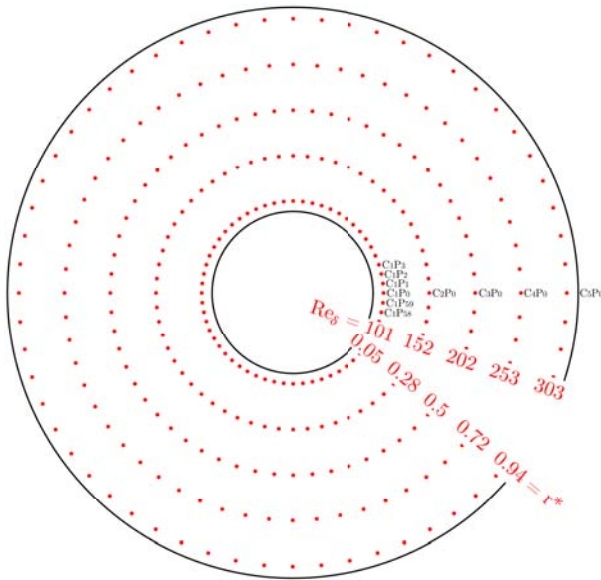

Figure 3.18 – Locations of the numerical probes in the cavity associated with **Case 3**. The bottom disc, the homogeneous core and the top disc have been instrumented with 300 probes arranged on 5 circles of 60 probes. Numbering example matches that of the rotor layer.

To be coherent with the presentation of the flow dynamics proposed in the previous paragraphs, Fig. 3.19 shows the Power Spectral Density (PSD) of the fluctuating axial velocity as registered by probes C_6P_0 to $C_{10}P_0$ in the top stationary disc boundary layer of **Case 3**. First, signals registered by the outermost probes C_9P_0 and $C_{10}P_0$ are on average 40 dB below the signals from the three other probes. This was expected from the absence of strong fluctuations of axial velocity close to the outer cylindrical shroud observed on Fig. 3.15 which shows that most of the activity is actually confined below $Re_\delta \simeq 260$. Furthermore, it appears that all five signals display the same set of peaking frequencies, some of which have been reported on the top axis of Fig. 3.19. The constituent frequencies with the strongest peaks exactly match F_2 and F_3 in all signals. Their relative magnitudes depend on the radial location and correspond to the domains of existence of the second and third modes. For example, C_7P_0 ($Re_\delta = 152$) registers its strongest peak at F_2 whereas C_8P_0 ($Re_\delta = 202$) highest peak is at F_3, which is in agreement with the fact that the second mode exists for $Re_\delta \in [0,185]$ and the third one becomes predominant for $Re_\delta \in [140, 260]$ only. It is noteworthy that the first mode frequency F_1 is also detected by some probes, although its presence is most strongly felt in the signal registered by C_7P_0, at a radial location that expectedly coincides with the strongest axial velocity fluctuations caused by the first mode (Fig. 3.15a). All the other identified peaks are weaker and are actually all located at frequencies $nF_2 \pm kF_1$ or $nF_3 \pm kF_1$ (k, n integers), once more supporting the fact that the three aforedescribed DMD modes are responsible for the dynamics of the statoric boundary layer.

Figure 3.20 further shows the PSD of the fluctuations of axial velocity registered at mid-height in the cavity (Fig. 3.20a) and in the rotating disc boundary layer (Fig. 3.20b). Both show data in complete agreement with the conclusions drawn from the previous study of the three constituent DMD modes. At mid-height in the cavity, the signals are closely similar, independently of the radial location, and especially all share F_1, F_2 and F_3 as constituent frequencies and with the same magnitudes. This phenomenon is indeed coherent with the azimuthal organizations induced by the three DMD modes at $z^* = 0.5$

Figure 3.19 – Power Spectral Densities (PSD) of the fluctuations of axial velocity in the stationary disc boundary layer of **Case 3** registered by probes C_6P_0 to $C_{10}P_0$ (darkest to lightest shade, respectively).

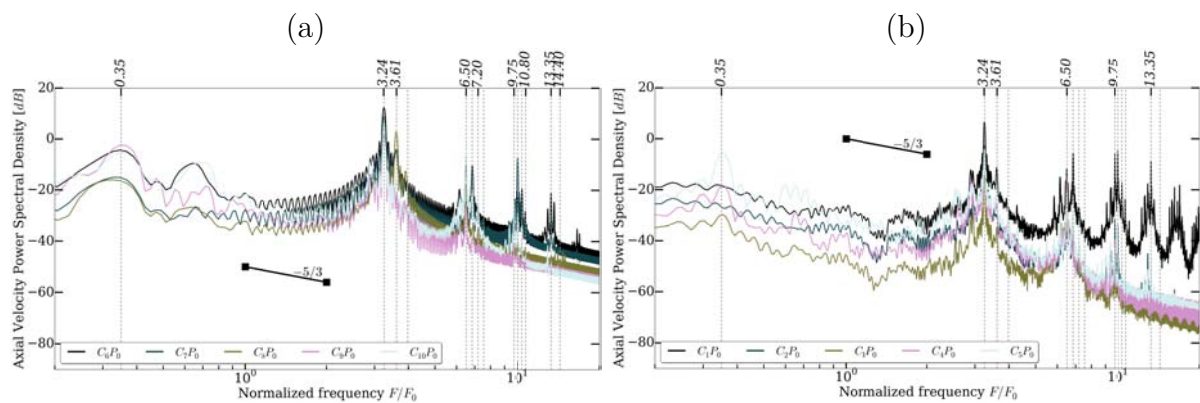**Figure 3.20** – Power Spectral Densities (PSD) of the fluctuations of axial velocity (a) at mid-height in the cavity registered by probes $C_{11}P_0$ to $C_{16}P_0$ and (b) in the rotating disc boundary layer registered by probes C_1P_0 to C_5P_0. In both cases, innermost probes have the darkest shade of grey, and outermost the lightest.

(see Fig. 3.16*a*, 3.16*b* & 3.16*c*) where they all display the same order of magnitude and span the whole radial extent of the cavity. It can also be verified on Fig. 3.20*a* that at high local Reynolds numbers $Re_\delta \gtrsim 170$, the magnitudes of the peaks located at $nF_3 \pm kF_1$ strongly decrease in accordance with the amplitude of the third mode at such Reynolds numbers (see Fig. 3.16*c*). In the bottom disc Ekman boundary layer on the other hand, the influence of the first mode (peak at F_1) is expectedly confined to the outermost radial locations (probes C_4P_0 and C_5P_0). The third mode and its harmonics are hardly visible anymore while the peak at F_2 and the linear combinations $nF_2 \pm kF_1$ dominate the signals at all radial locations due to the second mode inducing velocity fluctuations over the entire rotor boundary layer (see Fig. 3.16*e*). A final note about Fig. 3.19 and 3.20 concerns the overall trend of the curves. As a matter of fact, the magnitudes of the fifteen spectra are all overall decreasing as F/F_0 increases with a $-5/3$ slope. In other words, a turbulent Kolmogorov spectrum is present below large oscillatory structures. In the present case, the occurrence of distinct peaks indicates that LES predicts an oscillatory state flow in equilibrium with a fully turbulent flow, which supports the conclusions drawn earlier using for instance Fig. 3.5.

The analysis of the PSD at different radial extents as well as different heights in the cavity contributes in showing that the three constituent DMD modes primarily identified as pertinent to the dynamics of the statoric boundary layer are the only modes responsible for the dynamics of the whole cavity flow and thereby the spatial organization of the velocity fluctuations everywhere in the cavity.

At this point, it is interesting to focus on recent findings about the stability of rotor/stator cavity flows. On this matter, recent work by Gutierrez-Castillo & Lopez (2015) on flows in rapidly rotating split cylindrical cavities shows the importance of the corner between the rotating disc and the outer rotating shroud. The corner was indeed observed to drive the generation of inertial waves propagating within the cavity and sole responsible for the peaks detected by adequately located numerical probes. Among **Cases 1**, **2** & **3**, only the latter relies on a configuration similar to the one used by Gutierrez-Castillo & Lopez (2015) where the intersection between the rotating disc and the the inner rotating shaft is susceptible to play the role of inertial waves generator. On the other hand, recall that quantitatively linear inviscid theory on rotating flows (see e.g. Greenspan, 1988) shows that inertial waves can only be generated by perturbations whose pulsation is less than twice the angular speed of the flow driver. In the present cases the reference speed can be assimilated to the bottom disc rotation speed Ω. Consequently, as we non-dimensionalized the frequencies using $F_0 = \Omega/2\pi$ (see Fig. 3.19 & 3.20), the only perturbation susceptible to produce such an inertial wave is that found at $F_1 = 0.35F_0$, all other pulsation occurring at too high an angular frequency. To try visualizing these inertial waves, the same diagnostics as those used by Gutierrez-Castillo & Lopez (2015) have been applied to an instantaneous snapshot of **Case 3** taken for $\tilde{t} \gg 200$. Figure 3.21 presents the isocontours of the fluctuations of azimuthal vorticity in a meridional cut $(r^*, \theta = 0, z^*)$ from (*a*) the LES prediction and (*b*) the first DMD mode of frequency F_1. Contrary to the results presented by Gutierrez-Castillo & Lopez (2015), no wavelike structure emitted from the bottom-left corner can be observed in the cavity of **Case 3** in the full LES solution (Fig. 3.21*a*). On the other hand, the first DMD mode (Fig. 3.21*b*)

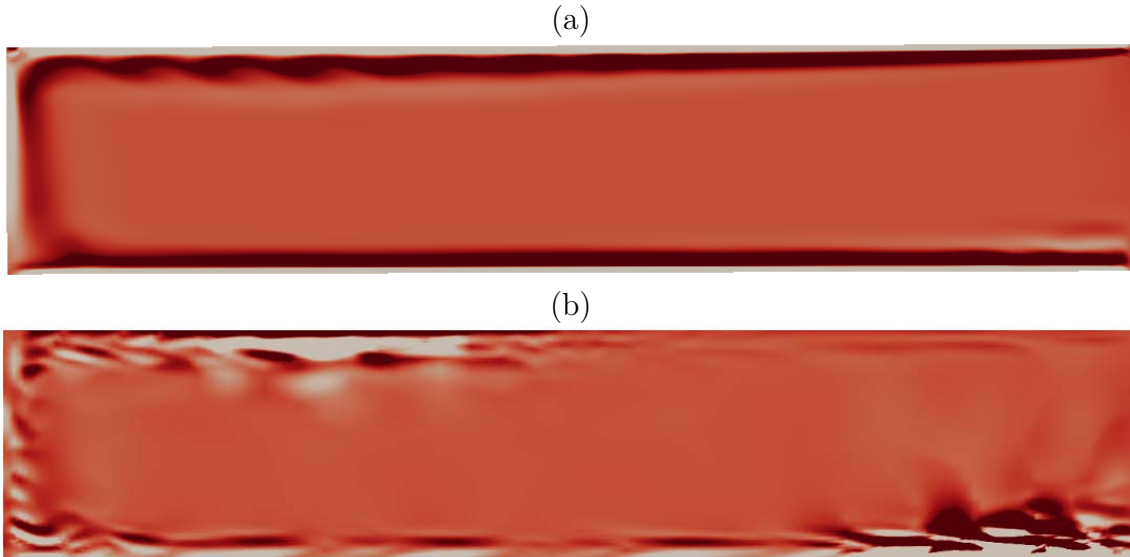***Relatively to the cuts below, the axis of rotation is located on the left.***

(a)

(b)

Figure 3.21 – Isocontours of the fluctuations of azimuthal vorticity η in a meridional cut $(r^*, \theta = 0, z^*)$ from (a) the LES solution $(\eta \in [-2.0, 2.0] \times 10^3)$ and (b) only the first constituent DMD mode pulsing at $2\pi F_1 \quad \Omega$ $(\eta \in [-30, 30])$.

presents clear vorticity oscillations in the vicinity of the shaft-rotor intersection but these waves are confined to the viscous boundary layers and do not seem to propagate within the homogeneous core of the cavity as the inertial waves observed by Gutierrez-Castillo & Lopez (2015).

Now that the possibility of inertial waves globally destabilizing the flow has been discarded, one must turn to other explanations for the sources of the observed DMD modes. To do so, the linear stability of the enclosed rotor/stator flows is investigated later in Sec. 3.7 to show the relation between the three-dimensional structures observed in the LES solutions and unstable global linear modes of the mean flow. Out of thoroughness however, the following section first presents the modal structure of the two cylindrical flows.

3.6.2 Spectral content of the cylindrical cavities

The last point of the present study is to extend the previous modal analysis to the other two cylindrical cavities (resp. **Case 2** & **1**, in this order) and prove that although both the aspect ratio and the mean curvature parameter have a marked effect on the behaviour of the flow, it remains driven by a small set of modes. As before, the two cavities are equipped with as many probes as in **Case 3** and they are organized as described on Fig. 3.18 to the exception of their radial locations which are given in Tab. 3.6.

As stated earlier, decreasing the mean curvature by removing the shaft from **Case 3**, has two major effects on the flow. First, it causes the disappearance of the annular-like near-shaft wavefront in the top Bödewadt boundary layer (see Fig. 3.8*b*) where the

	$C_{1,6,11}$	$C_{2,7,12}$	$C_{3,8,13}$	$C_{4,9,14}$	$C_{5,10,15}$
Case 1	0.194	0.388	0.582	0.776	0.971
Case 2	0.197	0.393	0.590	0.786	0.983

Table 3.6 – Dimensionless radial locations of the probes circles for **Case 1** and **Case 2**. Meaning of C_x detailed in section 3.6.1.c.

fluctuations rather organize as a spiral wavefront with 7 (resp. 16) arms for $Re_\delta \lesssim 150$ (resp. $Re_\delta \gtrsim 150$). This observation can also actually be extended to the organization of the homogeneous core of the cavity (see Fig. 3.11*b*). The second notable impact of the lack of shaft is the re-laminarization of the bottom rotating disc boundary layer that does not display any coherent azimuthal organization (section 3.5.2) in **Case 2**. Unlike the three constituent modes necessary to describe accurately the dynamics of **Case 3**, DMD shows that the fluctuations observed in the LES prediction (see Fig. 3.8*b* and 3.11*b*) are due to a single stationary mode ($F_p = 0.0$). This mode is expectedly closely similar to the LES patterns (see Fig. 3.22) both (*a*) in the top stationary disc boundary layer and (*b*) at mid-height in the cavity. The static nature of this mode also implies that the PSD at a given position (see Fig. 3.22*c*) does not show any peak similar to the ones relevant to **Case 3** (see section 3.6.1.c). The $-5/3$ slope relevant to the inertial range of a Kolmogorov spectrum in a fully turbulent flow (Pope, 2001) is also present, thus supporting a turbulent LES flow in the core and boundary layers that are not yet fully turbulent but rather in a transitional state.

Although the dependency of the flow dynamics on the mean curvature parameter seems limited, we will show now that increasing the aspect ratio of the cylindrical cavity from $G = 0.2$ to $G = 1.18$ leads to noteworthy changes in the way the flow is driven. The foremost difference stands in the minimum number of DMD modes required to adequately describe the patterns and the organization predicted by LES (see Tab. 3.7 for details, App. E.1, App. E.2 and App. E.3). This profusion of modes caused by the large aspect ratio of **Case 1** ($G = 1.18$), although impressive, is not unexpected. Gelfgat *et al.* (2001), Gelfgat (2015) and Lopez (2012), amongst others, indeed show how sensitive the flow in a tall rotating cylindrical cavity is to the Reynolds number. In particular, Gelfgat (2015) gives the critical Reynolds numbers for the triggering of modes $m = 0$ to $m = 25$ for cylindrical cavities with $0.1 \leq G \leq 1.0$ which by extension supports the fact that the co-existence of 11 constituent modes is not unreasonable. As previously, we present in Fig. 3.23 a comparison of the azimuthal organizations obtained from the LES prediction and the linear combination of the relevant DMD modes. Again the focus is first put on both the top Bödewadt boundary layer (Fig. 3.23*a*) and at mid-height in the cavity (Fig. 3.23*b*). The agreement between the two halves is very good in both cases. It also appears that the recombination slightly underestimates the amplitude of the axial velocity fluctuations in the stator boundary layer (Fig. 3.23*a*). However, as the reconstruction seems to match perfectly the mid-cavity pattern (Fig. 3.23*b*), both in amplitude and azimuthal organization, it appears that the DMD selection process discarded only one too many mode.

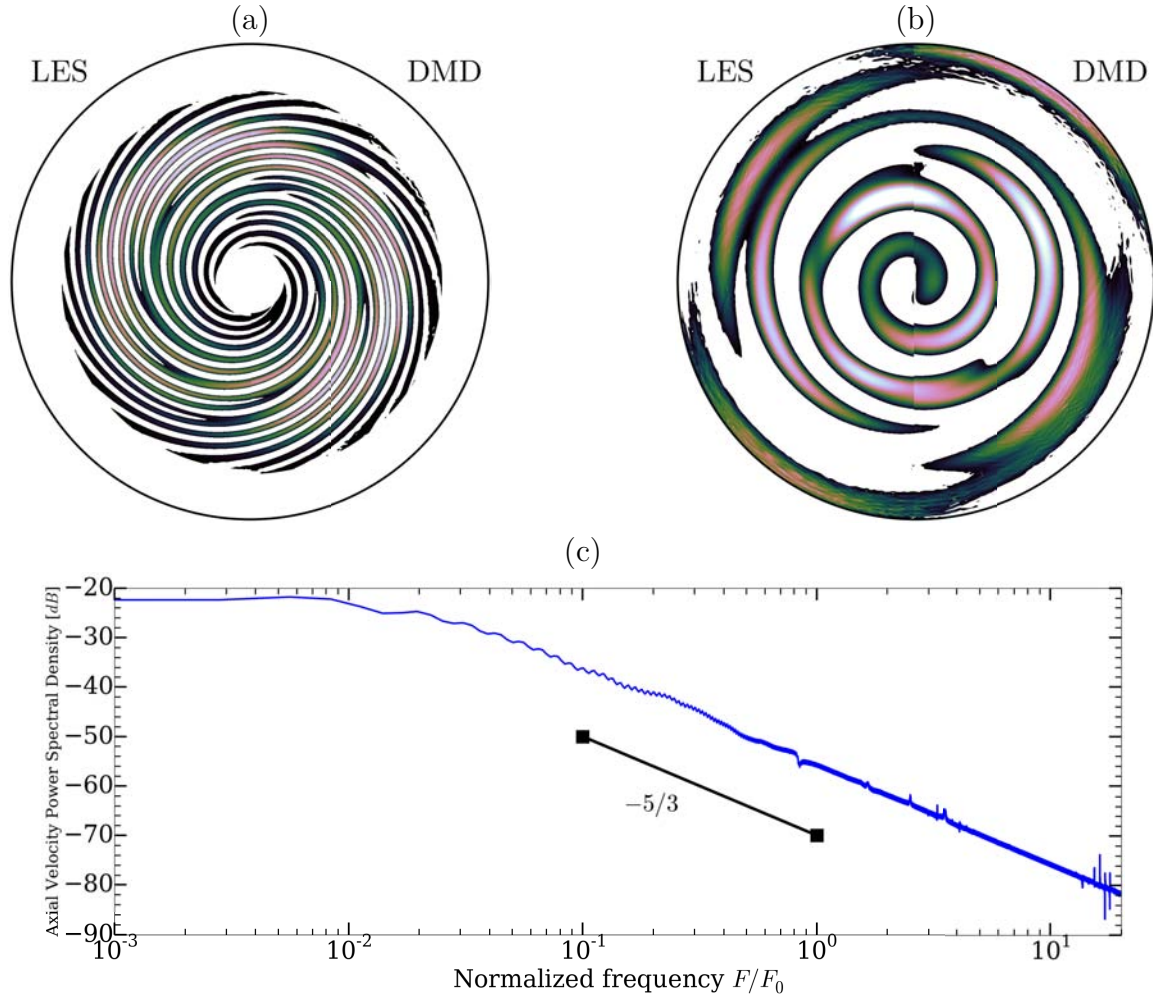***Relatively to the cuts below, the rotor rotation is counterclockwise***

Figure 3.22 − (*a-b*) Isocontours of $\tilde{u}_z \in [0, 0.05]$ for a composite made of the LES prediction for **Case 2** compared to the combination of the DMD mode at (*a*) $z^* = 1 - \delta/h$ (stator) and (*b*) $z^* = 0.5$ (mid-cavity). Values outside the colour range have been blanked out. (*c*) Power Spectral Densities (PSD) of the fluctuations of axial velocity in the stationary disc boundary layer of **Case 2** registered by probes $C_8 P_0$.

Mode No.	$F_{s,0}$	$F_{s,1}$	$F_{s,2}$	$F_{s,3}$	$F_{s,4}$	$F_{s,5}$	$F_{s,6}$	$F_{s,7}$	$F_{s,8}$	$F_{s,9}$	$F_{s,10}$
Frequency ($F_{s,i}/F_0$)	0.28	0.39	0.84	0.92	1.02	1.36	1.90	2.73	3.64	4.52	5.36
Harmonics							$2F_{s,3}$	$3F_{s,3}$	$4F_{s,3}$	$5F_{s,3}$	$6F_{s,3}$

Table 3.7 − Frequencies (of precession) of the eleven DMD constituent modes of **Case 1** non-dimensionalized by F_0. Fundamental/harmonics relation have been indicated.

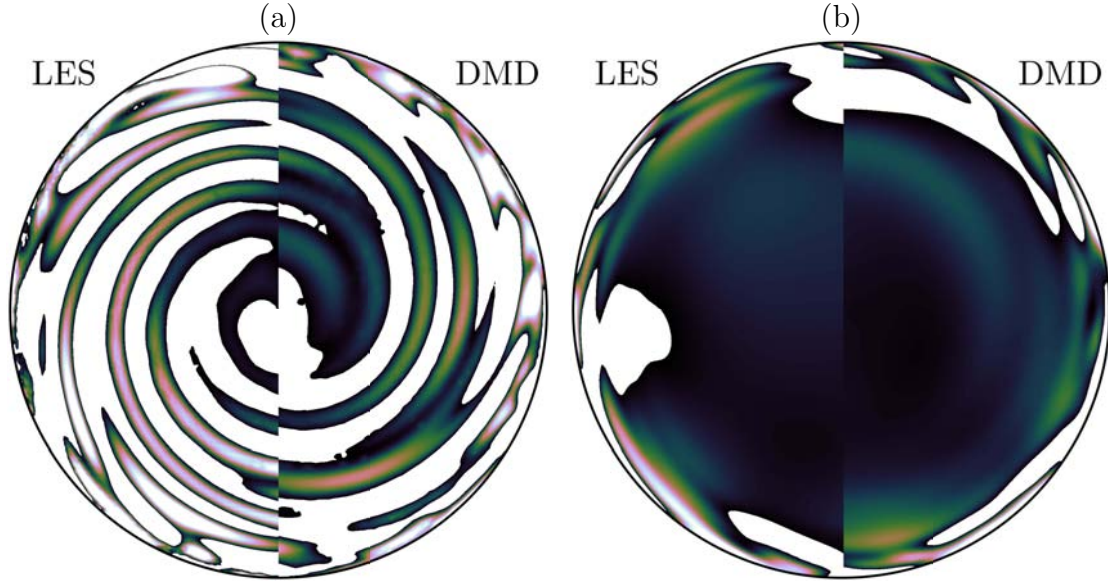***Relatively to the cuts below, the rotor rotation is counter-clockwise***

Figure 3.23 – Isocontours of $\tilde{u}_z \in [0, 0.05]$ for a composite made of the LES prediction for **Case 1** compared to the combination of the eleven DMD modes at (a) $z^* = 1 - \delta/h$ (stator) and (b) $z^* = 0.5$ (mid-cavity). Values outside the colour range have been blanked out.

For the sake of completeness we present in Fig. 3.24 the power spectral density of the axial velocity fluctuations as registered by probes $C_6 P_0$ to $C_{10} P_0$ in the top stationary disc boundary layer of **Case 1**. The conclusions are of the same kind as those drawn from Fig. 3.19 for **Case 3**. The first remark is that the frequencies at which the signals peak expectedly match the frequencies of the DMD modes. It can also be added that although DMD only yield up to the 6th harmonic of $F_{s,3}$ (see Tab. 3.7), the higher cut-off frequency of the Fourier transform allows to observe that near the edge of the disc, harmonics up to the 13th harmonic actually coexist with equal magnitudes (see Fig. 3.24, $C_{10} P_0$). Furthermore, it can be seen that the five signals have amplitudes of the same order of magnitude but that the highest frequencies are most strongly felt by the outermost probes, which is in agreement with the spatial organization of the corresponding modes (see App. E.1), comparably to **Case 3**.

To conclude, current predictions of high Reynolds number rotor/stator cavities evidence the potential establishment of highly oscillating large scale motions. These features seem to be strongly dependent on the cavity geometry as well as coupled to the dynamics of the different flow boundary layers and inviscid core. Although stability analyses of the individual flow layers present in such cavities are today mastered, in-cavity organization and coupling as well as selection mechanisms of the observed global features are still missing. In that respect and on the basis of LES as detailed here, numerical predictions can help qualifying potential scenarios or designs. However, as introduced earlier, the present work will now turn to linear stability analyses of the present enclosed flows with the intent to shed some light on the source of the structures observed by LES and their
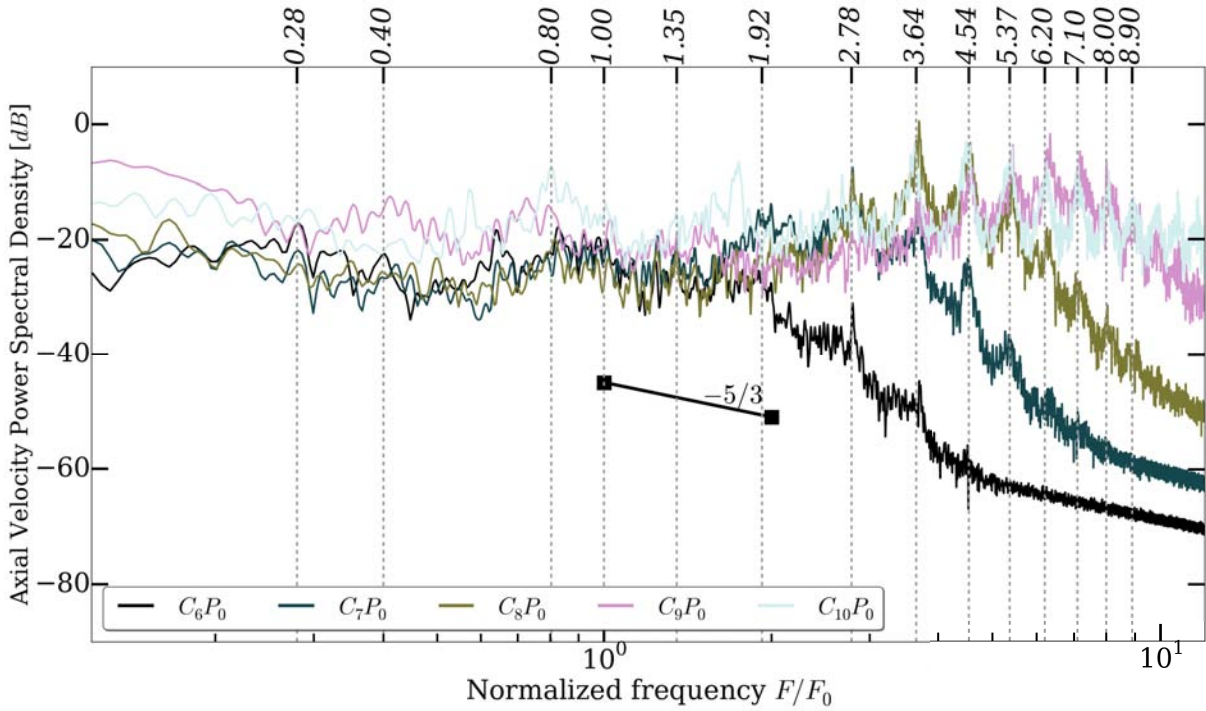
Figure 3.24 – Power Spectral Densities (PSD) of the fluctuations of axial velocity in the stationary disc boundary layer of **Case 1** registered by probes C_6P_0 to $C_{10}P_0$ (darkest to lightest shade, respectively).

frequency selection mechanism.

3.7 Stability analysis of the enclosed rotating flows

3.7.1 Motivation and approach

In all three cases investigated in the previous sections and numerous papers (Gauthier *et al.*, 1999; Serre *et al.*, 2001, 2004; Séverac *et al.*, 2007), the cavity macro-structures are observed to organize as three-dimensional spiral vortices or axisymmetric rolls similar to what is drawn on Fig. 2.8. On the other hand, Dynamic Modal Decomposition (DMD, Schmid (2010)) proved really effective to identify the dynamics of the flow as it indeed yields the modes responsible for the macro-structures marking the boundary layers and the homogeneous core and responsible for the unsteady pressure phenomena. It is of note at this point that, by definition, DMD is strictly equivalent to a global linear stability analysis (see Sec. 2.2.3 or the review by Theofilis (2011)) of linearised flow. For nonlinear flows on the other hand, the algorithm produces modes of a linear tangent approximation to the underlying flow. These two remarks naturally point to Linear Stability Analysis (LSA, see Sec. 2.2) as a potential tool for the prediction of the patterns appearing in a rotating flow. The sought instabilities would have a normal mode decomposition resembling the one given by Eq. (2.2.11) and presented in the previous chapter. We recall it

here for completeness:

$$[\tilde{u}, \tilde{v}, \tilde{w}, \tilde{p}] = [iu, v, w, p](z) \exp\left[i\left(\alpha r + m\theta - \omega t\right)\right], \qquad (3.7.1)$$

where $\tilde{u}$, $\tilde{v}$, $\tilde{w}$ and $\tilde{p}$ represent the fluctuations of the three velocity components and of pressure (see Eq. (2.2.1)). Also, $\alpha \in \mathbb{C}$ is the complex radial wavenumber, $m \in \mathbb{Z}$ the azimuthal wavenumber and $\omega \in \mathbb{C}$ the complex temporal frequency (refer to Sec. 2.2.2.c for more details). Inspired by the success of Juniper (2011) and Oberleithner (2011, 2012) who obtained the experimentally observed instability in a wake and a swirling jet (resp.) using mode reconstruction (resp. global and spatial), the following investigation aims at adapting such a procedure to rotating flows (the main steps are described in Sec. 2.2.3c, and shall be recalled when necessary).

First a concise presentation of the mean axisymmetric flows used as bases for the linear stability analyses in all three cases is proposed. Preliminary results obtained by temporal stability analyses are then presented. Remarking that a non-zero α_i is necessary to reconstruct properly the modes obtained by DMD, the discussion is then oriented towards the presence of global modes in the disc boundary layers and their relations with the unsteady phenomena present in the rotor/stator cavities.

3.7.2   Base flow

Any stability analysis, as discussed thoroughly in Sec. 2.2, is built upon a base flow. For instance, the theoretical cases of flows over- (Sec. 2.2.2.a) or between- (Sec. 2.2.2.b) infinite discs use a mean flow that is derived analytically from a set of simplified Navier-Stokes equations. Unfortunately, these auto-similar models do not hold anymore for enclosed rotor/stator cavity flows subject to confinement (refer to Fig. 3.4 for instance) so the base flow has to be derived by other means. In the present investigation, and in all following sections, the base flow is extracted from the temporally and azimuthally averaged LES predictions studied in Sec. 3.4.2 and made adequately dimensionless using the factors given in Sec. 2.2.2.b. Figure 3.25 shows an example at mid-radius of the profiles of the radial, azimuthal and axial velocity in **Case 1**, **2** and **3** used with AVLP along with the distribution of collocation points used for each configuration. In all three cases, the axial extent has been split into three sub-domains (Sec. 2.2.4.c) with characteristics summarized in Tab. 3.8. Note that in each case the number of Gauss-Lobatto points has been increased iteratively until the eigenvalues converge, i.e. their values do not depend on the discretization anymore. All other informations necessary to reproduce the perturbation analyses are given in Tab. 3.1.

To conclude this introductory paragraph, please note that for all computations only the molecular viscosity has been used to compute the local Reynolds numbers.

3.7.3   Temporal stability

To assess the ability of AVLP to deal with real enclosed rotor/stator flows, this first section discusses the results obtained from temporal stability analyses of the three flows.
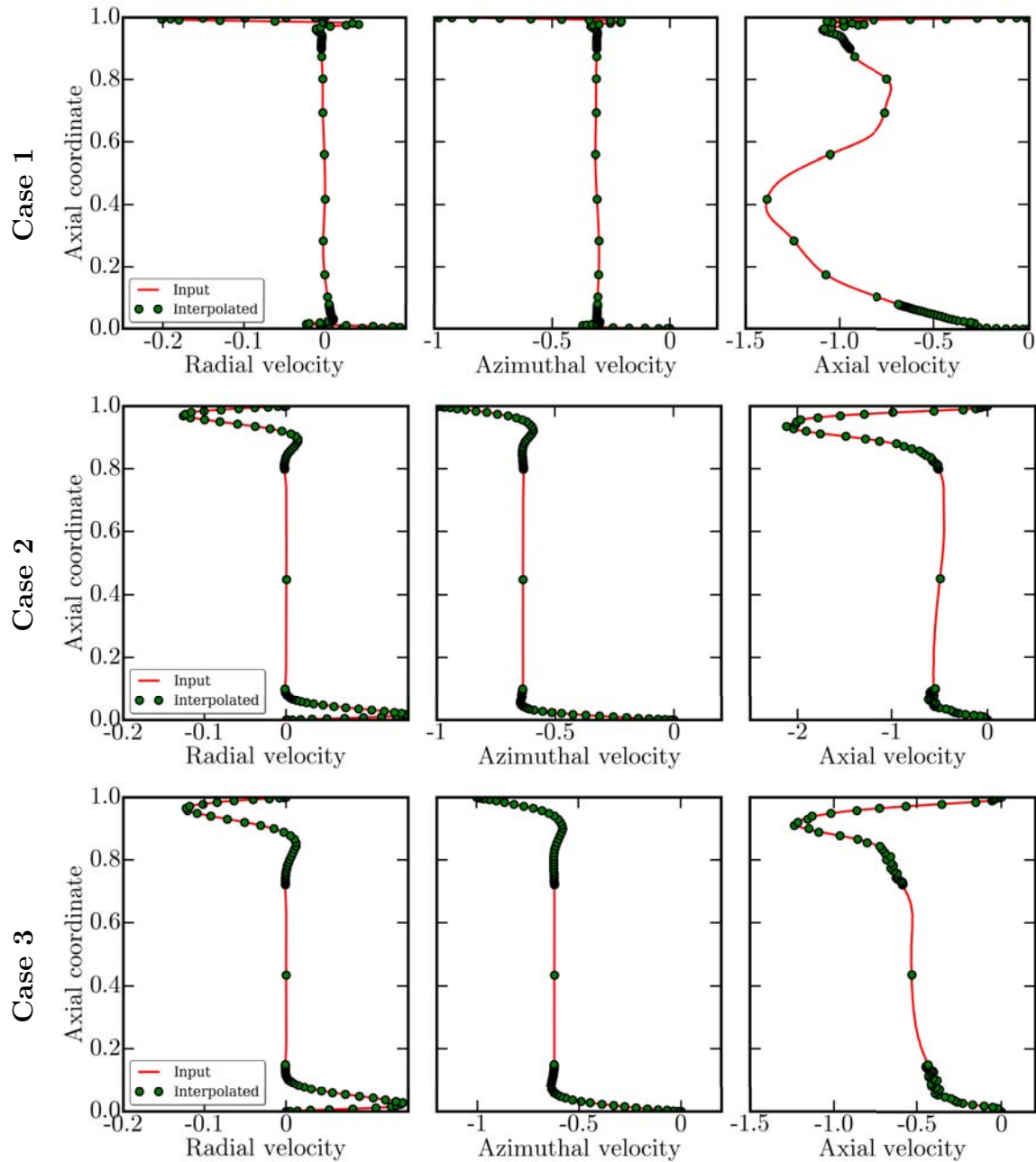
Figure 3.25 – Axial profiles of the three velocity components (radial, azimuthal and axial resp. from left to right) for **Case 1**, **Case 2** and **Case 3** (resp. top to bottom). Extraction made at $r^* = 0.5$. The distribution of collocation points used in AVLP is indicated by the markers.

Note that throughout this section, the region of *expression* of a mode refers to the region where the corresponding eigenvectors reach their maximum magnitude.

Throughout this investigation, the (α_r, m) plane is swept and for each pair of wavenumbers the dispersion relation (see Sec. 2.2.2.b) is solved for all possible values of $\omega \in \mathbb{C}$. In **Case 1**, the temporal stability analysis reveals two dominant modes exist-

	Case 1	**Case 2**	**Case 3**
N_{dom}	3	3	3
$\mathbb{I}_0$	$[0, 0.08[$	$[0, 0.1[$	$[0, 0.15[$
$\mathbb{I}_1$	$[0.08, 0.9[$	$[0.1, 0.8[$	$[0.15, 0.7228[$
$\mathbb{I}_2$	$[0.9, 1.0]$	$[0.8, 1.0]$	$[0.7228, 1.0]$
$N_{\mathrm{GL},0}$	40	40	40
$N_{\mathrm{GL},1}$	10	3	3
$N_{\mathrm{GL},2}$	40	40	40

Table 3.8 – Summary of the characteristics of the multiple sub-domains used in AVLP for **Case 1**, **Case 2** and **Case 3**.

ing in distinct Reynolds number regions:

- a dominant unstable mode which expresses itself in the stator boundary layer for all values of the local Reynolds number,

- a second less unstable mode, expressing itself in the rotating disc boundary layer and present only for large values of the local Reynolds number.

On the other hand, for **Cases 2** & **3**, two dominant unstable modes appear at all Reynolds numbers. Similarly to **Case 1** however, one mode expresses itself most in the rotor boundary layer whereas the eigenvectors of the second reach their greatest magnitude in the stator boundary layer. It is also remarkable that in all cases, the temporal branch with the greatest maximum amplification rate is related to the stator eigenvector, i.e. qualitatively consistent with the LES displaying a stronger unstable behaviour of the stator boundary layers. Finally, note that the branch expressing itself most in the stator (resp. rotor) boundary layer will be referred to as 'stator branch' (resp. 'rotor branch') thereafter.

In **Case 1**, at mid-radius, the stator branch (see Fig. 3.26a-c) reaches a maximum of amplification $\omega Re = 1.4346i - 2.22$ for $(\alpha_r/\sqrt{Re_h}, m) = (0.119, -2)$ as shown on Fig. 3.26a. Qualitatively, these results agree with the LES predictions. At mid-radius, one of the three strongest peaks (see Fig. 3.24) detected by the pointwise probes indeed corresponds to a mode marking the flow in the stator boundary layer as a two-armed co-winding spiral, i.e. $m = -2$. What is more, the two-armed spiral mark given by DMD (see App. E.1, Fig. g) has a radial wavenumber $k_r\delta \simeq 0.11975$ in the stator layer which is found to match well the value of α_r given by LSA. Finally, Fig. 3.26b shows that, also in agreement with the results yield by DMD (App. E), LSA indicates that most of the activity is shared between $m = -2, -3, -4$ and -5 modes at radial stations far enough from the $r = 0$ singularity and from the shroud.

The results obtained for **Case 2** are illustrated on Fig. 3.27. On this figure, a map of amplification rate at mid-radius $Re = 2.94$ (Fig. 3.27a), the evolution of the maximum of amplification with the Reynolds number (Fig. 3.27b) and an example of eigenvector for
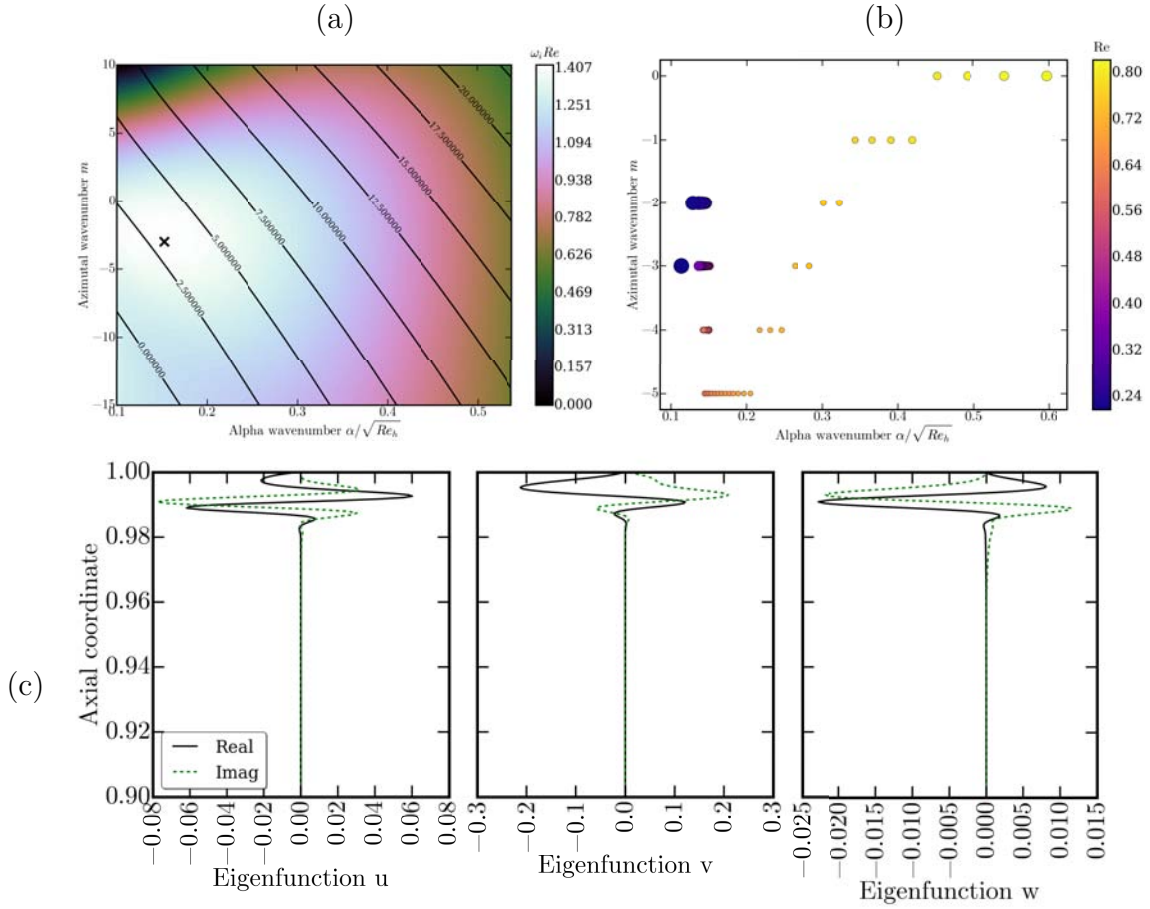
(a) (b)

(c)

Figure 3.26 – Results of the temporal stability analysis ($\alpha_i = 0$) in **Case 1**, 'stator branch'. (a) Amplification rate $\omega_i Re$ map overlaid with frequency $-\omega_r Re$ contours at $Re = 0.495$. (b) Progression of the most amplified point with the local Reynolds number Re (marker colour), characterized by the value of the amplification rate (marker size). (c) Example of eigenvector taken at the maximum of amplification.

this branch (Fig. 3.27c) are shown. The maximum of amplification $\omega Re = 1.501i - 13.67$ is reached for $(\alpha_r/\sqrt{Re_h}, m) = (0.272, 16)$ (see Fig. 3.27a). Similarly to the previous case, the temporal analysis, albeit local, provides interesting information about the dynamics of the rotor/stator flow and agrees with the characteristics of the statistically converged LES predictions. At mid-radius, the fluctuations of velocity in the stator boundary layer (see Fig. 3.22) are indeed organized as a counter-winding 16-armed spiral. Furthermore, extracting only that spiral mode by DMD, it is found that its radial wavenumber $k_r\delta \simeq 0.264$ agrees with the value obtained by LSA, i.e. $\alpha_r/\sqrt{Re_h} = 0.272$. However the frequency yield by LSA ($-\omega_r Re = 13.67$) at the present location is strongly positive whereas LES predicts the spiral structure to be steady with a temporal frequency of zero. The radial evolution of the structure as predicted by LES is also fairly well matched by LSA results. Figure 3.27b indeed shows a growth of the local radial wavenumber over the disc while the azimuthal wavenumber grows from $m = +7$ close to the axis to reach $m \simeq +18$ around $r \simeq 0.139$ - similar to the $r \simeq 0.150$ obtained by DMD. Note finally
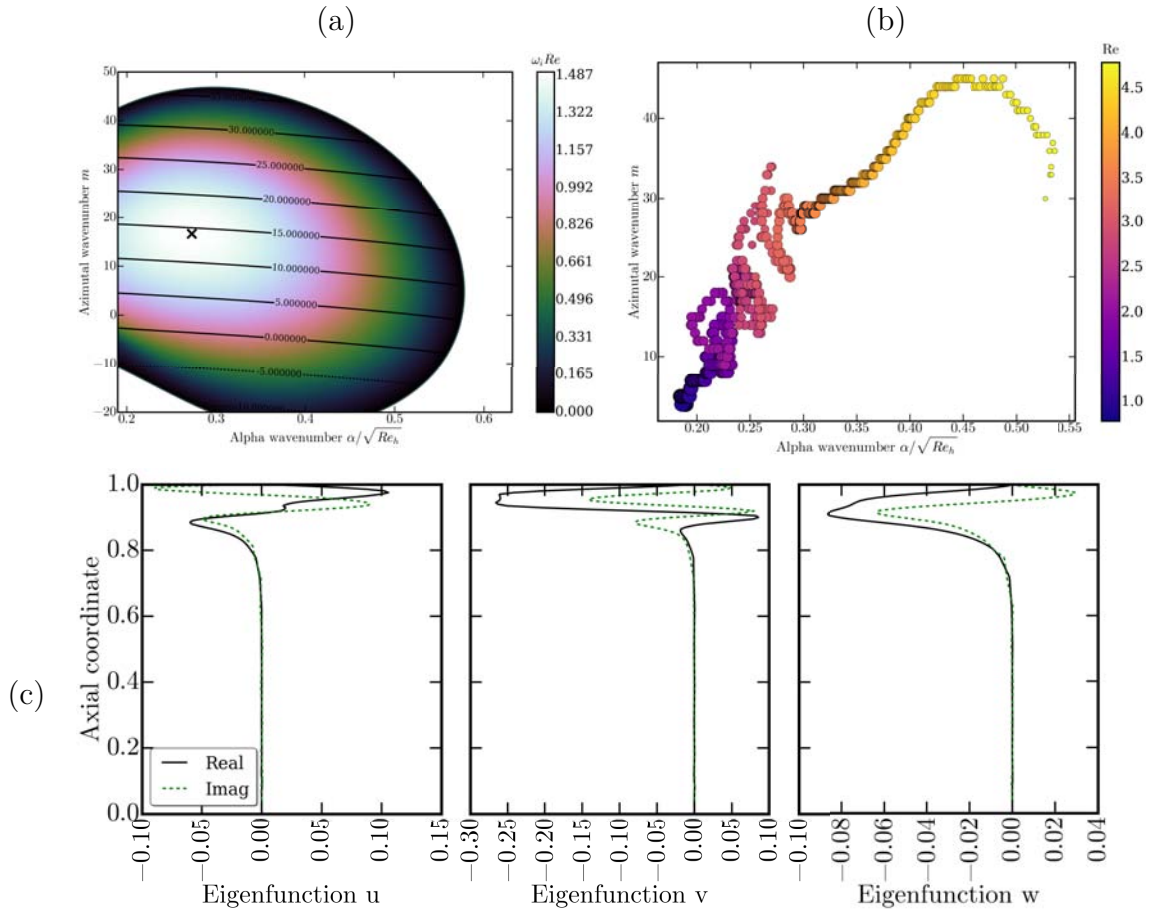
Figure 3.27 – Results of the temporal stability analysis ($\alpha_i = 0$) in **Case 2**, 'stator branch'. (*a*) Amplification rate $\omega_i Re$ map overlaid with frequency $-\omega_r Re$ contours at $Re = 2.94$. (*b*) Progression of the most amplified point with the local Reynolds number (marker colour), characterized by the value of the amplification rate (marker size). (*c*) Example of eigenvector taken at the maximum of amplification.

that the size of the region close to the discs where the eigenvector is non-zero varies in agreement with the corresponding value of $\sqrt{Re_h}$. The disc layer in **Case 1** (Fig. 3.26*c*) is indeed approximately 10 times thinner than the disc layer in **Case 2** (Fig. 3.27*c*), corresponding to the value of the ratio $\sqrt{Re_{h,1}/Re_{h,2}}$.

Regarding **Case 3**, it has been shown previously that the presence of the inner shaft promotes transition and triggers the appearance of spiral and axisymmetric structures in the rotating disc boundary layer. According to the results obtained by DMD, the dominant mode (in terms of magnitude) marks the stator boundary layer as a counter-winding spiral with 29 arms ($m = +29$) whereas the rotor layer dynamics is mostly driven by a co-winding spiral with 12 arms ($m = -12$). Both modes are present over the entire radial range of the discs, but recall that the stator structure is strongest for radial locations $r \lesssim 0.205$ m, whereas the rotor structure magnitude is greatest at the edge of the disc, for $r \gtrsim 0.16$ m. Figures 3.28 and 3.29 present respectively the stator (Fig. 3.28*c*) and rotor (Fig. 3.29*c*) branches obtained by LSA of **Case 3**. Contrary to the results yield
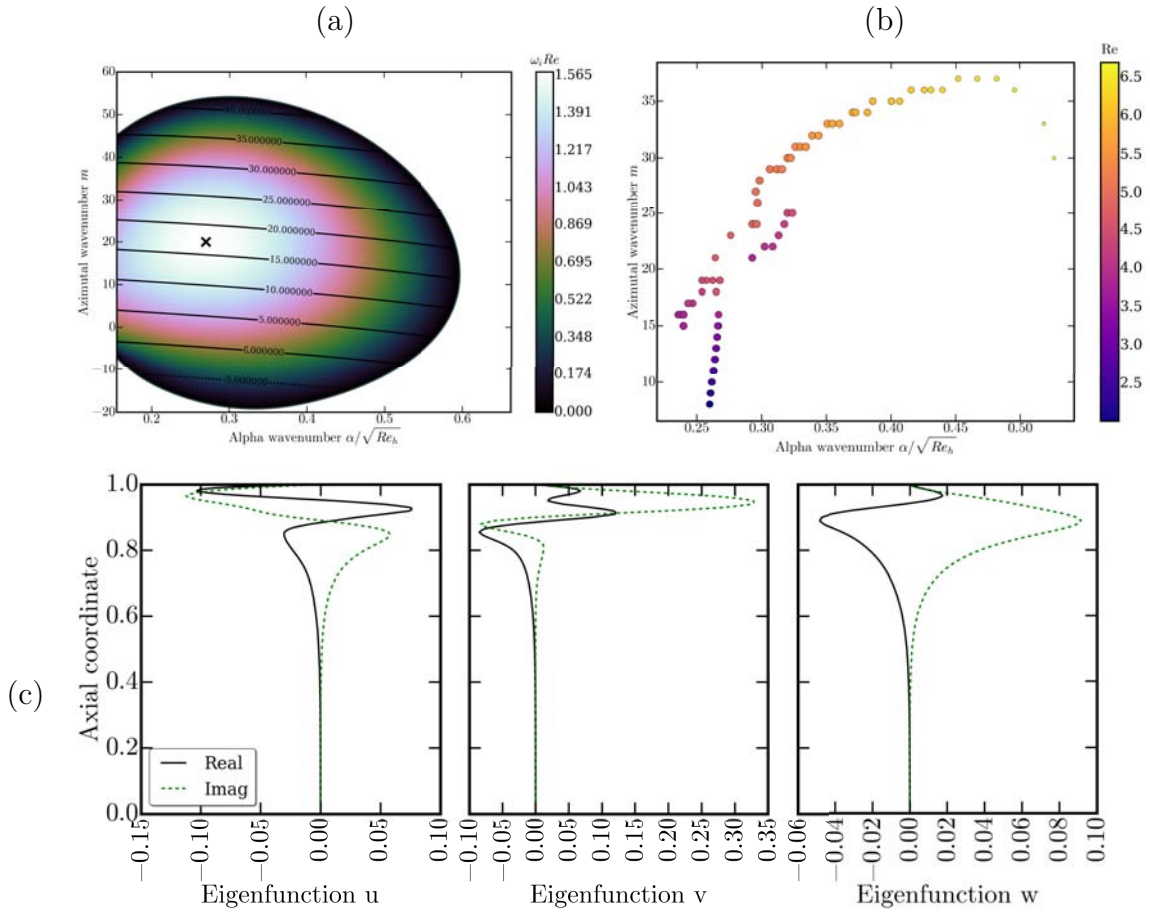
Figure 3.28 – Results of the temporal stability analysis ($\alpha_i = 0$) in **Case 3**, 'stator branch'. (a) Amplification rate $\omega_i Re$ map overlaid with frequency $-\omega_r Re$ contours at $Re = 4.48$. (b) Progression of the most amplified point with the local Reynolds number (marker colour), characterized by the value of the amplification rate (marker size). (c) Example of eigenvector taken at the maximum of amplification.

by LSA of **Case 1** and **Case 2**, the coordinates in parameters space $(\alpha_r/\sqrt{Re_h}, m)$ of the maxima of temporal amplification do not match the aforementioned DMD results. On one hand, the stator branch given by the LSA has its maximum $\omega_i Re = 1.58$ located at $(\alpha_r/\sqrt{Re_h}, m) = (0.269, 20)$ for a temporal frequency $-\omega_r Re = 17.15$. On the other hand, the rotor branch has its maximum $\omega_i Re = 1.19$ located at $(\alpha_r/\sqrt{Re_h}, m) = (0.226, -3)$ with a temporal frequency $-\omega_r Re = 7.52$. Consequently, for both branches although the local radial wavenumbers agree reasonably well with the values obtained by DMD (resp. $k_r\delta = 0.31$ and $k_r\delta = 0.26$), the azimuthal wavenumbers and the temporal frequencies are not found to correspond to the ones of the DMD modes. The radial evolutions of the maxima for both branches are also quite different from what is observed in the LES results. The computation indeed shows that the stator layer is dominated by the 29-armed spiral while LSA yields a constant growth of the azimuthal and radial wavenumbers over the disc. The rotor layer is however dominated by modes with $m = -5, -6$ at low radius, which is reasonably well reproduced by LSA and a mode at $m = -12$ at high radius that does not appear in the present linear results.
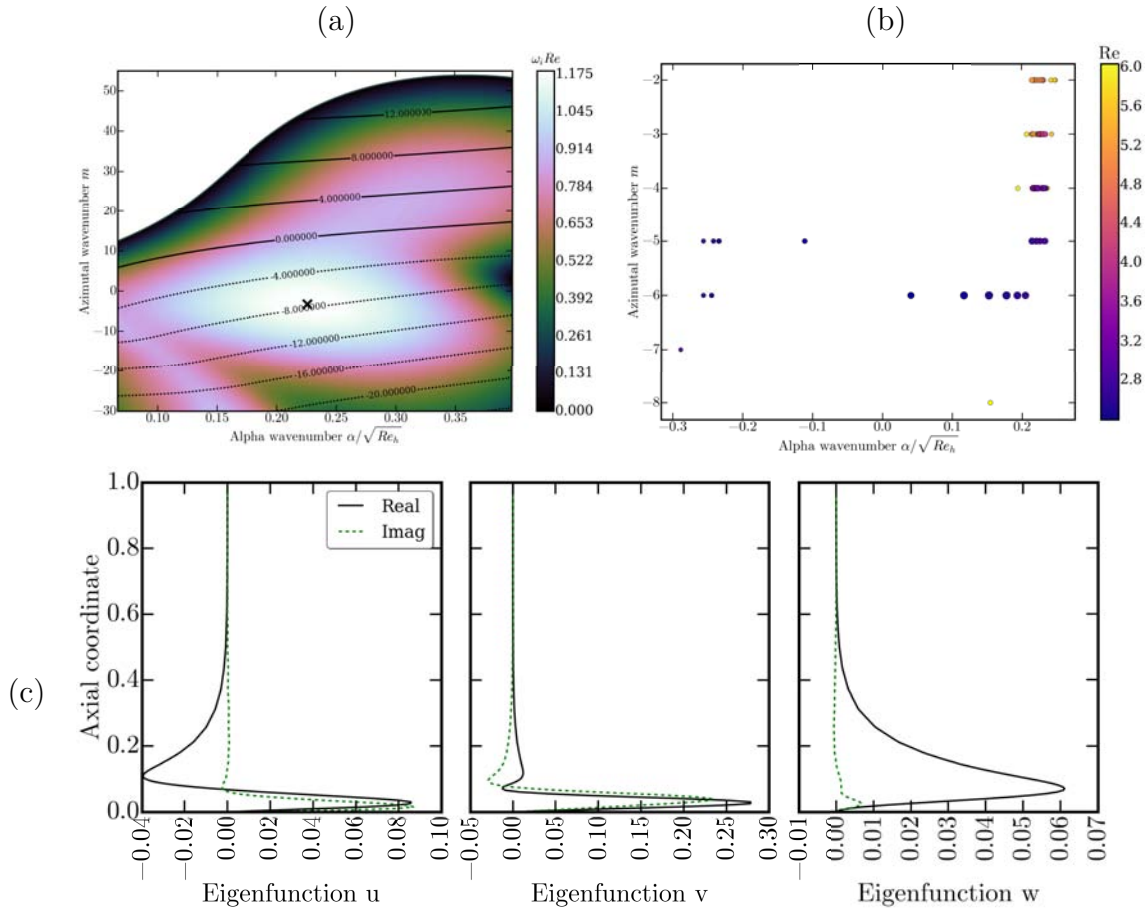
(a)   (b)

(c)

Figure 3.29 – Results of the temporal stability analysis ($\alpha_i = 0$) in **Case 3**, 'rotor branch'. (*a*) Amplification rate $\omega_i Re$ map overlaid with frequency $-\omega_r Re$ contours at $Re = 4.48$. (*b*) Progression of the most amplified point with the local Reynolds number (marker colour), characterized by the value of the amplification rate (marker size). (*c*) Example of eigenvector taken at the maximum of amplification.

The local temporal analyses of the three flows of interest in the present chapter (Sec. 3.2) therefore appear to yield interesting information about the structures observed in the LES solutions. However, this kind of analysis is not adequate for the reconstruction of the spatial organization of a mode due to a major shortcoming illustrated on Fig. 3.30. In this figure, a two dimensional $(r, \theta = 0, z)$-cut of 29-armed spiral DMD mode is compared with the same view of the LSA stator branch of **Case 3** (see Fig. 3.28) reconstructed by selecting at every radial location the eigenvector and the (α_r, m) pair corresponding to the greatest temporal amplification rate. Although the overall wavenumber of the structure seems well approximated by the technique, it is clear that letting $\alpha_i = 0$ at all radii makes it impossible to capture correctly the radial organization of the structure.

3.7.4   Absolute instability of a rotor/stator flow

In the previous paragraph, we concluded that a simple temporal stability analysis is not suitable to predict the instability of the studied rotating flows. To do so, it indeed
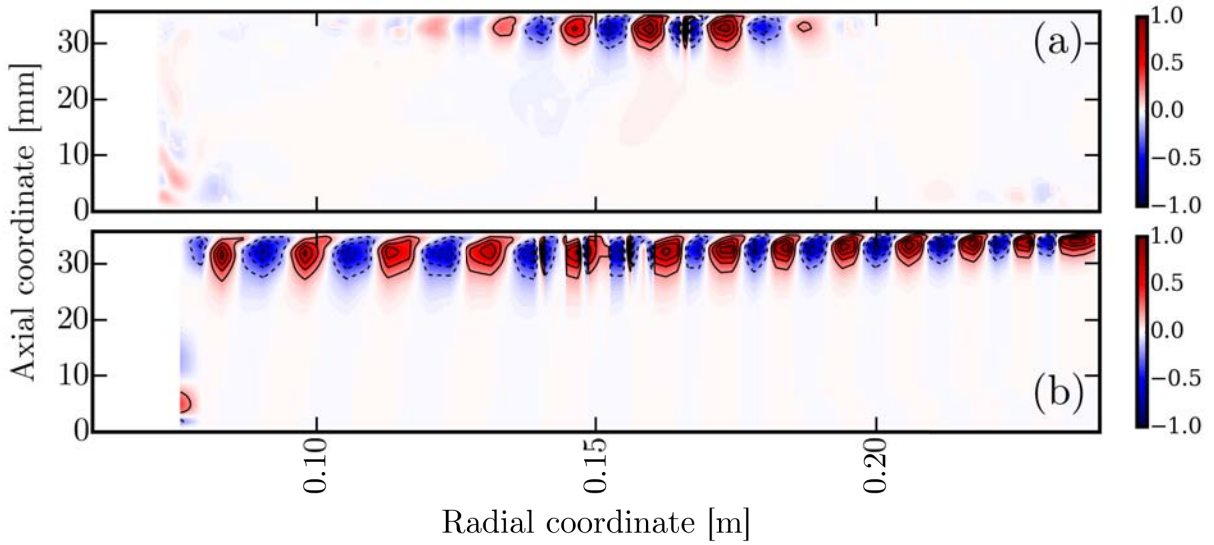
Figure 3.30 – Fluctuations of axial velocity w, normalized by their ∞-norm, in **Case 3**. (*a*) Strongest DMD mode in the stator boundary layer organizing as a 29-armed spiral confined in $r \in [0.110, 0.2]$ (see Sec. 3.6.1.a). (*b*) LSA stator mode reconstructed by selecting at each location the eigenvector and (α_r, m) pair corresponding to the greatest temporal amplification rate (see Fig. 3.28).

appears mandatory that the spatial amplification α_i of the selected linear modes evolves with the radial location. In a comprehensive paper about the stability of the Von Kármán (1921) boundary layer, Healey (2007) shows that the presence of an outer wall promotes the absolute instability of an otherwise convectively unstable rotating flow. Following these results, we use AVLP with a fixed azimuthal wavenumber m to track the saddle points in the (α_r, α_i) plane at all radial locations (which yields the absolute ω of a mode, see Sec. 2.2.3) and assess whether the associated eigenvectors are good candidates to reconstruct the corresponding DMD mode.

We focus the following discussion on the configuration that has the geometrical characteristics closest to that of an industrial turbine rotor/stator cavity, i.e. **Case 3**. In that case, recall that both disc boundary layers are unstable, although the rotating disc boundary layer of **Case 3** is, by nature, the least prone to instability and unsteady patterns develop therein only because of the presence of the inner shaft. Previous LSA results agree well with this remark as they show that the number of temporally amplified rotor branches is markedly less than the number of temporally amplified stator branches. We therefore detail first the reconstruction of the dominant rotor mode, the one that organizes the fluctuations as a co-winding 12-armed spiral with a frequency of $0.35F_0$. We then move on to the dominant stator mode that takes the form of a counter-winding 29-armed spiral with a frequency of $3.6F_0$.

Global reconstruction of the rotor branch in Case 3

Throughout the present paragraph, note that we fix the azimuthal wavenumber $m = +12$. Thanks to the symmetry inherent to the stability analysis (Eq. (2.2.30)), seeking

$m = +12$ is equivalent to seeking the mode $m = -12$ present in LES, only with the opposite temporal frequency.

First, a temporal stability analysis is performed at an arbitrarily chosen radial location in the flow where the maximum temporal growth rate of the rotor branch is identified. Under the parallel flow assumption, this growth rate indeed represents the upper bound for the absolute growth rate at this location (Chomaz *et al.*, 1991*a*). Consequently, if an absolute instability is to appear in the flow, it has to be greater than zero. The results of the temporal analysis for the rotor branch yield by LSA of **Case 3** are displayed on Fig. 3.31. In this figure, the temporal amplification rate $\omega_i Re$ and temporal frequency $-\omega_r Re$ are plotted as a function of the radial wavenumber $\alpha_r/\sqrt{Re_h}$, and the maximum $\omega Re = 0.85 + 0.94i$ is reached at $\alpha_r/\sqrt{Re_h} = 0.244$.
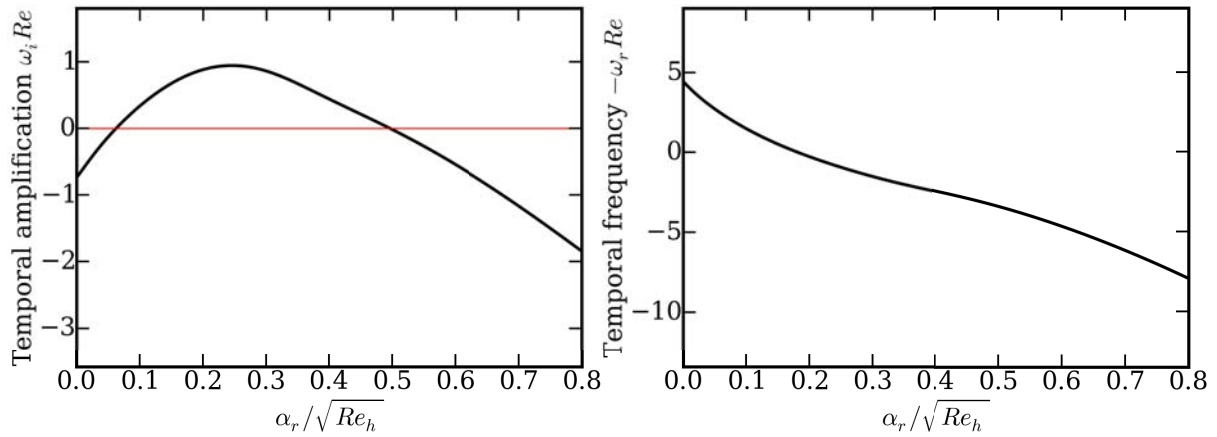

Figure 3.31 – Evolution of (left) the temporal amplification rate $\omega_i Re$ and (right) temporal frequency $-\omega_r Re$ with the radial wavenumber $\alpha_r/\sqrt{Re_h}$ at $m = 12$ for the rotor branch of **Case 3** at $Re = 4.48$. Zero amplification is marked by an horizontal line.

A spatio-temporal stability analysis is then performed by allowing α_i to be non-zero, and the absolute temporal growth rate is obtained by finding the saddle points of $\omega(\alpha)$, as shown on Fig. 3.32. In this case, only one saddle point can be identified at coordinates $(\alpha_r/\sqrt{Re_h}, \alpha_i/\sqrt{Re_h}) = (0.265, -0.155)$ where the absolute complex frequency is $\omega_0 Re = 1.135 - 0.1i$. Note the negative temporal amplification rate indicative of the convective nature of this instability at this radial location.

The saddle point is then followed downstream and upstream as the base flow changes. The values of ω_0 function of the radial coordinate are plotted in Fig. 3.33. In the present situation, there are three regions in which the branch is absolutely unstable (i.e. $\omega_{0,i} > 0$ at the saddle point), all confined close to the edge of the disc ($r \gtrsim 0.175$ m) and occupying no more than 10% of the radial extent of the cavity each. According to the procedure originally described in Chomaz *et al.* (1991*a*) and later used for instance by Juniper (2011) for the study of the global stability of confined planar wakes, we assume that the absolute complex frequency $\omega_0(r \in \mathbb{R})$ can be continued analytically into the complex r-plane, i.e. to become $\omega_0(r \in \mathbb{C})$. The complex frequency of the global mode ω_G is then found at the saddle point closest to the real axis. Here, the continued function in the complex r-plane and by extension the position of the aforementioned saddle point
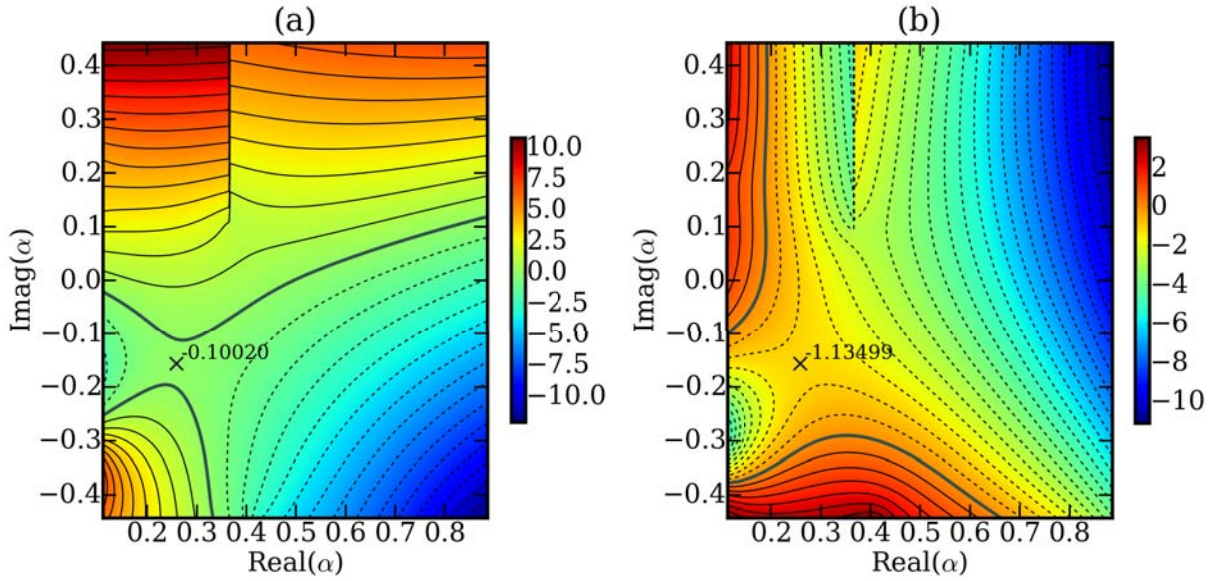
Figure 3.32 – Isocontours of (a) amplification rate $\omega_i Re$ and (b) temporal frequency $-\omega_r Re$ in the $(\alpha_r/\sqrt{Re_h}, \alpha_i/\sqrt{Re_h})$ plane for the rotor branch of **Case 3** at $Re = 4.48$. Zero-contours are represented by a thicker line.
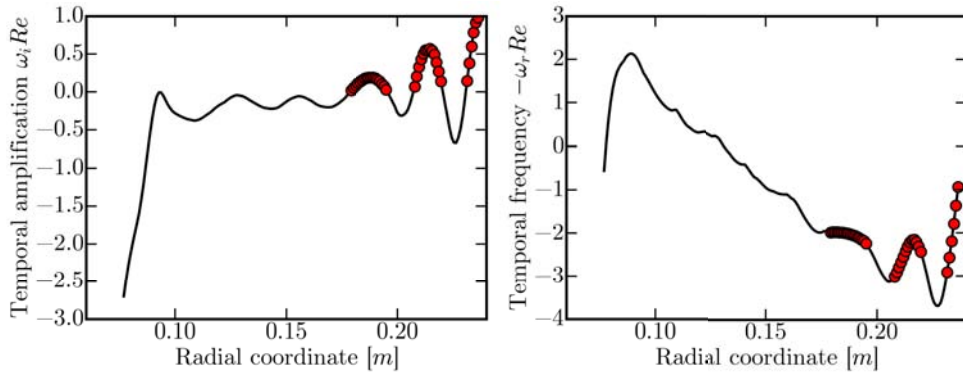

Figure 3.33 – Radial evolution of the absolute complex frequency $\omega_0 Re$ for the rotor branch of **Case 3**. Markers indicate all the datapoints with $\omega_{0,i} > 0$.

are estimated by selecting the region of $\omega_0(r)$ around the maximum of $\omega_{0,i}$ and then fitting these values by Padé polynomial that takes the form P/Q where P and Q are two polynomials of degrees n and $n-1$ respectively - see the thorough development by Cooper & Crighton (2000). Initially, the position of a saddle point is found for $n = 3$, and it is then followed as n increases until there is no significant change in its location in the $(\mathfrak{Re}(r), \mathfrak{Im}(r))$ plane. The position of $\omega_G Re = 2.16 + 0.54i$ after convergence of the fitting process (for $n = 9$) is displayed in Fig. 3.34 along with the isocontours of the imaginary and real part of the continued function $\omega_0(r \in \mathbb{C})$. The positive amplification rate $\omega_{G,i} Re$ suggests that an unstable global mode can indeed appear in the flow. Note finally the agreement between the frequency of the mode obtained by DMD $0.35F_0$ and the frequency obtained here $F_G = \mathfrak{Re}(\omega_G Re)/(2\pi) = 0.34F_0$.
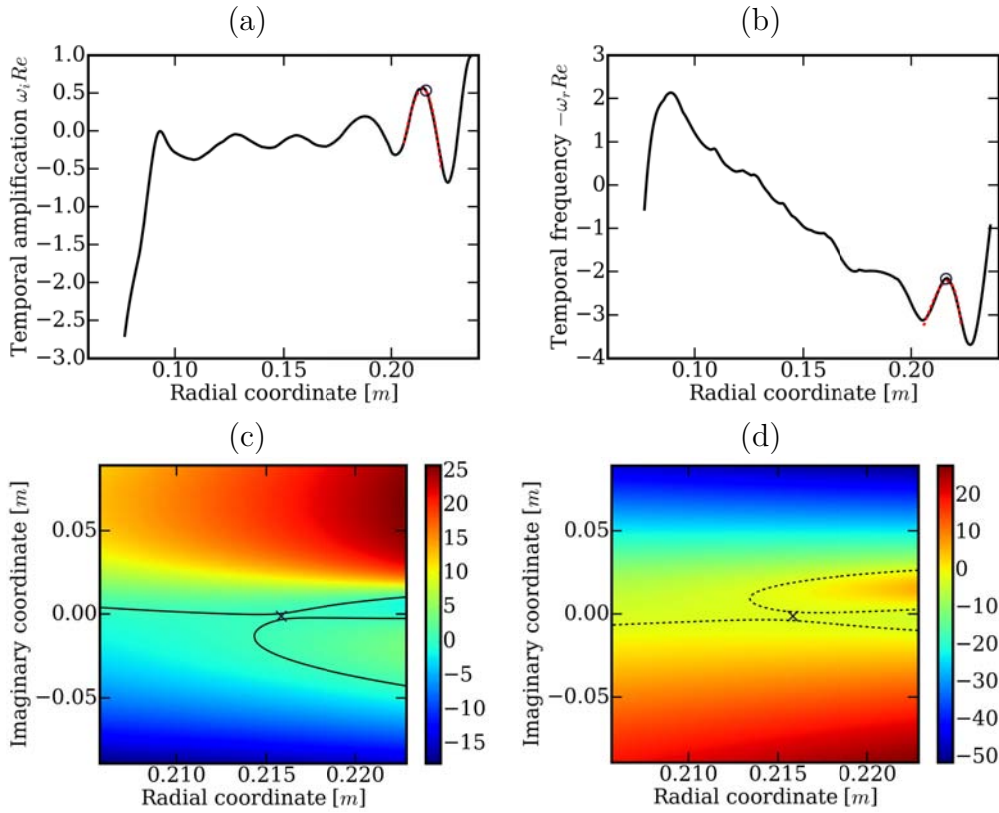
Figure 3.34 − (*a-b*) Radial evolution of the absolute complex frequency for the rotor branch of **Case 3** with the fitted Padé polynomial in the region of interest (dashed line) and the position of ω_G (marker). (*c-d*) Isocontours of (*c*) absolute amplification rate $\omega_{0,i}Re$ and (*d*) absolute temporal frequency $-\omega_{0,r}Re$ for the continued function $\omega_0(r)$ in the complex *r*-plane for the rotor branch of **Case 3** with the position of ω_G (marker) and the corresponding isolines.

The two-dimensional global mode shape can then be computed by seeking the response of the flow to a perturbation with complex frequency ω_G so that the integral Eq. (2.2.35) can be evaluated. To do so the third resolution method of AVLP, *tracking*, is used (refer to Sec. 2.2.4.d). Starting from the known value of α at the radial location r_G of ω_G, the evolution of α at fixed $\omega = \omega_G$ is followed as r varies slowly upstream and downstream of r_G. At each radial station, the eigenvector is also computed to consistently gather the local eigenfunctions contributing to the global solution. For this step, eigenvectors are normalized using their 2-norm (see Sec. 2.2.3*b*) and the phase angle is equalized at an arbitrary axial location (Sec. 2.2.3*b*). The resulting fluctuations of axial velocity are shown in Fig. 3.35 where they are compared to the fluctuations generated by the 12-armed DMD mode (Fig. 3.16*d*). As clearly seen, the AVLP computations agree well with the results obtained by DMD. The axial wavelength and the axial amplitude distribution are well estimated, as well as the radial amplification, with a maximum of amplitude at $r \simeq 0.24$ m and a decaying region upstream. Note however that the integration of the local stability analyses yield a slightly higher spatial growth rate that causes a slight shift of the global mode upstream of its position obtained by DMD. Such behaviour is not
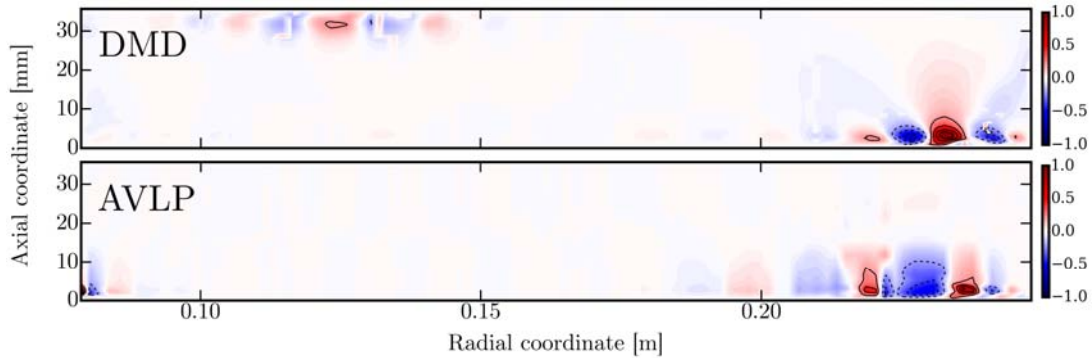
Figure 3.35 – Fluctuating axial velocity of the global rotor mode $m = 12$ of **Case 3**. Comparison between (*top*) the mode obtained by DMD and (*bottom*) the present results with AVLP. Eigenfunctions are clocked at an arbitrary phase angle. The contour lines represent $w/\max(w) = [-1.0, -0.8, -0.6, -0.4, -0.2, 0.2, 0.4, 0.6, 0.8, 1.0]$.

unexpected for the reconstruction of a global mode from local stability analyses and has already been observed for wake and jet flows (see e.g. Juniper, 2011).

Global reconstruction of the stator branch in Case 3

A similar strategy is applied on the stator branch of **Case 3** (see Fig. 3.28), with $m = +29$. After tracking the saddle point at all radial locations and upon convergence of the Padé fitting process, one obtains the results shown on Fig. 3.36. The plots reveal that $\omega_G Re = -24.19 + 1.37i$ which once again agrees well with the DMD frequency of $3.6F_0$ since $F_G = -\Re(\omega_G Re)/(2\pi) = 3.85F_0$.

The corresponding fluctuations of axial velocity are shown in Fig. 3.35 where they are compared to the fluctuations generated by the 29-armed DMD mode (Fig. 3.15c). Similarly to the previous reconstruction of the rotor branch, the AVLP computations agree well with the results obtained by DMD. The maximum amplitude of the fluctuations is correctly reached at $r \simeq 0.16$ m and they decay both up- and downstream of r_G as observed in the LES predictions. However, it is of note that similarly to the previous rotor branch, the spatial growth rate for $r < r_G$ and the spatial decay rate for $r > r_G$ are both slightly overestimated, causing the vortices to appear to shift to a region closer to the shaft.

These two successful reconstructions show that assimilating the modes driving the dynamics of an enclosed rotor/stator flow to unstable global linear modes of the mean flowfield is a very promising approach. Note also that when the azimuthal wavenumber is fixed at $m = 0$ to search for the mode responsible for the axisymmetric pattern obtained by DMD (Fig. 3.15b), no globally unstable mode can be found, i.e. for all radial locations, $\omega_{0,i} < 0$. This observation would tend to support the opinion of several workers (see e.g. Lopez *et al.*, 2009) that such axisymmetric waves are not self-sustained and could indeed maintain themselves in the boundary layer through some forcing. In the present situation, such forcing could be achieved due to numerical noise or nonlinear phenomena occurring
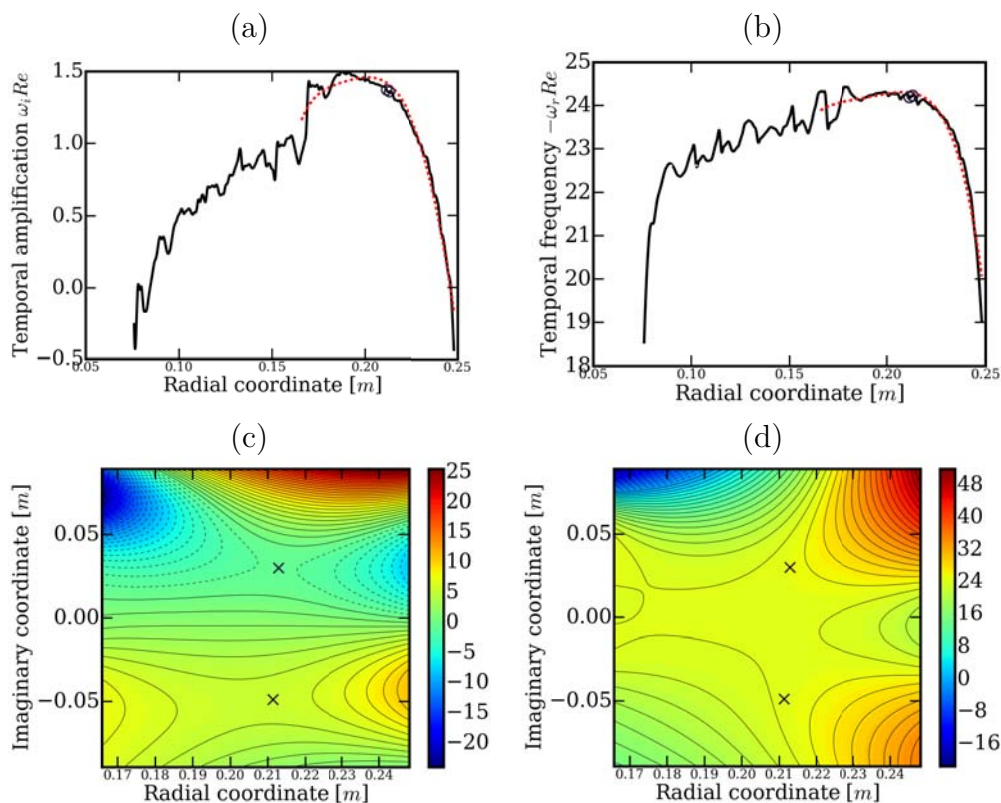
Figure 3.36 – (*a-b*) Radial evolution of the absolute complex frequency for the stator branch of **Case 3** with the fitted Padé polynomial in the region of interest (dashed line) and the position of ω_G (marker). (*c-d*) Isocontours of (*c*) absolute amplification rate $\omega_{0,i}Re$ and (*d*) absolute temporal frequency $-\omega_{0,r}Re$ for the continued function $\omega_0(r)$ in the complex r-plane for the rotor branch of **Case 3** with the position of ω_G (marker) and the corresponding isolines.
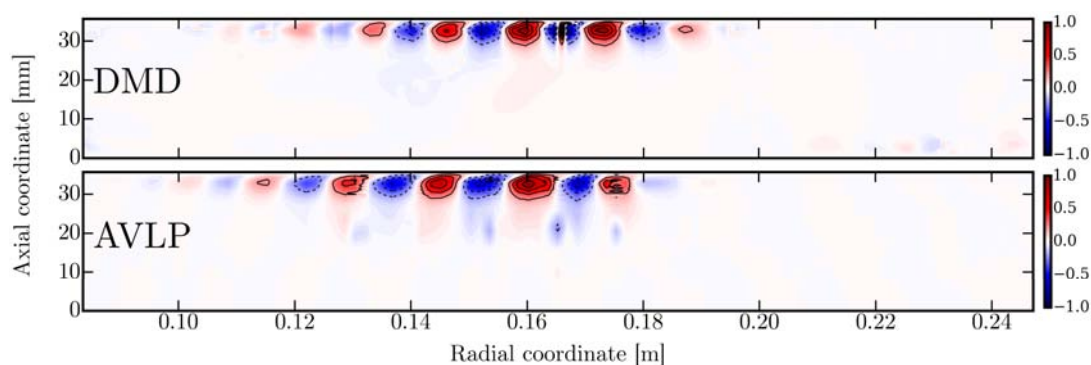
Figure 3.37 – Fluctuating axial velocity of the global stator mode $m = 29$ of **Case 3**. Comparison between (*top*) the mode obtained by DMD and (*bottom*) the present results with AVLP. Eigenfunctions are clocked at an arbitrary phase angle. The contour lines represent $w/\max(w) = [-1.0, -0.8, -0.6, -0.4, -0.2, 0.2, 0.4, 0.6, 0.8, 1.0]$.

in the boundary layer during the limit energetic cycle resulting from the interactions between the globally unstable modes and the convectively unstable modes.

It is now interesting to turn to **Cases 1** & **2** to assess whether the technique represents a general solution or a process that has to be adapted for each configuration.

Analysis of the low aspect ratio cylindrical cavity

In **Case 2**, recall that only the stationary disc boundary layer exhibits coherent structures. Similarly to the previous flow, the fluctuations in the Bödewadt layer organize as a spiral wavefront with a radially growing azimuthal wavenumber. In spite of this latter fact, DMD shows that a unique mode is at the source of the three-dimensional pattern (Fig. 3.22a) displaying 7 arms for $Re_\delta \lesssim 150$, 16 arms for $Re_\delta \gtrsim 150$ and up to 18 arms at $Re_\delta \simeq 250$. Note that the spiral is consistently counter-winding and therefore it can be associated with positive values of the azimuthal wavenumber m (Sec. 2.2.2.c).

In the previous search of the global mode at the origin of the dominant mode in the stator layer of **Case 3**, $m = 29$ was selected because the corresponding DMD mode has a unique azimuthal wavenumber at all radial locations. In the present case however, the difficulty comes from the unknown value of m at which to search for the potentially unstable global mode corresponding to the one obtained by DMD. This information being missing, it appears necessary to investigate all three possibilities, i.e. $m = 7$, $m = 16$ and $m = 18$, starting from radial locations where these azimuthal wavenumbers are observed, e.g. $Re = 1.96$, $Re = 2.94$ and $Re = 3.92$ respectively. Furthermore, given the structure is observed in the stationary disc boundary layer in LES results (Fig. 3.8b), we naturally choose to study the behaviour of the 'stator branch' (Fig. 3.27a) of **Case 2**.

Allowing α_i to be non-zero, it is possible to pinpoint the saddle points of $\omega(\alpha)$ corresponding to the absolutely unstable behaviour of the mean flow at each location. Figures 3.38, 3.39 & 3.40 show the isocontours of $\omega_{0,i}Re$ and $-\omega_{0,r}Re$ in the (α_r, α_i) for the three possibilities, i.e. at $Re = 1.96$, $Re = 2.94$ and $Re = 3.92$ for $m = 7$, $m = 16$ and $m = 18$ respectively. In all three cases, the saddle points have characteristics similar to the one found at $Re = 4.48$ in **Case 3** (previous paragraph), i.e. located in the $\alpha_i > 0$ half-plane with a positive temporal amplification rate $\omega_{0,i}Re$ indicative of a local absolute instability. Note however that the saddle point found at mid-radius in **Case 3** already had a frequency of $3.75F_0$ close to the frequency of the mode yield by DMD whereas in the present cases, all three saddle points have strongly positive frequencies that completely disagree with the frequency found by DMD.

As discussed previously, the next step is to follow the saddle point away from the initial location as the base flow changes. This allows to build the line $\omega_0(r)$ that can then be continued in the complex $r \in \mathbb{C}$ plane to find the position of the wavemaker. The positions of the wavemaker in each case are summarized in Tab. 3.9. First of all, note that in all cases, the global modes appear to be unstable ($\omega_{G,i} > 0$). Furthermore, it is remarkable that the global modes with $m = 16$ and $m = 18$ are predicted to have their sources located at the same radial location $r_G \simeq 1.55$ with frequencies that are close to each other. On the other hand, the location of the wavemaker of the global mode with $m = 7$ appears further away from the outer cylindrical wall and its frequency is much lower, i.e. $1.44F_0$ (see Tab. 3.9), but still far from the frequency obtained by DMD.

All this being said, the reconstructed fluctuations of the three global modes (Figs. 3.41-

Figure 3.38 − Isocontours of (*a*) amplification rate $\omega_i Re$ and (*b*) temporal frequency $-\omega_r Re$ in the $(\alpha_r/\sqrt{Re_h}, \alpha_i/\sqrt{Re_h})$ plane for the rotor branch of **Case 2** at $Re = 1.96$ and $m = 7$.

Figure 3.39 − Isocontours of (*a*) amplification rate $\omega_i Re$ and (*b*) temporal frequency $-\omega_r Re$ in the $(\alpha_r/\sqrt{Re_h}, \alpha_i/\sqrt{Re_h})$ plane for the rotor branch of **Case 2** at $Re = 2.94$ and $m = 16$.
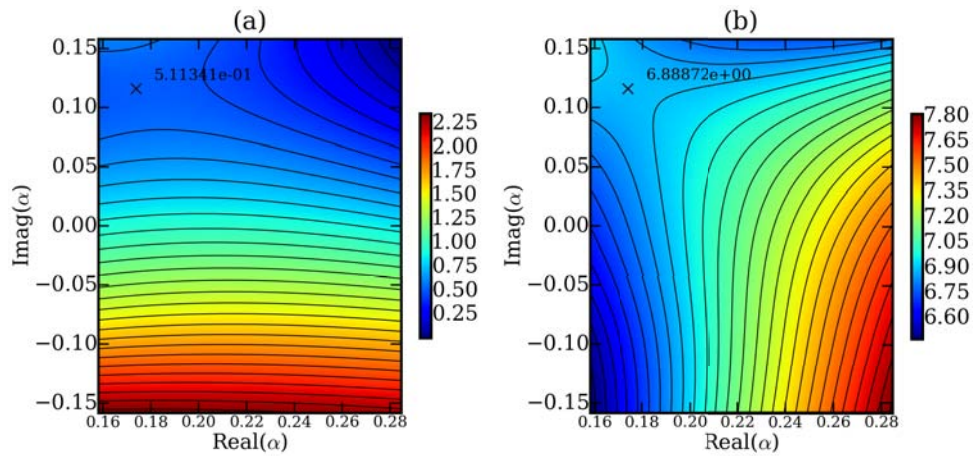

Figure 3.40 − Isocontours of (*a*) amplification rate $\omega_i Re$ and (*b*) temporal frequency $-\omega_r Re$ in the $(\alpha_r/\sqrt{Re_h}, \alpha_i/\sqrt{Re_h})$ plane for the rotor branch of **Case 2** at $Re = 3.92$ and $m = 18$.
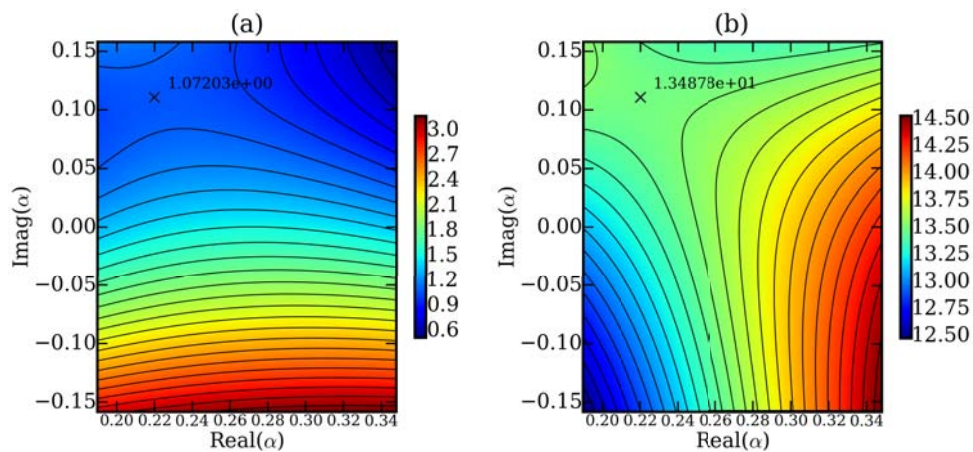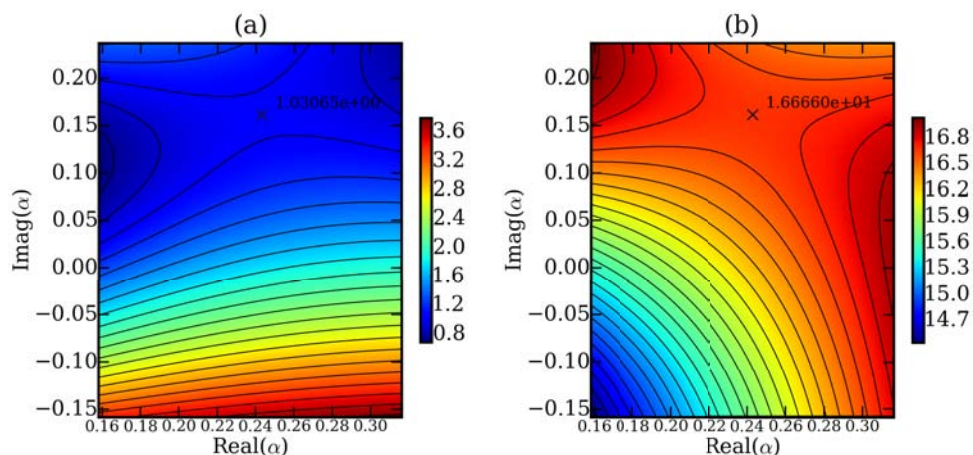
	Radial location r_G	Amplification $\omega_{G,i}Re$	Frequency $-\omega_{G,r}Re$	Normalized frequency $-\omega_{G,r}Re/(2\pi)$
Case $m = 7$	0.13	0.427	9.06	$1.44F_0$
Case $m = 16$	0.153	0.656	15.63	$2.49F_0$
Case $m = 18$	0.158	0.656	16.90	$2.69F_0$

Table 3.9 – Positions and characteristics of the wavemakers for the unstable global modes of **Case 2** sought at $m = 7$, $m = 16$ and $m = 18$. The normalized frequency can be directly compared to the frequency obtained by DMD.

Figure 3.41 – Fluctuating axial velocity of the global stator mode $m = 7$ of **Case 2**. Comparison between (*top*) the only mode obtained by DMD (Sec. 3.6) and (*bottom*) the present results with AVLP. Eigenfunctions are clocked at an arbitrary phase angle. The contour lines represent $w/\max(w) = [-1.0, -0.8, -0.6, -0.4, -0.2, 0.2, 0.4, 0.6, 0.8, 1.0]$.
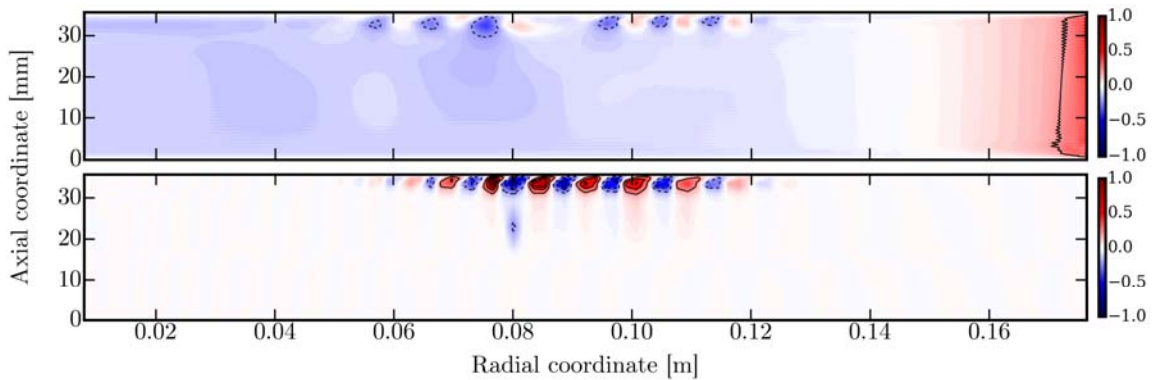
Figure 3.42 – Fluctuating axial velocity of the global stator mode $m = 16$ of **Case 2**. Comparison between (*top*) the only mode obtained by DMD (Sec. 3.6) and (*bottom*) the present results with AVLP. Eigenfunctions are clocked at an arbitrary phase angle. The contour lines represent $w/\max(w) = [-1.0, -0.8, -0.6, -0.4, -0.2, 0.2, 0.4, 0.6, 0.8, 1.0]$.

3.43) agree qualitatively well with the results obtained by LES. Naturally by definition the radial evolution of the azimuthal wavenumber cannot be found by LSA. However, the radial span of the three modes match the location of the strongest vortices given by DMD, i.e. for $0.06 \lesssim r \lesssim 0.12$, with a maximum of magnitude reached around $r \simeq 0.08$ as for
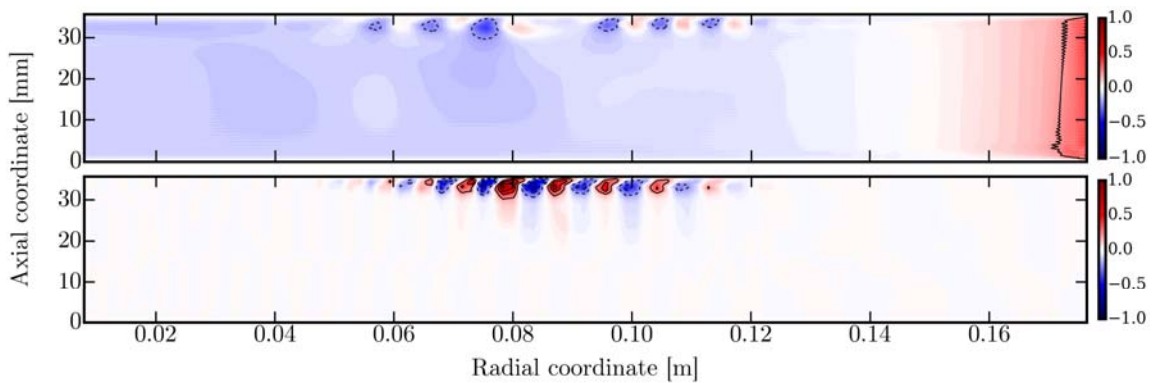
Figure 3.43 – Fluctuating axial velocity of the global stator mode $m = 18$ of **Case 2**. Comparison between (*top*) the only mode obtained by DMD (Sec. 3.6) and (*bottom*) the present results with AVLP. Eigenfunctions are clocked at an arbitrary phase angle. The contour lines represent $w/\max(w) = [-1.0, -0.8, -0.6, -0.4, -0.2, 0.2, 0.4, 0.6, 0.8, 1.0]$.
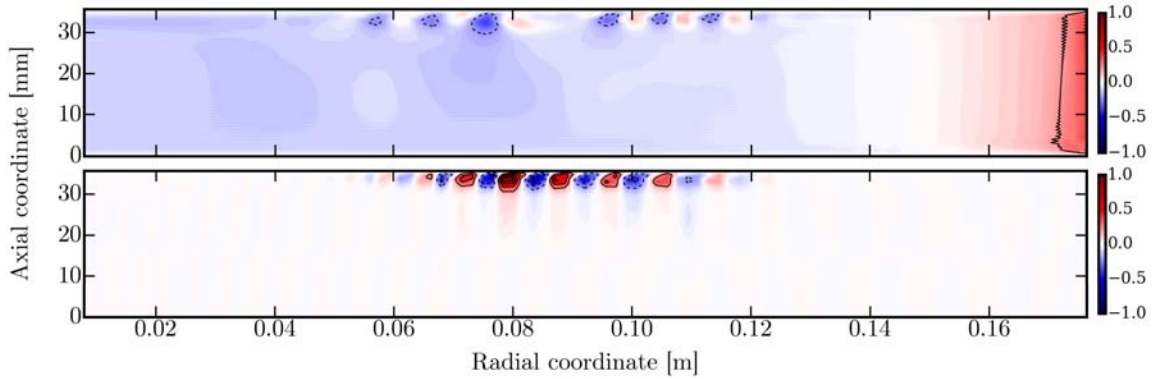
the DMD mode. Based on the results obtained previously for **Case 3**, it is reasonable to think that they are present in the flow obtained by LES, although the frequencies given by LSA (Tab. 3.9) do not appear on the pointwise spectra (Fig. 3.22c) or the DMD spectrum (Sec. 3.6.2). The three modes appearing in the same radial intervals indeed hints at the existence of interactions between them that could lead to nonlinear phenomena that are unpredictable by LSA and may induce the zero-frequency and fluctuating azimuthal wavenumber observed in LES.

Discussion about the high aspect ratio cylinder

The same strategy was finally applied to **Case 1**. In this case, only the stationary disc boundary layer is unstable and displays a spiral pattern resulting from the combination of 11 constituent modes according to the DMD results (App. E). Amongst these modes, a 3-armed counter-clockwise spiral with frequency $2.73F_0$ appears as the mode with the strongest magnitude, and we therefore detail in this paragraph our attempt to link it to a globally unstable linear mode of the mean cavity flow. The results obtained with LSA markedly disagree with the characteristics and the two-dimensional organization of the mode obtained by DMD, and hence we focus the present discussion on the potential causes of this discrepancy.

As usual, the investigation starts with a temporal stability analysis that we choose to conduct at mid-radius, i.e. $Re = 0.495$ in the present case, and at a constant azimuthal wavenumber $m = -3$. In accordance with the two previous low aspect ratio cases, the most amplified stator branch is selected to pursue the spatio-temporal analysis, and it is found that the maximum $\omega Re = -3.04 + 1.42i$ is reached at $\alpha_r/\sqrt{Re_h} = 0.15$.

These values being qualitatively similar to the ones obtained in **Cases 2** & **3**, the investigation continues by allowing α_i to be non-zero. Thereupon, only one saddle point in the (α_r, α_i) plane is found to be independent of the discretization in α and of the number of Gauss-Lobatto points N_{GL}. It is identified at coordinates $(\alpha_r/\sqrt{Re_h}, \alpha_i/\sqrt{Re_h}) = (0.035, 0.042)$ where the absolute complex frequency is $\omega_0 Re = -0.1 + 1.11i$ as shown in

Fig. 3.44. Unlike the values obtained for the stator branches of **Cases 2** & **3**, the saddle
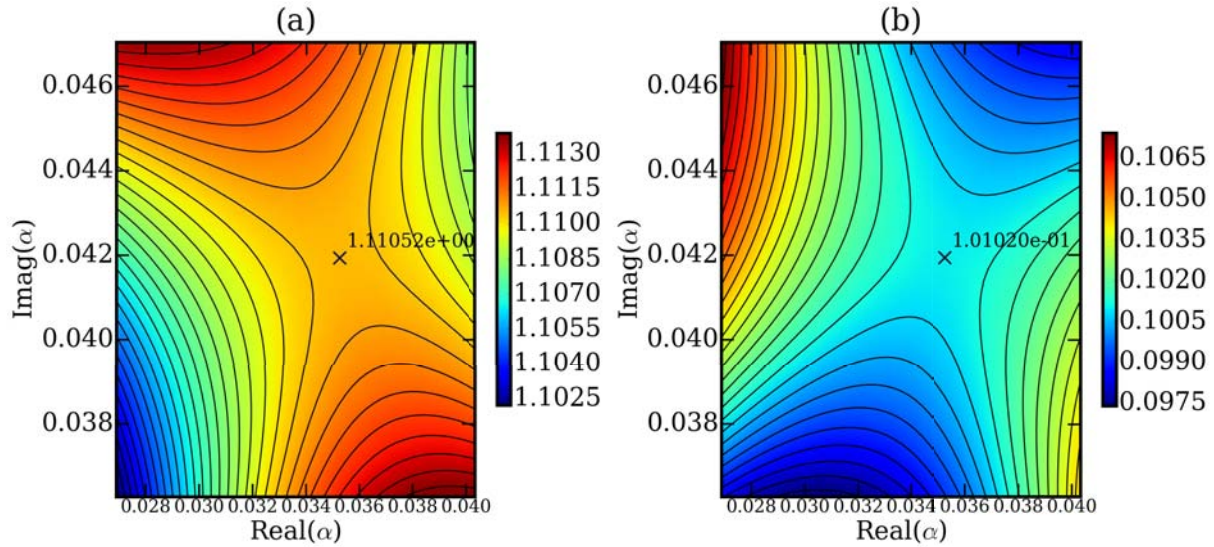
Figure 3.44 – Isocontours of (*a*) amplification rate $\omega_i Re$ and (*b*) temporal frequency $-\omega_r Re$ in the $(\alpha_r/\sqrt{Re_h}, \alpha_i/\sqrt{Re_h})$ plane for the rotor branch of **Case 1** at $Re = 0.495$. Zero-contours are represented by a thicker line.

point is not found at a value of $\alpha_r/\sqrt{Re_h}$ in the vicinity of $\alpha_r/\sqrt{Re_h} = 0.15$ maximizing the temporal growth rate. The value of $\alpha_i/\sqrt{Re_h}$ is also unusually close to zero.

These interesting remarks set aside, the next step of the investigation is to follow the saddle point away from the initial location as the base flow changes. The resulting evolution of $\omega_0(r \in \mathbb{R})$ with the radial coordinate is shown in Fig. 3.45 along with markers indicating the positions of the saddle points of the continued function $\tilde{\omega}_0(r \in \mathbb{C})$ upon convergence of the fitting process. The oscillating character of $\omega_r Re(r \in \mathbb{R})$ differs
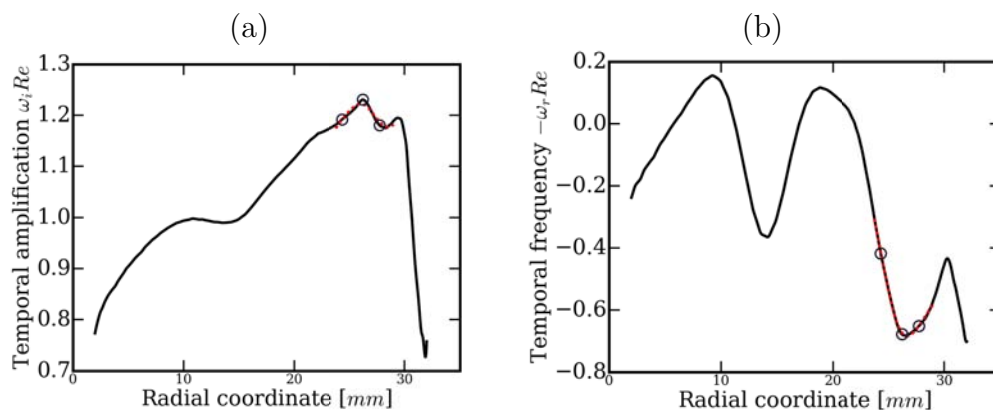
Figure 3.45 – Radial evolution of (*a*) the growth rate and (*b*) the temporal frequency of the stator branch of **Case 1** with the fitted Padé polynomial in the region of interest (dashed line) and the position of the saddle points of $\tilde{\omega}_0(r \in \mathbb{C})$.

from the trends obtained in **Cases 2** & **3** but the behaviour of $\omega_i Re(r \in \mathbb{R})$ is similar.

After convergence of the Padé polynomials fitting process, the location of the wavemaker $\omega_G Re = 0.67 + 1.23i$ is found at $r_G = 0.026$ m. Based on these results, a first remark concerns the positive sign of $\omega_{G,i} Re$ which expectedly implies the possible existence of a globally unstable linear mode with $m = -3$. On the other hand and similarly to the results of the LSA conducted for **Case 2**, the predicted frequency of this global mode, i.e. $\omega_{G,r} Re/(2\pi) = 0.1 F_0$ noticeably differs from the frequency $2.73 F_0$ yield by DMD. Furthermore in the present case, the two-dimensional organization of the LSA mode -
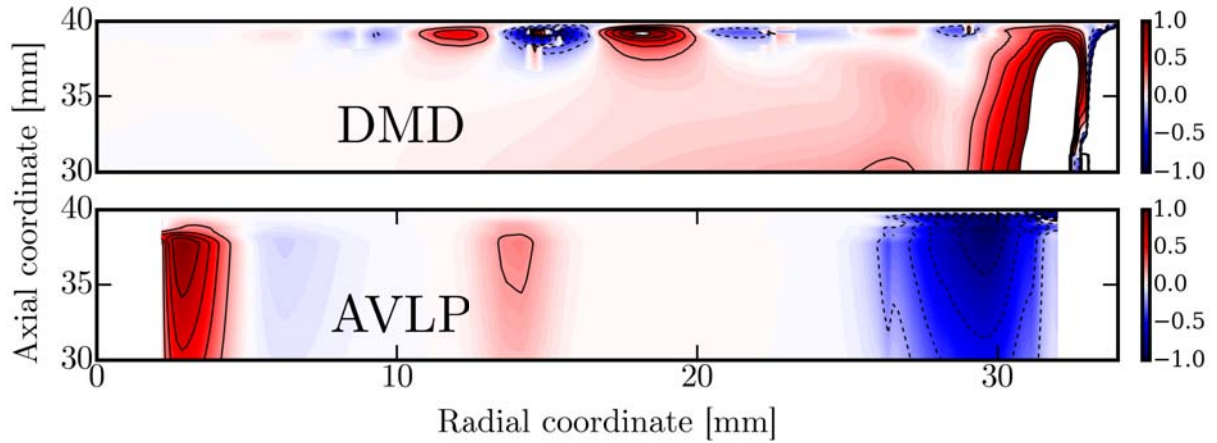
Figure 3.46 – Fluctuating axial velocity of the global stator mode $m = -3$ of **Case 1**. Comparison between (*top*) the mode obtained by DMD and (*bottom*) the present results with AVLP. Eigenfunctions are clocked at an arbitrary phase angle. The contour lines represent $w/\max(w) = [-1.0, -0.8, -0.6, -0.4, -0.2, 0.2, 0.4, 0.6, 0.8, 1.0]$.

shown on Fig. 3.46 - also disagrees significantly with the structure of the DMD mode. Figure 3.46 actually illustrates several issues.

1. The region of expression of the eigenvectors is located between $z \simeq 38$ mm and $z = 40$ mm according to the DMD results, but it is overestimated by LSA that yields vortices contained in the $[30, 40]$ mm interval. Although as usual the number of Gauss-Lobatto points has been optimized so that the eigenvalues are converged (Sec. 3.7.2), one can't exclude the possibility that this discrepancy hints the need for an even finer grid to resolve the eigenvectors.

2. Also, both the radial wavenumber and the radial amplification of the LSA structure are incorrect. This points to a wrong estimation of the eigenvalue α, either when the saddle points are searched at all radial locations or when the natural response of the flow to an excitation of frequency ω_G is studied.

Now that the attempt to link the $m = -3$ mode of **Case 1** to a globally unstable linear mode has been detailed, we centre the discussion on the potential causes of this lack of success. The difference between the frequency predicted by LSA and the one obtained by DMD can be attributed to nonlinear phenomena provoked by the interactions between the numerous modes constituting the dynamics of the flow. By nature, such phenomena

cannot indeed be captured by LSA and are known to induce modal pairing (see e.g. Ho & Huerre, 1984) and subsequent changes in the effective frequency of the structures. Regarding the difficulty to solve the dispersion relation, note that the value of the interdisc Reynolds number Re_h may play a significant role as in **Case 1** $Re_h \simeq 1.4 \times 10^5$ is two orders of magnitude greater than in **Cases 2** & **3**. Recall indeed that the interdisc Reynolds number had to be introduced during the development of the linearised equations for two-disc flows (Eqs. (2.2.22)-(2.2.25)) and more specifically appears directly as a factor of α in Eq. (2.2.23). This still has to be verified, but the large value of Re_h might cause the differential equations pertaining to the linear response of **Case 1** to be steeper and the different terms more unbalanced, hence inducing larger errors during the resolution of the system than in **Cases 2** & **3**. Finally, recall that **Case 1** displays two separate recirculation bubbles (Sec. 3.4.2) and other characteristics more common in tall cylinder enclosures than low aspect ratio rotor/stator cavities. They create among other things a thick outer cylindrical boundary layer and limit the region where the flow behaves like a rotor/stator flow to radial locations between 6 mm and 28 mm. Altogether, these two facts question our fundamental assumptions that the flow can be considered as locally parallel and one-dimensional. These two hypothesis are indeed mandatory for the results from local linear stability analyses to be valid and by extension the combination of local eigenmodes into a global mode to be physically meaningful. In the present case, the discrepancies with the reference data could therefore be explained by the greater three-dimensionality of **Case 1**, although a thorough investigation is left to be conducted to support this assumption.

Discussion of the results

A first spatio-temporal stability analysis was led based on the temporally and azimuthally averaged flow of **Case 3** (Sec. 3.4.2). In addition to the spectral characteristics of the DMD modes that can be predicted by LSA, the two-dimensional organization can also be reconstructed and is found to agree very well with each mode spatial representation. The principal conclusion of this investigation of **Case 3** is therefore that each boundary layer structure corresponds to the mark of a globally unstable linear mode of the rotor/stator cavity mean flow whose wavemaker is located close to the outer cylindrical boundary layer. It leads to several important remarks.

- First of all, our results agree with the observations of Healey (2007) that enclosing a rotor/stator flow turns a usually convectively unstable flow into a globally unstable flow.

- Contrary to swirling jets for instance (Oberleithner, 2012), the dynamics of a transitional rotor/stator flow appears to be driven by several global modes with different frequencies, cohabiting within the flow but expressing themselves most at distinct axial location.

- As a global mode propagates by definition to the whole flow, it is now easier to understand why the probes placed at different locations within the cavities (see

Fig. 3.18 and Tab. 3.6) would capture signals constituted of the same frequencies. These frequencies, that we previously identified as the frequencies of the DMD modes, are in fact the frequencies of the global modes of the mean flow.

- It is finally important to note that LSA did not reveal any global mode expressing itself at a height corresponding to that of the homogeneous core where only weak traces of the identified boundary layer modes are seen. This observation leads to the conclusion that the patterns observed at mid-height in the cavity (Sec. 3.5.3) result from the interactions between the cohabiting global modes and their influence on the mean flow. Note that this remark also agrees with the DMD that did not yield any mode present exclusively in the core flow.

All in all, this technique appears to be very promising for the prediction of the dominant instabilities responsible for the strong pressure fluctuations in an enclosed rotor/stator flow.

When a similar strategy is applied to the averaged flow of **Case 2**, a difficulty arises due to the radial evolution of the azimuthal wavenumber of the pattern in the boundary layer. Three different wavenumbers were therefore considered and for each one the corresponding global mode is found to be unstable. Also, the two-dimensional reconstructions of the velocity fluctuations show that all three modes exist in the same radial interval, and their radial wavenumber and radial amplification are found to agree with the results obtained by DMD. Although by nature LSA cannot capture the radial evolution of the azimuthal wavenumber of the pattern observed in the LES solutions, the three modes located at the same radial position hint at potential interactions that could trigger a combination of the vortices and a locking of their overall frequency at the value yield by LES.

In **Case 1**, the approach appears to find its limits. In this high aspect ratio configuration driven by numerous DMD modes, the link between these modes and globally unstable linear modes of the mean cavity flow cannot indeed be found. Aside from making this configuration unrepresentative of industrial turbine stages cavities, the large aspect ratio of **Case 1**, i.e. $G = 1.18$, causes the flow to exhibit characteristics commonly associated with tall rotating lid-cylinder flows (Gelfgat *et al.*, 2001). These are believed to generate a flow with a greater three-dimensionality that questions the fundamental assumptions of LSA, i.e. that the flow can be considered as locally parallel and one-dimensional. Although it requires a thorough verification, these facts are thought to constitute the reason why the DMD modes cannot be associated to global linear modes as directly as in **Cases 2** & **3**.

3.8   Conclusion

High Reynolds number rotating cavity flow is a recurrent and basic fundamental problem that often results in flow instabilities with the main consequence that in industrial applications they may yield system failure or mistuned operating conditions. Although fundamental, these flows and more importantly the occurrence of such instabilities need

to be further understood. With such an objective in mind and in an effort to contribute to this improved understanding several wall-resolved LES have been performed on rotor/stator cylindrical cavities ($R_m = 1$) with two aspect ratios $G = 1.18$ and $G = 0.2$ and on an annular cavity of aspect ratio $G = 0.2$ with a value of the curvature parameter $R_m = 1.8$. The flow high Reynolds number $Re = 10^5$ was the only constant between the different configurations. The literature (e.g. Séverac *et al.*, 2007) and well known auto-similar solutions (Rogers & Lance, 1962) of the flow between a rotating and a stationary disc allowed to validate the mean flows extracted from the LES predictions. The first observation is that such high Reynolds number rotor/stator cavity flows all organize the same way in the mean and belong to the fourth kind of rotor/stator flows according to Daily & Nece (1960) classification, with viscosity driven disc boundary layers separated by a homogeneous core rotating in bulk. Furthermore, adequate comparisons demonstrate the capacity of wall-resolved LES to accurately capture the level of turbulence (Lygren & Andersson, 2001) of such a high Reynolds number rotor/stator cavity flow as well as to resolve the disc boundary layers while predicting the correct thickness of the inviscid-like homogeneous core flow in the cavity.

Once validated, the LES predictions are used to investigate the dynamic behaviour and organization of the different layers of the flow. In all cases, the top stationary disc boundary layers were found unstable to circular and spiral waves akin to those described by Serre *et al.* (2001) whereas the bottom rotating disc boundary layers remained undisturbed except in the presence of an inner cylindrical shaft (**Case 3**). For the Bödewadt layer instabilities, the characteristic parameters (radial and azimuthal wavenumbers, spiral inclination angle, frequency, phase velocity) were found to be in good agreement with available results (Gelfgat, 2015; Itoh, 1991; Tuliszka *et al.*, 2002; Serre *et al.*, 2001; Gauthier *et al.*, 1999; Lopez *et al.*, 2009), either experimental, theoretical or numerical. The characteristic parameters of the patterns present in the Ekman layer also take expected values according to the theoretical development made for instance by Lingwood (1995*a*) or the numerical work by Serre *et al.* (2001), although the experimental or numerical description of an unstable rotating boundary layer is less common in the literature. In addition to the aforementioned descriptions of the well known boundary layer patterns, the LES predictions are used to show that in spite of its quasi-inviscid nature, the homogeneous core flow becomes unstable to annular and spiral patterns in all three cases too. These waves, although not described so far in the literature, might be compared to patterns observed for instance by Gelfgat *et al.* (2001) in the course of an investigation bearing on the flow in tall rotating-lid cylinder enclosures. Further study of the velocity fluctuations show that the core structures actually emerge in the stationary disc boundary layer and extend throughout the central core until they reach the rotating disc boundary layer. The structures in the boundary layers and within the inviscid-like core were therefore found to be dependent on each other, even though the azimuthal organization in the different layers of the flow are markedly different as well as the inclination of said structures with respect to the geostrophic flow.

The investigation is then pursued using dedicated tools such as three-dimensional Dynamic Modal Decomposition (DMD) (Schmid, 2010) to qualify in more details the flow patterns present in the entire cavities. It is first shown how, based on the visible pattern

predicted by the LES, only a few DMD modes are necessary to rebuild the dynamics of the stationary disc boundary layer (three modes in **Case 3**, a unique mode in **Case 2** and eleven modes in **Case 1**). The three-dimensional nature of the DMD modes allow to compare the induced azimuthal organization of the flow at every axial position within the cavity, and it actually shows that the superposition of the modes drives the dynamics of the stationary disc boundary layer as well as the dynamics of the whole flow, everywhere in the cavity. The different patterns observed in the LES predictions (annular and/or spiral waves in the boundary layers and the homogeneous core) are then found to simply be the result of the interactions between these atomic modes and the mean flow. Finally, to address more specifically the industrial or experimental data, the three cavities are equipped with pointwise probes to locally monitor the axial velocity fluctuations. All signals, wherever the probe is located, turn out to be based on the same few constituent frequencies whose magnitudes are seen to fluctuate with the position inside the cavity. These constituent frequencies are an exact match to the frequencies of the few DMD modes proven to be necessary to drive the dynamics of the rotor/stator cavity flow, and what is more the fluctuations in magnitude noticed between the pointwise signals also reflect exactly the space amplitude distribution pictured by the DMD modes.

Considering all three cavities with different values of R_m and G permits an exploration of the parametric space and allows us to extend the previous conclusions to all rotor/stator geometries: independently of the radial and axial confinements, an enclosed rotor/stator cavity flow unsteady activity seems likely to be driven by only few modes, either axisymmetric or three-dimensional, whose combination is responsible for the patterns observed in the predictions. Due to the three-dimensional nature of such modes, their respective frequencies are also the constituent frequencies of all signals monitored anywhere in the cavity using pointwise probes. This point also makes the connection with the potential application in turbomachinery or more generally industrial applications where strong velocity fluctuations are indeed monitored in rotor/stator cavities and which could correspond, according to the present investigation, to the frequencies of a handful dynamic modes responsible for the overall organization of the flow.

Finally we oriented the discussion towards the linear stability analyses of the enclosed rotating flows with the objective to propose a strategy to predict the appearance of the dominant modes observed in LES. It was shown that although temporal analyses yield interesting information about the local dynamics of the fluctuations, letting the radial amplification $\alpha_i = 0$ at all locations does not allow to capture the correct two dimensional shape of a mode. Inspired by well-known literature dealing with global mode reconstruction for jet and wake flows (see e.g. Juniper, 2011; Oberleithner, 2012), the attention was focused on spatio-temporal stability analyses in order to capture, at each radial location, the absolute stability of the base flow to a given perturbation. In some cases, the study shows that the unsteady phenomena observed in LES are related to globally unstable linear modes of the mean flow. Furthermore in these cases, integration of the successive local analyses and an adequate assembling of the local eigenmodes lead to an accurate estimation of the two-dimensional organization of the mode.

Chapter 4

Investigation of the flow in the first-stage of an industrial turbopump turbine

Contents

Following the previous investigation on smooth rotor/stator cavities flow dynamics, this chapter focuses on the large scale dynamics of high Reynolds number industrial grade rotor/stator cavities using Large Eddy Simulation (LES). In the present case, of specific interest are the unsteady pressure phenomena known as pressure bands and their dependency on geometrical and thermal parameters. Such dangerous operating modes are today not captured by CFD: the present primary goal is to investigate the ability of LES to accurately reproduce such flows and their sensitivity in terms of large scale motions and spectral content. After validation of LES based on two geometries and thermalization, we show that LES reproduces the spectral content overhaul triggered by the change of thermalization. The second objective is a study of the activity recorded in the different cases to improve our understanding of the pressure bands phenomena. To do so, Dynamic Modal Decomposition (DMD) reveals that the dynamics of the flow is driven by some atomic modes whose combination explains the oscillatory signals registered by pointwise-probes. These modes form macro-structures occupying the interdisc space and are at the origin of the large-scale flow dynamics. Finally, they are observed to significantly differ depending on the configuration, confirming the dependency of pressure bands phenomena on the operating condition and geometrical parameters.

4.1   Introduction

Benchmarking campaigns targeting cryogenic engines turbopumps often reveal the existence of unidentified unsteady pressure phenomena registered within the rotor/stator cavities of the first stage of the turbine. As mentioned in the introduction, the corresponding signals are often marked by a handful of constituent frequencies indicative of strong oscillatory and coherent phenomena that have proven highly detrimental to the proper operation of the turbopump, eventually threatening the structural integrity of the rocket. Furthermore, such features, named 'pressure bands' due to the patterns appearing on the spectrograms, have been observed to be highly sensitive to changes in the rotor/stator cavity geometry. As a consequence of such changes, the pressure fluctuations have been seen to cancel, be damped or amplified, their frequencies blue- or red-shifted. Interestingly, for a fixed geometry, this unsteady phenomenon has also proven to be very sensitive to the operating point and the thermal state of the machinery. The present study, using the diagnostics and post-processing techniques validated on academic cavities (Chap. 3) is intended to shed some light on these thermal and geometrical dependencies to improve our understanding of the 'pressure band' phenomenon. To do so, three different configurations are considered, with either different geometries or average flow temperature.

If all complex geometrical features of a turbine stage are neglected, the problem reduces to a flow between two coaxial disks, one of which is in rotation (the rotor) while the other is stationary (the stator). This similarity guided us towards a preliminary in-depth study of the dynamics of flows in academic smooth rotor/stator cavities (Chap. 3).

The results of such studies, albeit only first-order model for turbomachinery rotor/stator flows, led to a better understanding of the behaviours of rotating flows at all regimes. They indeed showed that the unsteady pressure phenomena registered everywhere in the cavities are modal in nature and constituted of a few modes that can be obtained by DMD. Following these conclusions, we use in the present chapter the same unstructured LES approach to simulate actual industrial turbine flows at extreme Reynolds numbers. Then, the post-processing techniques and diagnostics techniques validated on the academic flows are applied to the industrial flows to analyse the pressure fluctuations *in situ* and clarify the causes of the 'pressure bands'.

The chapter is organized as follows. First a discussion about the geometrical set-up is provided and the differences between the two geometries under study are given. Then a general presentation of the CFD software and of the numerical details follows. Second, as the primary goal of this paper is to qualify LES-based CFD tools in providing informations about such complex industrial turbomachinery flows, we establish a comparison between the mean flow fields predicted by LES and well-known results from the literature on enclosed smooth rotor/stator cavity flows. The last section focuses on an in-depth analysis of the dynamics of the flow, based on pointwise spectral analyses and a three-dimensional modal decomposition. At this point, influence of the geometry and of the thermal environment on the nature of the pressure fluctuations is analysed. Finally, conclusions and opening remarks are provided.

4.2   Presentation of the configurations

4.2.1   Geometries and modelling

During the course of this study, a total of three complex industry-like geometries have been computed. This section presents the geometrical and numerical configurations used in the three cases, in addition to the meshing strategies and the resulting grids.

4.2.1.a   Geometries and characteristics

A schematic of the base geometry used in the present investigation is seen in Fig. 4.1. It can be decomposed into three main cavities:

- the rotor/stator cavity, referred to as C_1, located at the bottom and outlined in light-grey;

- the outer channel, called C_2, outlined in dark-grey;

- the high-radius cavity, C_5, outlined in black.

To further simplify discussions, the portion of C_1 located between the locking ring and the C_1-C_2 pass (filled with darker grey on Fig. 4.1) will be referred to as C_3. Within C_1 and C_3, four radial locations of interest have been marked as they indicate four regions where the distance between the rotor and the stator do not vary much and where the flow
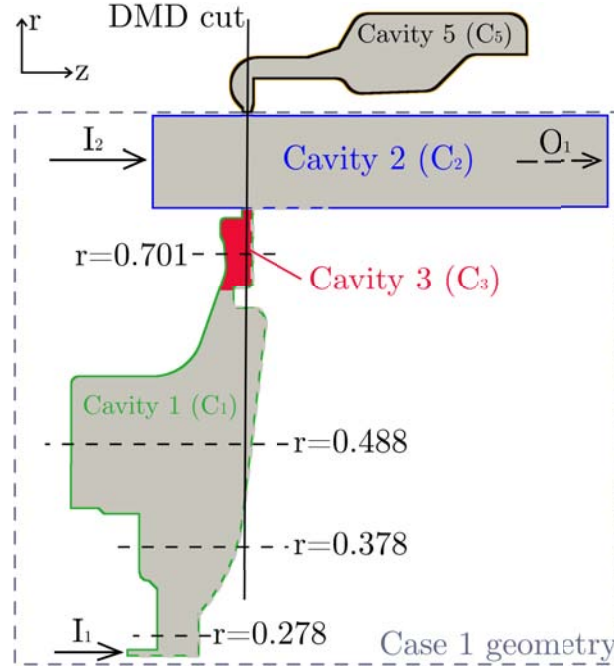
Figure 4.1 − (r,z)-cut of the axisymmetric geometry used for **Case 1** (without C_5) and **Case 2** & **3** marked with relevant notations pertaining to the names of the cavities, the inlets & outlets, the location of the rotor, four radial stations of special interest and the trace of the (r,θ)-cut used for the DMD algorithm (see Sec. 4.4.2.b).

can therefore be compared to the flow between two smooth discs. These locations will be referred to as $r_1 = 0.278$, $r_2 = 0.378$, $r_3 = 0.488$ and $r_4 = 0.701$. Also, we indicate on Fig. 4.1 the axial location at which (r, θ)-cuts were extracted to run the DMD algorithm (refer to Sec. 4.4.2.b). This location will be referred to as $z_{\text{pass}} = 0.165$. Note that all length mentioned in the present document, either radial or axial distances, have been normalized by the maximum radius of the geometry.

Both geometrical configurations to be detailed hereafter have the same flow inlets and outlets, respectively marked on Fig. 4.1 by full lines and dashed arrows. The inlet located at lowest radius, called I_1, represents the pure Species_1 leak that appears in real machines and due to the joint isolating the turbine stage from the turbopump fuel intake. The inlet of C_2, called I_2, corresponds to the flow of hot combustion products coming from the gas generator which drives the turbine stage. One can also identify on Fig. 4.1 the rotor wall marked with long dashed lines, whereas the rest of the stationary walls of the cavity are marked with full lines. Since one of the objectives of this study is to assess the capacity of LES to recover the geometrical sensitivity of pressure bands, two specific computational domains derived from the original configuration detailed on Fig. 4.1 are to be addressed. In the first LES named **Case 1**, the outermost cavity C_5 is omitted from the computational domain (see grey dashed box on Fig. 4.1) to serve as the reference prediction. **Case 2** is similar to **Case 1** but C_5 is kept in the computational domain to assess its impact on the flow and on the behaviour of the pressure bands. Finally, using the complete geometry, the temperature of the shaft leak-flow (inlet I_1, refer to

Fig. 4.1) is raised from its initial value to test whether the thermal state of the main cavity flow, often changing during the operation of the machine, markedly affects the unsteady pressure phenomena (**Case 3**). A summary of the cavities used in each case is provided in Tab. 4.1.

	Cavity C_1	Cavity C_2	Cavity C_5	I_1 fluid
Case 1	$\times$	$\times$		cold
Case 2	$\times$	$\times$	$\times$	cold
Case 3	$\times$	$\times$	$\times$	warm

Table 4.1 – Geometrical composition of the computational domains retained for the LES's along with the leak thermal state.

4.2.1.b Meshes

The two geometries used in the present investigation (see Tab. 4.1 and Fig. 4.1) have been meshed entirely with tetrahedrons. To ensure consistency between the computations, the mesh of the second geometry is simply a linear combination of the mesh used for the first geometry and the mesh created for C_5. In other words, the meshes used for C_1, C_2 and C_3 are identical for both geometries, and the mesh of C_5 is added for the computations of **Case 2** and **Case 3**.
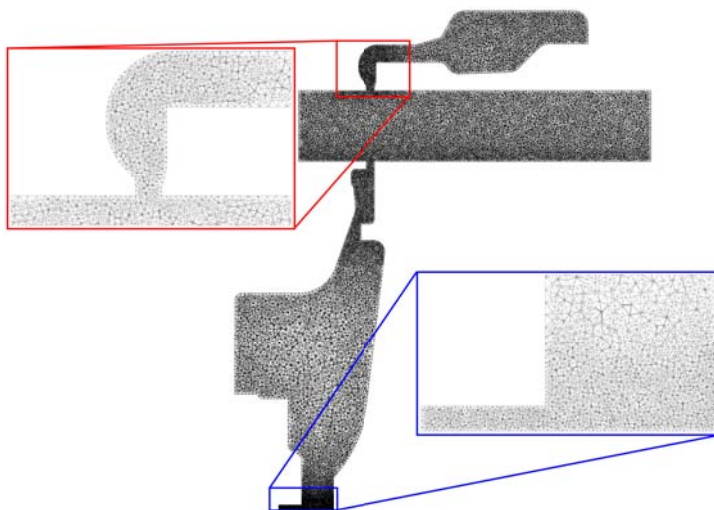
Figure 4.2 – (r,z)-cut of the three-dimensional mesh used for **Case 1**, **Case 2** & **Case 3**, supplemented with insets showing the areas of refinement: (top, red) C_2-C_5 pass, (bottom, blue) inlet I_1.

Figure 4.2 presents an overview of the mesh and of the multiple zones of refinement in a (r,z)-cut of the three-dimensional grid used for **Case 1** (if C_5 is omitted) and **Cases 2** & **3** (otherwise). To capture the shaft H_2 jet characteristics (inlet I_1, see Fig. 4.1), the low-radius area of the geometry (see Fig. 4.2, bottom-blue inset) has been refined such that tetrahedrons in this regions have, on average, half the volume of the tetrahedrons used in C_1. The same strategy has been applied to C_3 (see Fig. 4.1) and the C_2-C_5 pass (see Fig. 4.2, upper-red inset) so as to improve the resolution of the flow in these regions of strong mixing. No special treatment has been applied to C_2 where the mesh is radially and longitudinally homogeneous. The principal characteristics of the two meshes used respectively with **Case 1** and **Cases 2** & **3** are summarized in Tab. 4.2.

		Case 1	**Cases 2 & 3**	*Gain*
N_{tet}	—	82 551 252	109 578 962	*132 %*
N_{nodes}	—	14 686 682	19 551 603	*133 %*
V_{min}	$[m^3]$	6.8×10^{-14}	7.2×10^{-14}	*106 %*
V_{max}	$[m^3]$	3.2×10^{-10}	4.4×10^{-10}	*137 %*

Table 4.2 – Summary of the meshes principal characteristic values. Mesh growth induced by the addition of C_5 reported under the 'Gain' heading.

As mentioned in introduction, the purpose of the present investigation is to assess the ability of the LES to reproduce the unsteady phenomena occurring in these geometries. As a consequence, note that the two configurations are not sectors but rather full 360° geometries to capture all fluid motion, without any restrictions or simplifications and especially without forcing any azimuthal periodicity.

4.2.2   Numerics

The purpose of this work dedicated to industry-like configurations is to compare the behaviour of the flows and assess the impact of different factors (presence or not of the different cavities, temperature of the injected fluid) originally reported of importance in the experiments on the instability. To do so and in addition to the use of identical meshes, identical initialization processes, convergence criteria and numerical parameters have been devised for all three cases. These are detailed in the present section. A final note is made on the performances of the solver and the cost of the computations. The numerical parameters and models are kept constant for the three cases and can be organized according to two categories: the solver parameters and the turbulent closures as well as flow overall modelling.

As mentioned above (see Fig. 4.1), both geometries have two inlets (resp. I_1 and I_2) and a single outlet (O_1), the rest of the boundaries being fixed walls, to the exception of the rotor naturally. The three Cartesian velocity components (u, v, w) (along (z, x, y) resp.), the static temperature T_s and the species mass fraction $(Y_{\text{Species}_1}, Y_{\text{Species}_2})$ are imposed at the inlets, whereas a static pressure P_s is given at the outlet. All walls are chosen to be adiabatic, impermeable and the fluid is supposed to assume the velocity of the wall (no-slip condition), be it zero (stator) or some tangential velocity (rotor). Furthermore, due to the unreasonable CPU cost necessary to refine sufficiently the mesh near the walls to capture the flow boundary layers, a classical law-of-the-wall is used on all fixed walls in order to impose the wall shear stress instead of computing it. The expression of the law is equivalent to the formulation presented by Coles & Hirst (1968) and is as follow:

$$
\begin{aligned}
u^+ &= n^+ && \text{for } n^+ \leq 11.445 \\
u^+ &= k^{-1} \ln\left(E n^+\right) && \text{for } n^+ > 11.445
\end{aligned}
\tag{4.2.1}
$$

with $k = 0.41$ and $E = 9.2$, where $u^+ = \overline{u}/v^*$ and $n^+ = nv^*/\nu$ are respectively the inner velocity and normal wall distance, v^* being the wall-friction velocity defined using the

wall shear stress τ_w ($v^{*2} = \tau_w/\rho$), while ν is the kinematic viscosity of the fluid and ρ its density. Additionally, the wall-normal heat-flux and velocity is set to zero to induce respectively adiabaticity and impermeability. Note that to ease the computation, two exceptions have been made for a part of the channel immediately after I_1 and the channel extension in C_2. There, the fluid is allowed to slip on the adiabatic and impermeable walls. These conditions are summarized on the illustration shown in Fig. 4.3.
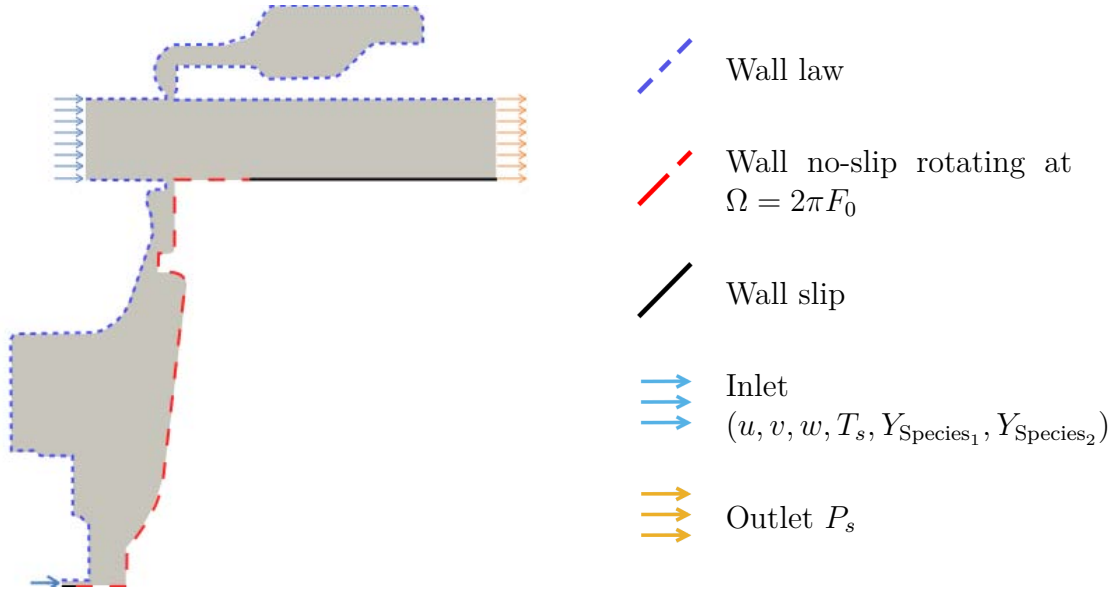

Figure 4.3 – Schematic representation of the boundary conditions used in **Case 1**, **Case 2** and **Case 3** along with relevant legend annotations.

The choice of a law-of-the-wall modelling approach *i.e.* so called wall modelled LES has a major impact on the meshing strategy. In the present case, the implementation of the law expressed in Eq. (4.2.1) indeed allows to capture best the boundary-layer dynamics when the first mesh nodes have a normal wall coordinate $n^+ \simeq 30$. This implies that once a mesh is produced, the values of the normal wall coordinate n^+ have to be checked *a posteriori* and if a majority of nodes does not approach the above criterion then corrections have to be applied to the mesh and an iterative process is needed leading to an optimized mesh. For the present studies, the values of n^+ at the last iteration are displayed under the form of probability densities in Fig. 4.4, for **Case 2** (Fig. 4.4a) and **Case 3** (Fig. 4.4b), the values obtained in **Case 1** being very similar to those predicted by the LES of **Case 2**. The densities are plotted separately to allow for a more accurate interpretation. The left black bars correspond to the upper channel (C_2) wall, the middle brown bars to the stator wall and the right light blue bars to the rotor wall. These values are obtained by azimuthal sampling of the last instantaneous LES field obtained for **Cases 2** & **3**, when the flow is statistically stationary. There is a marked difference between the values yield for **Case 2** and **Case 3**, the latter being smaller on average. The most important change occurs along the rotor wall where values of n^+ barely go beyond 50 in **Case 3** whereas there is a non-negligible proportion of nodes with $n^+ \geq 100$ in **Case 2**. All in all, these values give precious information relative to the accuracy of the
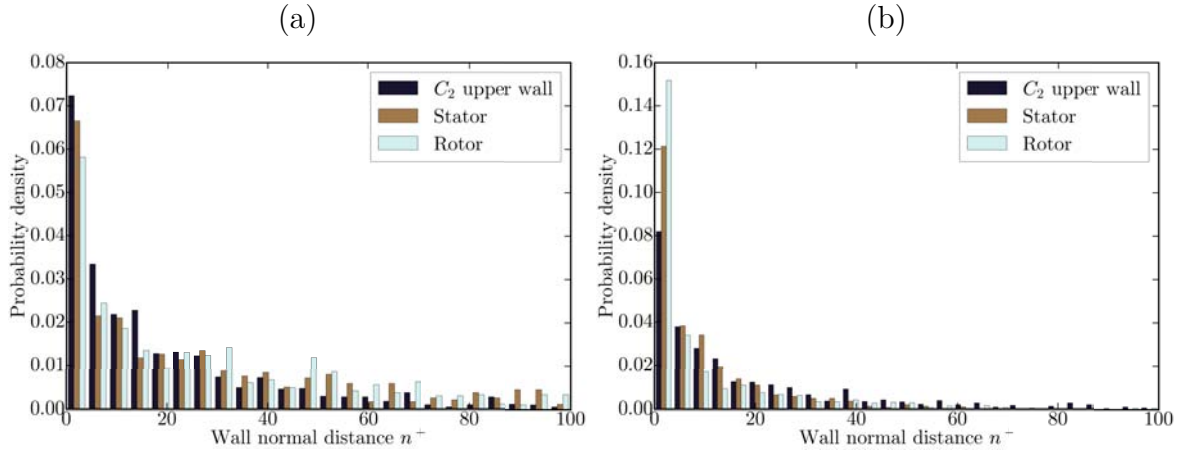
Figure 4.4 − Density probability of normal wall coordinate n^+ predicted by the LES of (*a*) **Case 2** and (*b*) **Case 3**. The repartition over C_2 upper wall (left black), the stator wall (middle brown) and the rotor wall (right light blue) have been separated from each other.

LES predictions close to the walls. The histograms indeed show that most points have $n^+ < 35$, ensuring that the mesh close to the walls is sufficiently refined to potentially allow for the right description of the wall turbulent boundary layers by the model as well as the in cavity flow dynamics (refer to Bridel-Bertomeu *et al.*, 2016, for more details - see App. F).

To conclude the discussion about the boundary conditions, it is noteworthy that the inlets I_1 and I_2 and the outlet O_1, as commonly done in the context of compressible LES, are treated with Navier-Stokes Characteristic Boundary Conditions (NSCBCs) (Poinsot & Lele, 1992; Lodato *et al.*, 2008; Pirozzoli & Colonius, 2013). It has been verified in the present cases that these treatments allowed for the correct prediction of the radial equilibrium is C_2 (see the thorough demonstration by Koupper *et al.* (2014) for more details and refer to App. G for the demonstration of the radial equilibrium formula).

Another necessity to ensure coherence between the three computations relates to the settings of the numerical solver and their relevance with regard to LES recommendations. The compressible multi-species Navier-Stokes equations are solved using a finite-element scheme TTGC (Colin & Rudgyard, 2000) based on a two step Taylor-Galerkin formulation that relies on a cell-vertex formalism and schemes (Lamarque, 2007; Colin & Rudgyard, 2000) specifically designed for LES. The solver possesses low diffusion and dispersion properties which make it highly suitable for LES by providing 3rd order space and time accuracy. The subgrid scale modelling is closed using the WALE model (Nicoud & Ducros, 1999), which allows for a better behaviour of the turbulent subgrid eddy viscosity for wall bounded flows, while the laminar dynamic viscosity, μ, assumes a power law. Note also that the fluid is assumed to follow the ideal gas law for complex mixtures: i.e. dependent on the local composition issued by the multi-species problem solved. To avoid the small-scale oscillations (a.k.a. wiggles) in the vicinity of steep variations and to smooth very strong gradients, artificial viscosity is introduced in the three computations, both 2nd order to smooth under-resolved gradients and 4th order to dissipate potential wiggles.

The artificial viscosity application is based on the 'Colin-sensor' (Colin & Rudgyard, 2000) modified for multi-species flow. All these parameters are summarized in Tab. 4.3.

Solver type	Navier-Stokes
Di usion scheme	Finite elements, 2Δ stencil
Convection scheme	Two-steps Taylor Galerkin TTGC $O(\Delta t^3)$, $O(\Delta x^3)$
Subgrid scales model	WALE
Laminar viscosity	$\mu = \mu_0(T/T_0)^n$
Arti cial viscosity	Colin-sensor Extra 10% 4th order onto conservative $(\rho u, \rho v, \rho w)$ Over- & undershoots in Y_k handled

Table 4.3 – Summary of the numerical parameters common to **Case 1**, **Case 2** and **Case 3**.

Finally, before moving on to the interpretation of the LES predictions, it is paramount to ensure that all transients, numerical and/or physical have been evacuated and that the flow under scrutiny is indeed statistically stationary. In the present investigation, two criteria have been considered to ensure the global equilibrium of the flow:

(a) that the total kinetic energy of the flow is at a plateau with zero-mean fluctuations,

(b) that the difference between the inflowing and outflowing mass is balanced.

Figure. 4.5 shows an example of global mass flow balance taken from **Case 2**. The behaviours in **Case 1** and **Case 3** are identical, and after about 0.015 s (10 periods) the flow reaches an oscillating equilibrium characterized by zero-mean fluctuations visible in the bottom-right inset of Fig. 4.5.

To conclude this presentation, indications on the solver performance for the afore-described settings, i.e. the related computational costs and its efficiency, are reported. All computations were performed for approximately 25 full rotations of the rotor using Intel Haswell processors (E5-2680v3, 12 cores per processor) mounted in a LENOVO cluster (peak performance of 242 Tflops/s) located within the facilities of CERFACS. **Case 1** was computed using 200 processors with a runtime of approximately 7 days, whereas **Case 2** and **Case 3** used only 60 processors and therefore have runtimes of approximately 19 days and 41 days, respectively. Tab. 4.4 summarizes all performance data.

4.3 Comparative study of the mean carrier flow

Now that the three configurations of interest have been described in details (Sec. 4.2), this section focuses on the characteristics of the predicted mean flowfields. The purpose of the present study is twofold: first the analysis of the averaged fields provides a
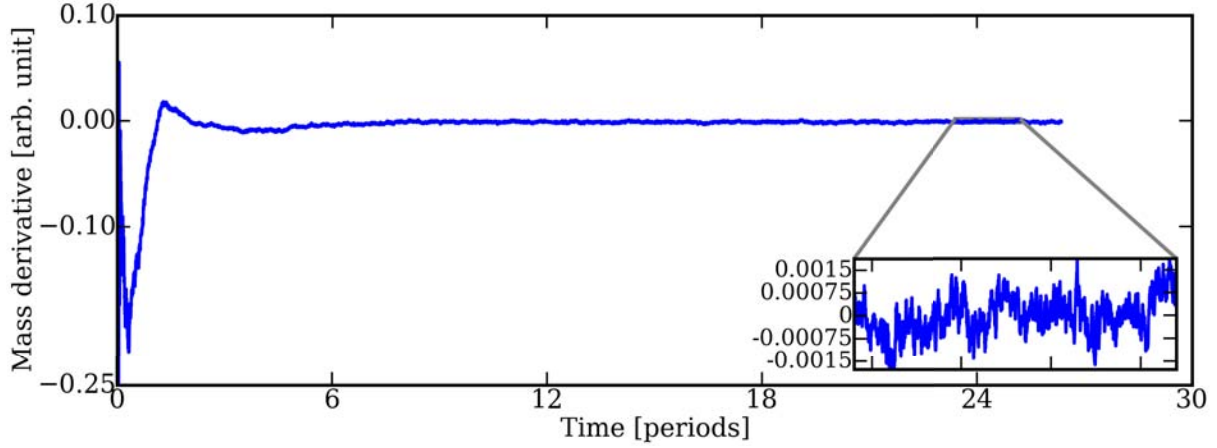
Figure 4.5 – Balance of the inflows and outflows of **Case 2** plotted as a global mass flow rate with an inset showing the convergence to zero.

	Case 1	Case 2	Case 3	
$\overline{\Delta t}$	1.540×10^{-5}	1.320×10^{-5}	8.718×10^{-6}	periods
N_{it}	1 697 200	1 980 000	4 365 000	—
$t_{phys,max}$	26.5	26	38.25	periods
t_{CPU}	203 042	330 926	708 794	h
N_{CPU}	2400	720	720	—
$t_{runtime}$	7	19	41	days

Table 4.4 – Summary of the solver performances for all three industrial cases and related computational costs. All computations have been performed on 60 or 200 Intel Haswell (E5-2680v3) processors (12 cores per processor).

first-order evaluation of the quality of the LES predictions, and second the use of more advanced diagnostics only based on the average data (root-mean square fields, stream lines computations, . . .) allows to pinpoint zones of high activity in the flow where it is most interesting to focus the investigations about the flow dynamic behaviour (Sec. 4.4).

4.3.1 Presentation of the averaging operators

The results presented in Sec. 4.3.2 are obtained through the application of one of three distinct averaging operators that will be referred to as 'temporal', 'azimuthal' and 'ensemble' averages.

The temporal average of a three-dimensional unsteady field $\mathbf{X}$, noted $\langle \mathbf{X} \rangle_t$ is the arithmetic average of multiple samples of $\mathbf{X}$ equireparted in time such that

$$\langle \mathbf{X} \rangle_t (r, \theta, z) = \frac{1}{N_t} \sum_{k=1}^{N_t} \mathbf{X} (r, \theta, z, t_0 + k\Delta t) \tag{4.3.1}$$

where t_0 represents the time at which the first sample is taken and Δt the time elapsed

between two successive samples. This quantity is therefore a three-dimensional field and as such it can be used to observe the mean flow motion within the geometries and provide information concerning, for instance, the privileged direction of the flow in the different cavities. Note that it is mathematically correct to omit the time dependence of $\langle \mathbf{X} \rangle_t$ if and only if all t_k are chosen over a period when the flow is temporally converged, i.e. statistically stationary - during the early stages of the computation for instance, changing the triplet $(t_0, \Delta t, N_t)$ will change the value of $\langle \mathbf{X} \rangle_t$. Fig. 4.6 provides a visual representation the operator $\langle \cdot \rangle_t$.
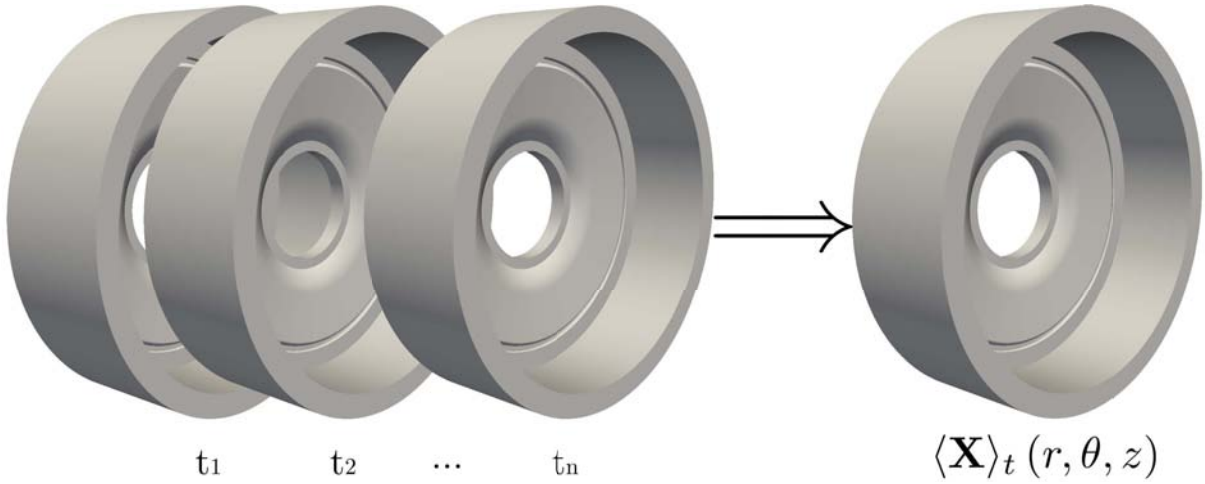

Figure 4.6 – Visual representation of the temporal averaging operator $\langle \cdot \rangle_t$ (Eq. (4.3.1))

The azimuthal average of $\mathbf{X}$, noted $\langle \mathbf{X} \rangle_\theta$ uses the same strategy as $\langle \cdot \rangle_t$ only it is based on the arithmetic average of multiple samples of $\mathbf{X}$ taken at a specific instant and equireparted in azimuth (the tangential direction along θ) such that

$$\langle \mathbf{X} \rangle_\theta (r, z, t) = \frac{1}{N_\theta} \sum_{k=1}^{N_\theta} \mathbf{X} (r, \theta_0 + k\Delta\theta, z, t) \tag{4.3.2}$$

where θ_0 represents the azimuthal position of the first sample, and $\Delta\theta$ the angle between two successive samples. This operator consequently yields a two-dimensional unsteady quantity that may be used to represent the temporal evolution of the three-dimensional mean flow projected on a (r, z) plane. Fig. 4.7 provides a visual representation the operator $\langle \cdot \rangle_\theta$.

Finally, the ensemble average of $\mathbf{X}$ can be seen as the combination of the two previous operators $\langle \cdot \rangle_t$ and $\langle \cdot \rangle_\theta$. It is noted $\overline{\mathbf{X}}$ and is built as the arithmetic average of azimuthally-equireparted slices of temporally-equireparted samples of $\mathbf{X}$ or in other words

$$\overline{\mathbf{X}} (r, z) = \frac{1}{N_t N_\theta} \sum_{i=1}^{N_t} \sum_{j=1}^{N_\theta} \mathbf{X} (r, \theta_0 + j\Delta\theta, z, t_0 + i\Delta t) \tag{4.3.3}$$

This operator produces a two-dimensional field located in the (r, z) plane that gives an axisymmetric approximation of the three-dimensional mean field - in other words

$$\text{if } \frac{\partial \mathbf{X}}{\partial \theta} \equiv 0 \text{ then } \forall\, \theta \in [0, 2\pi]\,,\ \langle \mathbf{X} \rangle_t(r, \theta, z) = \overline{\mathbf{X}}(r, z) \tag{4.3.4}$$
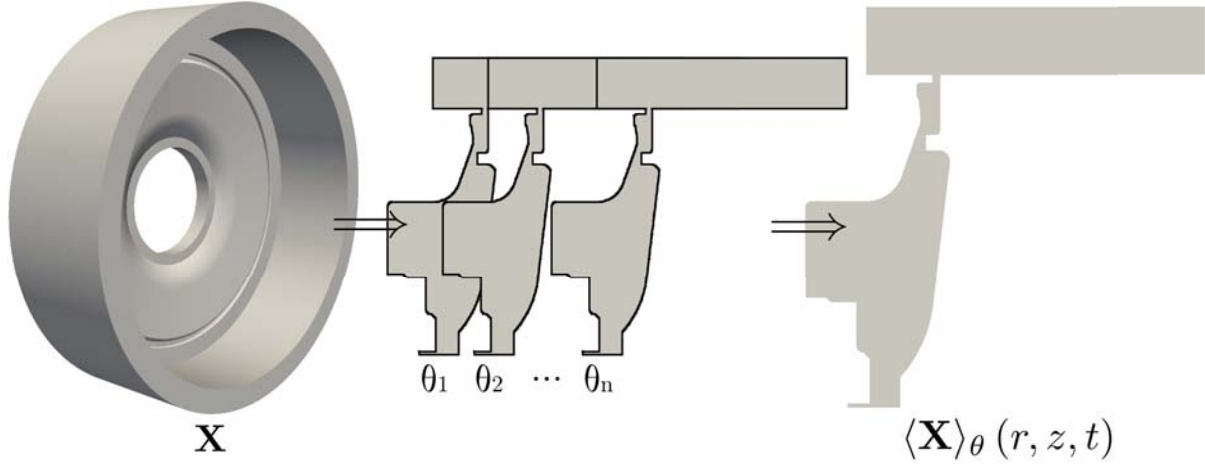
Figure 4.7 – Visual representation of the azimuthal averaging operator $\langle \cdot \rangle_\theta$ (Eq. (4.3.2))

Naturally, similarly to the temporal average (see Eq. (4.3.1)), this operator has no dependence on time if and only if the samples $\mathbf{X}(r, \theta_j, z, t_k)$ are all taken when the flow is temporally converged.

All such manipulations serve different purpose and all three will be used in what follows, but unless otherwise specified two discretization parameters will be kept constant, that is the number of azimuthal samples $N_\theta = 360$ and time samples $N_t = 40$, taken for $t \approx 3$ periods to $t \approx 26$ periods, i.e. $\Delta t \simeq 0.6$ periods apart. By default the transient (see Fig. 4.5) is consistently removed and the operators rely on solutions only extracted during the limit energetic cycle where the flow is statistically stationary.

4.3.2 Quality of the LES predictions

As mentioned in the introduction, the first goal of the present investigation is to assess the capacity of wall-modelled LES to correctly predict the flow in an industrial grade rotor/stator cavity. The literature is however scarce when it comes to experimental data or reference numerical simulations for such complex flows and as a consequence in this section we intend to compare the LES predictions for **Cases 1** to **3** against results obtained in smooth rotor/stator cavities at approximately the same characteristic dimensionless numbers. Within the portions of C_1 where the distance between the rotor and the stator is approximately constant, the base flow would indeed be expected to behave similarly to that within a smooth annular rotor/stator cavity such as those studied in Chap. 3 (refer to Serre *et al.*, 2001; Séverac *et al.*, 2007, for more details).

Based on this remark, four stations have been identified in C_1 and C_3 (see Fig. 4.1) around the radial locations r_1, r_2, r_3 and r_4 (see Sec. 4.2.1.a). Figure 4.8a (resp. *b*) shows the evolution of the axial (resp. radial) Reynolds number $Re_h = h^2\Omega/\hat{\nu}$ (resp. $Re_r = r^2\Omega/\hat{\nu}$) with the radial coordinate. Note that in those expressions, $\hat{\nu}$ is the mean kinematic viscosity at the corresponding radial station, i.e. $\hat{\nu}(r) = \int_{z_{\min}}^{z_{\max}} \nu(r, \xi)d\xi$. All trends are in very good agreement. It is however noteworthy that with a warm shaft Species$_1$ leak (I_1, **Case 3**), both Reynolds numbers everywhere in C_1 decrease by about an

order of magnitude due to the different evolution of viscosity with the temperature of the near wall fluid. Interestingly, this operating condition change brings the radial Reynolds number around r_1 and r_2 below 10^6, thus hinting at the possibility of a transitional rather than a fully turbulent flow in the rotor and stator boundary layers (see e.g. results by Séverac *et al.*, 2007; Serre *et al.*, 2001).
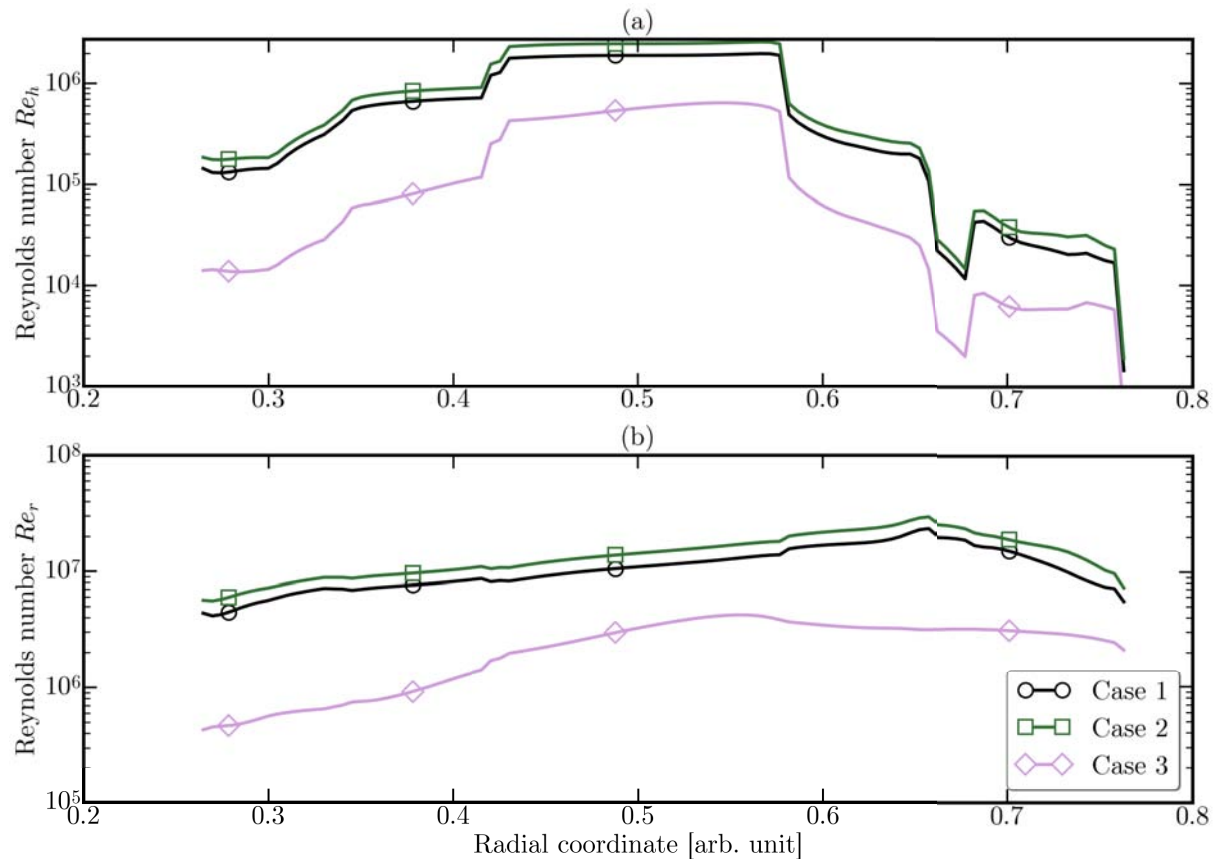

Figure 4.8 – Evolution with the dimensionless radial coordinate of (a) the axial Reynolds number $Re_h = h^2\Omega/\hat{\nu}$ and (b) the radial Reynolds number $Re_r = r^2\Omega/\hat{\nu}$. The four locations of extraction r_1, r_2, r_3 and r_4 are marked by symbols and the viscosity is defined by $\hat{\nu}(r) = \int_{z_{\min}}^{z_{\max}} \nu(r,\xi)d\xi$

Figure 4.9 shows the axial profiles of the dimensionless mean radial $u_r^* = \overline{u_r}/(r\Omega)$ and azimuthal $u_\theta^* = \overline{u_\theta}/(r\Omega)$ velocity components at all four extraction locations (see Fig. 4.1a) and for all three configurations, compared to the auto-similar laminar solution by Rogers & Lance (1962) computed at the corresponding axial Reynolds number Re_h. Note that strong caution is advised regarding the interpretation of the results that follow. First, the solutions proposed by Rogers & Lance (1962) were designed to match the evolution of a laminar flow between two infinite discs, which is not the case here as there are some strong geometrical effects due to the rapid changes in aspect ratio within C_1 (see below). Second, the flow in all three cases is undoubtedly strongly turbulent and as such may at best qualitatively behave like the self-similar solutions. All this being said, it is therefore not surprising that contrary to the academic cavities (Chap. 3) that could be exactly classified under the categories established by Daily & Nece (1960) (see Sec. 2.1.3,

Fig. 2.7), the present results show more variability.
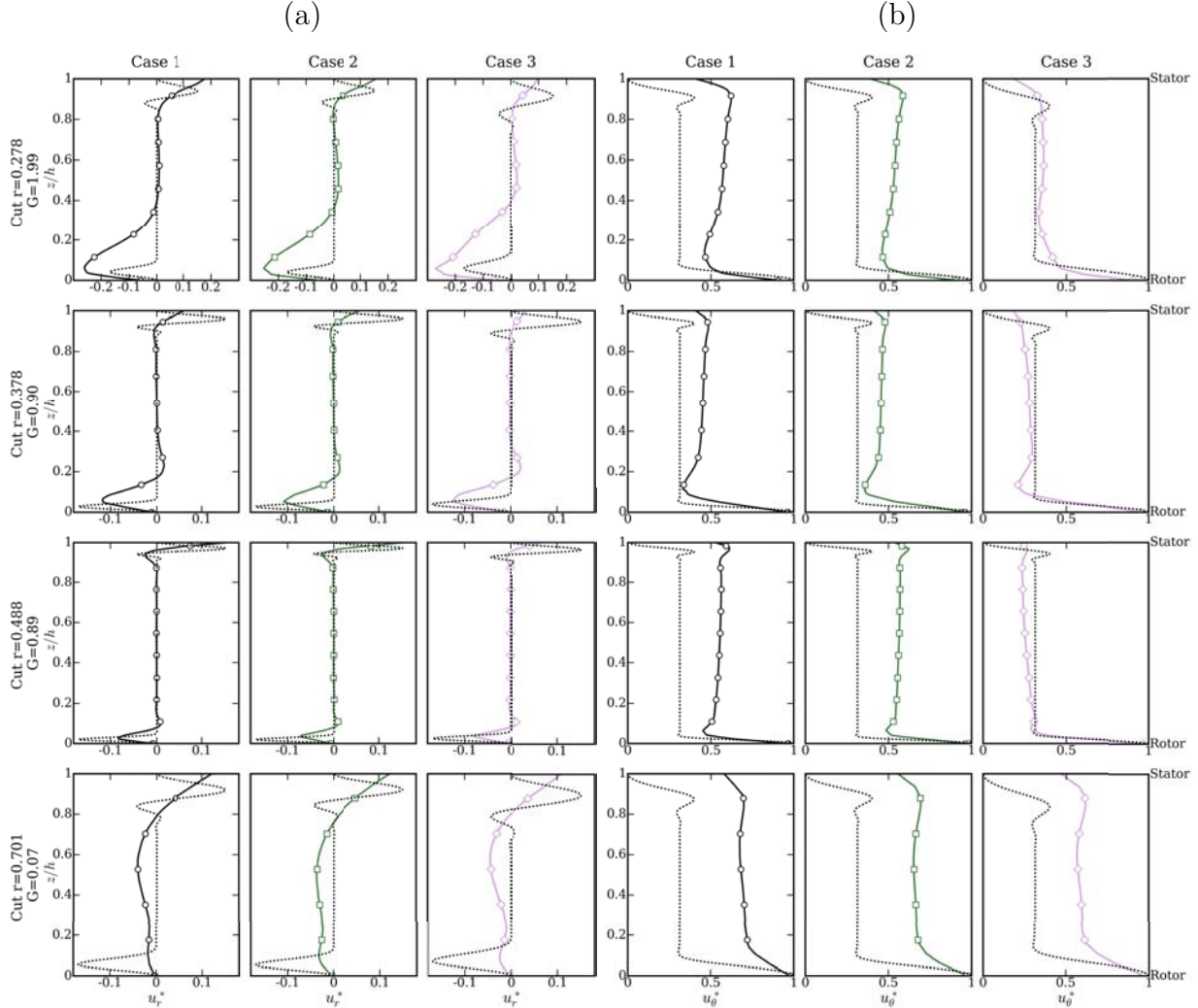
Figure 4.9 – Axial profiles of the dimensionless mean (*a*) radial u_r^* and (*b*) azimuthal u_θ^* velocity components extracted at the locations indicated on Fig. 4.8*a*. Comparison between (symbols) the LES results and (- -) the auto-similar laminar solution from Rogers & Lance (1962) at the ad-hoc axial Reynolds number (see Fig. 4.8*b*-top).

At r_1, r_2 and r_3 the mean flows display separated boundary layers. According to Daily & Nece (1960) predictions, such a behaviour coupled to the very high radial Reynolds numbers at the extraction locations qualifies all three flows as regime IV flows. However, and it is especially obvious at r_1 and r_2, the discs boundary layers predicted by the LES are markedly thicker than the laminar solution, when one would expect thinner boundary layers for the high rotor speed regime IV flows. This specific behaviour can however be better understood if one considers the two following points. First on the stationary disc, the law-of-the-wall (Eq. (4.2.1)) used as boundary treatment is constructed to work best if the normal coordinate at the wall $n^+ \simeq 30$ whereas in the present cases it is one to two orders of magnitude greater (Fig. 4.4), leading to a biased estimation of the velocity

Figure 4.10 − Locations of the seeds for the streamlines computations. (■) Single particle is tracked from that location. (▬) 10 particles are seeded at the corresponding radial location. All seeding locations are duplicated at azimuths $\theta = 0, \pi/2, \pi, 3\pi/2$.
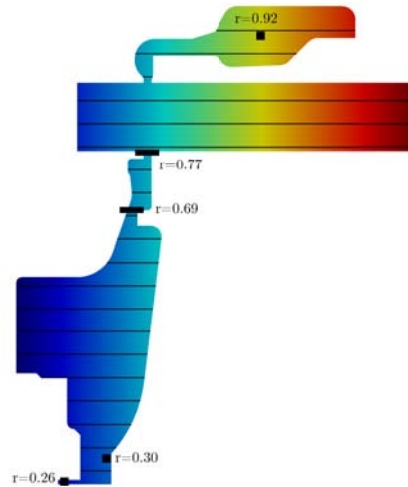
profiles close to the stator. Note that in **Case 3**, the values of n^+ are closest to the accepted range of accuracy of the law-of-the-wall, the differences between the theoretical and the LES azimuthal velocity profiles are smallest too. The same remark applies to the rotating disc, for which it was thoroughly proven (see Chap. 3) that obtaining a correct estimate of the boundary layer profiles on the disc is contingent upon the first mesh node being such that $n^+ \simeq 30$, whereas again in the present cases the probability of finding nodes with $n^+ \gg 30$ is not negligible. At r_4 on the other hand, the radial velocity u_r^* profile hardly resembles a classic rotor/stator velocity profile and it is therefore unreasonable to conclude on the nature of the mean flow. However, by comparison with the examples provided by Daily & Nece (1960), it can be seen that the azimuthal velocity profiles u_θ^* actually present two merged boundary layers, and one can say that these flows belong to regime III (described as "turbulent flow, close clearance" by the aforementioned authors).

Finally, the discrepancies between the values of u_θ^* predicted by the LES and given by the auto-similar laminar profile (Rogers & Lance, 1962) in the core of the flow (i.e. where $u_r^* \simeq 0$) provide an illustration of the effect of cavity enclosure on the mean flow that has already been discussed in Chap. 3. In the present configurations however, it is reasonable to think that the sudden changes in aspect ratio from one portion to the next are responsible for strong deviations of the flow from a self-similar (laminar) solution. Such geometrically different sub-cavities in the configurations is actually believed to be of utmost importance to qualify the mass exchanges and flow organization as well as unsteady activity inside the geometries and shall be discussed in more details in Sec. 4.3.3 and Sec. 4.4.1.

4.3.3 Streamlines and confinement

Mean flow streamlines issued by the three present cases gives a first approximation of the regions of mass exchanges between the cavities. Note that it is important to underline that the fluctuations of the velocity field might locally change the behaviour of the fluid particles, but these potential deviations are discussed more thoroughly in Sec. 4.4.1. To properly evaluate the fluid particles motion everywhere in the geometry, several seeding points have been used as starting positions for the streamlines reconstruction ; these locations are summarized on Fig. 4.10.

The two first locations at $r = 0.26$ and $r = 0.30$ have been chosen to study the mean trajectories of particles from their injection in the cavity through the inlet I_1 (see Fig. 4.1). Figure 4.11 shows the comparison of such streamlines for all three cases and obtained after an integration time of approximately 5 periods. As evidenced by these results, all particles injected through I_1 are projected axially downstream and move along the rotor, subject to a centrifugal acceleration. In all three cases, it is of note that within 5 periods of the rotor, all particles stay confined in C_1 and only about 25 % of the injected particles successfully move beyond the locking ring into C_3. As an intermediary conclusion, it therefore appears that the sharpness of the edge of the locking ring (i.e. at $r = 0.63$) expectedly acts as a non-isotropic stagnation point such that, in its vicinity, particles are only allowed to travel azimuthally.

Figure 4.11 – Streamlines seeded at $r = 0.26$ and $r = 0.30$ for (*a*) **Case 1**, (*b*) **Case 2** and (*c*) **Case 3**, integrated over 5 periods. The tubes are coloured by the age of the fluid particle.

The third seeding line (at $r = 0.69$) allows to focus on the behaviour of the fluid particles when they have already moved passed the locking ring - the results are shown on Fig. 4.12. Contrary to the quasi-homogeneous behaviour of the particles in the previous case, when particles are injected immediately after the locking ring, three different kind of trajectories can be observed. Most of the particles stay trapped in C_3 but they still appear to evolve radially and axially within the limit of this sub-cavity. Out of the

particles injected, between 16% (**Cases 1** & **2**) and 26% (**Case 3**) move beyond the pass and into C_2 where they are pushed by the strong axial flow towards the outlet O_1. The rest, about 30% of the particles injected on the lines at $(r, \theta) = 0.69 \times [0, \pi/2, \pi]$ travel centripetally along the stator wall and back into C_1.
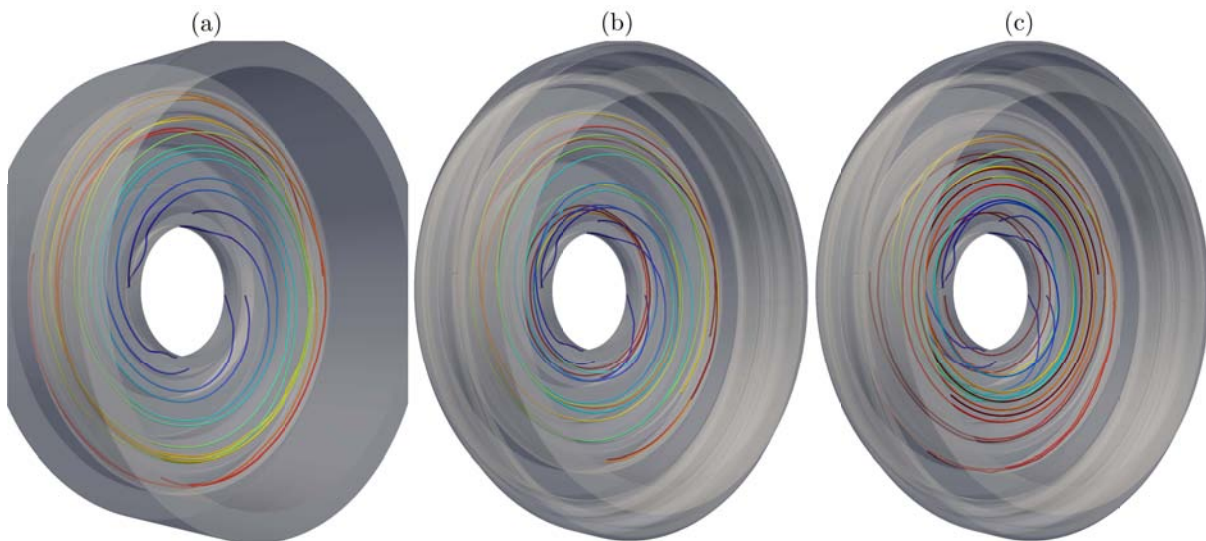

Figure 4.12 – Streamlines seeded at $r = 0.69$ for (*a*) **Case 1**, (*b*) **Case 2** and (*c*) **Case 3**, all integrated over 5 periods. The tubes are coloured by the age of the fluid particle.

The streamlines starting at $r = 0.77$ (see Fig. 4.13) represent the average path taken by particles funnelled through the shear layer between C_3 and C_2. To the exception of one particle that goes back towards C_1 (**Case 2**, Fig. 4.13*b*), all particles placed along the C_3-C_2 shear layer move into C_2 and are pushed towards O_1 by the strong axial flow. From the three previous observations, it can therefore be gathered that C_3 is a sub-cavity where, on average, a strong mixing takes place that prevents large mass exchanges from occurring between C_1 and C_2.

Finally, the outermost seeding location (at $r = 0.92$) allows to evaluate the mean motion of the fluid in C_5, mainly to assess whether there is some mass exchange between C_5 and C_2. Figure 4.14 shows the streamlines obtained in **Cases 2** & **3** for an integration time close to 5 periods. The conclusion is identical in both cases: on average, the fluid particles found in C_5 are confined in the sub-cavity and there is no interaction with the flow in C_2.

This analysis of the flow confinement is continued in the next section (Sec. 4.4) with the study of the time-resolved streaklines, but already it seems clear that the mass transfers between C_1 and C_2 (as well as between C_2 and C_5 in **Cases 2** & **3**) are very limited such that the unsteady phenomena that could be observed with the LES are rather likely to be caused by wave-like perturbations.
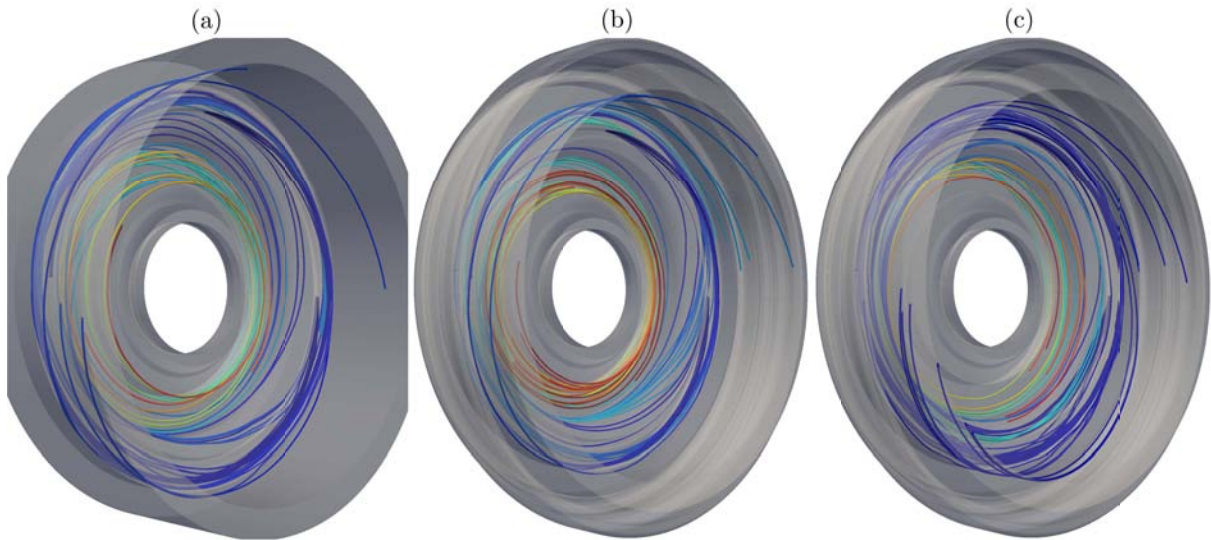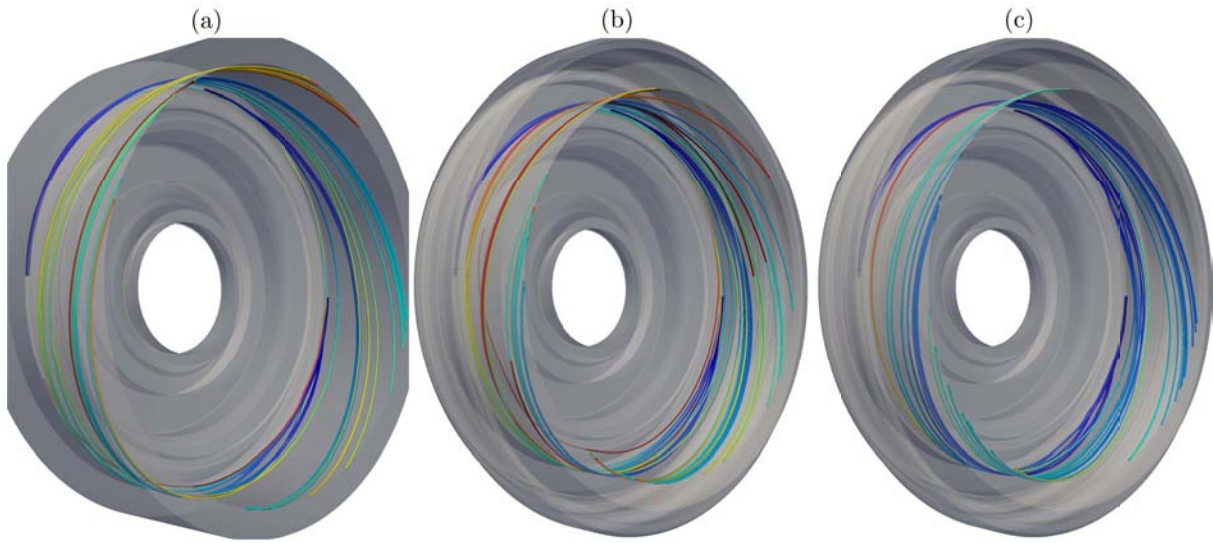
Figure 4.13 – Streamlines seeded at $r = 0.77$ for (a) **Case 1**, (b) **Case 2** and (c) **Case 3**, integrated over 5 periods. The tubes are coloured by the age of the fluid particle.
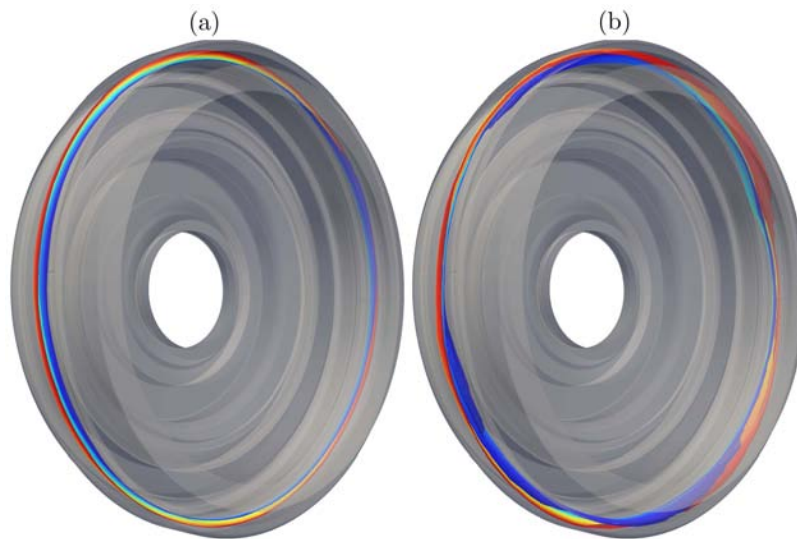
Figure 4.14 – Streamlines seeded at $r = 0.92$ for (a) **Case 2** and (b) **Case 3**, integrated over 5 periods. The tubes are coloured by the age of the fluid particle.

4.3.4   Base flow

To conclude this section detailing the mean behaviour of the flow in the three configurations under study, the following paragraphs present succinctly the base flow solutions, that we define as being axisymmetric and steady, along with the root-mean-square fluctuations as a first approximation of the zones of highest activity in the cavities. Given the definition of the 'base flow', please note that all averaged quantities below are produced using the ensemble operator $\overline{\mathbf{X}}$ described in Eq. (4.3.3).

Figure 4.15 shows the contours of the average static pressure field $\overline{P}_s$ in all three configurations - the colorbar indicated for **Case 1** (Fig. 4.15a) is also valid for **Cases**

2 & **3**. First of all, there is no doubt that in all three cases, the centrifugal acceleration created by the rotating disc induces a strong radial compression of the fluid, as expected. Comparing the two figures Fig. 4.15*a* and Fig. 4.15*b* also reveals that the addition of C_5, all other parameters being kept constant, induces a decrease in pressure in the bottom half of C_1. Injection of warm Species$_1$ through inlet I_1 (**Case 3**, see Fig. 4.1 for legend) on the other hand participates in reducing the levels of static pressure everywhere in the cavity, with a maximum reached in C_5 at approximately 0.875, to be compared to the 0.95 in **Case 2** and 0.9 at the top of C_2 in **Case 1**.

Figure 4.15 − Contours of the averaged static pressure $\overline{P}_s$ for (*a*) **Case 1**, (*b*) **Case 2** and (*c*) **Case 3**. The the range indicated in (*a*) is valid in all three cases.

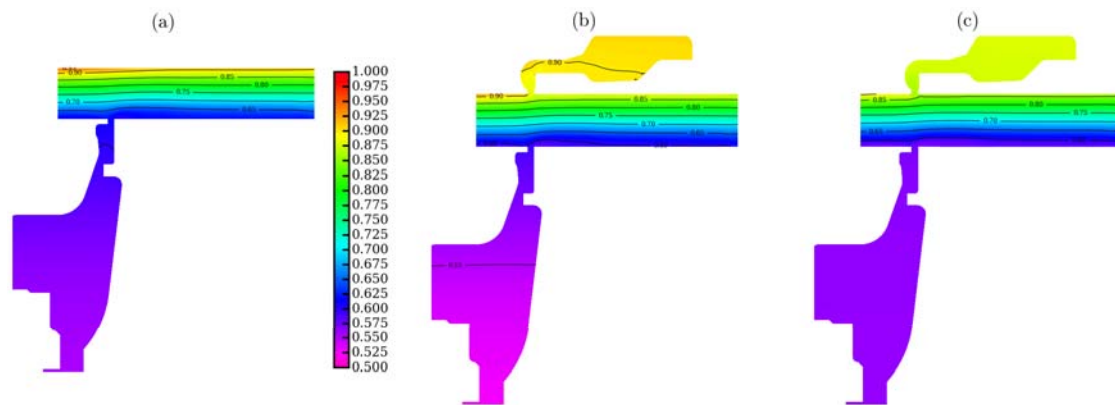The streamlines detailed in the previous section (Sec. 4.3.3) showed, among other things, that particles injected through I_1 were projected against the rotating disc and accelerated centrifugally along the rotor wall until they reached the sharp edge of the locking ring at $r \simeq 0.63$. This phenomenon is clearly visible on Figs. 4.16*a* & 4.16*b* where the stream of cold Species$_1$ is coloured in bright pink and can indeed be seen to follow the rotor wall closely. Again, the addition of C_5 induces some minor changes in the thermodynamic behaviour of the flow in the whole cavity and warming the fluid entering the cavity through I_1 participates in raising markedly the average level of static temperature everywhere in C_1.

The phenomenon occurring at the transition between C_3 and C_2 remains of greater interest: expectedly, the static temperature varies rapidly in the vicinity of the pass, but it is remarkable that the temperature gradient extends far in C_3 (down to $r \simeq 0.68$ approximately in **Case 1**). This supports the remark made previously (see Sec. 4.3.3) that C_3 appears to be a sub-cavity where most of the mixing between the warm flow from I_2 and the fluid in C_1 occurs. Naturally, as shown (for example) by the contours of static pressure RMS (Fig. 4.17), the C_3-C_2 pass concentrates most of the activity of the flow - and so does the C_2-C_5 pass where similar phenomena occur.

A final comment can be made about the thermal segregation of the fluid in C_2 (see Fig. 4.16), where colder fluid is concentrated in the centre of the channel and surrounded by warmer layers. It occurs both up- and downstream of the C_3-C_2 pass but while the temperature at the wall seems constant near I_2 for all three cases, the bottom of the channel extension (see Fig. 4.3) is markedly warmer in **Case 3**. These warmer layers
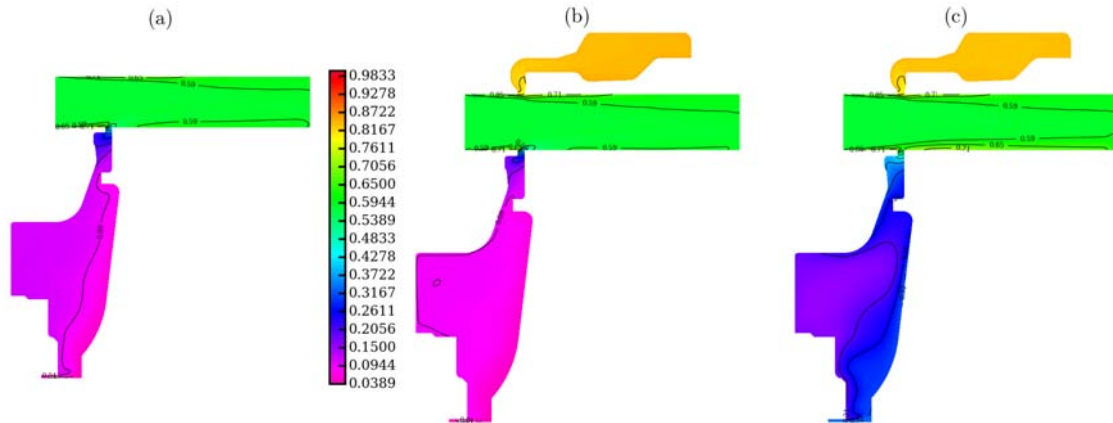
Figure 4.16 – Contours of the averaged static temperature $\overline{T}_s$ for (*a*) **Case 1**, (*b*) **Case 2** and (*c*) **Case 3**. The range indicated in (*a*) is valid in all three cases.
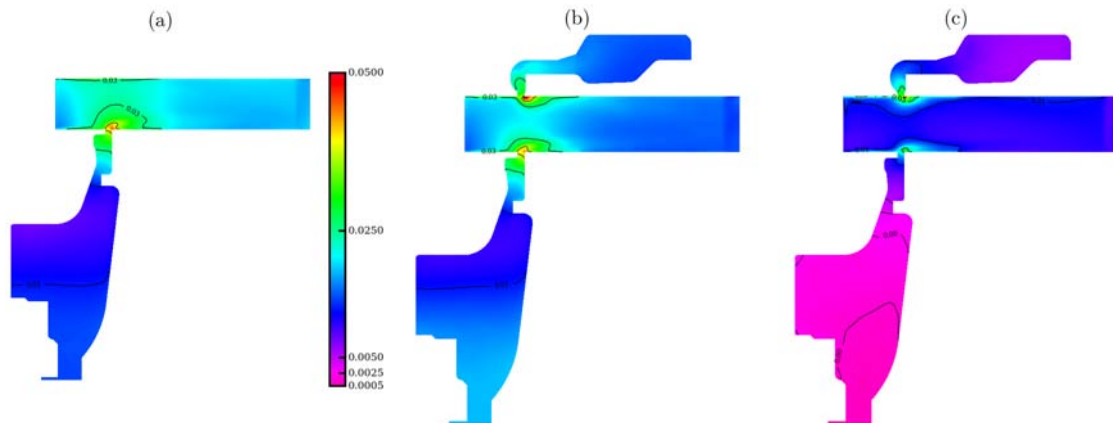
Figure 4.17 – Contours of the static pressure RMS P_s^{RMS} for (*a*) **Case 1**, (*b*) **Case 2** and (*c*) **Case 3**. The range indicated in (*a*) is valid in all three cases.

match zones of higher wall friction in C_2 as can be deduced from the contours of average axial velocity presented on Fig. 4.18.

4.4   Detailed analysis of the cavity flow dynamics

The main objective of the present section is to pursue the investigation of the three computations thanks to an in-depth study of the dynamics of the flows. A study of the streamlines obtained from the average velocity field (see Sec. 4.3.3) revealed how scarce the mass exchanges between the cavity seem to be: this issue will be tackled in more detailed by looking at how fluid particles travel within the instantaneous velocity field. The presentation of some root-mean-square fields (see Sec. 4.3.4, Fig. 4.17) allowed to pinpoint the zones of most activity in the turbine stage, and this analysis shall also be continued in the present section. The examination of these zones of oscillations is supplemented with spectral considerations to evidence the three-dimensional underlying
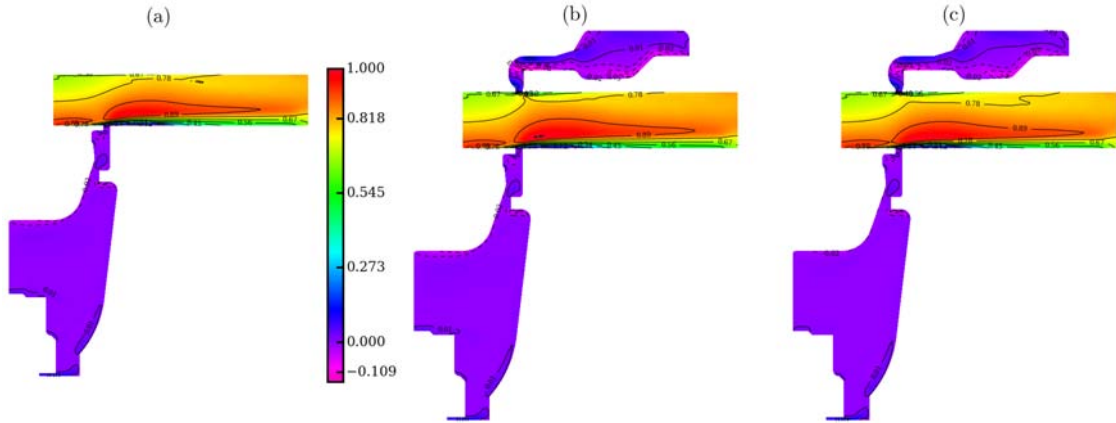
Figure 4.18 – Contours of the averaged axial velocity $\overline{u}$ for (*a*) **Case 1**, (*b*) **Case 2** and (*c*) **Case 3**. The velocity is expressed in m/s and the range indicated in (*a*) is valid in all three cases.

modal organization of the flow. All these diagnostics will allow us to ascertain whether mass exchanges occur in-between the sub-cavities (C_1, C_2, C_5), and aim at improving our understanding of the pressure fluctuations that were the original motivation for the present study (see Sec. 4.1) and use of LES.

4.4.1 Presentation of the inner dynamics

4.4.1.a Two-dimensional projection & particle tracking

As an introduction to the dynamics of the flow in the rotor/stator cavity, this section focuses on two-dimensional pathlines drawn from the LES predictions obtained for Case 3. Eventually, this investigation aims at supporting the conclusions about the confinement of the flow in sub-cavities reached in Sec. 4.3.3 and capturing the radial and axial displacements of the particles appears consequently more critical than accurately pinpointing their azimuthal motion. This allows us to reduce the cost of the pathlines computation by forcing to zero the azimuthal velocity component and therefore working in an (r, z) plane upon which we project all particle trajectories.

To avoid any misinterpretation due to numerical and/or physical transients not being fully evacuated, the pathlines are drawn from $t_{\text{path},0} = 0.0249$ s to $t_{\text{path,max}} = 0.0532$ s with $\Delta t_{\text{path}} = 10^{-4}$ s, such that all instantaneous solutions are taken when the flow has reached global equilibrium (see Fig. 4.5). As for streamlines, several injection stations were tested to characterize the behaviour of the different sub-cavities: in C_5, close to the inlet I_2 of the channel C_2 and close to the inlet I_1 of the rotor/stator cavity C_1 (refer to Fig. 4.1 for the notations). Figure 4.19 presents the results respectively in subplots (*a*), (*b*) and (*c*) where the particles have been coloured by their age relative to the seeding at $t = t_{\text{path},0}$.

The agreement with the behaviour suggested by the meanflow streamlines (Sec. 4.3.3) is excellent. The first remark is that the confinement of the particles within C_5 is indeed very effective, although it appears that given time, about 20% of the particles escape to C_2 where they are promptly driven towards O_1 by the strong axial current. The latter
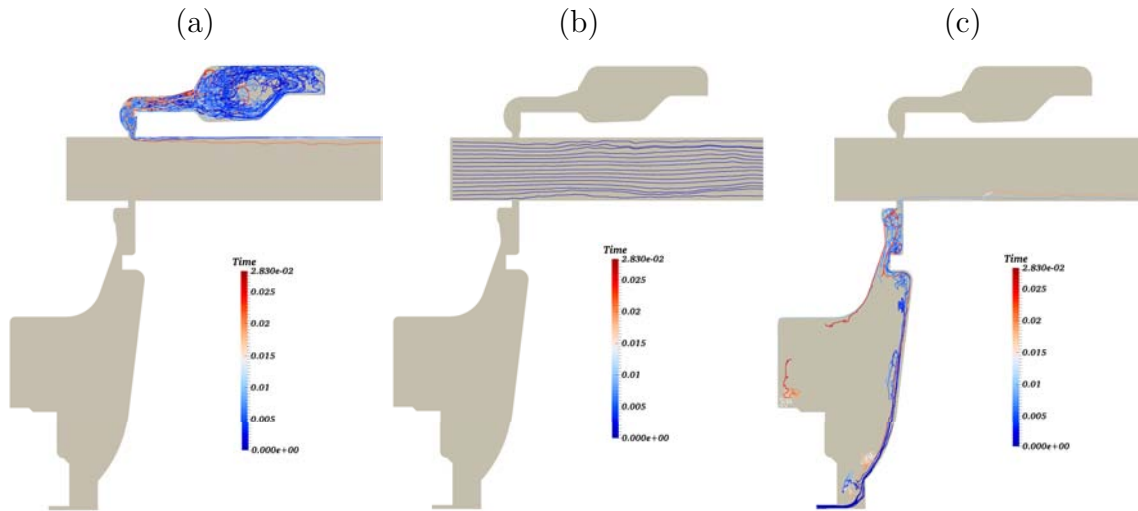
Figure 4.19 – Projection upon an (r, z) plane of pathlines obtained with solutions from Case 3, seeded (a) in C_5, (b) close to the inlet I_2 of the channel C_2 and (c) close to the inlet I_1 of the rotor/stator cavity C_1. Colormap is identical in all three subplots and represents the age of the fluid particles in seconds.

can be observed more clearly in Fig. 4.19b. All particles injected near I_2 move directly to O_1 and there is no evidence of particles flowing into C_3 or C_5 from there ; note the confinement of the pathlines towards the core of the channel downstream of the C_3-C_2 & C_2-C_5 passes corresponding to particles avoiding the boundary layers already discussed in Sec. 4.3.4. The data also support the fact that C_3 is a zone of intense mixing where most particles stay trapped since, even after almost 0.03 s, only about 10% of the particles injected close to I_1 find they way to C_2. All in all, considering those particles that flow from C_1 (or C_5) to C_2, it is clear that there are no direct mass exchanges between C_1 and C_5 because of the strong axial current present in C_2 that eject all particles out of the cavity through O_1.

This concludes the investigation about the mass exchanges between the sub-cavities within the geometry that have been proven to be scarce at best. It will be nonetheless shown later (see Sec. 4.4.2) that the sub-cavities still communicate together, only not with mass transfers but rather *via* hydrodynamic interactions.

4.4.1.b   Macro-structures development

Figure. 4.8b presents the evolution of the radial Reynolds number throughout the geometries and shows how independently of the location, we systematically have $Re_r > 10^5$. According to the literature (see e.g. Serre *et al.* (2001, 2004); Séverac *et al.* (2007)) and to the previous discussion about smooth rotor/stator cavities (see Chap. 3), such high values of Re_r suggest that the boundary layer on the stationary disc is fully turbulent at all radial locations, whereas there remains a possibility that the rotor boundary layer is in a transitional state. To confirm this assumption, Fig. 4.20 shows an isovolume of high Species$_1$ mass fractions ($Y_{\text{Species}_1} \geq 0.75$) in C_1 for all three cases - the walls have been made transparent and the cavities oriented so that the nearest wall is the rotor. Coloured
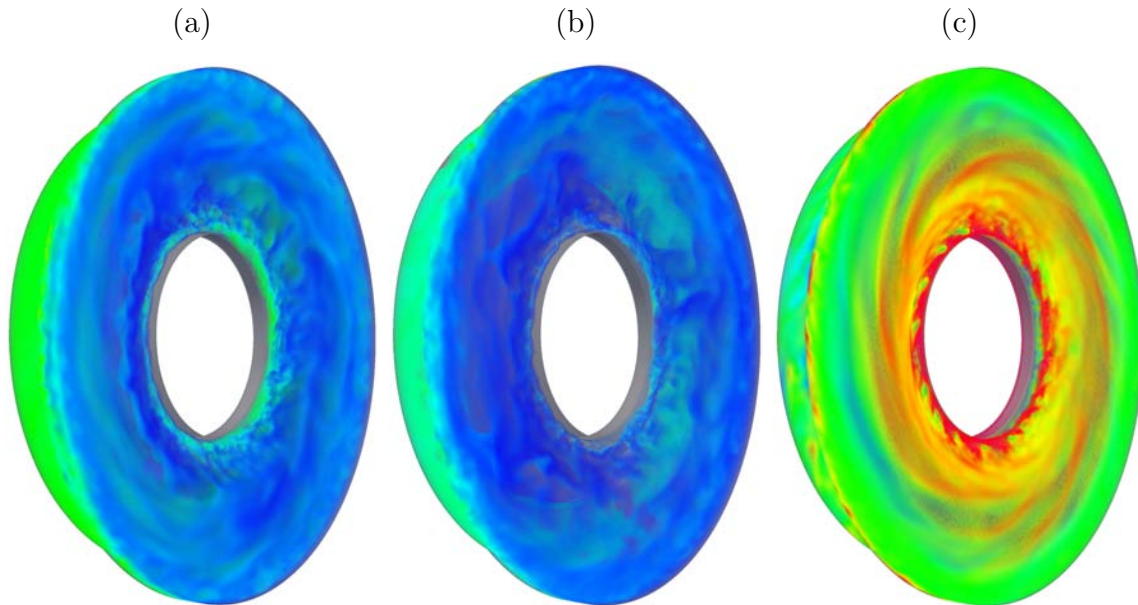
Figure 4.20 – Isovolume of Species$_1$ mass fraction $Y_{\text{Species}_1} \in [0.75, 1.0]$ coloured by the static temperature field T_s in (*a*) **Case 1**, (*b*) **Case 2** and (*c*) **Case 3**. View has been restricted to C_1. The closest wall (right hand side of each subplot) is the rotor wall.

by the static temperature field T_s and post-processed with a volumetric rendering algorithm (Levoy, 1988) to emphasize the hottest structures, the isovolumes of Y_{Species_1} reveal the formation of a spiral pattern along the rotor in **Case 3** similar to the boundary layer instability in a smooth enclosed rotor/stator cavity (refer e.g. to Serre *et al.* (2001), or Chap. 3), whereas the flow is obviously fully turbulent in both **Cases 1** & **2**. The spiral appears confined between the shaft and about mid-radius in the cavity, which is in agreement with what was shown on Fig. 4.8*b* i.e. in **Case 3**, $2 \times 10^5 < Re_r < 10^6$ for $r/r_{\text{max}} \lesssim 0.48$. Interestingly, when the diagnostic is extended to the whole geometry, a very clear coherent pattern also appears close to the bottom wall of C_2, downstream of the C_3-C_2 pass. This structure, present in all three cases, is seen on Fig. 4.21 (the same visualization technique as for Fig. 4.20 is applied to the entire geometry) for **Cases 1** & **2** with values of $Y_{\text{Species}_1} \in [0.5, 1.0]$, and is made of swirling plums of hot gas extending from the C_3-C_2 pass downstream to the outlet O_1 (see Fig. 4.1). In **Case 3** however, it seems that these arms can only be seen to extend throughout C_2 if the lower bound of the interval is slightly decreased, i.e. for an isovolume $Y_{\text{Species}_1} \in [0.48, 1.0]$. Although it is tempting to characterize these C_2-structures as spiral-like, one must note that there is no obvious relation between the C_1-spiral seen in **Case 3** and those C_2-spirals insofar as the author know. The former is indeed most likely due to the rotor boundary layer instability (discussed thoroughly in Chap. 3) whereas the latter follows from a cavity instability as is detailed in Sec. 4.4.2 of the present chapter.

The formation of coherent structures at such high radial location also suggests a departure from the fully turbulent state previously identified in C_3. As mentioned before, the arms appear immediately downstream of the C_3-C_2 pass, in a region where the flow
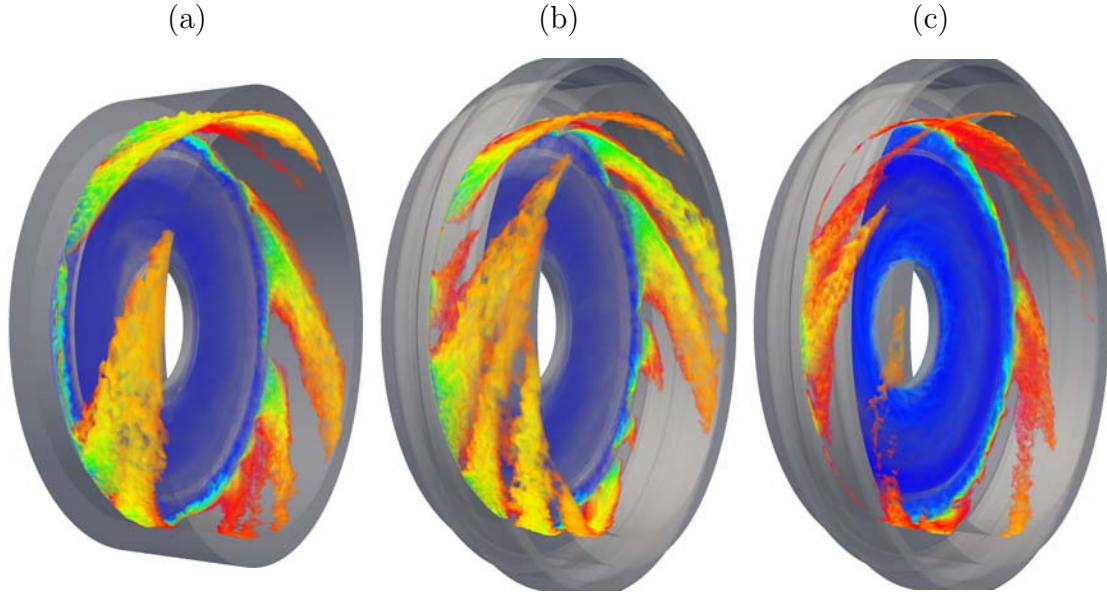
Figure 4.21 − Isovolume of Species$_1$ mass fraction Y_{Species_1} coloured by the static temperature field T_s in (*a*) **Case 1** for $Y_{\text{Species}_1} \in [0.5, 1.0]$, (*b*) **Case 2** for $Y_{\text{Species}_1} \in [0.5, 1.0]$ and (*c*) **Case 3** for $Y_{\text{Species}_1} \in [0.48, 1.0]$. The whole geometry is shown, orientation is similar to that in Fig. 4.20.

behaves like a cylindrical Couette flow due to the combination of the inner cylindrical rotating wall (the bottom wall of C_2, see Fig. 4.3) and the outer cylindrical stationary wall (the top wall of C_2). In this context, the characteristic numbers of the flow become (Andereck *et al.*, 1986; Grossmann *et al.*, 2016) the ratio of radii $= R_0/R_1$, the inner-cylinder Reynolds number $Re_i = R_0(R_1 - R_0)\Omega/\hat{\nu}$ and the Taylor number $Ta = 64(1 +)^4(R_1 - R_0)^2(R_1 + R_0)^2\Omega^2 {}^{-2}\hat{\nu}^{-2}$, where $R_0 \simeq 0.775$ and $R_1 \simeq 0.880$ are respectively the radius of the bottom and top walls of C_2 and $\hat{\nu}(z) = \int_{R_0}^{R_1} \nu(\rho, z)d\rho$. In the present cases, the values of the different dimensionless parameters are summarized in Tab. 4.5, where the abscissa immediately after the C_3-C_2 pass $z = z_{\text{pass}} \simeq 0.165$ was considered to compute $\hat{\nu}$.

	Case 1	Case 2	Case 3
	0.88	0.88	0.88
$\hat{\nu}(z_{\text{pass}})$ [m^2.s^{-2}]	1.95×10^{-5}	2.04×10^{-5}	2.4×10^{-5}
Re_i	3.3×10^5	3.2×10^5	2.7×10^5
Ta	5.2×10^{14}	4.8×10^{14}	3.5×10^{14}

Table 4.5 − Summary of the dimensionless parameters defining the cylindrical Couette flow downstream of the C_3-C_2 pass at the axial location $z_{\text{pass}} = 0.165$.

In spite of the impressive work done by Ostilla-Mónico *et al.* (2014) to extend the parameter space of Andereck *et al.* (1986) toward much larger Reynolds numbers, the three Couette flows obtained in the present cases are at the limit of the known space and
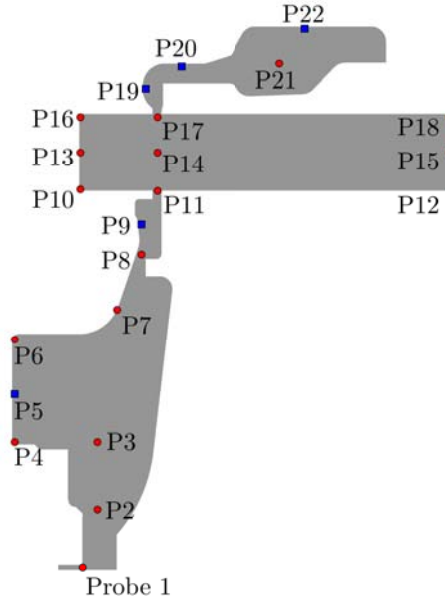
Figure 4.22 – Locations of the numerical probes. Each symbol corresponds to 60 equireparted azimuthally. Blue squares match the locations of probes used during the benchmarking campaigns. Red circles are additions to cover all the cavity.

one can hardly validate the behaviour observed in Fig. 4.21 against published results. Given the stationary character of the outer cylinder however, our three configurations are indeed limit cases about which there remains an uncertainty: it has been shown (see the review by Grossmann *et al.*, 2016) that the flows either display featureless fully developed turbulence, or a fully developed turbulence accompanied by some coherent Taylor rolls (Taylor, 1923), which might be what is observed here. It will however be concluded later that these 'spiral arms' observable in C_2 are simply the continuation of the rotor/stator cavity flow organization activated by the shear layer present at the C_3-C_2 pass.

4.4.2 Complete spectral investigation

This section focuses on a study of the spectral content of the three industrial flows, similar to the modal analysis lead previously in Chap. 3. To monitor the pointwise-temporal dynamics of the flows, a set of numerical probes has been added to the geometry according to the distribution presented on Fig. 4.22. There is a total of 22 circles ($N_p = 22$) of sixty probes ($N_\theta = 60$) positioned everywhere in the cavity to register the unsteady activity of the flow. In the following, note that the probes will be referred to as $P_{x,y}$ where $x \in [\![1, N_p]\!]$ indicates the number of the circle, i.e. the radial location (see Fig. 4.22) and $y \in [\![0, N_\theta - 1]\!]$ is such that $P_{x,y}$ is located at the azimuth $\theta_y = y\Delta\theta = 2\pi y/N_\theta$. Using the Power Spectral Densities (PSD) of the fluctuations of pressure and axial velocity registered by the different probes:

1. LES reports the existence of high-frequency, strong magnitude unsteady phenomena

in the turbine cavity and,

2. these fluctuations are organized spatially within the cavity, pinpointing to zones of greatest activity.

The addition of Cross-Spectral Densities (CSD) allows to characterize more finely the underlying fluctuation organization thanks to the analysis of frequency-dependent coherence factors and phase between sub-cavities. All the conclusions drawn using the pointwise data are finally supplemented by the investigation of the underlying modes using the Dynamic Modal (DMD, Schmid (2010)) analysis.

4.4.2.a   Pointwise temporal activity within the cavities

The study of the spectra yield by the numerous probes placed within the sub-cavities (see Fig. 4.22) revealed a rich spectral content of the cavity flow as well as a great variability of the constituent frequencies depending on the geometrical and thermal configurations. This is clearly visible in Tab. 4.6 where the dominant frequencies are given for each case: the addition of C_5 apparently mostly overrides the high-frequency content of the cavity flow when the temperature increase of the fluid injected through I_1 (see Fig. 4.1) triggers a complete overhaul of the natural response of the flow.

	F_f	F_1	F_2	F_3	F_4	F_5	F_6	F_7	F_8	F_9
Case 1	1.4	—	1.72	2.90	—	4.1	—	5.9	—	—
Case 2	—	—	1.78	—	3.48	—	—	—	—	—
Case 3	—	1.5	—	—	—	—	4.71	—	9.42	13.88

Table 4.6 – Dominant frequencies, in fractions of F_0, in **Case 1**, **Case 2** and **Case 3**. Subscript f indicates a fictitious fundamental frequency for the harmonics F_3, F_5 and F_7.

Figures 4.23-4.25 show the PSD of the fluctuations of static pressure predicted by the LES of **Cases 1**, **2** & **3** (resp.) as registered by probes located at diverse radial stations (refer to Fig. 4.22). In addition to the PSD of the signals, the right hand side of each figure is dedicated to the radial evolutions of the amplitudes of the most important constituent frequencies of the spectra. In **Case 1** (Fig. 4.23), the absence of the outermost cavity C_5 leads to the consideration of only 9 probes from P_1 to P_{17}, at the same axial coordinate. In **Case 2** & **3** however (resp. Figs. 4.24 & 4.25), P_{19}, P_{20} and P_{22} are added to report the activity inside C_5.

In **Case 1**, Fig. 4.23, it appears that the flow is dominated by hydrodynamic oscillations at four distinct frequencies F_2, F_3, F_5 and F_7 (refer to Tab. 4.6). If F_2 is set apart, note that it seems that the other registered frequencies are the second, third and fourth harmonics of a fundamental frequency F_f, that can unfortunately barely be identified on Fig. 4.23 due to a weak Signal to Noise Ratio (SNR) for $F/F_0 \lesssim 1.5$. It is noteworthy that all probes, independently of their location within the cavity, detect the same constituent frequencies only with varying amplitudes. The subplots on the right hand side of Fig. 4.23 indeed show that, for all four frequencies F_2, F_3, F_5 and F_7, the peak

Figure 4.23 – Power Spectral Densities (PSD) of the pressure fluctuations in **Case 1** (left) and radial evolutions of the amplitudes of the dominant frequencies (right).

magnitudes grow as r increases, plateauing at a maximum for $r \gtrsim 0.756$, i.e. in C_3 and C_2. It can also be pointed out that the higher the constituent frequency, the higher the amplitude of the PSD peaks throughout the geometry. A last remark concerns the radial evolution of the amplitude of F_2 which, contrary to the three harmonics of F_f, displays two local maxima: one in C_1 in the region between P_3 and P_7, and the second around P_9-P_{11} close to the C_3-C_2 pass.

For **Case 2**, Fig. 4.24, the addition of the outermost cavity C_5 leads to a simplification of the flow natural response, since only two frequencies now appear to be constitutive of the flow dynamics. First of all, regardless of how different the flows in **Case 1** and **Case 2** are, it appears that $F_2 = 1.78F_0$ is also a dominant frequency of this second case, hinting that adjoining C_5 has little to no impact on the low-frequency dynamics of the flow. The upper-right subplot of Fig. 4.24 shows however that the peak amplitude is on average higher than in **Case 1**, and that the maximum is now reached in the region around P_{19} near the C_2-C_5 pass. On the other hand, instead of the three harmonics of F_f, only one higher frequency remains and appears to be of importance: $F_4 = 3.48F_0$, interestingly such that $F_4 \simeq 2F_2$. The magnitude of this oscillation is greater than that of F_2 throughout the cavity, but it also reaches an absolute maximum around P_{19}. As mentioned during the analysis of Fig. 4.23, the evolution of the amplitude of the low-frequency oscillation (i.e. at $F_2 = 1.78F_0$) is marked by several local maxima, one of which is located within C_3.

For **Case 3**, Fig. 4.25, the temperature increase of the shaft leak (inlet I_1, see Fig. 4.1) induces drastic modifications in the natural response of the flow. In this case, the spectra
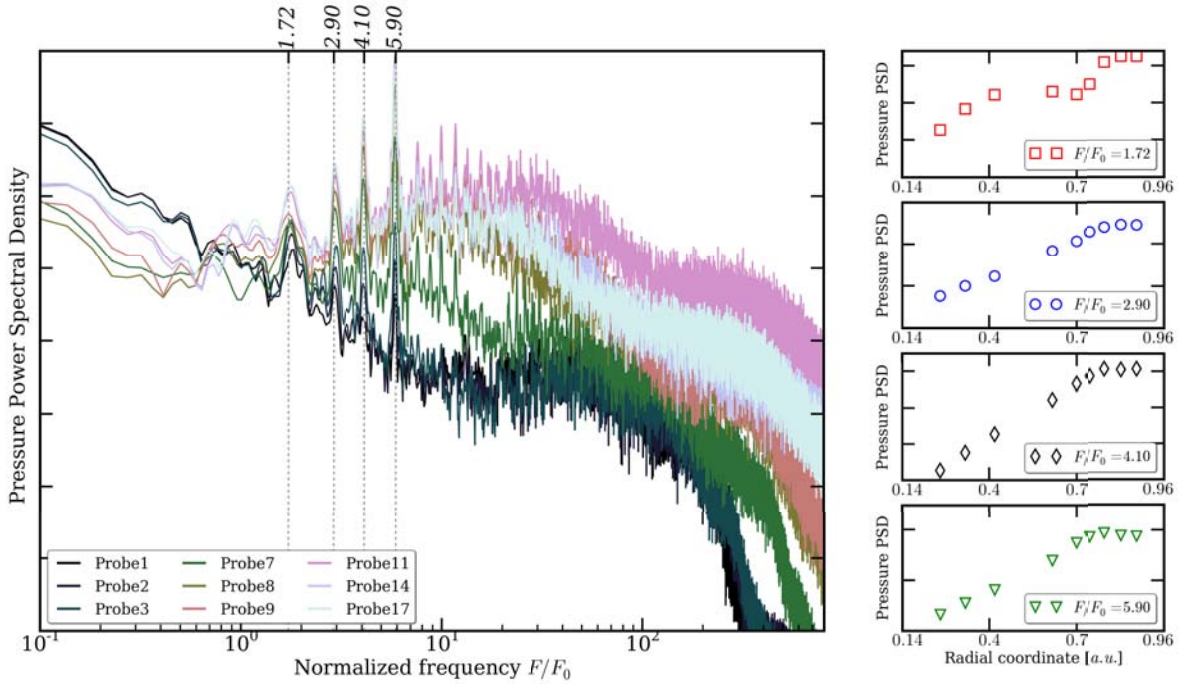
Figure 4.24 – Power Spectral Densities (PSD) of the pressure fluctuations in **Case 2** (left) and radial evolutions of the amplitudes of the dominant frequencies (right).
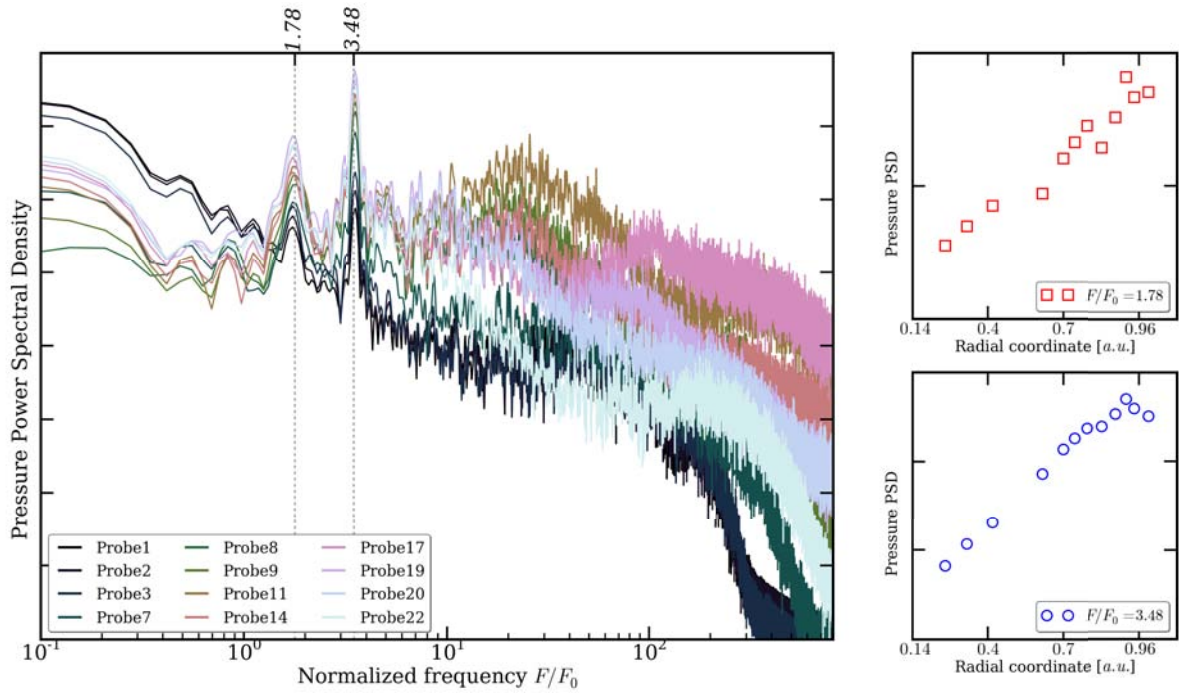

Figure 4.25 – Power Spectral Densities (PSD) of the pressure fluctuations in **Case 3** (left) and radial evolutions of the amplitudes of the dominant frequencies (right).
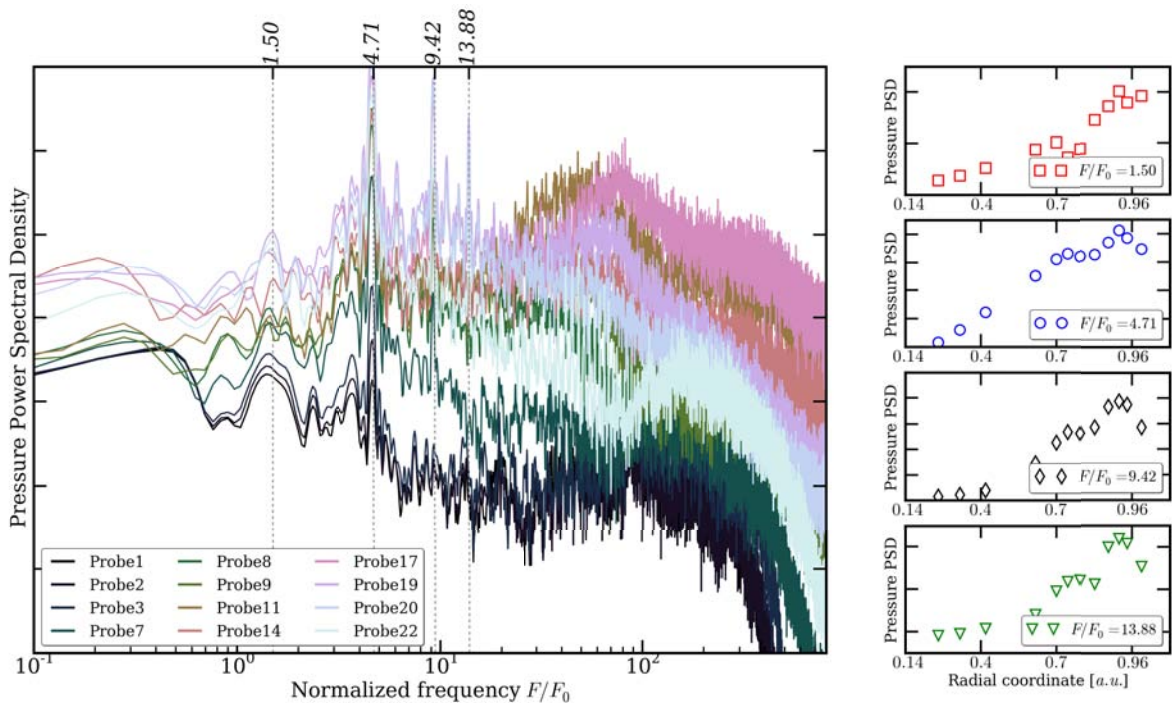
registered by the probes are dominated by four constituent frequencies F_1, F_6, F_8, F_9 (refer to Tab. 4.6), where $F_8 \simeq 2F_6$ and $F_9 \simeq 3F_6$ appear respectively as the second and third harmonics of F_6. It is also remarkable that this warm configuration supports at the same time the smallest and highest frequencies of all cases. In opposition to the previous cases, it is furthermore noteworthy that the constitution of the signals depends on the radial location, and the four aforementioned frequencies can indeed be sorted into two categories: the oscillations at F_1 and F_6 are detected by all probes without regard of their location, whereas the harmonics at F_8 and F_9 have a negligible magnitude within C_1 and only exist in C_3 and beyond. Regarding the radial evolutions of the amplitudes (see subplots on the right hand side of Fig. 4.25), the presence of multiple local maxima is now independent of the frequency, and all four oscillations display a maximum in amplitude in C_3 (in the vicinity of probe P_9, see Fig. 4.22) and another in the region around the C_2-C_5 pass - the latter being also the absolute maximum.
In conclusion, it can be noted that:

- The outermost cavity C_5 plays an important role in the frequency selection process of the rotor/stator cavity flow, and although its impact is limited on frequencies close to that of the rotor (i.e. for $F \quad F_0$), it acts as a band pass filter for higher frequencies, focusing all activity around a single constituent frequency ($F_4 = 3.48F_0$ in **Case 2** and $F_6 = 4.71F_0$ in **Case 3**)

- The temperature increase of the shaft leak in **Case 3** triggers an overhaul of the spectral content:

  - the low frequency F_2 common to both cold cases (**Cases 1** & **2**) is replaced by the lower pulsation F_1
  - while previously the whole cavity responded to the same frequencies, the high radius cavities (i.e. C_3, C_2 and C_5) now excites higher harmonics than the rotor/stator cavity C_1 itself

- Under the simple assumption that the amplitude is strongest close to its source, it can be concluded that the pressure fluctuations propagating within the geometry are created by the strong mixing in C_3 in **Case 1**, and the strong mixing occurring in the region close to the C_2-C_5 pass in **Cases 2** & **3**.

Interactions between the sub-cavities

Before moving on to the spatial description and the identification of specific modes, this last part addresses the question of the communication of the oscillatory activity between sub-cavities. In Sec. 4.4.1.a it was concluded that there is no mass exchange between C_1 & C_2 or between C_2 & C_5, mostly due to the strong axial current in C_2 propelling all fluid particles directly towards the outlet O_1. Nonetheless, the previous analysis shows that in all cases, probes placed in the different sub-cavities capture signals built of the same constituent frequencies, thus proving that energy is actually exchanged between the sub-cavities, albeit most likely *via* wave interactions. Based on this remark,

it is interesting to study the modifications of the wavefronts as they travel from one sub-cavity to the next, especially in terms of loss of coherence and phase-shift. Figure 4.26 shows, in **Case 2** (Fig. 4.26*a* & Fig. 4.26*b*) and **Case 3** (Fig. 4.26*c* & Fig. 4.26*d*), the coherence and phase-shift between pairs of probes at the constituent frequencies (refer to Figs. 4.24 & 4.25).
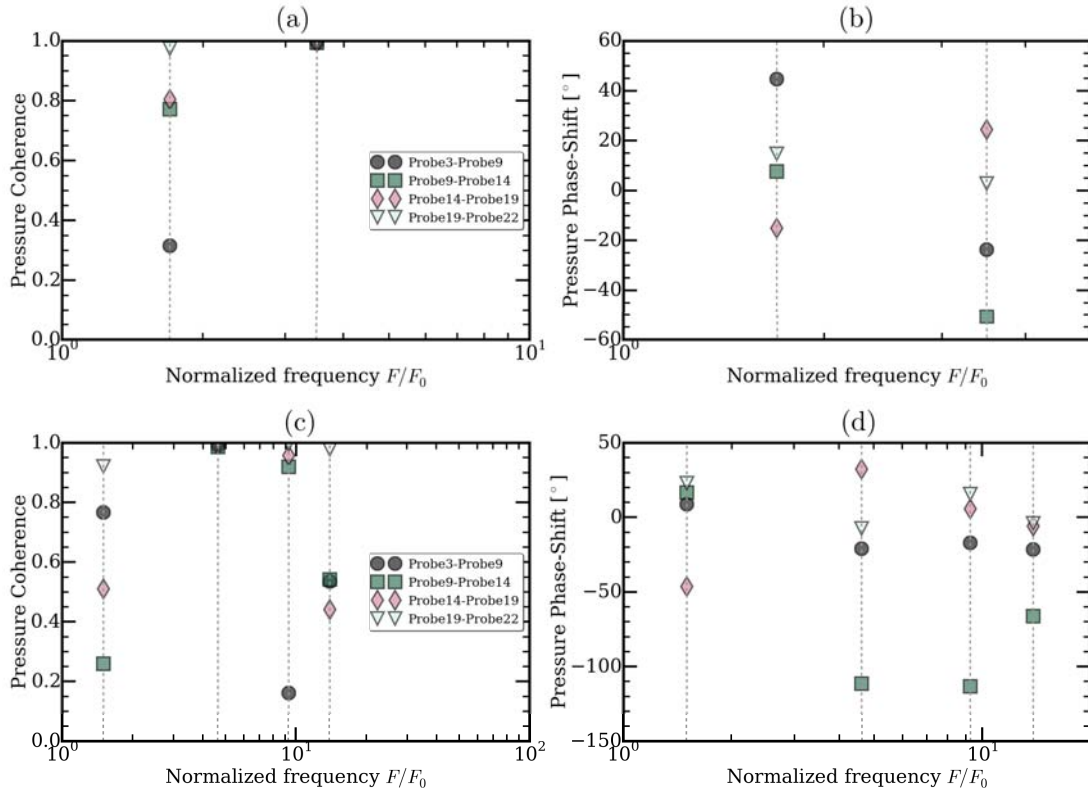
Figure 4.26 – Coherence (*a*, *c*) and phase-shift (*b*, *d*) of the wavefronts at the constituent frequencies spotted in (*a*, *b*) **Case 2** and (*c*, *d*) **Case 3**. Four pairs of probes have been considered to characterize the modal organization throughout the geometry.

In **Case 2** first, the coherence plot shows that the two principal modes do not behave identically in the different sub-cavities. While the geometry appears to act as a perfect linear system for the second mode (coherence at 1.0 everywhere), the first mode seems to organize in three different ways respectively in C_1, C_3 & C_2 as well as C_5. What is more, the weak coherence between the signals from P_3 and P_9 shows that the fluctuations induced by the first mode in C_1 have almost no influence on the behaviour of the mode in C_3, whereas the organization of the perturbations in C_3, C_2 and C_5 look closely related. With regard to the first mode, the phase-shifts between the sub-cavities actually support the conclusions drawn from the coherence data that this mode displays two strictly different behaviours: the fluctuations induced in C_1 on one hand and the fluctuations induced in C_3-C_2-C_5 on the other hand appear to be out of phase. The second mode is again markedly different: although the network of cavities forms a linear transfer function at this frequency, slight phase shifts appear at the transition from one sub-cavity to

the next. It can hence be concluded that in **Case 2**, the hydrodynamic mode with the strongest effect on the flow is the second mode pulsing at F_4.

Figures 4.26*c* & 4.26*d* also shows that in **Case 3**, it is possible to distinguish two types of modes based on their coherence within the geometry. The first mode (at F_1) produces fluctuations which are strongly independent from one sub-cavity to the other, whereas the three other modes (resp. at F_6, F_8 and F_9) appear very coherent within their respective domains of existence, thus indicating that the fluctuations they induce are closely related. According to the phase-shifts observed at these four constituent frequencies (Fig. 4.26*d*), the first mode appears to be strongly impacted by the transition from C_2 to C_5, whereas the spatial organizations of the phases of the three other modes appear very similar (F_8 and F_9 were actually said to be harmonics of F_6) and strongly impacted by the C_3-C_2 transition and weakly by the C_2-C_5 pass. All the remarks drawn from Fig. 4.25 and Figs. 4.26*c* & 4.26*d* tend to show that the second mode pulsating at F_6 seems to be the predominant driver of the dynamics of **Case 3**.

4.4.2.b   Three-dimensional modal organization

Now that a thorough presentation of the spectral content of the flow in each case has been made, this section is dedicated to the understanding of the flow composition or large scale motions and organisation, as it is most likely that each constituent frequency corresponds to a specific cavity mode with a specific underlying structure. To evidence such macro-structures, the DMD algorithm Schmid (2010) is systematically applied on a set of two-dimensional (r, θ)-cuts made at $z = z_{\text{pass}}$. This abscissa is chosen to coincide with the axial location of the C_3-C_2 and C_2-C_5 passes to visualize the spatial organization of the modes in all sub-cavities. The cuts used as input to the DMD algorithm are all taken during the steady phase of the flow every $\Delta t_{\text{DMD}} = 0.06$ periods of the rotor over a duration of 17 periods of the rotor.

An immediate way to present dynamically predominant modes detected by the DMD algorithm first is to plot the modal spectrum yield by the analysis. These spectra, somewhat similar to the PSD presented above, show the magnitude of the primary identified modes against their frequencies. For comparison purpose, Fig. 4.27 shows the DMD spectra obtained in all three cases (**Cases 1**, **2** & **3** resp. at the top, center & bottom), supplemented with markers distinguishing the modes previously identified on the PSD (refer to Figs. 4.23-4.25) and modes given by the DMD only. Note that because of the high value of $\Delta t_{\text{DMD}} = 0.06$ periods, the Nyquist frequency of the DMD process is fixed at $F_{\text{cut}} \simeq 8.3 F_0$, and as a consequence the high-frequency modes found previously in **Case 3** (F_8 and F_9, see Fig. 4.25) are aliased at lower frequencies as indicated in Fig. 4.27 (bottom) by green squares. DMD being not limited by a minimum frequency resolution $1/(N_{\text{DMD}}\Delta t_{\text{DMD}})$ like PSD (refer to Schmid (2010) for a detailed explanation), it usually yields slightly different modal frequencies than PSD if applied to the same signal. In the present cases, the modes of interest are summarized in Tab. 4.7 where the PSD frequencies and the DMD frequencies are compared. Reassuringly, it appears that the results yield by the two techniques do not differ by more than 4.5%.

If one considers the azimuthal organization of the four modes identified for **Case 1**
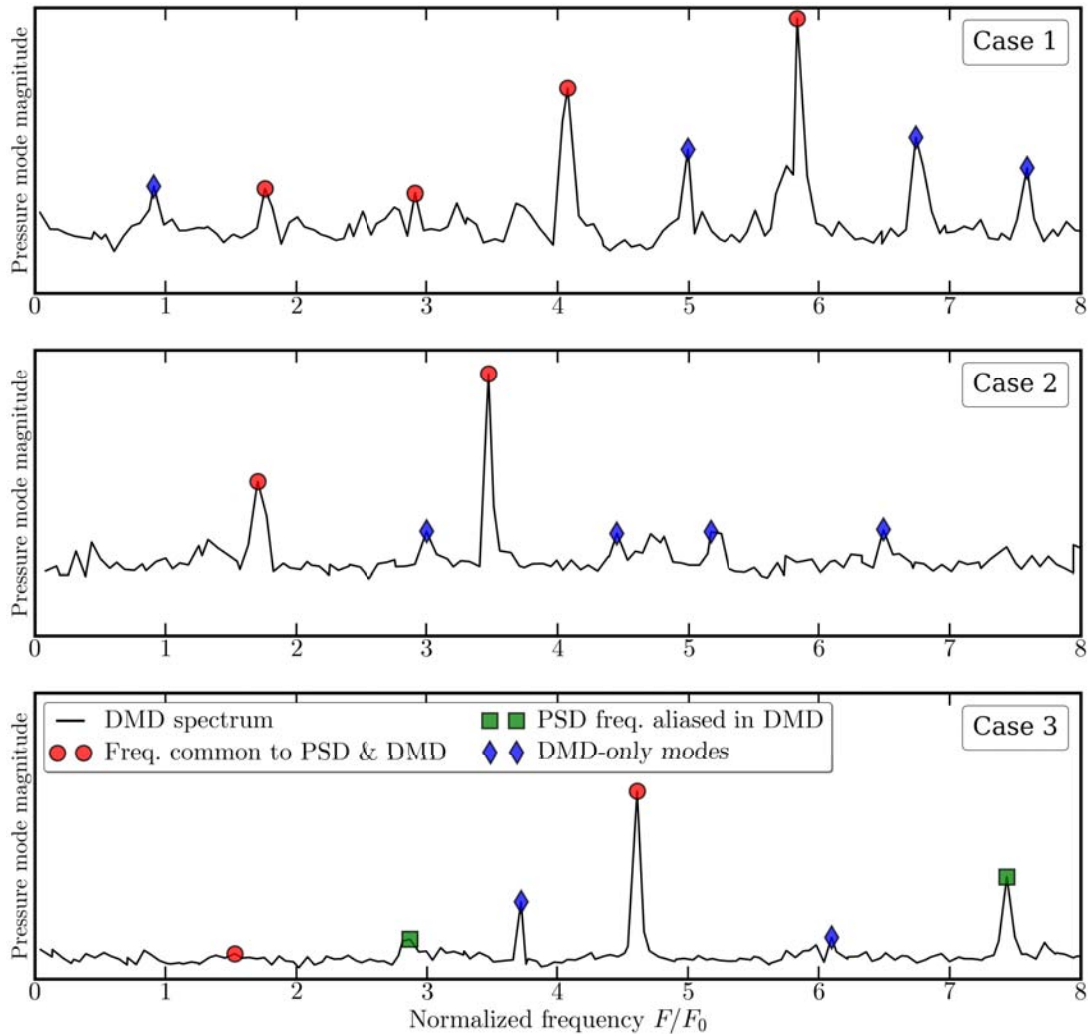
Figure 4.27 − DMD spectrum for (top) **Case 1**, (middle) **Case 2** and (bottom) **Case 3**, obtained with instantaneous snapshots sampled at $\Delta t_{\mathrm{DMD}} = 0.06$ period for a time $t_{\mathrm{DMD}} = 17$ periods. PSD frequencies are indicated with dots. Aliased PSD frequencies are indicated with squares. Extra modes only given by the DMD are indicated with diamonds.

| | Case 1 | | | Case 2 | | | Case 3 | | |
	PSD	DMD	*Rel.*	PSD	DMD	*Rel.*	PSD	DMD	*Rel.*
Mode 1	1.72	1.76	*2.32*	1.78	1.70	*-4.5*	1.50	1.53	*2.0*
Mode 2	2.90	2.91	*0.34*	3.48	3.47	*-0.29*	4.71	4.61	*-2.12*
Mode 3	4.10	4.08	*-0.49*	—	—	—	9.42	9.23	*-2.02*
Mode 4	5.90	5.84	*-1.02*	—	—	—	13.88	13.79	*-0.65*

Table 4.7 − Frequencies (in fractions of F_0) of the modes of interest in **Case 1**, **Case 2** and **Case 3** as given by the PSD (Sec. 4.4.2.a) and the DMD (Sec. 4.4.2.b), and relative difference (in percent). Aliases are unfolded to ease the comparison.

(Fig. 4.28) by DMD, it can be seen that they correspond to four consecutive azimuthal modes whose wavenumber go respectively from $m = 1$ to $m = 4$. This observation would tend to support the first hypothesis formulated during the analysis of Fig. 4.23, that theses modes are four harmonic representations of a fundamental mode pulsating at $F_f \simeq 1.4F_0$.

(a)	(b)	(c)	(d)
$1.76F_0$	$2.91F_0$	$4.08F_0$	$5.84F_0$

Figure 4.28 – Isocontours of the phase of the pressure fluctuations $\arg\left(\tilde{P}_s\right)$ for the four major DMD modes constituting **Case 1** sorted out by their respective frequencies.
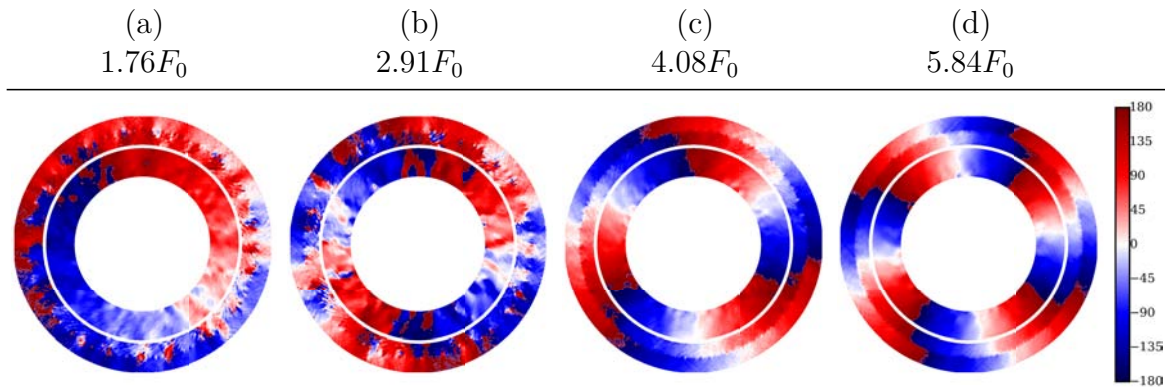
Based on this assumption, it can be further determined that the four extra peaks in the DMD spectrum (see Fig. 4.27, top, blue diamonds) match respectively (from lowest frequency to highest) the 11th, 8th, 7th and 5th harmonics of F_f and that the three first are therefore aliases of the real frequencies. These modes are represented on Fig. 4.29, sorted by the frequency they appear at on Fig. 4.27 (top) and with an indication of their natural frequency if necessary. Put all together, an obvious linear dispersion relation therefore appears between the expressed azimuthal wavenumber and the temporal frequency, that is $F/F_0 \simeq 1.45m$. This dispersion relation is verified by all the modes with a maximum deviation of 21% reached for F_{11} and an otherwise average deviation of 2.2%. A final note about the four main frequencies F_2, F_3, F_5 & F_7 is that the associated DMD modes (Fig. 4.28) exhibit strong phase shifts when passing from to inner cavities to the outer channel C_2. In all cases, the modes are approximately clocked the same way in C_1 and C_3, but going through the shear layer located at the C_3-C_2 pass induces approximate phase shifts of $-90°$, $-70°$, $-45°$ and $-45°$ respectively.

In **Case 2**, as aforementioned, the addition of C_5 to the geometry decreases the number of constituent frequencies driving the dynamics of the flow to two: F_2 & F_4, and we hypothesized that F_4 was most likely a harmonic of F_2. The azimuthal organization of the modes would, once again, tend to support this assumption. Figures 4.30*a* & 4.30*b* indeed show that the mode with frequency F_2 has an azimuthal wavenumber $m = 1$ whereas the one with frequency F_4 organizes the fluctuations as a two-armed spiral, i.e. $m = 2$. The relation between the temporal frequency and the azimuthal wavenumber is then naturally $m = h$, where h is the number of the harmonic of F_2. It can also be expressed as the dispersion relation $F/F_0 \simeq 1.7\,m$ verified by all modes of interest with an average deviation of 1.14%. This linear behaviour is also supported by a third mode that the DMD places at $5.17F_0 \simeq 3F_2$ which displays an azimuthal wavenumber $m = 3$.
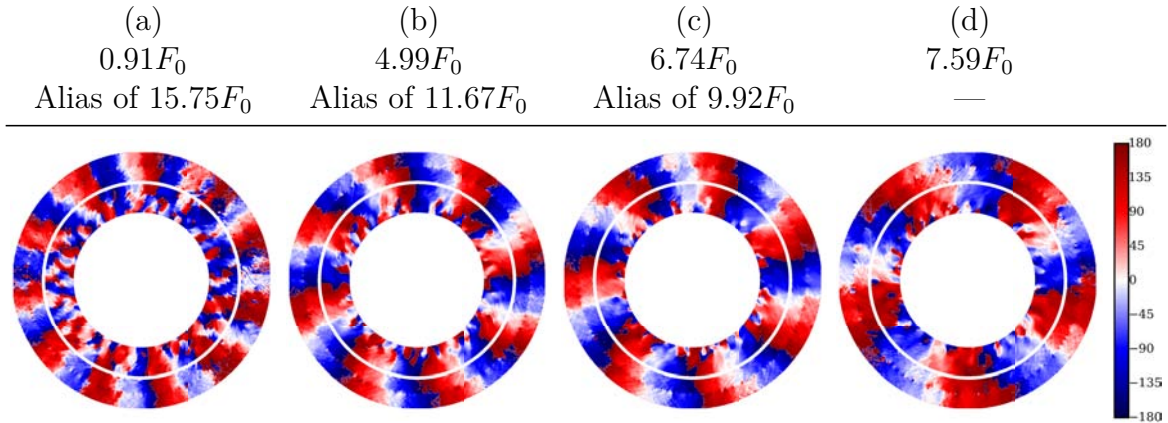
(a)	(b)	(c)	(d)
$0.91F_0$	$4.99F_0$	$6.74F_0$	$7.59F_0$
Alias of $15.75F_0$	Alias of $11.67F_0$	Alias of $9.92F_0$	—

Figure 4.29 − Isocontours of the phase of the pressure fluctuations $\arg\left(\tilde{P}_s\right)$ for the four extra DMD modes constituting **Case 1** sorted out by their respective frequencies.

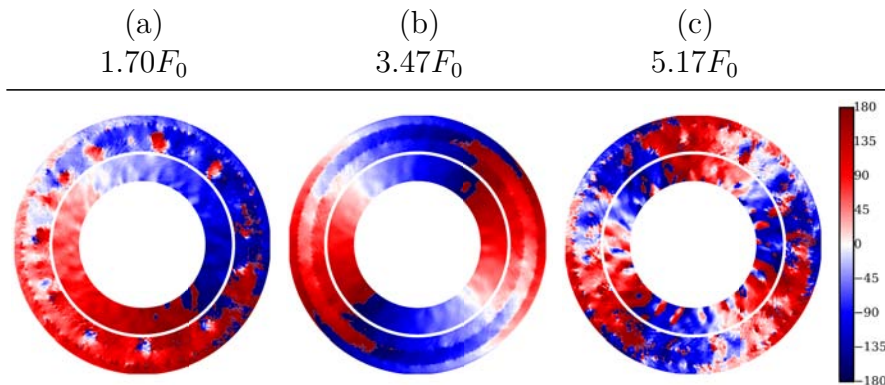Two-dimensional visualizations also support the results presented in Fig. 4.26a. First,

(a)	(b)	(c)
$1.70F_0$	$3.47F_0$	$5.17F_0$

Figure 4.30 − Isocontours of the phase of the pressure fluctuations $\arg\left(\tilde{P}_s\right)$ for (a)-(b) the two major DMD modes and (c) the least noisy extra DMD mode constituting **Case 2**, sorted out by their respective frequencies.

amongst all the modes characterized by a peak in the DMD spectrum of **Case 2** (see Fig. 4.27, middle), only the mode at F_4 exhibits a high SNR, whereas the first and third modes display very noisy spatial organizations coherent with the weak SNR visible on the CSD at those frequencies. Also, for both the modes at F_2 and F_4, the phase-shifts have the same sign between C_1 & C_3 and C_3 & C_2 but change sign between C_2 & C_5 when the wavefront goes through the shear layer present at the C_2-C_5 pass.

These remarks also apply to the results yield by the DMD algorithm for **Case 3**: only the modes pulsing at F_6 and F_8 are not too noisy whereas the two others can hardly be seen as coherent patterns - refer to Fig. 4.31. Not considering the latter, it appears that the azimuthal wavenumbers of the two modes are $m = 4$ and $m = 8$ for F_6 and F_8 respectively, with therefore a linear relation $m = 4h$ if F_6 is assumed to be the fundamental frequency, i.e. a dispersion relation $F/F_0 \simeq 1.15m$ that is verified with an average deviation of 0.16%. Consequently, the highest harmonic (i.e. pulsing at F_9)

is expected to have an azimuthal wavenumber $m = 12$: this is indeed supported by Fig. 4.31b on which one can indeed count 12 lobes at the maximum radius in C_5.
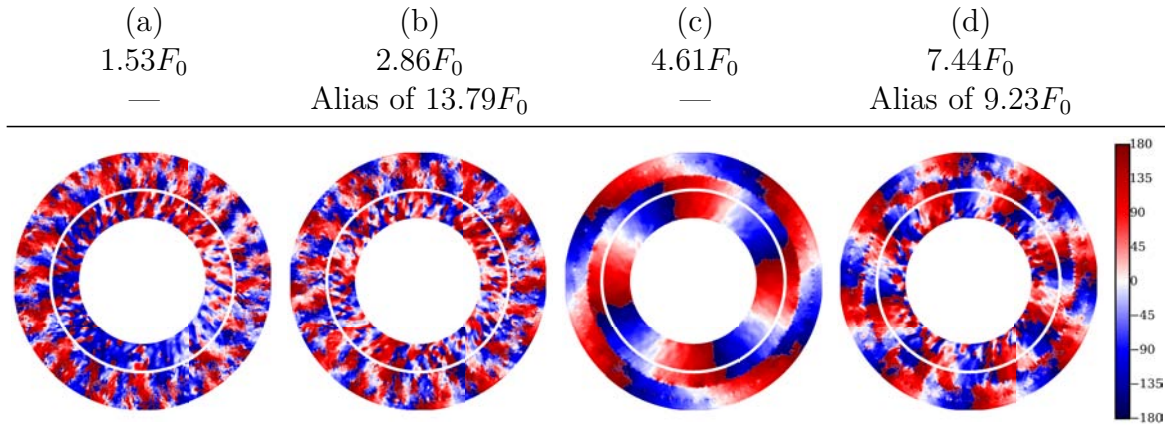
(a)	(b)	(c)	(d)
$1.53F_0$	$2.86F_0$	$4.61F_0$	$7.44F_0$
—	Alias of $13.79F_0$	—	Alias of $9.23F_0$

Figure 4.31 – Isocontours of the phase of the pressure fluctuations $\arg\left(\tilde{P}_s\right)$ for the four major DMD modes constituting **Case 3** sorted out by their respective frequencies.

Out of thoroughness, we present on Fig. 4.32 the two extra modes identified by DMD as important to the dynamics of the flow. Interestingly, their frequencies and azimuthal wavenumbers do not satisfy the assumed dispersion relation $F/F_0 \simeq 1.15\ m$ which is contrary to the behaviours observed in **Case 1** and **Case 2** for which all modes identified by DMD verify a unique dispersion relation.

(a)	(b)
$3.71F_0$	$6.09F_0$
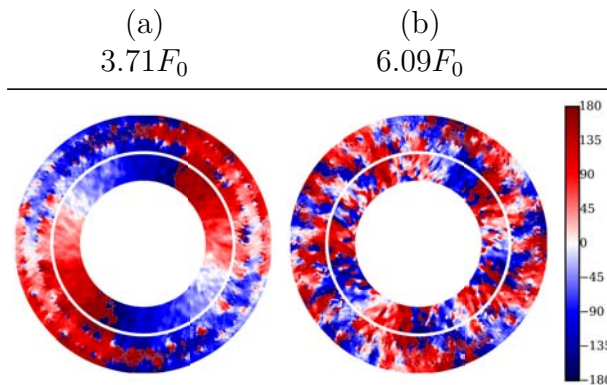
Figure 4.32 – Isocontours of the phase of the pressure fluctuations $\arg\left(\tilde{P}_s\right)$ for the two extra DMD modes constituting **Case 3** sorted out by their respective frequencies.

To conclude this section, Fig. 4.33 presents the patterns made from the combinations of the constituent modes identified above by DMD, marched forward in time so as to be as close as possible from the perturbations of the flow in the limit energetic cycle. The resulting shapes issued by the dynamics of these structures at the bottom radius of C_2 can be compared to the three dimensional motifs discussed in Sec. 4.4.1.b during the analysis of Fig. 4.21. In **Case 1** and **Case 3** (resp. Fig. 4.33a and Fig. 4.33c), the flow is dynamically dominated by a fourfold mode that matches exactly the number of

spiral arms found attached at the bottom of C_2 visible respectively on Fig. 4.21a and Fig. 4.21c. On the other hand, the reconstruction issued by the main DMD modes of **Case 2** (Fig. 4.33b) yields a two-lobed structure that is hardly discernible on Fig. 4.21b as the spiral arms rapidly separate downstream of the C_3-C_2 pass, although immediately at the pass it might be argued that all spiral arms indeed join together.

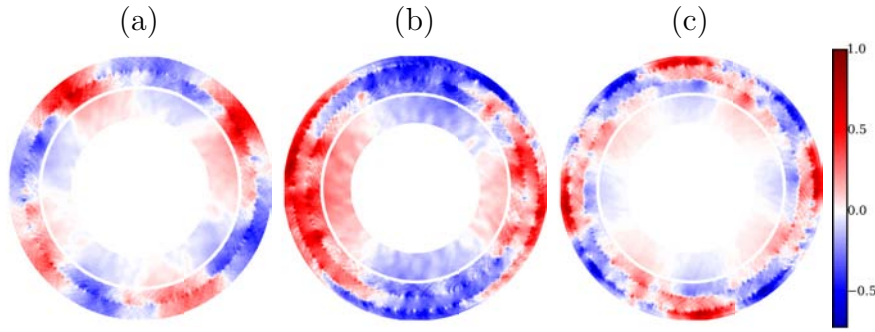**Figure 4.33** – Isocontours of the pressure fluctuations $\tilde{P}_s$ obtained by combination of the constituent DMD modes in (a) **Case 1**, (b) **Case 2** and (c) **Case 3**. The scalar fields have been normalized by their maximum values.

4.5   Conclusion

A LES-based numerical study of three configurations of an industrial turbine first stage cavity is proposed to investigate the unsteady pressure phenomenon known as "pressure band" within a turbomachinery rotor/stator cavity. In all cases, the LES is observed to be able to capture the flow dynamics and its sensitivity to geometrical and operating condition changes. In terms of geometry, the addition of the outermost cavity C_5 has little influence on the low-frequency content of the flow whereas it acts as a band pass filter on the higher frequencies. A change in the temperature of the fluid entering the cavity through the shaft leak (I_1) provokes on the other hand a complete overhaul of the flow dynamics, confirming the sensitivity of such devices to the operating point of the machine. Furthermore and for all cases, the LES high-amplitude pressure fluctuations registered are proven to be composed of basic constituent frequency, each one corresponding to an underlying three-dimensional mode, with a four-lobed mode dominating the flow in **Cases 1** & **3** and a two-lobed mode dominating the flow in **Case 2**. Also of note from these fully unsteady three dimensional full cavity simulations, is that all modes are most likely generated in the general vicinity of one of the two shear layers, located respectively at the pass between C_3 & C_2 and between C_2 & C_5, and their magnitudes tend to decrease when moving through C_5 or through C_1. Combined together, all these cavity modes also appear to be linked to coherent structures (spiral arms) observed close to the bottom wall of the channel C_2.

All in all, we showed that our unstructured LES approach is able to reproduce accurately the flow in an actual industrial turbine stage. In this matter, the dependence of the flow on geometrical changes and on the operating point is captured and the results

agree well with the qualitative experimental observations. Furthermore the 'pressure bands' phenomena as well as their sensitivity to the configurations parameters are also observed, and their characteristics are close to the experimental data. Similarly to the academic cavities, we finally find that the 'pressure bands' phenomena are associated to the presence of a few three-dimensional cavity modes driving the dynamics of the entire flow that can be predicted by DMD. Since **Case 3** displays a coherent spiral pattern in the rotor boundary layer, the next step would be to investigate the potential links between the macro-structures and globally unstable linear modes of the mean cavity flow, as was done in Sec. 3.7 for the academic flows. The technique would however have to be adapted to take into account all the intricacies of the industrial configuration, i.e. the strong temperature gradient and the complex geometry.

Chapter 5

Conclusion

The enclosed rotating flow configuration combines numerous physical mechanisms whose understanding is very challenging. In spite of the obvious scientific challenge, identifying and explaining the sources of their interactions is paramount for the design of space engines turbopumps (see for instance the review by Owen & Rogers, 1989). The present thesis aims at shedding some light on the origins of the 'pressure bands' phenomenon known to disrupt the operation of modern turbopumps turbine stages. Throughout this work, results are collected and conclusions are drawn by means of Large Eddy Simulations (LES) supplemented with state-of-the-art post-processing techniques, in conjunction with linear stability analyses.

The theoretical concepts used in this document are classic and have already been presented by many workers. Nonetheless, we find their thorough description a necessary step to push their applications further than what is commonly done. Numerical simulations of enclosed rotating flows are indeed usually restricted to purely academic investigations based on low to medium Reynolds numbers Direct Numerical Simulations (DNS) or using dedicated simulation models (rotating frame Reynolds-Averaged Navier-Stokes closure terms, specific subgrid-scale modelling in LES, ...). In the present work, a general-purpose LES solver is used on high-Reynolds number academic configurations to study the dynamics of the flows and the formation of macro-structures in relation with unsteady pressure phenomena. The good agreement between the mean flowfields yield by the simulations and the reference data confirms that our unstructured LES approach is suitable for the accurate description of transitional rotating flows. This allows the dedication of our LES solver to the study of 'pressure bands' in actual industrial flows rotating at extreme Reynolds numbers.

The major part of this thesis deals with numerical simulations of rotating flows, academic in a first time, then real turbine flows. The detailed investigation of the academic cavities confirms the well-known sensitivity of the disc boundary layers to crossflow instabilities inducing therein the formation of three-dimensional and axisymmetric patterns. In supplement to these commonly discussed phenomena, the wall-resolved simulations show that the homogeneous core flow also becomes unstable. It displays an instability similar to vortex breakdown and the velocity and pressure fluctuations are observed to also form annular and/or spiral patterns. State-of-the-art post-processing techniques, e.g. Dynamic Modal Decomposition (DMD), applied onto the instantaneous LES solutions then prove that the dynamics of the boundary layers and of the core are closely related. The different spiral and annular patterns visible at different heights within the cavities indeed result from the interaction of the mean flow with a few three-dimensional DMD modes driving the entire dynamics of the flow. This point leads us to the application of our unstructured LES approach to real turbomachinery applications. Due to the three-dimensional nature of the constituent modes, their frequencies are naturally captured by probes placed anywhere in the cavity, independently of their locations. As this is one of the major characteristics of the 'pressure bands' phenomenon, similar advanced diagnostics are applied to the LES of actual industrial flows. Expectedly, they lead to the conclusion that the strong unsteady pressure fluctuations called 'pressure bands' are the result of the combination of a few three-dimensional cavity modes and their interaction with the mean rotating flow.

Given the three-dimensional nature of the modes responsible for the 'pressure bands', the present work finally attempts to relate them to global stability concepts. Temporal stability analyses are commonly used in the literature to gather some information on academic rotating flows, but they prove insufficient to obtain the actual characteristics of a constituent mode or its three-dimensional representation. In Chap. 3, we therefore extend the analyses to spatio-temporal investigations. They show that in some cases, the boundary layer modes are actually related to globally unstable linear modes whose wavemakers are located close to the outer cylindrical boundary layer. Furthermore, in these cases, the integration of successive local linear stability analyses yields an accurate representation of the three-dimensional structure of the corresponding mode. Finally, it is noteworthy that the successful analyses point to the fact that the 'pressure bands' in some smooth rotor/stator cavities are driven by cohabitating globally unstable linear modes born in the disc boundary layers.

In other cases with low aspect ratios, where a DMD reveals that the combination of a larger number of modes is responsible for the dynamics of the cavity flow, the success of the linear stability analyses is limited. Although it appears that each DMD mode taken separately corresponds to a globally unstable linear mode, their frequencies usually disagree with the frequencies obtained by DMD. Nonetheless, upon reconstruction of the two-dimensional structures of these global linear modes it is of note that their regions of expression (see Sec. 3.7) coincide with the region where the DMD mode has its largest magnitude. This fact points to the possibility of interactions between the global modes leading to a potentially nonlinear state of the system. The existence of this nonlinear response could explain in itself the different overall frequency obtained by DMD as well as the pairing of the different structures (Ho & Huerre, 1984). A careful investigation of this hypothesis is however necessary before one draws any further conclusions. On the other hand, in the very specific case of the high aspect ratio cavity studied in the present work, the approach proves unsuccessful. It is believed that because of the high aspect ratio, the flow exhibits characteristics commonly attributed to tall rotating lid-cylinder enclosures that increase the three-dimensionality of the flow. Subsequently, it questions the validity of the fundamental hypothesis in LSA that the flow can be assumed to be locally parallel and one-dimensional. Although it remains to be confirmed, these facts are proposed as the cause for this lack of success.

Regarding the application of such techniques to actual industrial turbine flows such as the ones studied in Chap. 4, several remarks can be made. First of all, even if the Reynolds numbers at the rim of the turbines rotors were expected to be too large for the flows to sustain any coherent structure, **Case 3** displays a spiral structure in the rotor boundary layer (Fig. 4.20c) that is consistent with the patterns observed in the academic LES solutions. Based on the results presented in Sec. 3.7, a perturbation analysis could therefore be performed on the base flow obtained in **Case 3** to assess whether the spiral is related to a globally unstable linear mode. However in this situation, the comparison between the modes reconstructed by LSA and the structures observed in the LES solutions should be established carefully. Due to the unreasonable CPU cost necessary to refine sufficiently the mesh near the walls to capture the flow boundary layers, recall indeed that a classical law-of-the-wall is used to solve for the boundary layers dynamics close

to the walls. Although the impact of this wall model on the boundary layer patterns is found to be limited in academic configurations (App. F), the greater complexity of the industrial flow may benefit from a wall-law specifically dedicated to rotating flows. The implementation and the use of such a law can then reasonably be thought to be a necessary step before drawing any conclusions on the nature of the rotor layer instability patterns, their link with globally unstable linear modes and their relation to the 'pressure bands' phenomenon. Another interesting investigation could then be dedicated to the potential interactions between the rotor/stator cavity (called C_1 in Chap. 4) boundary layer modes and the shear layer at the pass with the outer channel (called C_2 in Chap. 4). Such a study could indeed provide more information regarding the coherent structures observed in the boundary layer at the bottom of C_2 as well as explain how the rotor/stator cavity global modes propagate to the outermost cavity C_5.

Note finally that the current Ph.D. work has resulted in the following publications and conferences.

Ranked *A* papers

- T. Bridel-Bertomeu, L.Y. Gicquel, G. Staffelbach, *Large scale unsteady features from LES of a complex geometry turbopump turbine cavity*, under review for **AIAA Journal**, 2016

Conferences

- T. Bridel-Bertomeu, *Unsteady pressure phenomena encountered in rotor/stator cavities*, **Space Propulsion Presentation**, 2016

- L. Lacassagne, T. Bridel-Bertomeu, E. Riber, B. Cuenot, G. Casalis, F. Nicoud, *Lateral blowing impact on corner vortex shedding in solid rocket motors*, **Space Propulsion Paper**, 2016

- T. Bridel-Bertomeu, *Instability of the ow in rotor/stator cavities*, **Meeting of the CRCT**, 2016

- T. Bridel-Bertomeu, L.Y. Gicquel, G. Staffelbach, *Wall modeled LES and its impact on rotor/stator cavity unsteady features*, **ASME Turbo Expo Paper**, 2016

Appendix A

Non-dimensionalizing BEK equations

Let the dimensional Navier-Stokes equations in cylindrical-polar coordinates in a frame rotating at Ω_d^* be written as

$$\frac{1}{r^*}\frac{\partial(r^*U^*)}{\partial r^*} + \frac{\partial W^*}{\partial z^*} = 0 \tag{A.1}$$

$$U^*\frac{\partial U^*}{\partial r^*} + W^*\frac{\partial U^*}{\partial z^*} - \frac{V^{*^2}}{r^*} - 2\Omega_d^*V^*$$
$$= -\frac{1}{\rho^*}\frac{\partial P^*}{\partial r^*} + \nu^*\left(\frac{1}{r^*}\frac{\partial}{\partial r^*}\left(r^*\frac{\partial U^*}{\partial r^*}\right) + \frac{\partial^2 U^*}{\partial z^{*2}} - \frac{U^*}{r^{*2}}\right) \tag{A.2}$$

$$U^*\frac{\partial V^*}{\partial r^*} + W^*\frac{\partial V^*}{\partial z^*} + \frac{U^*V^*}{r^*} + 2\Omega_d^*U^* = \nu^*\left(\frac{1}{r^*}\frac{\partial}{\partial r^*}\left(r^*\frac{\partial V^*}{\partial r^*}\right) + \frac{\partial^2 V^*}{\partial z^{*2}} - \frac{V^*}{r^{*2}}\right) \tag{A.3}$$

$$U^*\frac{\partial W^*}{\partial r^*} + W^*\frac{\partial W^*}{\partial z^*} = -\frac{1}{\rho^*}\frac{\partial P^*}{\partial z^*} + \nu^*\left(\frac{1}{r^*}\frac{\partial}{\partial r^*}\left(r^*\frac{\partial W^*}{\partial r^*}\right) + \frac{\partial^2 W^*}{\partial z^{*2}}\right) \tag{A.4}$$

Let us then plug the non-dimensionalized expressions for U, V, W and P from Eqs. (2.1.5)-(2.1.8) in the above Eqs. (A.1)-(A.4).

$$\frac{1}{r^*}\frac{\partial(r^*r^*\Omega^*RoU)}{\partial r^*} + \frac{\partial L^*\Omega^*RoW}{\partial z^*} = 0 \tag{A.5}$$

$$r^*\Omega^*RoU\frac{\partial r^*\Omega^*RoU}{\partial r^*} + L^*\Omega^*RoW\frac{\partial r^*\Omega^*RoU}{\partial z^*} - \frac{r^{*2}\Omega^{*2}Ro^2V^2}{r^*} - 2\Omega_d^*r^*\Omega^*RoV$$
$$= -\frac{1}{\rho^*}\frac{\partial \rho^*L^{*2}\Omega^{*2}Ro^2P}{\partial r^*} + \nu^*\left(\frac{1}{r^*}\frac{\partial}{\partial r^*}\left(r^*\frac{\partial r^*\Omega^*RoU}{\partial r^*}\right) + \frac{\partial^2 r^*\Omega^*RoU}{\partial z^{*2}} - \frac{r^*\Omega^*RoU}{r^{*2}}\right) \tag{A.6}$$

$$r^*\Omega^*RoU\frac{\partial r^*\Omega^*RoV}{\partial r^*} + L^*\Omega^*RoW\frac{\partial r^*\Omega^*RoV}{\partial z^*} + \frac{r^{*2}\Omega^{*2}Ro^2UV}{r^*} + 2\Omega_d^*r^*\Omega^*RoU$$
$$= \nu^*\left(\frac{1}{r^*}\frac{\partial}{\partial r^*}\left(r^*\frac{\partial r^*\Omega^*RoV}{\partial r^*}\right) + \frac{\partial^2 r^*\Omega^*RoV}{\partial z^{*2}} - \frac{r^*\Omega^*RoV}{r^{*2}}\right) \tag{A.7}$$

$$r^*\Omega^* RoU \frac{\partial L^*\Omega^* RoW}{\partial r^*} + L^*\Omega^* RoW \frac{\partial L^*\Omega^* RoW}{\partial z^*}$$
$$= -\frac{1}{\rho^*}\frac{\partial \rho^* L^{*2}\Omega^{*2} Ro^2 P}{\partial z^*} + \nu^* \left(\frac{1}{r^*}\frac{\partial}{\partial r^*}\left(r^*\frac{\partial L^*\Omega^* RoW}{\partial r^*}\right) + \frac{\partial^2 L^*\Omega^* RoW}{\partial z^{*2}}\right) \tag{A.8}$$

After a few preliminary simplifications we get

$$2\Omega^* RoU + \Omega^* Ro\frac{\partial W}{\partial z} = 0 \tag{A.9}$$

$$r^*\Omega^{*2} Ro^2 U^2 + r^*\Omega^{*2} Ro^2 W\frac{\partial U}{\partial z} - \Omega^{*2} Ro^2 r^* V^2 - \Omega^* Cor^*\Omega^* RoV$$
$$= -L^*\Omega^{*2} Ro^2 \frac{\partial P}{\partial r} + \Omega^* L^{*2}\left(\frac{1}{r^*}\frac{\partial}{\partial r^*}\left(r^*\Omega^* RoU\right) + r^*\Omega^* Ro\frac{\partial^2 U}{\partial z^{*2}} - \frac{\Omega^* RoU}{r^*}\right) \tag{A.10}$$

$$r^*\Omega^{*2} Ro^2 UV + r^*\Omega^{*2} Ro^2 W\frac{\partial V}{\partial z} + r^*\Omega^{*2} Ro^2 UV + \Omega^* Cor^*\Omega^* RoU$$
$$= \Omega^* L^{*2}\left(\frac{1}{r^*}\frac{\partial}{\partial r^*}\left(r^*\Omega^* RoV\right) + r^*\Omega^* Ro\frac{\partial^2 V}{\partial z^{*2}} - \frac{\Omega^* RoV}{r^*}\right) \tag{A.11}$$

$$L^*\Omega^{*2} Ro^2 W\frac{\partial W}{\partial z} = -L^*\Omega^{*2} Ro^2 \frac{\partial P}{\partial z} + \Omega^* L^{*2}\left(L^*\Omega^* Ro\frac{\partial^2 W}{\partial z^{*2}}\right) \tag{A.12}$$

In turn, this set of equations leads to

$$2U + W = 0 \tag{A.13}$$

$$r^* Ro^2 U^2 + r^* Ro^2 WU - Ro^2 r^* V^2 - Cor^* RoV = -L^* Ro^2 \frac{\partial P}{\partial r} + r^* RoU \tag{A.14}$$

$$RoUV + RoWV + RoUV + CoU = V \tag{A.15}$$

$$RoWW = -Ro\frac{\partial P}{\partial z} + W \tag{A.16}$$

To formulate Eq. (2.1.12) it is necessary to determine the radial pressure gradient from the azimuthal flow as $z \to \infty$, i.e. $V \to 1$. Assuming that $U(z \to \infty) = U(z \to \infty) = U(z \to \infty) = 0$, we get

$$Ro + Co = \frac{Ro}{r}\frac{\partial P}{\partial r} \tag{A.17}$$

which is taken as a constant in z. Thus the dimensionless pressure has the form

$$P(r, z) = \frac{r^2(Ro + Co)}{2Ro} + P(z) + \text{const.} \tag{A.18}$$

Plugging Eq. (A.18) in the four equations above leads to Eqs. (2.1.11)-(2.1.14).   □

Appendix B

Non-dimensionalizing two discs equations

Again, let the dimensional Navier-Stokes equations in cylindrical-polar coordinates (r^*, θ, z^*) in a frame rotating at Ω_d^* be written as

$$\frac{1}{r^*}\frac{\partial(r^* U^*)}{\partial r^*} + \frac{\partial W^*}{\partial z^*} = 0 \tag{B.1}$$

$$U^*\frac{\partial U^*}{\partial r^*} + W^*\frac{\partial U^*}{\partial z^*} - \frac{V^{*2}}{r^*} - 2\Omega_d^* V^*$$
$$= -\frac{1}{\rho^*}\frac{\partial P^*}{\partial r^*} + \nu^*\left(\frac{1}{r^*}\frac{\partial}{\partial r^*}\left(r^*\frac{\partial U^*}{\partial r^*}\right) + \frac{\partial^2 U^*}{\partial z^{*2}} - \frac{U^*}{r^{*2}}\right) \tag{B.2}$$

$$U^*\frac{\partial V^*}{\partial r^*} + W^*\frac{\partial V^*}{\partial z^*} + \frac{U^* V^*}{r^*} + 2\Omega_d^* U^* = \nu^*\left(\frac{1}{r^*}\frac{\partial}{\partial r^*}\left(r^*\frac{\partial V^*}{\partial r^*}\right) + \frac{\partial^2 V^*}{\partial z^{*2}} - \frac{V^*}{r^{*2}}\right) \tag{B.3}$$

$$U^*\frac{\partial W^*}{\partial r^*} + W^*\frac{\partial W^*}{\partial z^*} = -\frac{1}{\rho^*}\frac{\partial P^*}{\partial z^*} + \nu^*\left(\frac{1}{r^*}\frac{\partial}{\partial r^*}\left(r^*\frac{\partial W^*}{\partial r^*}\right) + \frac{\partial^2 W^*}{\partial z^{*2}}\right) \tag{B.4}$$

Let us then plug the non-dimensionalized expressions for U, V, W and P from Eq. (2.1.17)-(2.1.20) in the above Eq. (B.1)-(B.4).

$$\frac{1}{r^*}\frac{\partial(r^* r^* \Omega_d^* U)}{\partial r^*} + \frac{\partial L^* \Omega_d^* W}{\partial z^*} = 0 \tag{B.5}$$

$$r^*\Omega_d^* U \frac{\partial r^* \Omega_d^* U}{\partial r^*} + L^*\Omega_d^* W \frac{\partial r^* \Omega_d^* U}{\partial z^*} - \frac{r^{*2}\Omega_d^{*2} V^2}{r^*} - 2\Omega_d^* r^* \Omega_d^* V$$
$$= -\frac{1}{\rho^*}\frac{\partial \rho^* L^{*2}\Omega_d^{*2} P}{\partial r^*} + \nu^*\left(\frac{1}{r^*}\frac{\partial}{\partial r^*}\left(r^*\frac{\partial r^* \Omega_d^* U}{\partial r^*}\right) + \frac{\partial^2 r^* \Omega_d^* U}{\partial z^{*2}} - \frac{r^* \Omega_d^* U}{r^{*2}}\right) \tag{B.6}$$

$$r^*\Omega_d^* U \frac{\partial r^* \Omega_d^* V}{\partial r^*} + L^*\Omega_d^* W \frac{\partial r^* \Omega_d^* V}{\partial z^*} + \frac{r^{*2}\Omega_d^{*2} UV}{r^*} + 2\Omega_d^* r^* \Omega_d^* U$$
$$= \nu^*\left(\frac{1}{r^*}\frac{\partial}{\partial r^*}\left(r^*\frac{\partial r^* \Omega_d^* V}{\partial r^*}\right) + \frac{\partial^2 r^* \Omega_d^* V}{\partial z^{*2}} - \frac{r^* \Omega_d^* V}{r^{*2}}\right) \tag{B.7}$$

$$r^*\Omega_d^*U\frac{\partial L^*\Omega_d^*W}{\partial r^*} + L^*\Omega_d^*W\frac{\partial L^*\Omega_d^*W}{\partial z^*}$$
$$= -\frac{1}{\rho^*}\frac{\partial \rho^*L^{*2}\Omega_d^{*2}P}{\partial z^*} + \nu^*\left(\frac{1}{r^*}\frac{\partial}{\partial r^*}\left(r^*\frac{\partial L^*\Omega_d^*W}{\partial r^*}\right) + \frac{\partial^2 L^*\Omega_d^*W}{\partial z^{*2}}\right) \qquad (B.8)$$

After a few preliminary simplifications we get

$$2\Omega_d^*U + \frac{\Omega_d^*}{\sqrt{Re_h}}\frac{\partial W}{\partial z} = 0 \qquad (B.9)$$

$$r^*\Omega_d^{*2}U^2 + r^*\frac{\Omega_d^{*2}}{\sqrt{Re_h}}W\frac{\partial U}{\partial z} - \Omega_d^{*2}r^*V^2 - 2r^*\Omega_d^{*2}V$$
$$= -L^*\frac{\Omega_d^{*2}}{\sqrt{Re_h}}\frac{\partial P}{\partial r} + \Omega_d^*L^{*2}\left(\frac{1}{r^*}\frac{\partial}{\partial r^*}(r^*\Omega_d^*U) + r^*\Omega_d^*\frac{\partial^2 U}{\partial z^{*2}} - \frac{\Omega_d^*U}{r^*}\right) \qquad (B.10)$$

$$r^*\Omega_d^{*2}UV + r^*\frac{\Omega_d^{*2}}{\sqrt{Re_h}}W\frac{\partial V}{\partial z} + r^*\Omega_d^{*2}UV + 2r^*\Omega_d^{*2}U$$
$$= \Omega_d^*L^{*2}\left(\frac{1}{r^*}\frac{\partial}{\partial r^*}(r^*\Omega_d^*V) + r^*\Omega_d^*\frac{\partial^2 V}{\partial z^{*2}} - \frac{\Omega_d^*V}{r^*}\right) \qquad (B.11)$$

$$L^*\frac{\Omega_d^{*2}}{\sqrt{Re_h}}W\frac{\partial W}{\partial z} = -L^*\frac{\Omega_d^{*2}}{\sqrt{Re_h}}\frac{\partial P}{\partial z} + \Omega_d^*L^{*2}\left(L^*\Omega_d^*\frac{\partial^2 W}{\partial z^{*2}}\right) \qquad (B.12)$$

In turn, this set of equations leads to

$$2\sqrt{Re_h}U + W = 0 \qquad (B.13)$$

$$r^*U^2 + \frac{r^*}{\sqrt{Re_h}}WU - r^*V^2 - 2r^*V = -\frac{L^*}{\sqrt{Re_h}}\frac{\partial P}{\partial r} + \frac{r^*}{Re_h}U \qquad (B.14)$$

$$UV + \frac{1}{\sqrt{Re_h}}WV + UV + 2U = \frac{1}{Re_h}V \qquad (B.15)$$

$$\frac{1}{\sqrt{Re_h}}WW = -\frac{1}{\sqrt{Re_h}}\frac{\partial P}{\partial z} + \frac{1}{Re_h}W \qquad (B.16)$$

Finally, plugging the dimensionless expression for $P(r,z)$ given in Eq. (2.1.20) leads to Eqs. (2.1.21)-(2.1.24). $\qquad\qquad\qquad\qquad\qquad\qquad\qquad\qquad\qquad\qquad\qquad\qquad\qquad\qquad\square$

Appendix C

BEK flow generator

Although the equations yielding the auto-similar velocity and pressure profiles of a disc flows are simplified version of the Navier-Stokes equations, a numerical resolution remains necessary to solve the system. To ensure repeatability when solving the sets of equations for one- or two-disc flows, the boundary value problem (BVP) is systematically solved by use of Shampine *et al.* (2006) algorithm. Starting from an initial solution for all variables and unknown parameters, the solver iterates the system of ordinary differential equations (reduced to the form $y(x) = f(x, y, p)$ where x is the scalar independent variable and y the vector of dependent variables) using a 2nd, 4th or 6th Runge-Kutta scheme until a user-prescribed precision ε is reached. Throughout Sec. 2.1.2, a 4th order Runge-Kutta scheme is used with a tolerance $\varepsilon = 10^{-9}$.

Listing C.1 - Single-disc and two-discs meanflow generator, according to Eq. (2.1.11)-(2.1.14) and Eq. (2.1.21)-(2.1.24).

```
1  '''
2  This script generates solutions of the simplified
3  Navier-Stokes equations for auto-similar flows related to
4  disk flows (Bodewadt, Ekman, Karman and two-discs flows)
5
6  Necessary libraries : numpy,matplotlib,scikits
7
8  :Author:          Thibault Bridel Bertomeu
9  :Creation:        10/11/2015
10
11 :Last Modification: April 22, 2016
12 :Purpose:         Working for any rossby now
13 '''
14
15 # ==============================
16 # Load libraries
17 # ==============================
18
19 import sys as sys
```

```python
20
21  import scikits.bvp_solver as scbs
22  import numpy as np
23
24  import matplotlib as mpl
25  mpl.use('Agg')
26  font = {'family': 'serif', 'weight': 'medium', 'size': 40}
27  mpl.rc('font', **font)
28  mpl.rcParams['axes.linewidth'] = 5.0
29  import matplotlib.pyplot as plt
30  import matplotlib.cm as cm
31
32  # ==============================
33  # Parse user input
34  # ==============================
35
36  if len(sys.argv) == 1 or (len(sys.argv) == 2 and 'help' in sys.argv[2]):
37      exit()
38  else:
39      for arg in sys.argv:
40          if arg[:4] == '--re':
41              reynolds = float(arg.split('=')[1])
42          elif arg[:4] == '--ka':
43              kappa = float(arg.split('=')[1])
44              if not abs(kappa) <= 1.0:
45                  exit()
46          elif arg[:5] == '--ver':
47              verbose = int(arg.split('=')[1])
48              if verbose != 0 and verbose != 1 and verbose != 2:
49                  exit()
50          elif arg[:4] == '--rk':
51              rk = int(arg.split('=')[1])
52              if rk != 2 and rk != 4 and rk != 6:
53                  exit()
54          elif arg[:5] == '--tol':
55              tol = float(arg.split('=')[1])
56          elif arg[:5] == '--num':
57              disks = int(arg.split('=')[1])
58              if disks != 1 and disks != 2:
59                  exit()
60
61  # ==============================
62  # Define the ODEs
63  # ==============================
64
65
66  def oneDiskODE(z, y):
```

```python
     # Y0 = H, Y1 = F', Y2 = F, Y3 = G', Y4 = G
     dydz = np.array([-
                      2.0 *
                      y[2], kappa *
                      (y[2] *
                       y[2] +
                          y[0] *
                          y[1] -
                          (y[4] *
                           y[4] -
                           1.0)) -
                      (2.0 -
                          kappa -
                          kappa**2) *
                      (y[4] -
                          1.0), y[1], kappa *
                      (2.0 *
                          y[2] *
                          y[4] +
                          y[0] *
                          y[3]) +
                      (2.0 -
                          kappa -
                          kappa**2) *
                      y[2], y[3]])
     return dydz


def oneDiskBC(y0, yinf):
     res0 = np.array([y0[0],
                      y0[2],
                      y0[4]])

     resinf = np.array([yinf[2],
                        yinf[4] - 1.0])
     return (res0, resinf)


def twoDiskODE(z, y, k):
     # Y0 = H, Y1 = F', Y2 = F, Y3 = G', Y4 = G
     dydz = np.array([-
                      2.0 *
                      np.sqrt(reynolds) *
                      y[2], reynolds *
                      (y[0] *
                          y[1] /
                          np.sqrt(reynolds) +
```

```python
114                             y[2] *
115                             y[2] -
116                             (y[4] +
117                              1.0)**2 +
118                             k), y[1], reynolds *
119                         (y[0] *
120                             y[3] /
121                             np.sqrt(reynolds) +
122                             2.0 *
123                             y[2] *
124                             (y[4] +
125                              1)), y[3]])
126     return dydz
127
128
129 def twoDiskBC(y0, yinf, k):
130     res0 = np.array([y0[0],
131                      y0[2],
132                      y0[4]])
133
134     resinf = np.array([yinf[0],
135                        yinf[2],
136                        yinf[4] + 1.0])
137     return (res0, resinf)
138
139 # =============================
140 # Define the problem
141 # =============================
142
143 if disks == 1:
144     problem = scbs.ProblemDefinition(num_ODE=5,
145                             num_parameters=0,
146                             num_left_boundary_conditions=3,
147                             boundary_points=(0.0, np.sqrt(reynolds)),
148                             function=oneDiskODE,
149                             boundary_conditions=oneDiskBC)
150
151     if kappa == -1:
152         solguess = [1.0, 0.0, 0.0, 0.0, 1.0]
153     elif kappa == 1:
154         solguess = [1.2, 0.0, 0.0, 0.0, 1.0]
155     else:
156         solguess = [1.0, 0.0, 0.0, 0.0, 1.0]
157     solguess = np.array(solguess)
158
159     solution = scbs.solve(
160         problem,
```

```
161          solution_guess=solguess,
162          initial_mesh=np.linspace(
163              0.0,
164              np.sqrt(reynolds),
165              2000),
166          method=int(rk),
167          tolerance=float(tol),
168          max_subintervals=1000000,
169          trace=int(verbose))
170
171      vecZ = np.linspace(0.0, np.sqrt(reynolds), 2000)
172
173  elif disks == 2:
174      solution = None
175      solguess = np.array([0.0, 0.0, 0.0, 0.0, 0.3])
176
177      problem = scbs.ProblemDefinition(num_ODE=5,
178                              num_parameters=1,
179                              num_left_boundary_conditions=3,
180                              boundary_points=(0.0, 1.0),
181                              function=twoDiskODE,
182                              boundary_conditions=twoDiskBC)
183
184      solution = scbs.solve(problem,
185                              solution_guess=solguess,
186                              parameter_guess=0.09,
187                              initial_mesh=np.linspace(0.0, 1.0, 2000),
188                              method=int(rk),
189                              tolerance=float(tol),
190                              max_subintervals=1000000,
191                              trace=int(verbose)
192                              )
193
194      vecZ = np.linspace(0.0, 1.0, 2000)
195
196  # ==============================
197  # Plot the solution
198  # ==============================
199
200  if disks == 2:
201      print solution.parameters
202
203  vecH, vecFp, vecF, vecGp, vecG = solution(vecZ)
204
205  fig = plt.figure(figsize=(30, 20), dpi=300)
206  ax = plt.subplot(111)
207  plt.plot(vecH, vecZ, '-k', lw=4, label='Axial')
```

```python
208  plt.plot(vecG, vecZ, '-b', lw=4, label='Azimutal')
209  plt.plot(vecF, vecZ, '-r', lw=4, label='Radial')
210  plt.legend(loc='best')
211  plt.savefig('meanflow.png', bbox_inches='tight')
212  plt.close()
213
214  # ===============================
215  # Export the solution
216  # ===============================
217
218  fid = open('mean.dat', 'w')
219  for idx in xrange(vecZ.size):
220      fid.write('%+.12f %+.12f %+.12f %+.12f %+.12f %+.12f %+.12f\n' %
221                (vecF[idx], vecG[idx], vecH[idx], vecFp[idx], vecGp[idx], -
222                 2.0 *
223                 np.sqrt(reynolds) *
224                    vecF[idx], vecZ[idx]))
225  fid.close()
```

Appendix D

Perturbation equations for a jet flow

Starting from the dimensional Navier-Stokes equations in cylindrical-polar coordinates written in an inertial frame, and following the same procedure as for the development of Eqs. (2.2.12)-(2.2.15), the linearized Navier-Stokes implemented in AVLP (see Sec. 2.2.4) for jet flows read

$$0 = u + \frac{u}{r} + \frac{m}{r}v + \alpha w, \tag{D.1}$$

$$
\begin{aligned}
\frac{i}{Re}u &= \left(\frac{i}{Re}\left(\frac{m^2+1}{r^2} + \alpha^2 \right) - \alpha W - \frac{m}{r}V + i\frac{dU}{dr} + \omega \right) u + i \left(U - \frac{1}{rRe} \right) u \\
&+ \left(\frac{2im}{r^2 Re} - \frac{2V}{r} \right) v + p,
\end{aligned}
\tag{D.2}
$$

$$
\begin{aligned}
\frac{1}{Re}v &= \left(\frac{1}{Re}\left(\frac{m^2+1}{r^2} + \alpha^2 \right) + i\alpha W + \frac{im}{r}V + \frac{U}{r} - i\omega \right) v + \left(U - \frac{1}{rRe} \right) v \\
&+ \left(\frac{2m}{r^2 Re} + \frac{iV}{r} + i\frac{dV}{dr} \right) u + \frac{im}{r}p,
\end{aligned}
\tag{D.3}
$$

$$
\begin{aligned}
\frac{1}{Re}w &= \left(\frac{1}{Re}\left(\frac{m^2}{r^2} + \alpha^2 \right) + i\alpha W + \frac{im}{r}V - i\omega \right) w + \left(U - \frac{1}{rRe} \right) w \\
&+ i\frac{dW}{dr}u + i\alpha p,
\end{aligned}
\tag{D.4}
$$

$$\tag{D.5}$$

where the modal decomposition is radially normal, i.e.

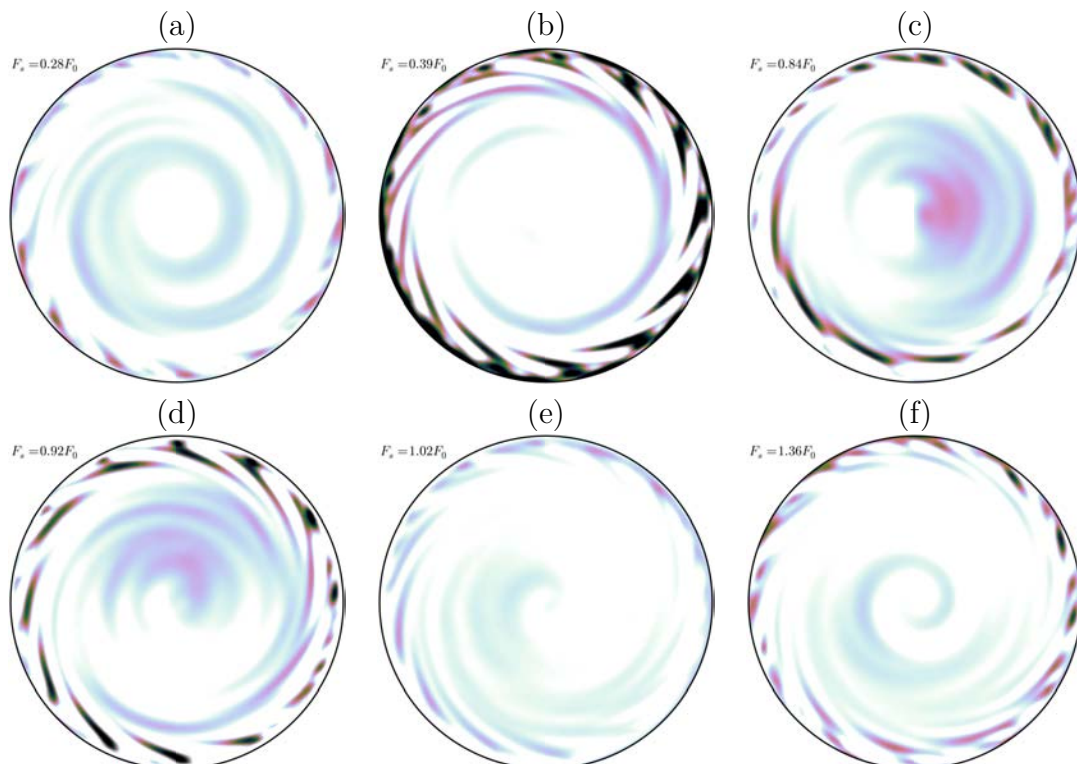$$[\tilde{u}, \tilde{v}, \tilde{w}, \tilde{p}] = [iu, v, w, p](r)\exp\left(i\left[\alpha z + m\theta - \omega t\right]\right). \tag{D.6}$$
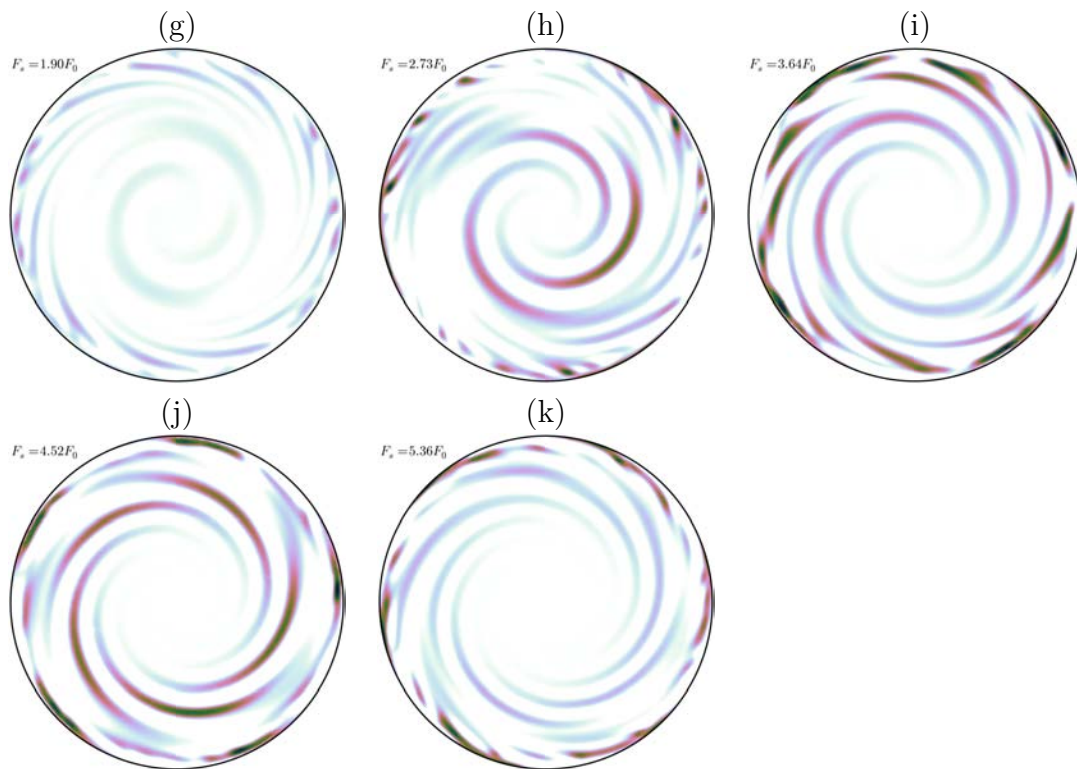
Appendix E

Constituent DMD modes for the dynamics of Case 1

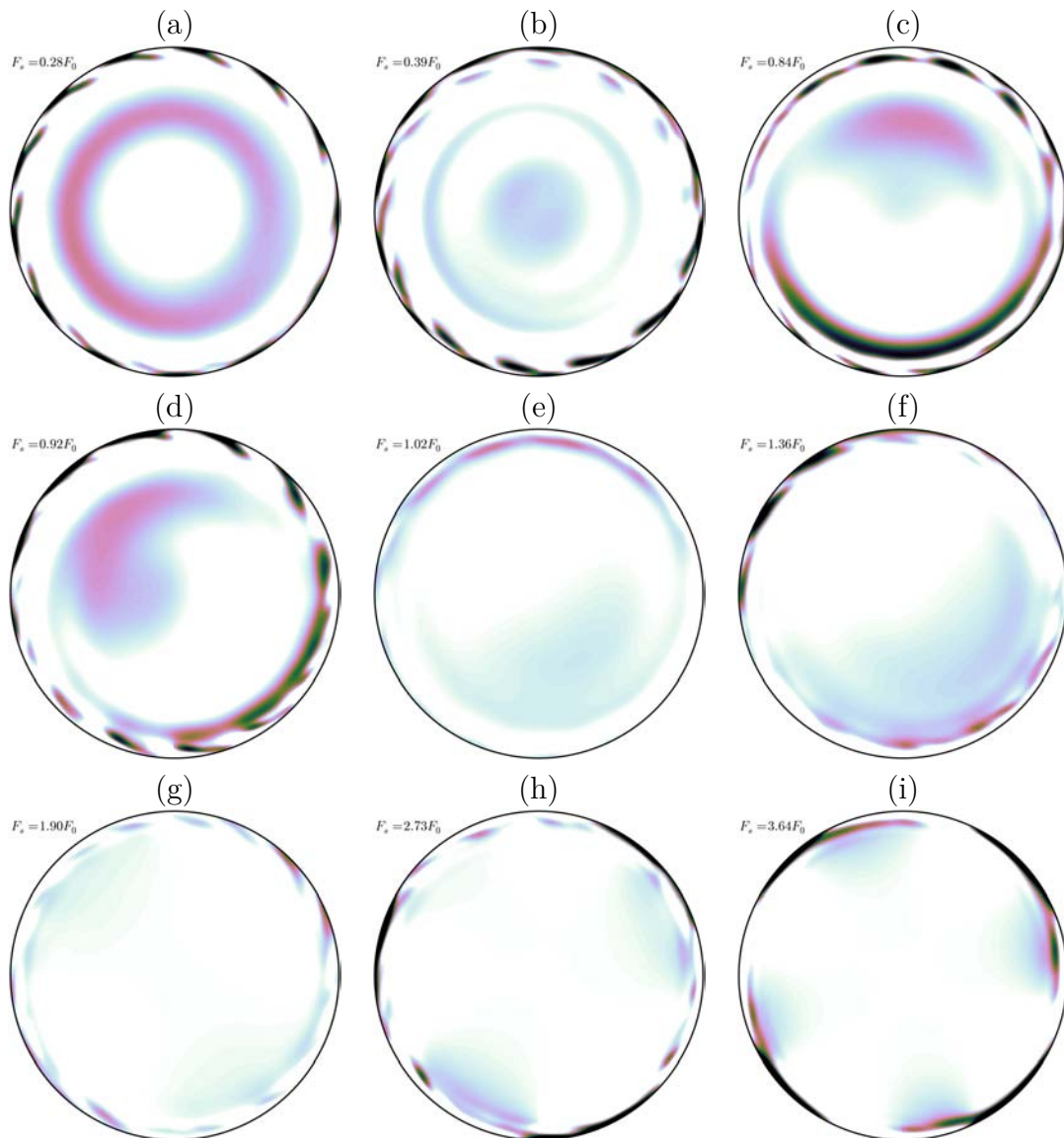## E.1 Isocontours of $\tilde{u}_z \in [0, 0.05]$ at $z^* = 1 - \delta/h$ (stator)

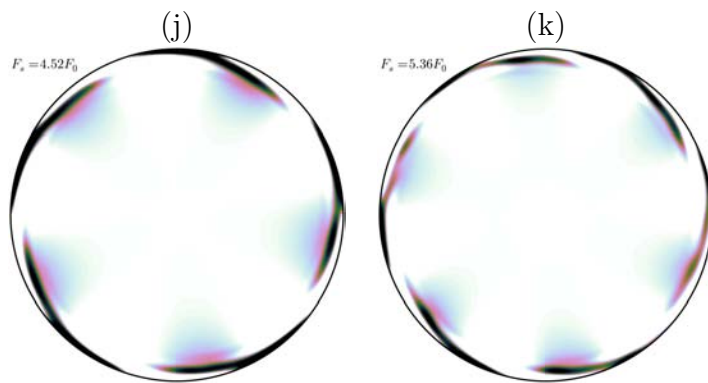*Relatively to the cuts below, the rotor rotation is counterclockwise*

(g)

$F_s = 1.90F_0$

(h)

$F_s = 2.73F_0$

(i)

$F_s = 3.64F_0$

(j)

$F_s = 4.52F_0$

(k)

$F_s = 5.36F_0$

E.2 Isocontours of $\tilde{u}_z \in [0, 0.05]$ at $z^* = 0.5$ (mid-cavity)

Relatively to the cuts below, the rotor rotation is counterclockwise

E.3 Isocontours of $\tilde{u}_z \in [0, 0.05]$ at $z^* = \delta/h$ (rotor)

Relatively to the cuts below, the rotor rotation is counterclockwise

Appendix F

Wall modeled LES and rotor/stator cavity unsteady features

GT2016-57244

WALL MODELED LES AND ITS IMPACT ON ROTOR/STATOR CAVITY UNSTEADY FEATURES

Thibault Bridel-Bertomeu[*]
CERFACS
42, Av. Gaspard Coriolis
31057 Toulouse, France
Email: tbridel@cerfacs.fr
CNES/DLA
Rue Jacques Hillairet
75612 Paris, France

Laurent Y. Gicquel
Gabriel Staffelbach
CERFACS
42, Av. Gaspard Coriolis
31057 Toulouse, France

ABSTRACT

Cavity flows are essential components of many aeronautical and spatial engines. For example, in gas turbines a network of cavities is calibrated and managed to divert part of the main cold stream which is then re-injected in the hot regions of the engine to shield walls from the hot combustion products. For pumps, cavities are naturally present at the junction of fixed and rotating parts. In both contexts, mastering the flow stability in rotor/stator cavities is essential to avoid imposing too large flow variations which could lead to miss-tuned operating conditions in the engine and a drastic loss of performance or life-span. Although stability of these flows has been widely studied in the literature, a lack of clear understanding of the triggering mechanisms from stable to unstable flow solutions remains, especially in the context of industrial applications where Reynolds numbers are very high and difficult to handle. To cope with such complex geometry, fully unsteady flows, the so-called Large Eddy Simulation (LES) approach appears as a very promising method. However and for such high Reynolds number industrial applications, wall modeling still remains a necessity to alleviate the computational cost of LES. Understanding the impact of such a strong modeling hypothesis on the mean flow features and unsteady energetic content

is hence mandatory and the objective of the present discussion. To do so, the present paper studies LES flow solutions in an enclosed rotor-stator configuration with a stationary shroud. These simulations are performed using a two-steps Taylor-Galerkin finite-element scheme coupled to a WALE subgrid scale model giving a better prediction of the eddy viscosity in zones of strong shear. This allows capturing the unsteady structures known to be present in the boundary layers. Two sets of statoric boundary conditions are investigated: the dynamics of the boundary layer is either resolved using a fine mesh grid or modeled using a classic boundary layer law of the wall. It is shown that the modeling of the stationary disc layer induces an underestimation of the flow velocity at low radii and loss of accuracy in the radial description of the boundary layer structures. Despite these differences, the most energetic structures are found to have the same azimuthal organization as in the wall resolved configuration as well as the same pulsation, which in turn produces a boundary layer with the same spectral content as in the wall resolved test case.

INTRODUCTION

Rotating disc flows have been a subject of renewed interest over the last years because of their relevance to many

---

[*]Address all correspondence to this author.

1

industrial applications, e.g. turbines, compressors, turbopumps, electrical machinery or even hard-drives (see the review by Owen and Rogers [1, 2]). Numerous studies have been dedicated to the flow between a smooth rotating disc and a fixed parallel disc to serve as a first-order model for turbomachinery rotor/stator flows [3–6] and because the rotating disc flow is one of the simplest cases where the turbulent boundary layers are fully three-dimensional [7–9]. So far all kinds of numerical studies have been attempted: axisymmetric flows using Reynolds Averaged Navier-Stokes (RANS) [10], annular cavities using Large Eddy Simulations (LES) [5, 11], or enclosed rotor/stator cavities at lower Reynolds numbers using Direct Numerical Simulation (DNS) [4, 12].

The structure of a rotor-stator flow is in large part dependent on the combination of the interdisc height h and the rotation speed Ω. An extensive coupled theoretical and experimental study has been lead by Daily and Nece [13] who found out that four different flow regimes could exist. Two of those regimes are laminar (respectively noted I and II), and two are fully turbulent (III and IV), each characterized either by merged (I and III) or separated (II and IV) boundary layers. In the latter case, the two boundary layers are separated by a central rotating core, and are said to be of the Ekman [14] type on the rotating disc and of the Bödewadt [15] type on the stationary disc. The authors also proposed an estimation of the critical Reynolds number beyond which the separated boundary layers from a flow of category II or IV become fully turbulent; i.e. $Re_r = \Omega r^2/\nu \sim 10^5$ for aspect ratios $G = h/(R_1 - R_0) \geq 0.04$ where r is the radial coordinate and R_1 & R_0 are respectively the outer and inner radii of the cavity. It is also known that transitional Ekman and Bödewadt layers present characteristic patterns (see the review by Serre *et al.* [16]). These coherent fluctuations of the axial velocity component are both time- and Reynolds-dependent and often take the form of annuli at low Reynolds numbers (see e.g. Tuliszka-Sznitko *et al.* [12]) or spiral arms at intermediate Reynolds numbers (see e.g [17] or the review by Launder *et al.* [18]).

Extensive experimental work around this transition regime has been performed by Itoh *et al.* [19, 20] in a closed cavity. By capturing the meanflow and all the Reynolds tensor components they were able to characterize accurately the turbulence in the cavity and then pointed out the existence of a re-laminarized zone near the axis at high rotation rates. From these detailed measurements, Itoh *et al.* [20] reported that the critical Reynolds number for transition was lower on the stator side than on the rotor for $G = 0.08$, and respectively evaluated at $Re_r = 8 \times 10^3$ and $3.6 \times 10^5 < Re_r < 6.4 \times 10^5$. These results agree with the experiments of Cheah *et al.* [21] performed for rotational Reynolds numbers in the range $3 \times 10^5 < Re_r < 1.6 \times 10^6$ within an en-

closed rotor/stator cavity of aspect ratio $G = 0.127$. In this last work, the rotor boundary layer indeed becomes turbulent for $Re_r \geq 4 \times 10^5$ whereas the stator boundary layer is turbulent over the whole range of Reynolds numbers.

As evidenced above, many specific features are present in such rotor/stator cavity flows and many parameters are at play. This in part explains the difficulty to simulate reliably such problems especially in the range of high-velocity regimes relevant to industrial applications. A typical feature of rotor/stator cavity flows is indeed the existence of multiple flow regions where very different scalings apply: boundary layers on the two discs driven by viscosity separated by an inviscid bulk flow rotating at constant speed. Furthermore, the turbulence, when present, is strongly inhomogeneous and anisotropic due to rotation and finite-cavity effects. Therefore RANS approaches can hardly capture accurately at the same time the inviscid-like bulk structure and the transitional behavior of the boundary layers. On the other extreme, computer capabilities only permit today low to medium Reynolds number DNS. Wu and Squires [22] were the first to use LES to predict the behavior of a three-dimensional turbulent boundary layer over a rotating disc in an attempt to provide detailed flow information and organization. They tested several subgrid-scale models and compared the results to the experimental data that Littell and Eaton [8] obtained for $Re_R = Re_r(r = R_1) = 6.5 \times 10^5$. Their results supported the observations of [8] that crossflow interactions promote sweeping structures if the streamwise vortices and the mean flow vorticity have an opposite sign, or favor centrifugal ejections if the streamwise vortices and the mean flow vorticity share the same sign. Since then, several numerically-oriented works (e.g. [5, 16]) have reported the existence of coherent concentric and/or spiral structures in the layers immediately above the discs and Andersson and Lygren [23] concluded with the help of numerical simulations that the mean flow three-dimensionality plays a major role in the generation of near-wall vortices, as evidenced by Littell and Eaton [8] in their early experimental work.

Although the existence of coherent near-wall vortices in industrial configurations has not been reported in the literature *per se* to the authors knowledge, data-gathering campaigns dealing with industrial turbomachinery stages (e.g. a turbopump turbine stage, a compressor, . . .) or more academic experimental facilities confirm the strong unsteady character of such flows. One intent of the current contribution is to qualify LES-based CFD tools in providing informations on such unsteady flow features. The choice of LES is due, as aforementionned, to the high Reynolds numbers imposed by the end-use of LES on industrial operating points preventing the use of DNS. With this in mind, we investigate here in a simplified cylindrical configuration, the
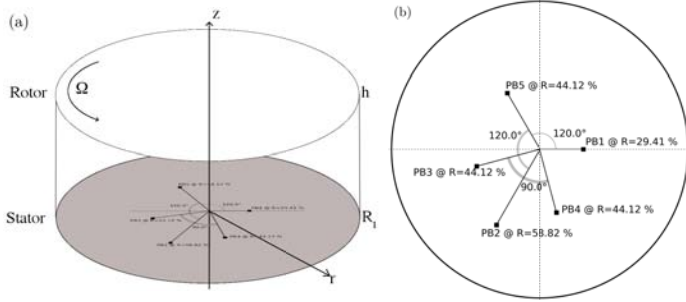
FIGURE 1. (a) Schematic representation of the rotating cavity with relevant notations: radius R_1, height h and rotation speed Ω. (b) Detail of the five probes used in the experimental configuration.

effects of using a wall modeled LES approch at the stationary disc and evaluate its impact on the unsteady structures known to appear in the flow. Whether a wall-modeled LES satisfactorily preserves the unstable nature of the configuration is assessed by comparing the dynamics of the flow against a wall-resolved LES simulation.

The document is organized as follows. First the origin of the geometrical set-up is discussed, followed by a general presentation of the CFD software and the numerical details. The second section of this document is then dedicated to an in-depth study of the reference wall resolved LES. The last section further focuses on the wall modeled LES and the assessment of its ability to capture accurately unsteady phenomena occurring in the boundary layer. Finally, conclusions and opening remarks are provided.

THE EXPERIMENTAL SET-UP

The cavity showed in Fig. 1(a) is composed of a smooth stationary disc (the stator) and a smooth rotating disc (the rotor) delimited by an outer stationary cylinder (the shroud). The rotor rotates at the uniform angular velocity $\Omega = \Omega \vec{e_z}$, $\vec{e_z}$ being the unit vector pointing in the axial direction. The origin of the z-axis is located on the stator.

The mean flow is controlled by two physical parameters which are the Reynolds number, Re, and the cavity aspect ratio, $G = h/R_1 = 1.176$. Note that such an enclosed geometry can be characterized by two distinct length scales, the radius R_1 or the height h, either of which can be used to define the Reynolds number. In this document, we consider a radial Reynolds number $Re_R = R_1^2 \Omega / \nu = 1.0 \times 10^5$ (used for instance by Séverac et al. [5] or Serre et al. [4]) where ν is the kinematic viscosity of the fluid, $R_1 = 34$ mm is the outer radius of the rotating disc and $\Omega = 2\pi F_0 \simeq 525 \, \text{rad.s}^{-1}$ its rotation speed (we call F_0 the frequency of the rotor).

The values of the geometrical parameters have been

chosen by the first team who studied this configuration experimentally (see [24]) in order to be relevant to industrial devices and to ease technical constraints such as the pressurization and the thermalization of the cavity. In the experimental set-up there exists a small clearance $\delta_1 = 2$ mm between the rotor and the shroud ($\delta_1/h = 0.05$) because of obvious mechanical constraints, that will not be resolved in the numerical simulations described further in this document.

Measurements are performed using five pressure probes located on the stationary disc at the positions shown on Fig. 1(b): three probes (PB_1, PB_5 and PB_2) separated by a constant angle of 120° with a low temporal resolution provide time-averaged pressure data whereas the last two probes (PB_3 and PB_4) monitor time-resolved pressure fluctuations. The sensors can achieve a maximum sampling rate of 200 kHz but it was bounded to 10 kHz during the experiments, yielding a resolution ΔF of the order of 10^{-2} Hz or $\Delta(F/F_0) \simeq 10^{-4}$. The experimental signal has been converged over about 5000 rotations of the disc before any spectral analysis was attempted.

THE NUMERICAL MODELING

Numerical method

The code chosen to perform the simulations, AVBP [25], is widely used both for basic research and applied research of industrial interest. This parallel code solves the full compressible Navier-Stokes equations using a finite-element scheme TTGC [26] based on a two steps Taylor-Galerkin formulation. It also relies on a cell-vertex diffusion scheme [26, 27] specifically designed for LES on multi-element meshes: low diffusion and low dispersion properties of this explicit scheme makes it indeed highly suitable for LES by providing 3$^{\text{rd}}$ order space and time accuracy. The subgrid scales are modeled using the WALE model [28]. It allows for a better behavior of the eddy viscosity production than the classical Smagorinsky [29] formulation for wall bounded flows. It is also known to produce zero eddy viscosity in case of pure shear, thus leading to a better prediction of the laminar to turbulent transition process through the growth of linear unstable modes.

Computational details

For all simulations the fluid is initially at rest in the cavity and the discs are stationary. At $t = 0$, the upper disc is instantaneously brought to its velocity (Ω rad/s) and the fluid is subsequently put in motion due to viscous interactions.

Radial and axial no-slip boundary conditions are ap-

3

plied on the rotating disc. There, $u_r = u_z = 0$ whereas the azimuthal velocity is set to $u_\theta = r\Omega$, where $\mathbf{u} = (u_r, u_\theta, u_z)$ are the three components of velocity in the cylindrical coordinates system (r, θ, z). On the contrary a slip-wall condition is applied to the outer shroud i.e. $\mathbf{u} \cdot \vec{n} = 0$ and $d\left(\mathbf{u} \cdot \vec{t}\right)/d\vec{t} = 0$ where $\vec{n}$ and $\vec{t}$ represent respectively the normal and tangential vectors to the walls. Two different statoric boundary conditions are used to study the impact of wall modeling on the structures present in the flow

(BC$_1$) a no-slip wall boundary with $\mathbf{u} = 0$

(BC$_2$) a wall model imposing Coles *et al.* law-of-the-wall [30] $u^+ = \kappa^{-1} \log\left(y^+\right) + E$, with $\kappa = 0.41$ and $E = 5.4$.

Note also that all boundaries are set to be adiabatic, so the flow is said to be in a converged state as soon as the volume-averaged kinetic energy reaches a plateau and the slope of the volume-averaged temperature becomes constant, i.e. when the heating due to viscous friction within the flow and on adiabatic walls in the enclosed cavity stabilizes.

The present investigation has been carried out using four different configurations for which either the mesh, the set of boundary conditions, or both, were modified. Three different meshes were involved: a refined grid, an average quality LES mesh and a coarse mesh designed specifically for the use of (BC$_2$). The three meshes are made exclusively of prismatic elements to facilitate the resolution of the two discs boundary layers. The first layer close to the stator always has a height proportional to $\delta = \sqrt{\nu/\Omega}$ as it is known to be a factor relevant to the boundary layer thickness in rotating flows [1,15,31]. The results obtained with the computation on the most refined mesh (see next section) will serve as reference for the other simulations.

Comparing the results obtained on the first mesh and on the third mesh will indeed allow us to assess the discrepancies in the flow dynamics introduced by the law-of-the-wall model used on the stationary disc and to check whether a wall modeled LES preserves the unstable nature of the flow, and subsequently whether it can be used in an industrial-grade computation.

WALL RESOLVED LES

This section is dedicated to the detailed study of the wall resolved LES - ran on the most refined mesh with (BC$_1$) - to serve as a reference for the other three configurations. It principally focuses on the coherent structures expected to be present in the Bödewadt layer and that may be most impacted by the changes in the boundary profile described in more details in the next section. Figure 2(a) shows the skeleton of the refined mesh used for the reference simulation: it is made of layers of prisms of constant thickness
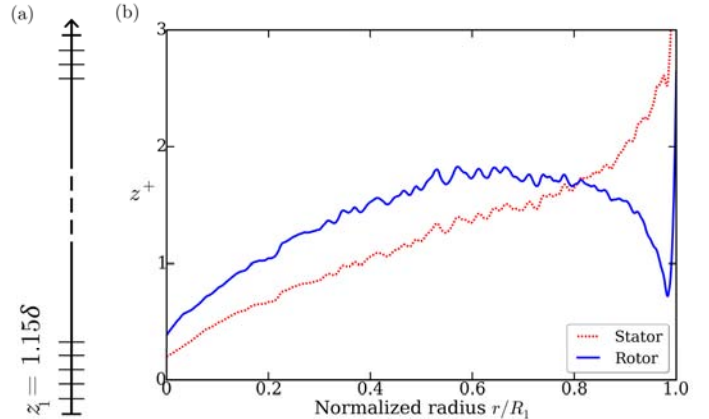

FIGURE 2. (a) Schematic structure of the wall-resolved LES mesh. (b) Radial evolution of the wall normal coordinate z^+ near the rotor and the stator.

$z_1 = 1.15\delta$ where $\delta = \sqrt{\nu/\Omega}$, i.e. $z_1/h \simeq 3.2 \times 10^{-3}$. In addition, Fig. 2(b) presents the radial distribution of the axial wall coordinate near the two discs $z^+ = z_1 v^*/\nu$ where v^* is the wall-friction velocity. It shows that $z^+ \lesssim 2$ and is greatest at the tip of the stationary disc, thus confirming the mesh meets the conditions of a wall-resolved LES [32].

Given the nature of the diagnostics used during the experimental campaign, and the primary interest which focuses on the unsteady features of the flow, a first paragraph is dedicated to an analysis of the spectral content of the stationary disc boundary layer. Once it has been shown that the resolved LES matches the experimental results on a spectral level, a more detailed study of the mean fields and turbulence statistics is presented that leads to the display of the coherent structures captured by the simulation.

Spectral content

It has been noticed during the experiments and the simulation that both PB$_3$ and PB$_4$ (see Fig. 1(b)) gathered the same data and yield the same temporal spectra. Therefore we shall work with the data from PB$_3$ thereafter, unless explicitly stated otherwise.

As noted in the previous section, all configurations use water-tight geometries and adiabatic boundary conditions hence the strain exerted by the flow on the walls heats up the fluid inside the cavity and induces a proportional increase in mean pressure. Consequently, and in order to prevent high-amplitude low-frequency content from polluting the spectra, we extract the pressure fluctuations $\tilde{p}$ from the ever-increasing static pressure signal P_s using a moving average as shown on Fig. 3.
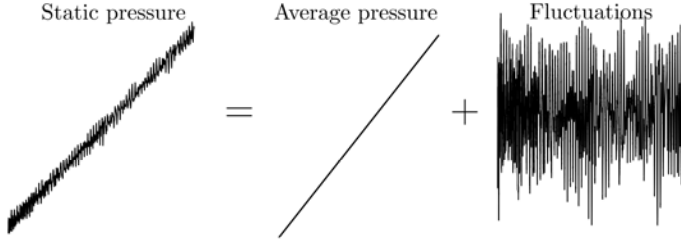
The signal is then processed through the Discrete Fast

FIGURE 3. Demonstration of the separation between mean carrier signal and superimposed fluctuations using a moving average.

FIGURE 4. Temporal power spectral density of the pressure fluctuations (1) registered at the pointwise probe PB$_3$ (see Fig. 1(b)) plotted against the normalized frequency. Constituent frequencies from the experiments (dot-dashed lines) and from the LES (dashed lines) are also presented.

Fourier Transform algorithm [33] to reveal its constituent frequencies. The power spectral density, defined by

$$\text{PSD}\,(\tilde{p}) = 10 \log_{10}\left(\left|\mathcal{F}\left[P_s - \overline{P_s}\right]\right|^2\right) \quad \text{dB} \qquad (1)$$

is plotted on Fig. 4 for the reference LES, with a resolution $\Delta(F/F_0) \simeq 2 \times 10^{-3}$. The three principal experimental frequencies detected by Lachize *et al.* [24] are located at $0.25F_0$, $0.5F_0$, $0.75F_0$ and F_0 respectively and reported on the bottom axis of Fig. 4 ; on the other hand, the constituent frequencies of the LES signal are indicated on the top axis and with dashed lines. Figure 4 shows that the fundamental frequency the stationary disc boundary layer responds to is close to $F_f = 0.4F_0$: the first $(2F_f)$ and second even harmonics $(4F_f)$ are present albeit in intervals with high dispersion, followed by marked peaks at odd higher harmonics $(7F_f, 9F_f, \text{etc}\dots)$. Besides from the $2F_f$ peak which can be associated with the third experimental frequency $(0.75F_0)$, it is of note that the LES signal also shows peaks at $0.54F_0$ and F_0 as expected according to the experimental data.

These observations, made for a high aspect-ratio cavity, are qualitatively similar to the conclusions reached by Gauthier *et al.* [34]. The authors indeed show that, without any external forcing, a low aspect-ratio rotor/stator flow $(G = 0.047)$ displays its strongest peak around $4F_0$ and weaker amplitudes aligned with multiples of F_0. On the other hand, in our high aspect-ratio configuration the strongest peak is located around F_0 and weaker waves align both with fractions and multiples of F_0.

Meanflow profiles

All the calculated quantities presented in the following paragraphs are averaged in time and/or in the azimuthal direction using a generic discrete averaging operator defined as follows:
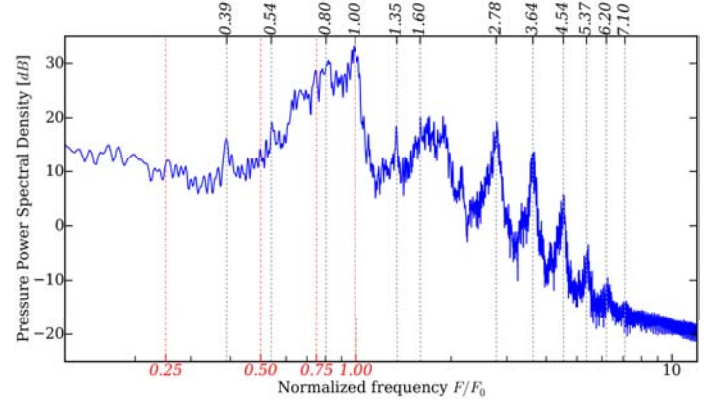
$$\langle \mathbf{X}(x_i; \chi) \rangle_\chi = \frac{1}{N_\chi} \sum_{k=1}^{N_\chi} \mathbf{X}(x_i; \chi_k) \qquad (2)$$

where χ represents either the temporal discretization or azimuthal discretization in N_χ instantaneous snapshots equidistributed in time or azimuth, respectively, x_i being all the other independent variables. All the data has been averaged both in time and in the tangential direction using $N_t \Delta t = 100\Omega^{-1}$ and $N_\theta = 360$.

The axial profiles of the time- and θ-averaged radial, azimuthal and axial velocity components at mid-radius $(r = 0.5R_1)$ are shown in Fig. 5, non-dimensionalized respectively by $r\Omega$, $r\Omega$ and $\sqrt{\nu\Omega}$. A comparison is established with the auto-similar solution suggested by Batchelor [35] and developed mathematically by Lance and Rogers [36] amongst others.

The mean flow (Fig. 5) clearly exhibits separated boundary layers, thus confirming it belongs to regime IV according to the classification by Daily and Nece [13]. In terms of organization, the fluid close to the rotor is directed outward $(u_r > 0)$ due to centrifugal acceleration and this outflow is compensated by the fluid going towards the hub near the stator $(u_r < 0)$. As for single-disc flows (see e.g. the analysis by Lingwood [37]), the layer close to the rotor is referred to as the Ekman layer while the boundary layer close to the stator is known as the Bödewadt layer. In these two boundary layers the three components of velocity vary rapidly but they are separated by a homogeneous region where no radial flow occurs $(u_r = 0)$ and where the az-
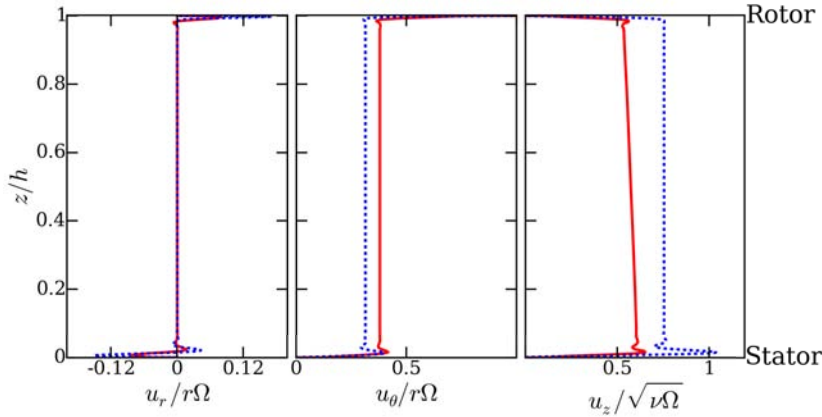
FIGURE 5. Axial profiles of the dimensionless time- and theta-averaged ($N_\theta = 360$, $N_t \Delta t = 100 \Omega^{-1}$) radial, azimuthal and axial velocity components (from left to right) at mid-radius $r = 0.5 R_1$. Comparison with the auto-similar solution by Lance *et al.* [36] ($--$).

FIGURE 6. Polar plot of the dimensionless time- and theta-averaged ($N_\theta = 360$, $N_t \Delta t = 100 \Omega^{-1}$) velocity distribution at mid-radius $r = 0.5 R_1$. Comparison between (-) the LES results, ($--$) the auto-similar solution by Lance *et al.* [36] and (o–o) the DNS results of Lygren and Andersson [9].

imuthal velocity remains constant, equal to a dimensionless value $u_\theta/r\Omega = K \simeq 0.38$, where K is called the entrainment coefficient. It is of note that K is below 0.5 between the two discs, which is the limit value obtained for the plane Couette flow (see e.g. [38]). Besides, the entrainment coefficient can be compared to the value $K \simeq 0.35$ measured by Cheah *et al.* [21] for Re_R up to 2.6×10^5 and to the one $K \simeq 0.4$ obtained by Andersson and Lygren [23] at $Re_R = 6.4 \times 10^5$ ($G = 0.1$). The comparison with the auto-similar solution to two-discs rotating flows developed by Lance *et al.* [36] (see Fig. 5 [$--$]) also shows that the confinement due to the outer cylindrical wall induces an overestimation of the entrainement coefficient and an underestimation of the core axial velocity, but that the LES is able to capture the boundary layers thickness with fair accuracy.

Extra information about the meanflow can be gathered from the polar plot of the azimuthal and radial velocity components in the whole space between the discs, at $r = 0.5 R_1$ as given on Fig. 6. Both the polar plot part corresponding to the rotating disc boundary layer ($u_r > 0$) and that corresponding to the stationary disc boundary layer ($u_r < 0$) largely differ from the laminar auto-similar solution by Lance *et al.* [36] (see also [31, 35]) as already observed on Fig. 5. In addition, the LES solution does not exactly match the DNS results obtained by Lygren *et al.* [9] for a larger Reynolds number $Re_R = 4 \times 10^5$. What is more, according to these authors, the distance to the laminar solution provides a direct evaluation of the level of turbulence of the two boundary layers. This means that the stationary disc boundary layer produced by the LES is less turbulent than the DNS layer as expected, however the LES
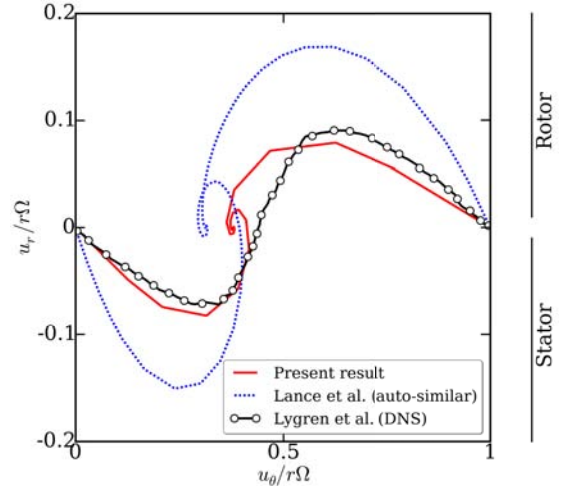
slightly overpredicts the turbulent behavior of the rotating disc boundary layer (see Fig. 6).

Boundary layers

Due to the presence of the outer stationary cylinder at $r = R_1$, the flow is radially confined and so behaves differently than rotor/stator flows between infinite discs as described originally by Batchelor [35] (see [36] for more details). Contrary to the latter, the confined flow does not have a constant entrainment coefficient K but it rather increases with the radius as shown on Fig. 7. The comparison with the auto-similar solution of Batchelor actually shows that the combination of the confinement and the high aspect-ratio prevents the flow from behaving like the theoretical case at all radii, partly explaining the differences with theory observed on the polars of Fig. 6. Current profiles of K compare well with the trend reported by Poncet [39] for a slimmer cavity $G = 0.036$ and an equivalent Reynolds number $Re_R \simeq 5 \times 10^5$. Note that the line corresponding to Poncet *et al.* (Fig. 7 ($\circ$)) does not start strictly at $r^* = r/R_1 = 0$ for lack of data in this part of the cavity (see [39]). Differences in terms of magnitude may be linked to the difference in aspect ratio, but as well to the treatment used on the outer cylinder. Indeed a slip-wall condition is used in this document making the entrainement coefficient converge to 1 at the outer wall whereas a no-slip condition is imposed by Poncet [39] which forces K to go to 0 at this extremity, although his line (Fig. 7 ($\circ$)) is clipped before it
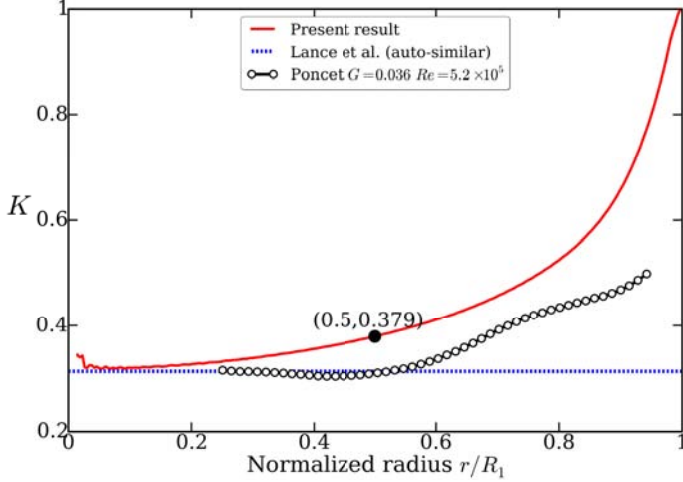
6

FIGURE 7. Radial evolution of the entrainement coefficient K for the confined flow. Comparison with the auto-similar solution from Lance *et al.* [36] (– –) and the results obtained by Poncet [39] for a cavity with $G = 0.036$ and $Re_R \simeq 5 \times 10^5$ (∘).

FIGURE 8. Radial distributions of the boundary layer thicknesses, non-dimensionalized by the factor $\delta = \sqrt{\nu/\Omega}$, plotted against the dimensionless radius r/R_1. Both the stationary disc δ_B and the rotating disc δ_E boundary layers are presented. Comparison with the experimental results of Gauthier *et al.* [34].

reaches the outer cylinder.

The confinement typically present in industrial rotor/stator cavities will not only have repercussions in the core of the configuration where the flow is in solid body rotation, but it also implies that the flow along the discs is no longer perfectly parallel contrary to the flows between infinite discs [35, 36]. Such non-parallel evolutions will in turn have an impact on the boundary layers spatial evolutions. Radial evolutions of the discs boundary layers are presented on Fig. 8, together with the experimental results obtained by Gauthier *et al.* [34] for a cavity with $G = 0.047$ and Reynolds numbers $2.0 \times 10^4 < Re_R < 6.3 \times 10^4$. The stationary (resp. rotating) disc boundary layer thickness is noted δ_B (resp. δ_E) and is defined as the distance between the stationary (resp. rotating) disc and the first point where $u_r = 0$ away from the disc.

In spite of the strong differences in aspect ratios between the two cases, the results are qualitatively in agreement. Both on the stator and on the rotor sides the boundary layer thicknesses are found to strongly decrease with the radius, even in the inner regions $0.2 < r/R_1 < 0.8$ where the flow is expected to follow the auto-similar solution of Lance *et al.* (see Fig. 5) i.e. of constant thickness [35,36] as evidenced experimentally by Gauthier *et al.* results. To explain this phenomenon, one may have to consider the local Reynolds number $Re_r = r^2\Omega/\nu$, that increases linearly with the radius which naturally causes the boundary layer to get thinner with increasing r. This inverse dependency between the local Reynolds number and the thickness of the boundary layers has indeed been pointed out by several authors
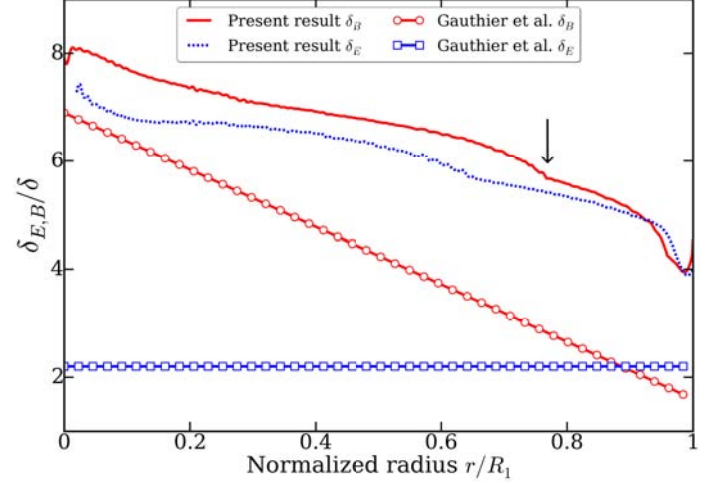
(see e.g. [5,13,39]), but such a trend is not always confirmed and only a few authors produce configurations that possess radially diminishing boundary layers. For one, Gauthier *et al.* [34] showed experimentally that, for their low aspect ratio configuration, the Bödewadt boundary layer thickness decreased from the hub to the shroud while the Ekman layer kept constant. Another example is the work by Lopez [40]: it can indeed be seen that the Bödewadt boundary layer gets thinner as the radius increases, and so does the Ekman layer.

Flow Structures

For all cases investigated in this document, and in particular for the wall resolved LES, instability patterns exist in the stationary disc boundary layer whereas the Ekman layer remains globally undisturbed. This observation is in qualitative agreement with previous LES of enclosed rotor/stator flows (e.g. [5,41]) that predict the Ekman layer to become turbulent from $Re_r \simeq 4 \times 10^5$, while the Bödewadt layer is already turbulent at $Re_r = 7 \times 10^4$. Figure 9 shows the isolines of the axial velocity component u_z in an azimuthal section at $z/h = 0.025$ ($z/\delta \simeq 9.0$, $\delta = \sqrt{\nu/\Omega}$) located above the stationary disc and in a vertical cut parametrized by $\theta = 0$ and $0.0 \leq z/h \leq 0.1$ ($0 \leq z/\delta \lesssim 35$). It exposes the existence of a three-armed spiral structure contained between two local Reynolds numbers $Re_I \simeq 8 \times 10^3$ and $Re_{II} \simeq 5.5 \times 10^4$ and reveals the presence of a centered concentric structure. It is noteworthy that the outermost location Re_{II} can also be identified on Fig. 8 as the upside-down feature
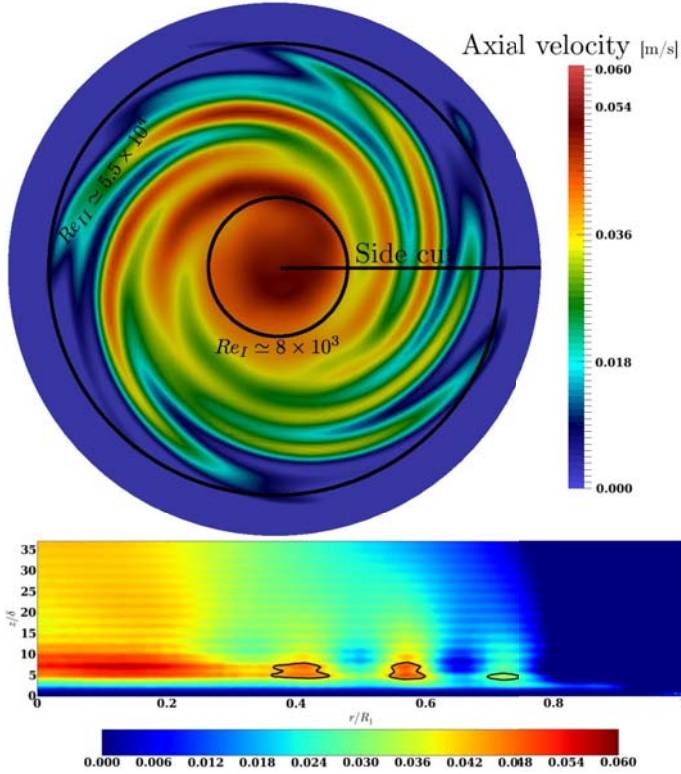
7

Axial velocity [m/s]

FIGURE 9. Top: $(r/R_1, \theta, z/h = 0.025)$ slice (stator) colored by u_z with relevant notations. Bottom: $(r/R_1, 0, 0.0 \leq z/h \leq 0.1)$ slice colored by axial velocity u_z and selected contours $u_z = [0.02, 0.04]$.

(marked by an arrow) displayed by $\delta_B(r/R_1)$ in the vicinity of $r/R_1 \simeq 0.75$.

All in all, these results are not surprising as several publications showed the existence of coherent patterns in the Bödewadt layer for different kinds of enclosed rotor/stator cavities, often with a peculiar focus on the nature and characteristics of the spiral vortices. Schouveiler *et al.* [42, 43] lead two comprehensive experimental studies revealing the co-existence of circular and spiral rolls, for values of the aspect ratio $0.07 \leq G \leq 0.15$, in which the circular rolls were confined below a local Reynolds number $Re_I \simeq 9.0 \times 10^3$ after which the spiral rolls extended to the edge of the disc. From the numerical point of view, a very complete review has been written by Serre, Crespo del Arco and Bontoux [16]. For a cylindrical cavity of aspect ratio $G = 0.5$, at a very low Reynolds number $Re_R = 1.6 \times 10^4$, they noted the presence of circular rolls from $Re_I \simeq 450$ and the transition to spiral rolls at $Re_{II} \simeq 1000$. Unfortunately, as far as the authors know, the presentation of the Bödewadt layer structures has never been done before for $G \gtrsim 1.0$ hence the comparison with the literature can be no more than quali-

TABLE 1. Summary of the four configurations studied to assess the impact of wall modelisation on the structures of rotating flows boundary layers. Boundary conditions and mesh properties are given to characterize each configuration.

	MR_1	MR_2	MM_1	MM_2
Mesh	cst.	cst.	cst.	var.
Prism height	1.15δ	2δ	2δ	var.
$z^+\left(\frac{R_1}{2}\right)$	1	8	11	31
Stator b.c.	(BC_1)	(BC_1)	(BC_2)	

tative and approximative at this point.

WALL MODELED LES PREDICTIONS

Now that the reference wall resolved LES has been studied extensively and that it has been shown it compared qualitatively well with the literature and the experimental data, this part focuses on the other configurations investigated. Table 1 summarizes the characteristics of all four configurations, MR_1 corresponding to the wall resolved LES presented in details in the previous section of this document. Figure 10 shows the skeletons of the two meshes used respectively with the cases MR_2 and MM_1, and the wall modeled case MM_2, along with a comparison of the radial distributions of the axial wall coordinate close to the stator (see [32]). Interest is first focused on how the mean flow differs from that of the reference LES. We then look at the structures present in the Bödewadt layer, and conclude this section with a comparison of the pressure spectra and energetic content of all predictions to statuate on the impact of the wall model.

Mean fields and boundary layers

The axial profiles of the time- and θ-averaged radial velocity component at mid-radius $(r = 0.5R_1)$ for all four configurations are compared on Fig. 11. Note that from now on the core flow is omitted since all the differences between the four configurations are confined to the boundary layers. Looking at Fig. 11(top), it appears that the three configurations MR_2, MM_1 and MM_2 based on the same near-rotor mesh produce qualitatively consistent results. The Ekman boundary layer thickness is overestimated in all three cases due to the poor mesh resolution close to the rotating disc, and one can also note that the amplitude of the centrifugal ejection is underestimated by MM_2. Discrepancies can also be observed on the stationary disc side (Fig. 11(bottom)): at this location $(r = 0.5R_1)$
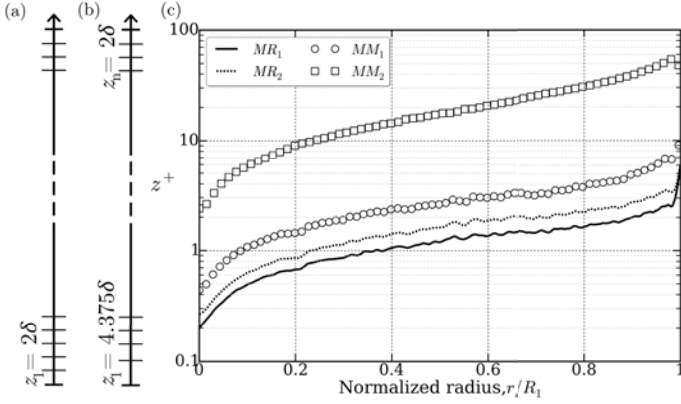
FIGURE 10. (a) Schematic structure of the mesh for MR_2 and MM_1. (b) Schematic structure of the mesh for MM_2. (c) Radial evolution of the wall normal coordinate z^+ near the stator for all four cases (see Tab. 1).

TABLE 2. Summary of the entrainement coefficients obtained from the four configurations at mid-radius $r = 0.5R_1$.

	MR_1	MR_2	MM_1	MM_2
K	0.38	0.34	0.36	0.53

the thickness of the Bödewadt layer fluctuates around the reference value provided by MR_1, and it is also remarkable that in the two cases with a law-of-the-wall boundary condition (MM_1 and MM_2), the velocity profiles do not have the same two inflection points as in MR_1 and MR_2. The differences in boundary layer thickness at all radial locations can be assessed on Fig. 12. Configuration MR_2 strongly overestimates the boundary layer thickness due to the lack of resolution usually requested by a wall resolved LES. On the other hand, configurations MM_1 and MM_2 provide qualitatively good results and of the same order of magnitude as MR_1. It is furthermore noticeable that configuration MM_2 yields a stator boundary layer of approximately constant thickness as reported in the literature (e.g. [5, 39, 41, 44]) although in constrast with the behavior of the reference case.

All configurations produce values of K at $r = 0.5R_1$ (see Tab. 2) of the same order of magnitude to the exception of MM_2 which fails to capture the rotation velocity of the fluid core and shows a behavior closer to that of an equivalent plane Couette flow.

Flow structures and unsteadiness

It has been shown in the previous section that the wall modeling used for configuration MM_2 introduces differences
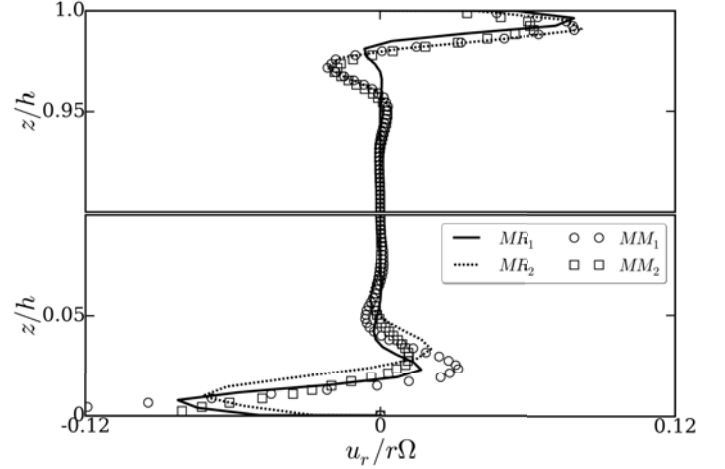

FIGURE 11. Axial profiles of the dimensionless time- and theta-averaged ($N_\theta = 360$, $N_t \Delta t = 100 \Omega^{-1}$) radial velocity components at mid-radius $r = 0.5R_1$. Comparison between the four configurations of Tab. 1. Rotor layer at the top, stator layer at the bottom.
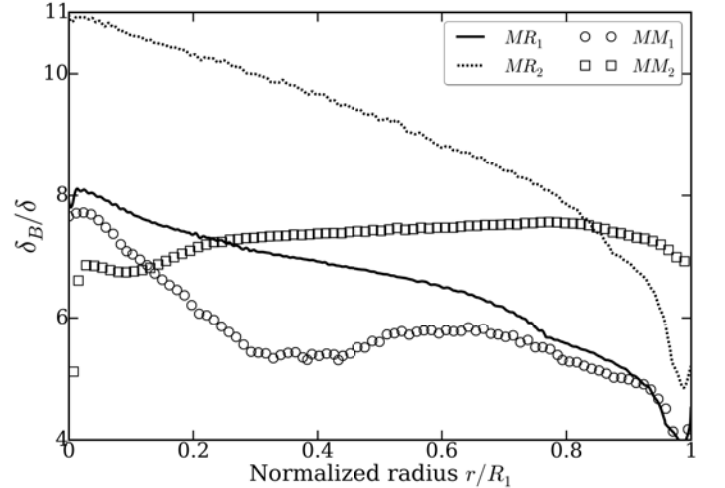

FIGURE 12. Radial distributions of the Bödewadt boundary layer thickness, non-dimensionalized by the factor $\delta = \sqrt{\nu/\Omega}$, plotted against the dimensionless radius r/R_1. Comparison between the four cases discussed in this document (see Tab. 1).

in the boundary layer thickness radial evolution and fails to properly capture the bulk behavior of the core. This paragraph now concentrates on the structures already known to exist in the Bödewadt boundary layer (see Fig. 9) and the related unsteady pressure signals found for all simulations to see if the discrepancies in meanflow do impede the unsteady character of the cavity flow.

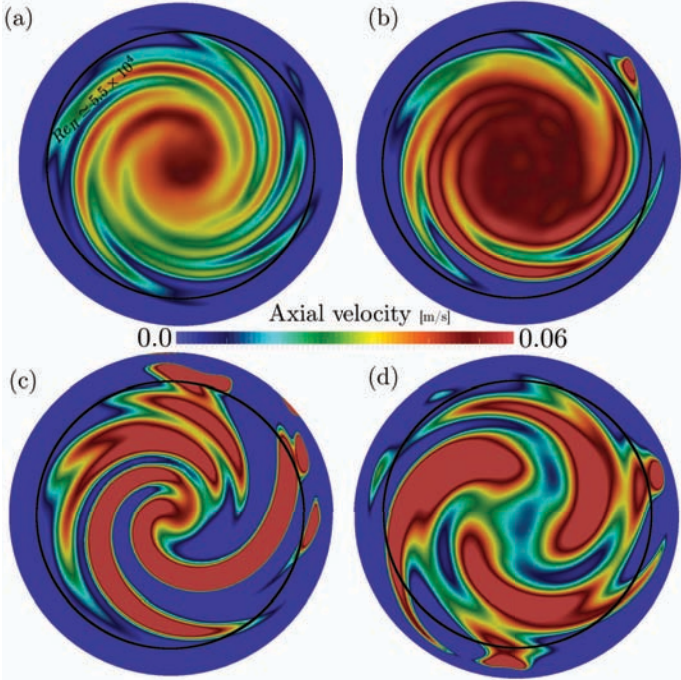To this end, Fig. 13 compares the isolines of axial veloc-

9

FIGURE 13. $(r/R_1, \theta, z/h = 0.025)$ slice colored by u_z with relevant notations. From (a) to (d), configurations MR_1 to MM_2, respectively. Re_{II} indicates the outermost Reynolds number of flow coherence observed in all four configurations.

FIGURE 14. Temporal power spectral density of the pressure fluctuations (1) registered at probe PB_3 (Fig. 1(b)). Comparison between all four configurations, MR_1 to MM_2 (see Tab. 1).

ity in the stator boundary layer in an azimuthal section at $z/h = 0.025$ ($z/\delta \simeq 9.0$) for all four configurations. First of all, it appears as expected that the density of the mesh immediately above the stationary disc has a direct impact on the resolution of the spiral arms, with the radial wavenumber decreasing when the mesh becomes more resolved as shown from Fig. 13(d) to Fig. 13(a). This phenomenon is accompanied by an increase in the average amplitude of the perturbation reflected by the saturation of the color scale in the figure. It is also of note that while configurations MR_1 and MR_2 display a high-velocity kernel from which the spiral arms spread, configurations MM_1 and MM_2 yield a lower critical Reynolds number and no disturbed kernel at all. The influence of the wall modeling is most obvious between configurations MR_2 and MM_1 (resp. Fig. 13(b) and Fig. 13(c)) for which the mesh is conserved and only the differences in boundary conditions influence the flow.

In conclusion, as mentioned before, all simulations agree on the existence of two types of unstable structures in the stationary disc boundary layer: two-dimensional annuli confined close to the singularity $r/R_1 = 0$ and three-dimensional structures occurring at higher Reynolds numbers, as often described in the literature e.g. [5,16,41,45,46]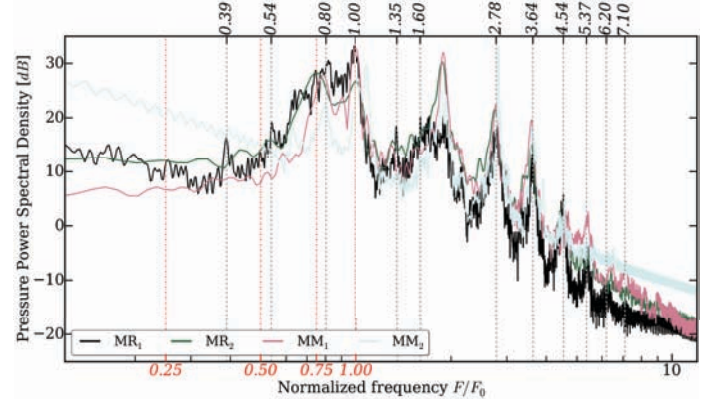. The structures themselves look markedly different from one configuration to another, but Fig. 13 proves that the wall modeling introduced in MM_2 preserves the azimuthal organization of the flow, albeit slightly different radially. In order to come back to our initial investigation bearing on the unsteady pressure signals obtained during the experimental campaign (see [24]), we compare in Fig. 14 the constituent frequencies of the unsteady signals obtained for the four configurations MR_1 to MM_2. Figure 14 mainly shows that the natural response of the flow appears to be independent of the mesh and/or the statoric boundary condition. First of all, although the fundamental F_f does not appear as clearly as in MR_1, all three signals display pronounced peaks around the two first even harmonics $2F_f$ and $4F_f$, and around the odd harmonics beyond the third ($7F_f$, $9F_f$, etc...) as it was the case in the reference LES. It is also noteworthy that contrary to the reference LES, the three test cases obviously show a strong response of the fluid to the second odd harmonic $5F_f \simeq 2.0F_0$. The fluid also happens to be excited at the frequency of the rotor F_0 in all three test cases, whereas the peak located at $0.54F_0$ in MR_1 does not stand out of the ambiant noise in any of the test cases. Nonetheless, it could be argued that in case MM_2 the fluid has a response at a frequency close to $0.6F_0$ which could be associated with the experimental $0.5F_0$. All in all, Fig. 13 and Fig. 14 show that although the stationary disc boundary layer somewhat loses its radial organization because of the law-of-the-wall modeling, the modal (azimuthal) organization as well as the spectral fauna are conserved. It is therefore reasonable to consider the use of a law-of-the-wall to simulate and characterize the unsteady character of the pressure field in a rotor/stator configuration.

CONCLUSION

Large Eddy Simulations of the turbulent flow in a cylindrical rotor-stator cavity has been performed. We focused on the impact of boundary conditions on the flow dynamics and particularly on the development of coherent structures in the stationary disc boundary layer. Four different sets of boundary conditions have been investigated, each using either a no-slip boundary condition on the stator or modeling the boundary layer using a classical law-of-the-wall model, and a dedicated mesh. The results obtained on the most refined mesh with a no-slip statoric boundary condition served as reference.

The time- and theta-averaged flow has been closely studied in terms of extracted axial profiles and boundary layers. From these quantities the current prediction is shown to be in good agreement with previous results and experimental data. Below a certain Reynolds number, the modeling of the stationary disc boundary layer is found to induce an underestimation of the velocity of the flow that leads to the disappearance of the low-Reynolds coherent bulbous structure observable in the reference flow. Overall, the law-of-the-wall boundary condition deteriorates the radial resolution of the spiral structure found in the stationary disc boundary layer. Nonetheless, the 3/4-armed spiral structure found in the reference configuration appears in all three configurations which indicates that the transition to the modeling of the stator boundary layer conserves the azimuthal resolution of the structures. What is more, a spectral analysis of the pressure signals yield by numerical probes located close to the stationary disc proved that although the amplitudes of the peaks slightly fluctuate between the configurations, the overall spectral content of the boundary layer stays identical. Altogether these observations validate the ability of a wall modeled LES to preserve the unstable nature of a high-Reynolds enclosed rotor-stator flow and to reproduce satisfactorily the coherent structures expected in the stationary disc boundary layer.

REFERENCES

[1] Owen, J. M., and Rogers, R. H., 1989. *Flow and Heat Transfer in Rotating Disc Systems, Volume 1 : Rotor-stator systems*. Taunton, U.K.: Research Studies Press.

[2] Owen, J. M., and Rogers, R. H., 1995. *Flow and Heat Transfer in Rotating Disc Systems, Volume 2 : Rotating Cavities*. Taunton, U.K.: Research Studies Press.

[3] Tuliszka-Sznitko, E., Zielinski, A., and Majchrowski, W., 2009. "Large Eddy Simulation of transitional flows in rotor/stator cavity". *Arch. Mech.,* **61**(2), pp. 95–120.

[4] Serre, E., Tuliszka-Sznitko, E., and Bontoux, P., 2004. "Coupled numerical and theoretical study of the flow transition between a rotating and a stationary disk". *Phys. Fluids,* **16**(3), p. 688.

[5] Séverac, E., Poncet, S., Serre, E., and Chauve, M.-P., 2007. "Large eddy simulation and measurements of turbulent enclosed rotor-stator flows". *Phys. Fluids,* **19**(8), pp. 85–113.

[6] Tuliszka-Sznitko, E., and Zielinski, A., 2007. "Instability of the flow in rotating cavity". *J. Theor. Appl. Mech.,* **45**(3), pp. 685–704.

[7] Kang, H. S., Choi, H., and Yoo, J. Y., 1998. "On the modification of the near-wall coherent structures in a three-dimensional turbulent boundary layer on a free rotating disk". *Phys. Fluids,* **10**(2315).

[8] Littell, H. S., and Eaton, J. K., 1994. "Turbulence characteristics of the boundary layer on a rotating disk". *J. Fluid Mech.,* **266**, pp. 175–207.

[9] Lygren, M., and Andersson, H. I., 2001. "Turbulent flow between a rotating and a stationary disk". *J. Fluid Mech.,* **426**, Jan., pp. 297–326.

[10] Poncet, S., Chauve, M. P., and Schiestel, R., 2005. "Batchelor versus Stewartson flow structures in a rotor-stator cavity with throughflow". *Phys. Fluids,* **17**(7), pp. 1–15.

[11] Severac, E., and Serre, E., 2007. "A spectral vanishing viscosity for the LES of turbulent flows within rotating cavities". *J. Comput. Phys.,* **226**(2), Oct., pp. 1234–1255.

[12] Tuliszka-Sznitko, E., and Zielinski, A., 2006. "Numerical Investigation of Transitional Flow in Co- and Counter-Rotating Annular Cavity". *J. Theor. Appl. Mech.*(1997), pp. 405–420.

[13] Daily, J. W., and Nece, R. E., 1960. "Chamber dimension effects on induced flow and frictional resistance of enclosed rotating disks". *J. Fluids Eng.,* **82**(1), pp. 217–230.

[14] Ekman, V. W., 1905. "On the influence of the Earth's rotation on ocean currents.". *Ark. för Mat. Astron. och Fys.,* **2**, pp. 1–53.

[15] Bödewadt, U., 1940. "Die Drehströmung über fes-

[15] tem Grunde". *Zeitschrift für Angew. Math. und Mech.,* ***20***(5), pp. 241–253.

[16] Serre, E., Crespo Del Arco, E., and Bontoux, P., 2001. "Annular and spiral patterns in flows between rotating and stationary discs". *J. Fluid Mech.,* ***434***, pp. 65–100.

[17] Poncet, S., Serre, E., and Le Gal, P., 2009. "Revisiting the two first instabilities of the flow in an annular rotor-stator cavity". *Phys. Fluids,* ***21***, pp. 1–30.

[18] Launder, B., Poncet, S., and Serre, E., 2010. "Laminar, Transitional, and Turbulent Flows in Rotor-Stator Cavities". *Annu. Rev. Fluid Mech.,* ***42***, pp. 229–248.

[19] Itoh, M., Yamada, Y., Imao, S., and Gonda, M., 1992. "Experiments on turbulent flow due to an enclosed rotating disk". *Exp. Therm. Fluid Sci.,* ***5***(3), pp. 359–368.

[20] Itoh, M., and Hasegawa, I., 1994. "Turbulent Boundary Layer on a Rotating Disk in Infinite Quiescent Fluid". *JSME Int. J.,* ***37***(3).

[21] Cheah, S., Iacovides, H., Jackson, D., Ji, H., and Launder, B., 1994. "Experimental investigation of enclosed rotor-stator disk flows". *Exp. Therm. Fluid Sci.,* ***9***(4), Nov., pp. 445–455.

[22] Wu, X., and Squires, K. D., 2000. "Prediction and investigation of the turbulent flow over a rotating disk". *J. Fluid Mech.,* ***418***, pp. 231–264.

[23] Andersson, H. I., and Lygren, M., 2006. "LES of open rotor-stator flow". *Int. J. Heat Fluid Flow,* ***27***(4), Aug., pp. 551–557.

[24] Lachize, C., Verhille, G., and Le Gal, P., 2015. "Structures non-axisymmétriques grandes échelles en cavité rotor/stator à grands nombres de Reynolds". In 22ème Congrès Français de Mécanique.

[25] Gourdain, N., Gicquel, L., Staffelbach, G., Vermorel, O., Duchaine, F., Boussuge, J.-F., and Poinsot, T., 2009. "High performance parallel computing of flows in complex geometries: I. Methods". *Comput. Sci. Discov.,* ***2***.

[26] Colin, O., and Rudgyard, M., 2000. "Development of High-Order Taylor–Galerkin Schemes for LES". *J. Comput. Phys.,* ***162***(2), Aug., pp. 338–371.

[27] Lamarque, N., 2007. "Schémas numériques et conditions limites pour la simulation aux grandes échelles de la combustion diphasique dans les foyers d'hélicoptère". Phd, INP Toulouse.

[28] Nicoud, F., and Ducros, F., 1999. "Subgrid-scale stress modelling based on the square of the velocity gradient tensor". *Turbul. Combust.,* ***62***(3), pp. 183–200.

[29] Smagorinsky, J., 1963. "General Circulation Experiments with the Primitive Equations I : the basic experiment". *Mon. Weather Rev.,* ***91***(3), pp. 99–164.

[30] Coles, and Hirst, 1968. "Computation of Turbulent Boundary Layers". In AFOSR-IFP Stanford Conf.

[31] Von Kármán, T., 1921. "Über laminare und turbulente Reibung". *Zeitschrift für Angew. Math. und Mech.,* ***1***(4), pp. 233–251.

[32] Schlichting, H., 1960. *Boundary Layer Theory*, 4th ed. McGraw-Hill.

[33] Cooley, J., and Tukey, J., 1965. "An Algorithm for the Machine Calculation of Complex Fourier Series". *Math. Comput.,* ***19***(90), pp. 297–301.

[34] Gauthier, G., Gondret, P., and Rabaud, M., 1999. "Axisymmetric propagating vortices in the flow between a stationary and a rotating disk enclosed by a cylinder". *J. Fluid Mech.,* ***386***, pp. 105–126.

[35] Batchelor, G. K., 1951. Note on a class of solutions of the navier-stokes equations representing steady rotationally-symmetric flow.

[36] Rogers, M., and Lance, G., 1962. "The Axially Symmetric Flow of a Viscous Fluid Between two Infinite Rotating Disk". *Proc. R. Soc. Lond. A,* ***266***, pp. 109–121.

[37] Lingwood, R. J., 1997. "Absolute instability of the Ekman layer and related rotating flows". *J. Fluid Mech.,* ***331***, pp. 405–428.

[38] White, F. M., 2006. *Viscous Fluid Flow*, 3rd ed. McGraw-Hill.

[39] Poncet, S., 2005. "Ecoulements de type rotor-stator soumis à un flux axial : de Batchelor à Stewartson". Phd, Université de Provence.

[40] Lopez, J. M., 1996. "Flow between a stationary and a rotating disk shrouded by a corotating cylinder". *Phys. Fluids,* ***8***(10), pp. 2605–2613.

[41] Séverac, E., Poncet, S., Serre, E., and Chauve, M. P., 2007. "Large eddy simulation and measurements of turbulent enclosed rotor-stator flows". *Phys. Fluids,* ***19***(8), pp. 1–47.

[42] Schouveiler, L., Gal, P. L., Chauve, M., and Takeda, Y., 1999. "Spiral and circular waves in the flow between a rotating and a stationary disk". *Exp. Fluids*, pp. 9–30.

[43] Schouveiler, L., 2001. "Instabilities of the flow between a rotating and a stationary disk". *J. Fluid Mech.,* ***443***, pp. 329–350.

[44] Poncet, S., and Chauve, M.-P., 2005. "Crossflow instability in rotor-stator flows with axial inward throughflow". *J. Fluid Mech.,* ***545***(-1), Dec., p. 281.

[45] Tuliszka-Sznitko, E., and Soong, C., 2001. "Instability of the non-isothermal flow between a rotating and a stationary disks". *TASK Q.,* ***5***(4), pp. 557–566.

[46] Crespo del Arco, E., Serre, E., Bontoux, P., and Launder, B., 2005. "Stability , transition and turbulence in rotating cavities". In *Instab. Flows*, M. Rhaman, ed. WIT PRESS, pp. 141–195.

Appendix G

Radial equilibrium analysis

Let an infinitesimal element be in a rotating fluid (Fig.). It is subject to the centrifugal force

$$F_c = (\rho r dr d\theta)\omega^2 r = \rho u_\theta^2 dr d\theta \qquad (G.1)$$

The pressure force on the element, on the other hand, is

$$F_p = r dp d\theta \qquad (G.2)$$

All other forces being neglected, the particle will move at constant radius if and only if

$$F_p = F_c \Leftrightarrow dp = \rho u_\theta^2 dr/r \Leftrightarrow \boxed{\rho/\rho_0 = (r/r_0)^{u_\theta^2/R_g T_s}} \qquad (G.3)$$

where R_g is the gas constant, T_s the static pressure, the 0-subscripted variables are integration constants and the perfect gas law gives $p = \rho R_g T_s$.
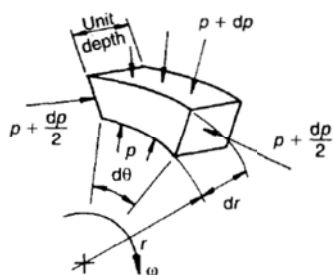

Figure G.1 – Schematic representation of a fluid element in a rotating fluid with relevant annotations.

Bibliography

ABU-IRSHAID, ESAM M., MAJDALANI, JOSEPH & CASALIS, GRÉGOIRE 2007 Hydrodynamic stability of rockets with headwall injection. *Phys. Fluids* **19** (2). (Cited on page 42.)

ANDERECK, C. DAVID, LIU, S. S. & SWINNEY, HARRY L. 1986 Flow regimes in a circular Couette system with independently rotating cylinders. *J. Fluid Mech.* **164**, 155. (Cited on page 148.)

ANDERSON, E, BAI, Z, BISCHOF, C, BLACKFORD, S, DEMMEL, J, DONGARRA, J, DU CROZ, J, GREENBAUM, A, HAMMARLING, S, MCKENNEY, A & SORENSEN, D 1999 *LAPACK Users Guide*, 3rd edn. Philadelphia, PA: Society for Industrial and Applied Mathematics. (Cited on page 40.)

ANDERSSON, HELGE I. & LYGREN, MAGNE 2006 LES of open rotor-stator flow. *Int. J. Heat Fluid Flow* **27** (4), 551–557. (Cited on page 64.)

APPELQUIST, E 2014 Direct numerical simulations of the rotating-disk boundary-layer flow. *Tech. Rep.*. (Cited on page 47.)

APPELQUIST, E. & IMAYAMA, SHINTARO 2014 Revisiting the stability analysis of the flow over a rotating disk. *Tech. Rep.*. (Cited on pages 45, 48, and 49.)

ASH, ROBERT L. & KHORRAMI, MEHDI R. 1995 Vortex Stability. In *Fluid Vor.*, 1st edn. (ed. Sheldon I. Green), chap. VIII, p. 49. Vancouver, Canada: Springer-Science+Business Media. (Cited on page 50.)

BALACHANDAR, S, STREET, CL & MALIK, MR 1992 Secondary instability in rotating-disk flow. *J. Fluid Mech.* **242**, 323–347. (Cited on pages 42, 45, 46, 47, and 48.)

BATCHELOR, G. K. 1951 Note on a class of solutions of the navier-stokes equations representing steady rotationally-symmetric flow. *Q. J. Mech. Appl. Math.* **4** (1), 29–41. (Cited on pages 13, 14, 15, and 18.)

BILLANT, P, CHOMAZ, J-M & HUERRE, P 1998 Experimental study of vortex breakdown in swirling jets. *J. Fluid Mech.* **376**, 183–219. (Cited on page 50.)

BÖDEWADT, U.T. 1940 Die Drehströmung über festem Grunde. *Zeitschrift für Angew. Math. und Mech.* **20** (5), 241–253. (Cited on pages 13, 14, 16, 17, 19, 20, 23, 57, 61, 63, 74, 75, 76, 78, 79, 81, 83, 85, 87, 88, 89, 90, 92, 97, 98, 115, and 123.)

BRIDEL-BERTOMEU, THIBAULT, GICQUEL, LAURENT & STAFFELBACH, GABRIEL 2016 Wall modeled LES and its impact on rotor/stator cavity unsteady features. *ASME Turbo Expo 2016* . (Cited on page 132.)

BUISINE, DANIEL, OBLE, FRÉDÉRIC & ANDRIANARAHINJAKA, HERINIRINA 2000 Étude numérique des structures spirales tridimensionnelles à la périphérie d'une cavité interdisque. *Comptes Rendus l Academie des Sci. Paris* **328** (II b), 237–246. (Cited on page 83.)

CANUTO, C., HUSSAINI, M. Y., QUARTERONI, A. & ZANG, T. A. 1988 *Spectral Methods in Fluid Dynamics.* (Cited on pages 34, 35, 39, and 47.)

CHOMAZ, JM, HUERRE, P & REDEKOPP, LG 1991*a* A frequency selection criterion in spatially developing flows. *Stud. Appl. Math* . (Cited on pages 22, 33, and 110.)

CHOMAZ, J-M, HUERRE, P. & REDEKOPP, L.G 1991*b* A frequency selection criterion in spatially developing flows. *Stud. Appl. Math.* **84**, 119–144. (Cited on page 33.)

COCHRAN, W.G. 1934 The flow due to a rotating disc. *Math. Proc. Cambridge Philos. Soc.* **30** (3), 365–375. (Cited on pages 12, 13, and 14.)

COLES & HIRST 1968 Computation of Turbulent Boundary Layers. *AFOSR-IFP Stanford Conf.* . (Cited on page 130.)

COLIN, OLIVIER & RUDGYARD, MICHAEL 2000 Development of High-Order Taylor–Galerkin Schemes for LES. *J. Comput. Phys.* **162** (2), 338–371. (Cited on pages 65, 132, and 133.)

COOPER, ALISON J. & CRIGHTON, DAVID G. 2000 Global modes and superdirective acoustic radiation in low-speed axisymmetric jets. *Eur. J. Mech. B/Fluids* **19** (5), 559–574. (Cited on pages 34 and 111.)

COUSIN-RITTEMARD, NATHALIE 1996 Contribution à l'étude des instabilités des écoulements axisymétriques en cavité interdisques de type rotor-stator. PhD thesis, Univ. de Paris VI. (Cited on page 15.)

CRESPO DEL ARCO, EMILIA, SERRE, ERIC, BONTOUX, PATRICK & LAUNDER, BRIAN 2005 Stability , transition and turbulence in rotating cavities. In *Instab. Flows* (ed. M Rhaman), pp. 141–195. WIT PRESS. (Cited on page 67.)

CRIGHTON, D. G. & GASTER, M. 1976 Stability of slowly diverging jet flow. *J. Fluid Mech.* **77** (1976), 397. (Cited on pages 22 and 31.)

CZARNY, O, IACOVIDES, H & LAUNDER, BE 2002 Precessing vortex structures in turbulent flow within rotor-stator disc cavities. *Flow, Turbul. Combust.* **69**, 51–61. (Cited on page 64.)

DAILY, J W & NECE, R E 1960 Chamber dimension effects on induced flow and frictional resistance of enclosed rotating disks. *J. Fluids Eng.* **82** (1), 217–230. (Cited on pages 20, 60, 61, 63, 64, 70, 74, 123, 137, 138, and 139.)

DAVIS, STEPHEN H 1976 The stability of time-periodic flows. *Annu. Rev. Fluid Mech.* **8**, 57–74. (Cited on page 33.)

DIJKSTRA, D. & HEIJST, G. J. F. VAN 1983 The flow between two finite rotating disks enclosed by a cylinder. *J. Fluid Mech.* **128**, 123–154. (Cited on page 63.)

EKMAN, VAGN WALFRID 1905 On the influence of the Earth's rotation on ocean currents. *Ark. för Mat. Astron. och Fys.* **2**, 1–53. (Cited on pages ix, 5, 12, 13, 14, 16, 17, 18, 19, 20, 23, 57, 60, 63, 75, 80, 82, 83, 88, 90, 92, 96, and 123.)

FALLER, ALAN J 1963 An experimental study of the instability of the laminar Ekman boundary layer. *J. Fluid Mech.* **15** (4), 560–576. (Cited on pages 23, 75, and 76.)

FALLER, ALAN J. 1991 Instability and transition of disturbed flow over a rotating disk. *J. Fluid Mech.* **230**, 245–269. (Cited on pages 14, 23, 25, and 63.)

FALLER, ALAN J. & KAYLOR, ROBERT E. 1966*a* A Numerical Study of the Instability of the Laminar Ekman Boundary Layer. *J. Atmos. Sci.* **23** (5), 466–480. (Cited on page 23.)

FALLER, ALAN J. & KAYLOR, ROBERT E. 1966*b* Investigations of stability and transition in rotating boundary layers. *Dyn. Fluids Plasmas* **1**, 309. (Cited on page 23.)

FERRARI, A, MASSAGLIA, S & TRUSSONI, E 1982 Magnetohydrodynamic Kelvin-Helmholtz instabilities in astrophysics - 3. Hydrodynamic flows with shear layers. *Mon. Not. R. Astron. Soc.* **198**, 1065–1079. (Cited on page 5.)

FERRARI, A, TRUSSONI, E & ZANINETTI, L 1981 Magnetohydrodynamic Kelvin-Helmholtz instabilities in astrophysics - 2. Cylindrical boundary layer in vortex sheet approximation. *Mon. Not. R. Astron. Soc.* **196**, 1051–1066. (Cited on page 5.)

FERZIGER, JOEL 1997 *New Tools in Turbulence Modelling*. Springer Berlin Heidelberg. (Cited on page 61.)

FERZIGER, J. H. & PERIC, M. 2002 *Computational Methods for uid Dynamics*, 3rd edn. Springer. (Cited on page 65.)

FJORTOFT, RAGNAR 1949 Application of integral theorems in deriving criteria of stability for laminar flows and for the baroclinic circular vortex. *Geofys. Publ.* **17** (6). (Cited on page 23.)

GALLAIRE, FRANÇOIS & CHOMAZ, JEAN-MARC 2003*a* Mode selection in swirling jet experiments: a linear stability analysis. *J. Fluid Mech.* **494**, 223–253. (Cited on pages 22, 50, 51, and 52.)

GALLAIRE, FRANÇOIS & CHOMAZ, JEAN-MARC 2003*b* Mode selection in swirling jet experiments: a linear stability analysis. *J. Fluid Mech.* **494**, 223–253. (Cited on page 42.)

GALLAIRE, FRANÇOIS, RUITH, MICHAEL, MEIBURG, ECKART, CHOMAZ, JEAN-MARC & HUERRE, PATRICK 2006 Spiral vortex breakdown as a global mode. *J. Fluid Mech.* **549**, 71–80. (Cited on page 32.)

GARG, V. K. & ROULEAU, W. T. 1972 Linear spatial stability of pipe Poiseuille flow. *J. Fluid Mech.* **54** (1), 113–127. (Cited on pages 43 and 44.)

GAUTHIER, G., GONDRET, P. & RABAUD, M. 1999 Axisymmetric propagating vortices in the flow between a stationary and a rotating disk enclosed by a cylinder. *J. Fluid Mech.* **386**, 105–126. (Cited on pages 61, 63, 75, 76, 78, 81, 101, and 123.)

GELFGAT, AY, BAR-YOSEPH, P. Z & SOLAN, A 1996 Stability of confined swirling flow with and without vortex breakdown. *J. Fluid Mech.* **311**, 1–36. (Cited on page 82.)

GELFGAT, AY, BAR-YOSEPH, P. Z & SOLAN, A 2001 Three-dimensional instability of axisymmetric flow in a rotating lid – cylinder enclosure. *J. Fluid Mech.* **438**, 363–377. (Cited on pages 83, 98, 122, and 123.)

GELFGAT, A YU 2015 Primary oscillatory instability in a rotating disk–cylinder system with aspect (height/radius) ratio varying from 0.1 to 1. *Fluid Dyn. Res.* **47** (3), 035502. (Cited on pages 74, 76, 83, 98, and 123.)

GICQUEL, L. Y M, STAFFELBACH, G. & POINSOT, T. 2012 Large Eddy Simulations of gaseous flames in gas turbine combustion chambers. *Prog. Energy Combust. Sci.* **38** (6), 782–817. (Cited on page 65.)

GODDARD, E. C. & PENDRAY, G. E. 1970 *The Papers of Robert H. Goddard*. McGraw-Hill Book Company. (Cited on page 2.)

GODDARD, R. H 1919 *A Method for Reaching Extreme Altituded*. (Cited on page 2.)

GOURDAIN, N, GICQUEL, L, STAFFELBACH, G, VERMOREL, O, DUCHAINE, F, BOUSSUGE, J-F & POINSOT, T 2009 High performance parallel computing of flows in complex geometries: I. Methods. *Comput. Sci. Discov.* **2**. (Cited on page 65.)

GREENSPAN, H 1988 The theory of rotating fluids . (Cited on page 96.)

GREGORY, N, STUART, J. T. & WALKER, W. S. 1955 On the stability of three-dimensional boundary layers with application to the flow due to a rotating disk. *Philos. Trans. R. Soc. A Math. Phys. Eng. Sci.* **248**, 155–199. (Cited on pages 23, 45, 61, 75, and 76.)

GRIFFOND, JÉRÔME, CASALIS, GRÉGOIRE & PINEAU, JEAN PHILIPPE 2000 Spatial instability of flow in a semiinfinite cylinder with fluid injection through its porous walls. *Eur. J. Mech. B/Fluids* **19** (1), 69–87. (Cited on page 42.)

GROHNE, D 1956 Zur laminaren Strömung in einer kreiszylindrischen Dose mit rotierendem Deckel. *Zeitschrift für Angew. Math. und Mech.* **15** (1935), 17–20. (Cited on page 15.)

GROSSMANN, SIEGFRIED, LOHSE, DETLEF & SUN, CHAO 2016 High–Reynolds Number Taylor-Couette Turbulence. *Annu. Rev. Fluid Mech.* **48**, 53–80. (Cited on pages 31, 148, and 149.)

GUTIERREZ-CASTILLO, PALOMA & LOPEZ, JUAN M. 2015 Instabilities of the sidewall boundary layer in a rapidly rotating split cylinder. *Eur. J. Mech. B/Fluids* **52**, 76–84. (Cited on pages 96 and 97.)

HEALEY, J J 2007 Enhancing the absolute instability of a boundary layer by adding a far-away plate. *J. Fluid Mech.* **579**, 29–61. (Cited on pages 109 and 121.)

HELMHOLTZ, H. 1868 On discontinuous movements of fluids. *Philos. Mag.* **36** (4), 337–346. (Cited on page 21.)

HENDRIKS, F 2010 On Taylor vortices and Ekman layers in flow-induced vibration of hard disk drives. *Microsyst. Technol.* **16**, 93–101. (Cited on page 5.)

HO, CM & HUERRE, P 1984 Perturbed Free Shear Layers. *Annu. Rev. Fluid Mech.* (16), 365–424. (Cited on pages 31, 121, and 165.)

HOLODNIOK, M 1981 Computation of the flow between two rotating coaxial disks multiplicity of steady-state solutions. *J. Fluid Mech.* **108**, 227–240. (Cited on pages 15, 19, and 26.)

HOLODNIOK, M., KUBÍCEK, M. & HLAVÁCEK, V. 1977 Computation of the flow between two rotating coaxial disks. *J. Fluid Mech.* **81** (4), 689–699. (Cited on pages 15 and 19.)

HUERRE, PATRICK & MONKEWITZ, PETER A. 1990 Local and Global Instabilities in Spatially Developing Flows. (Cited on pages 24, 31, 32, and 33.)

ITOH, MOTOYUKI 1991 On the instability of the flow between coaxial rotating disks. *Bound. Layer Stab. Transit. to Turbul. ASME FED* **114**, 83–89. (Cited on pages 26, 77, 81, and 123.)

JIMENEZ, J. & MOIN, P. 1991 The minimal flow unit in near-wall turbulence. *J. Fluid Mech.* **225**, 231–240. (Cited on page 65.)

JONES, ERIC, OLIPHANT, TRAVIS & PETERSON, PEARU 2001 Scipy: Open Source Scientific Tools for Python. (Cited on pages 40 and 41.)

JUNIPER, MP 2011 The local and global stability of confined planar wakes at intermediate Reynolds number. *J. Fluid Mech.* pp. 218–238. (Cited on pages 31, 32, 34, 102, 110, 113, and 124.)

Kang, Hyung Suk, Choi, Haecheon & Yoo, Jung Yul 1998 On the modification of the near-wall coherent structures in a three-dimensional turbulent boundary layer on a free rotating disk. *Phys. Fluids* **10** (2315). (Cited on page 60.)

Kelvin, Lord 1871 Hydrokinetic solutions and observations. *Philos. Mag.* **42** (4), 362–377. (Cited on page 21.)

Khorrami, Mehdi R., Malik, Mujeeb R. & Ash, Robert L. 1989 Application of spectral collocation techniques to the stability of swirling flows. *J. Comput. Phys.* **81**, 206–229. (Cited on pages 34, 42, 43, and 44.)

Kobayashi, R, Kohama, Y & Takamadate, C 1980 Spiral Vortices in Boundary Layer Transition Regime on a Rotating Disk. *Acta Mech.* **82**, 71–82. (Cited on pages 45, 60, and 61.)

Koch, W. 1985 Local instability characteristics and frequency determination of self-excited wake flows. *J. Sound Vib.* **99** (1), 53–83. (Cited on page 33.)

Koupper, C, Poinsot, T, Gicquel, L & Duchaine, F 2014 Compatibility of Characteristic Boundary Conditions with Radial Equilibrium in Turbomachinery Simulations. *AIAA J.* **52** (12), 2829–2839. (Cited on page 132.)

Kreiss, HO & Parter, SV 1983 On the swirling flow between rotating coaxial disks: existence and nonuniqueness. *Commun. Pure Appl. Math.* **XXXVI**, 55–84. (Cited on page 15.)

Lachize, Cécile, Verhille, Gautier & Le Gal, Patrice 2015 Structures non-axisymmétriques grandes échelles en cavité rotor/stator à grands nombres de Reynolds. *22ème Congrès Français de Mécanique* . (Cited on pages 64 and 83.)

Lamarque, Nicolas 2007 Schémas numériques et conditions limites pour la simulation aux grandes échelles de la combustion diphasique dans les foyers d'hélicoptère. Phd, INP Toulouse. (Cited on pages 65 and 132.)

Launder, Brian, Poncet, Sébastien & Serre, Eric 2010 Laminar, Transitional, and Turbulent Flows in Rotor-Stator Cavities. *Annu. Rev. Fluid Mech.* **42**, 229–248. (Cited on page 61.)

Lehoucq, R.B., Sorensen, D.C. & Yang, C. 1998 *ARPACK Users Guide: Solution of Large-Scale Eigenvalue Problems with Implicitely Restarted Arnoldi Methods*. SIAM. (Cited on page 41.)

Lessen, Martin, Sadler, Stanley & Liu, TingYung 1968 Stability of Pipe Poiseuille Flow. *Phys. Fluids* **11** (7), 1404. (Cited on pages 42, 43, and 44.)

Levoy, Marc 1988 Volume Rendering - Display of Surfaces from Volume Data. *IEEE Comput. Graph. Appl.* **8** (3), 29–37. (Cited on page 147.)

LILLY, DOUGLAS K. 1966 On the instability of Ekman Boundary Flow. *J. Atmos. Sci.* **23**, 481–494. (Cited on page 76.)

LIN, C.C. 1955 *The theory of hydrodynamic stability*. Cambridge University Press. (Cited on page 22.)

LINGWOOD, REBECCA J. 1995*a* Absolute instability of the boundary layer on a rotating disk. *J. Fluid Mech.* **299**, 17–33. (Cited on pages 14, 23, 60, 63, 76, 82, and 123.)

LINGWOOD, R. J. 1995*b* Stability and Transition of the Boundary Layer on a Rotating Disk. Phd, Cambridge University. (Cited on pages 23, 25, 32, and 42.)

LINGWOOD, REBECCA J. 1997 Absolute instability of the Ekman layer and related rotating flows. *J. Fluid Mech.* **331**, 405–428. (Cited on pages 14, 23, 42, 48, 49, 60, 63, 76, 78, and 81.)

LITTELL, HOWARD S. & EATON, JOHN K. 1994 Turbulence characteristics of the boundary layer on a rotating disk. *J. Fluid Mech.* **266**, 175–207. (Cited on pages 45, 60, 61, and 63.)

LIU, J.T.C. 1989 Coherent structures in transitional and turbulent free shear flows. *Annu. Rev. Fluid Mech.* **21**, 285–315. (Cited on page 22.)

LODATO, GUIDO, DOMINGO, PASCALE & VERVISCH, LUC 2008 Three-dimensional boundary conditions for direct and large-eddy simulation of compressible viscous flows. *J. Comput. Phys.* **227** (10), 5105–5143. (Cited on page 132.)

LOPEZ, JUAN M. 1996 Flow between a stationary and a rotating disk shrouded by a corotating cylinder. *Phys. Fluids* **8** (10), 2605–2613. (Cited on pages 60, 61, 63, 74, 75, and 82.)

LOPEZ, JUAN M. 1998 Characteristics of endwall and sidewall boundary layers in a rotating cylinder with a differentially rotating endwall. *J. Fluid Mech.* **359**, 49–79. (Cited on page 75.)

LOPEZ, JUAN M. 2012 Three-dimensional swirling flows in a tall cylinder driven by a rotating endwall. *Phys. Fluids* **24** (1). (Cited on pages 60, 88, and 98.)

LOPEZ, JUAN M., MARQUES, FRANCISCO, RUBIO, ANTONIO M. & AVILA, MARC 2009 Crossflow instability of finite Bödewadt flows: Transients and spiral waves. *Phys. Fluids* **21** (11). (Cited on pages 60, 61, 64, 69, 74, 75, 78, 81, 113, and 123.)

LOPEZ, JUAN M. & WEIDMAN, P. D. 1996 Stability of stationary endwall boundary layers during spin-down. *J. Fluid Mech.* **326**, 373–398. (Cited on pages 61 and 63.)

LUMLEY, J. L. 1970 *Stochastic Tools in Turbulence*. Academic Press. (Cited on page 88.)

LYGREN, MAGNE & ANDERSSON, HELGE I. 2001 Turbulent flow between a rotating and a stationary disk. *J. Fluid Mech.* **426**, 297–326. (Cited on pages 60, 71, 72, and 123.)

MALIK, MR, WILKINSON, SP & ORSZAG, SA 1981 Instability and transition in rotating disk flow. *AIAA J.* **19** (9), 1131–1138. (Cited on pages 23, 25, 34, and 42.)

MALIK, MUJEEB R. 1986 The neutral curve for stationary disturbances in rotating-disk flow. *J. Fluid Mech.* **164**, 275–287. (Cited on pages 23, 42, and 48.)

MALIK, M. R., ZANG, T. A. & HUSSAINI, M. Y. 1985 A spectral collocation method for the Navier-Stokes equations. *J. Comput. Phys.* **61**, 64–88. (Cited on page 34.)

MARCHAND, O 1986 Sur les écoulements entre deux disques. PhD thesis, Univ. de la Méditerranée Aix-Marseille II. (Cited on page 20.)

METCALFE, R W & ORSZAG, S A 1973 Numerical Calculation of Linear Stability of Pipe Flows. *Bull. Am. Phys. Soc.* **18** (11), 1492. (Cited on page 44.)

MICHALKE, ALFONS 1971 Instability of a Compressible Circular free Jet with Consideration of the Influence of the Jet Boundary Layer Thickness. *Nasa Tech. Memo.* **75190**, 25. (Cited on page 22.)

MOLLO-CHRISTENSEN, E. 1967 Jet noise and shear flow instability seen from an experimenter's viewpoint. *J. Appl. Mech.* pp. 1–7. (Cited on page 22.)

MONKEWITZ, PA 1988 The absolute and convective nature of instability in two dimensional wakes at low Reynolds numbers. *Phys. Fluids* **31** (May), 999–1006. (Cited on pages 32, 50, and 52.)

NANSEN, FRIDTJOF 1902 Oceanography of the North Polar Basin. The Norwegian North Polar Expedition. *Sci. Results* **3**. (Cited on page 12.)

NELDER, J.A. & MEAD, R. 1965 A simplex method for function minimization. *Comput. J.* **7** (4), 308–313. (Cited on page 41.)

NICOUD, FRANCK & DUCROS, FRÉDÉRIC 1999 Subgrid-scale stress modelling based on the square of the velocity gradient tensor. *Turbul. Combust.* **62** (3), 183–200. (Cited on pages 65 and 132.)

NYDAHL, J.E. 1971 Heat transfer for the Bödewadt problem. PhD thesis, Colorado State University. (Cited on page 14.)

OBERLEITHNER, KILIAN 2011 Three-dimensional coherent structures in a swirling jet undergoing vortex breakdown: stability analysis and empirical mode construction. *J. Fluid Mech.* **679**, 383–414. (Cited on pages 50, 51, 52, 53, 54, and 102.)

OBERLEITHNER, KILIAN 2012 On Turbulent Swirling Jets: Vortex Breakdown, Coherent Structures, and their Control. PhD thesis, Technische Universität Berlin. (Cited on pages 22, 32, 50, 51, 52, 53, 102, 121, and 124.)

OBERTH, HERMANN 1923 Die Rakete zu den Planetenräumen. (Cited on page 2.)

Orr, William M'F 1907 The Stability or Instability of the Steady Motions of a Perfect Liquid and of a Viscous Liquid. *Proc. R. Irish Acad. Sect. A Math. Phys.* **27**, 9–68 and 69–138. (Cited on pages 21 and 24.)

Orszag, Steven a. 1971 Accurate solution of the Orr–Sommerfeld stability equation. *J. Fluid Mech.* **50** (04), 689–703. (Cited on page 34.)

Ostilla-Mónico, Rodolfo, van der Poel, Erwin P., Verzicco, Roberto, Grossmann, Siegfried & Lohse, Detlef 2014 Exploring the phase diagram of fully turbulent Taylor–Couette flow. *J. Fluid Mech.* **761** (1890), 1–26. (Cited on page 148.)

Owen, J M & Rogers, R H 1989 *Flow and Heat Transfer in Rotating Disc Systems, Volume 1 : Rotor-stator systems*. Taunton, U.K.: Research Studies Press. (Cited on pages 5, 21, 22, 60, 63, and 164.)

Owen, J M & Rogers, R H 1995 *Flow and Heat Transfer in Rotating Disc Systems, Volume 2 : Rotating Cavities*. Taunton, U.K.: Research Studies Press. (Cited on pages 5 and 60.)

Pan, Jixing 1987 On the Origin of Rockets. *T oung Pao* **73** (1), 2–15. (Cited on page 2.)

Panton, Ronald L. 1996 *Incompressible ow*, 2nd edn. John Wiley & Sons, Inc. (Cited on page 13.)

Parras, L. & Fernandez-Feria, R. 2007 Spatial stability and the onset of absolute instability of Batchelor's vortex for high swirl numbers. *J. Fluid Mech.* **583**, 27. (Cited on page 42.)

Pier, Benoît 2003 Finite-amplitude crossflow vortices, secondary instability and transition in the rotating-disk boundary layer. *J. Fluid Mech.* **487**, 315–343. (Cited on page 60.)

Pierrehumbert, R. T. 1984 Local and Global Baroclinic Instability of Zonally Varying Flow. (Cited on page 33.)

Piomelli, Ugo 2008 Wall-layer models for large-eddy simulations. *Prog. Aerosp. Sci.* **44** (6), 437–446. (Cited on page 65.)

Pirozzoli, Sergio & Colonius, Tim 2013 Generalized characteristic relaxation boundary conditions for unsteady compressible flow simulations. *J. Comput. Phys.* **248**, 109–126. (Cited on page 132.)

Poinsot, T J & Lele, S K 1992 Boundary Conditions for Direct Simulation of Compressible Viscous Flows. *J. Comput. Phys.* **101**, 104–129. (Cited on page 132.)

Poncet, S 2005 Ecoulements de type rotor-stator soumis à un flux axial : de Batchelor à Stewartson. Phd, Université de Provence. (Cited on page 71.)

PONCET, SÉBASTIEN, SERRE, ÉRIC & LE GAL, PATRICE 2009 Revisiting the two first instabilities of the flow in an annular rotor-stator cavity. *Phys. Fluids* **21**, 1–30. (Cited on page 61.)

POPE, STEPHEN B. 2001 *Turbulent ows*. Cambridge: Cambridge University Press. (Cited on pages 60 and 98.)

RANDRIAMAMPIANINA, A., ELENA, L., FONTAINE, J. P. & SCHIESTEL, R. 1997 Numerical prediction of laminar, transitional and turbulent flows in shrouded rotor-stator systems. *Phys. Fluids* **9** (6), 1696–1713. (Cited on page 75.)

RASMUSSEN, H. 1971 High Reynolds number flow between two infinite rotating disks. *J. Aust. Math. Soc.* **12** (4), 483–501. (Cited on page 20.)

RAYLEIGH, LORD 1879 On the instability of jets. *Proc. London Math. Soc.* **10**, 4–13. (Cited on page 21.)

REED, HELEN L. & SARIC, WILLIAM S. 1989 Stability of three-dimensional boundary layers. *Annu. Rev. Fluid Mech.* **21**, 235–284. (Cited on pages 61 and 76.)

REYNOLDS, OSBORNE 1883 An experimental investigation of the circumstances which determine whether the motion of water shall be direct or sinuous, and of the law of resistance in parallel channels. *Philos. Trans. R. Soc.* **174**, 935–982. (Cited on pages 21, 24, and 42.)

ROGERS, M.H. & LANCE, G.N. 1959 The rotationally symmetric flow of a viscous fluid in the presence of an infinite rotating disk. *J. Fluid Mech.* **7**, 617–631. (Cited on page 14.)

ROGERS, M.H. & LANCE, G.N. 1962 The axially symmetric flow of a viscous fluid between two infinite rotating disk. *Proc. R. Soc. A Math. Phys. Eng. Sci.* **266**, 109–121. (Cited on pages 20, 70, 71, 72, 74, 123, 137, 138, and 139.)

SAGAUT, PIERRE 2006 *Large Eddy Simulation for Incompressible Flows*, 3rd edn. Springer Berlin Heidelberg. (Cited on pages 60, 61, 65, and 68.)

SAVAS, O. 1983 Circular waves on a stationary disk in rotating flow. *Phys. Fluids* **26** (12), 3445. (Cited on pages 23 and 61.)

SAVAS, O. 1987 Stability of Bodewadt flow. *J. Fluid Mech.* **183** (77). (Cited on pages 23 and 61.)

SCHLICHTING, HERMANN 1960 *Boundary Layer Theory*, 4th edn. McGraw-Hill. (Cited on pages 13, 14, and 68.)

SCHMID, PETER J. 2010 Dynamic mode decomposition of numerical and experimental data. *J. Fluid Mech.* **656**, 5–28. (Cited on pages 8, 88, 89, 101, 123, 150, and 155.)

SCHOUVEILER, L 2001 Instabilities of the flow between a rotating and a stationary disk. *J. Fluid Mech.* **443**, 329–350. (Cited on page 61.)

SCHOUVEILER, L, LE GAL, PATRICE, CHAUVE, M.-P. & TAKEDA, Y 1999 Spiral and circular waves in the flow between a rotating and a stationary disc. *Exp. Fluids* **26**, 179. (Cited on page 76.)

SCHULTZ-GRUNOW, F. 1935 Der Reibungswiderstand rotierender Scheiben in Gehäusen. *ZAMM - Zeitschrift für Angew. Math. und Mech.* **15** (4), 191–204. (Cited on pages 63 and 74.)

SERRE, ERIC, CRESPO DEL ARCO, EMILIA & BONTOUX, PATRICK 2001 Annular and spiral patterns in flows between rotating and stationary discs. *J. Fluid Mech.* **434**, 65–100. (Cited on pages 6, 60, 61, 63, 64, 67, 69, 75, 76, 77, 78, 81, 82, 83, 101, 123, 136, 137, 146, and 147.)

SERRE, ERIC, TULISZKA-SZNITKO, EWA & BONTOUX, PATRICK 2004 Coupled numerical and theoretical study of the flow transition between a rotating and a stationary disk. *Phys. Fluids* **16** (3), 688. (Cited on pages 6, 30, 60, 61, 63, 64, 76, 78, 81, 82, 101, and 146.)

SÉVERAC, ÉRIC, PONCET, SÉBASTIEN, SERRE, ERIC & CHAUVE, MARIE-PIERRE 2007 Large eddy simulation and measurements of turbulent enclosed rotor-stator flows. *Phys. Fluids* **19** (8), 85–113. (Cited on pages 6, 60, 63, 64, 69, 70, 71, 72, 101, 123, 136, 137, and 146.)

SHAMPINE, LF, MUIR, PH & XU, H 2006 A User-Friendly Fortran BVP Solver. *J. Numer. Anal. Ind. Appl. Math.* **1** (2), 201–217. (Cited on page 171.)

SHIRAI, KATSUAKI, BÜTTNER, LARS, OBI, SHINNOSUKE & CZARSKE, JÜRGEN 2013 An experimental study on the flow behavior near the read-and-write arm in a hard disk drive model with a shroud opening. *Microsyst. Technol.* **19**, 1519–1527. (Cited on page 5.)

SIRIVAT, A 1991 Stability experiment of flow between a stationary and a rotating disk. *Phys. Fluids A* **3** (11), 2664–2671. (Cited on page 20.)

SIROVICH, LAWRENCE 1987 Turbulence and the dynamics of coherent structures - part 1: coherent structures. *Q. Appl. Math.* **XLV** (3), 561–571. (Cited on page 88.)

SMITH, NEWELL H. 1947 Exploratory investigation of laminar-boundary-layer oscillations on a rotating disk. *Tech. Rep.* NACA No. 1227. Langley Memorial Aeronautical Laboratory, Langley Field, Va. (Cited on pages 23, 45, 61, 75, and 76.)

SOMMERFELD, A. 1908 Ein beitrag zur hydrodynamischen erklaerung der turbulenten fluessigkeitsbewegungen. *Proc. 4th Int. Congr. Math. III* **174** (1883), 116–124. (Cited on pages 21 and 24.)

STEWARTSON, K. 1953 On the flow between two rotating coaxial disks. *Proc. Camb. Philol. Soc.* **49**, 333–341. (Cited on pages 14 and 15.)

SUTTON, GEORGE P. 2006 *History of Liquid Propellant Rocket Engines*. AIAA. (Cited on page 2.)

SUTTON, GEORGE P. & BIBLARZ, OSCAR 2001 *Rocket Propulsion Elements*, 7th edn. (Cited on pages 3 and 4.)

TATRO, PETER R. 1966 Experiments on Ekman layer instability. PhD thesis, Massachusetts Institute of Technology. (Cited on page 14.)

TATRO, P. R. & MOLLO-CHRISTENSEN, E. L. 1967 Experiments on Ekman layer instability. *J. Fluid Mech.* **28** (03), 531–543. (Cited on page 14.)

TAYLOR, G. I. 1923 Stability of a Viscous Liquid Contained between Two Rotating Cylinders. *Philos. Trans. R. Soc. A Math. Phys. Eng. Sci.* **223**, 289–343. (Cited on page 149.)

THEOFILIS, VASSILIOS 2011 Global Linear Instability. *Annu. Rev. Fluid Mech.* **43** (1), 319–352. (Cited on page 101.)

TSIOLKOVSKY, K.E. 1903 The Exploration of Cosmic Space by Means of Reaction Device. *Guigoz. Sci. Rev.* **3**. (Cited on page 2.)

TULISZKA, EWA, SERRE, ERIC & BONTOUX, PATRICK 2002 On the nature of the boundary layers instabilities in a flow between a rotating and a stationary disc. *Comptes Rendus Mécanique* **330** (2), 91–99. (Cited on pages 77, 81, and 123.)

TULISZKA-SZNITKO, E & SOONG, CY 2000 Instability of non-isothermal flow between coaxial rotating disks. *Eur. Congr. Comput. Methods Appl. Sci. Eng.* (September), 11–14. (Cited on pages 23, 26, 30, and 47.)

TULISZKA-SZNITKO, E & SOONG, CY 2001 Instability of the non-isothermal flow between a rotating and a stationary disks. *TASK Q.* **5** (4), 557–566. (Cited on page 47.)

TULISZKA-SZNITKO, E & ZIELINSKI, ARTUR 2006 Numerical Investigation of Transitional Flow in Co- and Counter-Rotating Annular Cavity. *J. Theor. Appl. Mech.* (1997), 405–420. (Cited on page 61.)

TULISZKA-SZNITKO, E & ZIELINSKI, ARTUR 2007 Instability of the flow in rotating cavity. *J. Theor. Appl. Mech.* **45** (3), 685–704. (Cited on pages 60 and 64.)

TULISZKA-SZNITKO, E., ZIELINSKI, A. & MAJCHROWSKI, W. 2009 Large Eddy Simulation of transitional flows in rotor/stator cavity. *Arch. Mech.* **61** (2), 95–120. (Cited on pages 60 and 64.)

VON BRAUN, WERNHER & ORDWAY, F. 1974 *History of Rocketry and Space Travel*, 3rd edn. New York. (Cited on page 2.)

VON KÁRMÁN, THEODORE 1921 Über laminare und turbulente Reibung. *Zeitschrift für Angew. Math. und Mech.* **1** (4), 233–251. (Cited on pages 12, 14, 16, 17, 23, 45, 46, 47, 48, and 109.)

WEIDEMAN, J. A. C. & REDDY, S. C. 2000 A MATLAB differentiation matrix suite. *ACM Trans. Math. Softw.* **26** (4), 465–519. (Cited on page 35.)

WHITE, FRANK M. 2006 *Viscous Fluid Flow*, 3rd edn. McGraw-Hill. (Cited on pages 13 and 74.)

WU, XIAOHUA & SQUIRES, KYLE D. 2000 Prediction and investigation of the turbulent flow over a rotating disk. *J. Fluid Mech.* **418**, 231–264. (Cited on page 61.)

YUR'YEV, B. N. 1951 *Collected Works of K.E. Tsiolkowski*. USSR Academy of Sciences. (Cited on page 2.)

Résumé court

Ce manuscrit présente une étude couplée, numérique et théorique, portant sur les écoulements tournants transitionnels et turbulents. L'accent y est mis sur la formation de structures macroscopiques cohérentes au sein de l'écoulement, générées par des procédés rendus fortement tri-dimensionnels par la présence des couches limites sur les disques et le long des parois cylindriques extérieure (carter) et/ou intérieure (moyeu). La complexité de ces écoulements pose de véritables difficultés en recherche fondamentale mais les résultats de ces travaux ont aussi une importance non négligeable pour les machines industrielles tournantes, depuis les disque-durs jusqu'aux turbopompes spatiales, la conception de ces dernières étant la motivation première pour ces travaux de thèse.

Ce travail peut être divisé en deux sous-parties. Dans un premier temps, les cavités industrielles sont modélisées par de simples cavités rotor/stator lisses pour y étudier la dynamique de l'écoulement. Comme les campagnes expérimentales sur les machines industrielles ont révélé de dangereux phénomènes instationnaires en leur sein, l'accent est mis sur l'obtention et l'étude des fluctuations de pression dans les écoulements modèles. Ensuite, les SGE de trois configurations de turbine industrielle réelle sont réalisées pour étudier les fluctuations de pression *in situ* et appliquer les diagnostiques éprouvés sur les géométries modèles.

Short abstract

This thesis provides a numerical and theoretical investigation of transitional and turbulent enclosed rotating flows, with a focus on the formation of macroscopic coherent flow structures. The underlying processes are strongly three-dimensional due to the presence of boundary layers on the discs and on the walls of the outer (resp. inner) cylindrical shroud (resp. shaft). The complexity of these flows poses a great challenge in fundamental research however the present work is also of importance for industrial rotating machinery, from hard-drives to space engines turbopumps - the design issues of the latter being behind the motivation for this thesis.

The present work consists of two major investigations. First, industrial cavities are modeled by smooth rotor/stator cavities and therein the dominant flow dynamics is investigated. For the experimental campaigns on industrial machinery revealed dangerous unsteady phenomena within the cavities, the emphasis is put on the reproduction and monitoring of unsteady pressure fluctuations within the smooth cavities. Then, the LES of three configurations of real industrial turbines are conducted to study *in situ* the pressure fluctuations and apply the diagnostics already vetted on academic problems.